

UNIVERSITY OF STRATHCLYDE  
Department of Physics

**Microfabrication of high-density  
optoelectronic devices for opto-  
genetic studies of neural tissue**

Robert Scharf



A thesis presented in fulfilment of the requirements  
for the degree of Doctor of Philosophy

October 2016



# Copyright Statement

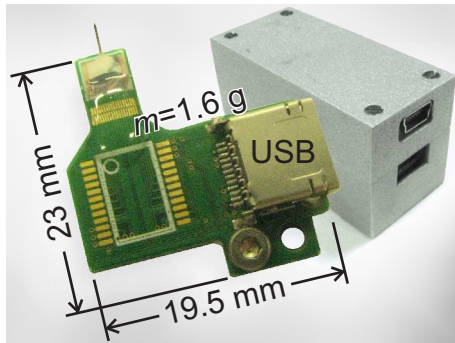
This thesis is the result of the author's original research. It has been composed by the author and has not been previously submitted for examination which has led to the award of a degree. The copyright of this thesis belongs to the author under the terms of the United Kingdom Copyright Acts as qualified by University of Strathclyde Regulation 3.50. Due acknowledgement must always be made of the use of any material contained in, or derived from, this thesis.

Glasgow, 20/02/17

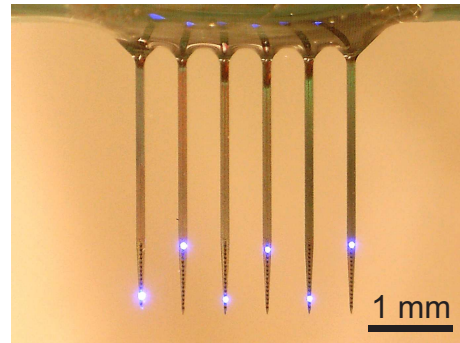
---

Robert Scharf

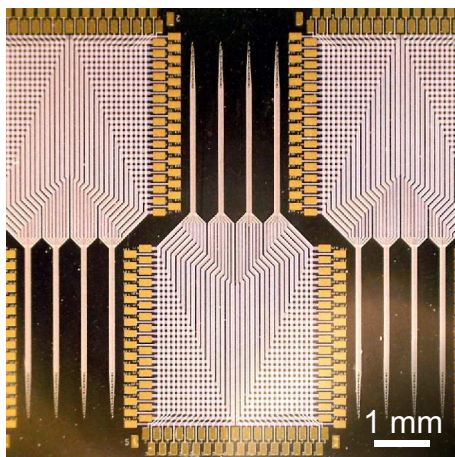
# Frontispiece



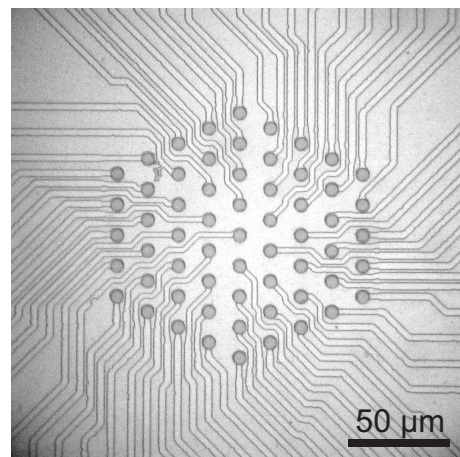
16-channel  $\mu$ LED probe system for selective optogenetic stimulation of cortical layers



Patterned stimulation using six-shank 96-channel  $\mu$ LED probe for optogenetic stimulation across brain regions



Microprobes for optogenetic stimulation and simultaneous electrical recording from the brain, devices on-chip during fabrication



Transparent planar high-density (15  $\mu$ m pitch) 61 electrode array for optogenetic studies of the retina *in vitro*

# Abstract

Control of neural activity is a powerful tool for studying circuits in the brain. Although optogenetics offers innovative approaches to achieve this in a cell-type-specific manner with millisecond precision, there are still significant challenges. For example, it is still difficult to activate cell populations at high spatial resolution *in vivo* as well as to record responses from individual neurons in large groups both *in vivo* and *in vitro*. The present work covers the development and improvement of optoelectronic microdevices to this end, that can be divided into two categories: novel silicon probes using micro-scale light emitting diodes ( $\mu$ LEDs) for *in vivo* circuit manipulation and analysis, and *in vitro* electrode arrays for massively parallel recording. Compact penetrating needle probes have been designed to contain up to 96 independently controllable  $\mu$ LEDs, emitting up to  $400 \text{ mW/mm}^2$  of light at 450 nm. Standard operation regimes entail only a minimum rise in temperature. The devices allow coverage of brain structures, such as the mouse cortex, at high spatial resolution and are capable of inducing rich spatiotemporal patterns of neural activity *in vivo*. The devices can also be extended to offer recording capabilities in the future, and prototype devices are shown. In order to demonstrate how electrode density is important for obtaining good recordings from single, densely-packed neurons, existing planar retinal recording devices have been adapted and fabricated, containing electrodes with a pitch as low as  $15 \mu\text{m}$ . Versions with increased electrode counts have been designed and will be fabricated in the future, extending the toolbox for a better understanding of complex neural circuits.

# Acknowledgements

I would like to thank Prof. Martin Dawson and my supervisor Dr. Keith Mathieson for giving me the opportunity to prepare this PhD thesis at the Institute of Photonics. I would like to thank Keith for his guidance, support and encouragement. I am also very grateful to Dr. Shuzo Sakata for being a long-term collaborator in this project and for helping tremendously with his biological expertise. Being part of the Neurophotonics group, I have been privileged to have worked with great people and I would like to thank everyone for being so welcoming and supportive. I would like to thank the microfabrication team for their help in the cleanroom and all remaining IoP colleagues, past and present, for making the institute such an enjoyable place.

# Contents

<b>List of Figures</b>	<b>i</b>
<b>List of Tables</b>	<b>iv</b>
<b>Nomenclature</b>	<b>v</b>
<b>1 Introduction</b>	<b>1</b>
1.1 Motivation . . . . .	1
1.2 Thesis Outline . . . . .	3
<b>2 Neuroscience and Optogenetics</b>	<b>5</b>
2.1 Nervous Systems . . . . .	5
2.1.1 Neurons . . . . .	6
2.1.2 The Eye . . . . .	9
2.1.3 The Brain . . . . .	12
2.2 Optogenetic Neural Stimulation . . . . .	14
2.2.1 Opsins . . . . .	16
2.2.1.1 Opsins for Excitation . . . . .	17
2.2.1.2 Opsins for Inhibition . . . . .	17
2.2.1.3 Opsin Expression . . . . .	18
2.2.2 Alternative Methods . . . . .	19
2.3 Neural Recording . . . . .	20
2.3.1 Optical Methods . . . . .	20
2.3.2 Electrophysiology . . . . .	21
2.3.3 Data Analysis . . . . .	23
2.4 LED Light Sources . . . . .	25
2.5 Neural Probes . . . . .	30
2.5.1 Optical Stimulation . . . . .	30
2.5.2 Electrical Recording . . . . .	33
2.5.3 Integrated Devices . . . . .	37
2.6 Conclusion . . . . .	40
<b>3 Microfabrication</b>	<b>41</b>
3.1 Photolithography . . . . .	43
3.2 Material Deposition . . . . .	45
3.3 Annealing . . . . .	47
3.4 Etching . . . . .	47
3.4.1 Wet Etching . . . . .	48
3.4.2 Dry Etching . . . . .	49

3.5	Testing . . . . .	50
3.6	Substrate Thinning . . . . .	50
3.7	Dicing . . . . .	51
3.8	Bonding . . . . .	51
3.9	Encapsulation . . . . .	51
3.10	Conclusion . . . . .	53
<b>4</b>	<b><math>\mu</math>LED Needle Probes</b>	<b>54</b>
4.1	Design . . . . .	55
4.2	Fabrication . . . . .	58
4.2.1	Front-End . . . . .	60
4.2.2	Back-End . . . . .	65
4.3	Simulation . . . . .	66
4.3.1	Light Propagation . . . . .	67
4.3.2	Device Heating . . . . .	69
4.4	Characterization . . . . .	78
4.4.1	Electrical Characteristics and Light Output . . . . .	78
4.4.2	Device Heating . . . . .	80
4.5	Probe Controlling . . . . .	82
4.5.1	Control Hardware . . . . .	82
4.5.1.1	Headstages . . . . .	83
4.5.1.2	Interface Board . . . . .	84
4.5.2	Control Software . . . . .	85
4.6	Conclusion . . . . .	86
<b>5</b>	<b><math>\mu</math>LED Probes <i>In Vivo</i></b>	<b>87</b>
5.1	GABAergic Interneurons . . . . .	88
5.2	Experimental Setup . . . . .	89
5.3	Signal Processing . . . . .	92
5.3.1	Spike Sorting . . . . .	92
5.3.2	Depth Estimation of Single Units . . . . .	93
5.3.3	Local Field Potentials . . . . .	93
5.3.4	Current Source Density Analysis . . . . .	93
5.3.5	Classification Analysis . . . . .	95
5.4	Depth-Specific Neural Activation . . . . .	95
5.5	Depth-Specific Neural Population Activation . . . . .	97
5.6	Histology . . . . .	100
5.7	Discussion and Outlook . . . . .	101
5.8	Conclusion . . . . .	103
<b>6</b>	<b>Recording <math>\mu</math>LED Needle Probes</b>	<b>104</b>
6.1	Device Overview . . . . .	105
6.2	Fabrication . . . . .	106
6.3	Characterization . . . . .	109
6.4	Probe Controlling . . . . .	111
6.5	Conclusion . . . . .	112

<b>7</b>	<b>Planar <i>In Vitro</i> Electrode Arrays</b>	<b>113</b>
7.1	61 Electrode Arrays . . . . .	115
7.1.1	Mask Layout . . . . .	115
7.1.2	Fabrication . . . . .	116
7.1.2.1	ITO Etching . . . . .	117
7.1.2.2	Passivation . . . . .	118
7.1.2.3	Vias Etching . . . . .	118
7.1.2.4	Electroplating . . . . .	120
7.1.2.5	Alternative Methods for Passivation . . . . .	120
7.1.3	Characterization . . . . .	121
7.2	519 Electrode Arrays . . . . .	122
7.3	Readout Hardware . . . . .	125
7.4	Outlook . . . . .	126
7.4.1	512 Electrode Arrays, Second Generation . . . . .	126
7.4.2	2048 Electrode Arrays . . . . .	127
7.5	Conclusion . . . . .	128
<b>8</b>	<b>Future Work</b>	<b>129</b>
8.1	$\mu$ LED Needle Probes . . . . .	129
8.1.1	Wireless Probes . . . . .	129
8.1.2	Multi-Colour Probes . . . . .	130
8.1.2.1	Colour-Tunable LEDs . . . . .	130
8.1.2.2	Colour Converters . . . . .	131
8.1.2.3	Transfer Printing . . . . .	132
8.1.3	Thermal Management . . . . .	133
8.1.4	LED Addressing . . . . .	134
8.1.5	3D $\mu$ LED Arrays . . . . .	136
8.1.6	Further Improvements . . . . .	137
8.2	$\mu$ LED Probes <i>In Vivo</i> . . . . .	137
8.3	Recording $\mu$ LED Needle Probes . . . . .	138
8.3.1	Wireless Probes . . . . .	138
8.3.2	Electronics On-Chip . . . . .	139
8.3.3	3D LED / Electrode Arrays . . . . .	139
8.4	Planar <i>In Vitro</i> Electrode Arrays . . . . .	140
<b>9</b>	<b>Conclusion</b>	<b>142</b>
<b>A</b>	<b>Appendix</b>	<b>145</b>
	<b>Bibliography</b>	<b>166</b>
	<b>List of Publications</b>	<b>182</b>

# List of Figures

1.1	Caenorhabditis elegans . . . . .	1
2.1	Signalling between neurons (anatomy) . . . . .	6
2.2	Signalling between neurons (physiology) . . . . .	7
2.3	The eye . . . . .	10
2.4	Types of neurons in the retina . . . . .	11
2.5	Organization of the human neocortex . . . . .	12
2.6	Electrical and optogenetic neural modulation . . . . .	15
2.7	Optogenetic constructs . . . . .	16
2.8	Brain-electrode interface . . . . .	22
2.9	Electrophysiological data analysis steps . . . . .	23
2.10	LED working principles . . . . .	27
2.11	Manufacturing approaches for implantable neural probes . . . . .	31
2.12	Overview of devices for optogenetic stimulation . . . . .	32
2.13	Devices for electrophysiological recording <i>in vitro</i> . . . . .	34
2.14	Overview of devices for electrophysiological recording <i>in vivo</i> . . . . .	36
2.15	Overview of devices for integrated stimulation and recording . . . . .	39
3.1	Microfabrication tools . . . . .	42
3.2	Positive and negative types of photoresist . . . . .	44
3.3	Microtechnological structuring mechanisms . . . . .	44
3.4	Material deposition mechanisms used in microfabrication . . . . .	45
3.5	Etch profiles resulting from different dry and wet etch processes . . . . .	48
3.6	Encapsulation quality . . . . .	52
3.7	Parylene deposition (schematic) . . . . .	52
4.1	Working principle of LED needle probes . . . . .	54
4.2	1D single-shank $\mu$ LED array (schematic) . . . . .	56
4.3	Overview of designed and fabricated $\mu$ LED needle probes . . . . .	57
4.4	Comparison of optogenetic stimulation devices . . . . .	58
4.5	Fabrication steps of $\mu$ LED needle probes (front-end) . . . . .	61
4.6	Fabrication steps of LED needle probes (back-end) . . . . .	65
4.7	Simulated light propagation in brain tissue . . . . .	67
4.8	Simulated $\mu$ LED resolution . . . . .	68
4.9	COMSOL model of heat transfer in $\mu$ LED probe and environment . . . . .	71
4.10	Simulated tissue temperatures during LED probe operation . . . . .	72
4.11	Arrhenius damage integrals for $\mu$ LEDs . . . . .	75
4.12	Influence of various model parameters on simulated temperature (1) . . . . .	76
4.13	Influence of various model parameters on simulated temperature (2) . . . . .	76

---

4.14	Electrical and optical characterization of $\mu$ LEDs . . . . .	79
4.15	Probe heating as detected by a thermal camera . . . . .	81
4.16	Simplified schematic of $\mu$ LED probe control hardware . . . . .	82
4.17	$\mu$ LED probe headstages . . . . .	83
4.18	$\mu$ LED probe interface board . . . . .	84
4.19	Control software (screenshot) . . . . .	85
5.1	GABAergic interneurons in the cortex . . . . .	88
5.2	Parallel implantation of $\mu$ LED probe and NeuroNexus optrode . . . . .	90
5.3	Irradiance values on electrodes from an angled $\mu$ LED probe . . . . .	91
5.4	Example of a voltage trace recorded from a microelectrode . . . . .	92
5.5	Depth-dependent activation of PV+ neurons <i>in vivo</i> . . . . .	96
5.6	Distinct neural population activity induced by $\mu$ LEDs <i>in vivo</i> . . . . .	98
5.7	Histological assessment of $\mu$ LED probe invasiveness . . . . .	101
6.1	$\mu$ LED arrays with integrated recording electrodes . . . . .	106
6.2	Fabrication steps of recording $\mu$ LED needle probe . . . . .	107
6.3	Recording $\mu$ LED probe with electrode vias . . . . .	109
6.4	Crosstalk between LED and electrode tracks in needle probes . . . . .	110
6.5	Interface hardware for recording $\mu$ LED probes . . . . .	111
7.1	61 electrode array channel map . . . . .	114
7.2	61 electrode arrays (schematic) . . . . .	115
7.3	Fabrication of 61 electrode arrays . . . . .	116
7.4	61 electrode array with 15 $\mu$ m pitch . . . . .	117
7.5	Parylene passivation of electrode arrays . . . . .	121
7.6	Inter-channel capacitance of a 61 MEA with 15 $\mu$ m electrode pitch . . . . .	122
7.7	519 electrode array with 30 $\mu$ m electrode pitch (schematic) . . . . .	123
7.8	Fabrication of 61 electrode arrays . . . . .	124
7.9	61 electrode array adapter board . . . . .	126
7.10	High density 512 electrode array (schematic) . . . . .	127
7.11	High density 2048 electrode arrays (schematic) . . . . .	128
8.1	Selective deposition of colour converters on $\mu$ LED probes . . . . .	131
8.2	Transfer-printable $\mu$ LEDs . . . . .	133
8.3	Nine-shank multiplexed probe containing 576 $\mu$ LEDs (schematic) . . . . .	135
8.4	3D chip stacking . . . . .	136
8.5	Optogenetic receptive field mapping <i>in vivo</i> . . . . .	138
8.6	3D multi-shank $\mu$ LED/electrode arrays (schematic) . . . . .	140
8.7	Spatial undersampling using a 61 electrode array (15 $\mu$ m pitch) . . . . .	140

A.1	Explanation of device codes for fabricated $\mu$ LED devices . . . . .	151
A.2	Photomasks for LED probe fabrication (Set 1) . . . . .	151
A.3	Photomasks for LED probe fabrication (Set 2) . . . . .	152
A.4	Material for LED needle probe fabrication . . . . .	152
A.5	LED driver circuit schematic . . . . .	153
A.6	LED driver printed circuit board . . . . .	154
A.7	LED probe holder . . . . .	154
A.8	Simulated tissue temperatures during LED probe operation . . . .	155
A.9	Effect of reaction parameter uncertainties on Arrhenius damage .	156
A.10	Simulated $\mu$ LED resolution (2 sources) . . . . .	156
A.11	Cross-section of a conductor (schematic) . . . . .	157
A.12	Fractions of $\mu$ LED light detected by a photodiode . . . . .	158
A.13	LEDs with 10 $\mu$ m diameter . . . . .	159
A.14	First generation control hardware . . . . .	160
A.15	Control software for 3D $\mu$ LED arrays . . . . .	160
A.16	Transconductance amplifier (schematic) . . . . .	162
A.17	Photomask for fabrication of individual transfer-printable $\mu$ LEDs	163

# List of Tables

3.1	Chemicals used for wet etching and their etch rates . . . . .	49
4.1	Overview of designed and fabricated $\mu$ LED needle probes . . . . .	56
4.2	Material properties used in thermal simulations . . . . .	70
4.3	Peak temperature from simultaneous pulse on 16 $\mu$ LEDs . . . . .	77
6.1	Overview of recording $\mu$ LED needle probes . . . . .	105
8.1	Thermal properties of silicon and diamond . . . . .	133
8.2	LED addressing schemes . . . . .	135
A.1	RIE 1 silicon dioxide etch recipes . . . . .	145
A.2	RIE 1 silicon nitride etch recipe . . . . .	145
A.3	RIE 1 parylene C etch recipe . . . . .	146
A.4	RIE 1 oxygen clean . . . . .	146
A.5	RIE 2 nickel/gold (Ni/Au) current spreading metal layer etch . . .	146
A.6	ICP 1 titanium/aluminium (Ti/Al) etch . . . . .	147
A.7	ICP 1 indium tin oxide (ITO) etch . . . . .	147
A.8	ICP 2 gallium nitride (GaN) etch . . . . .	148
A.9	Deep reactive ion etch (Bosch process) for silicon (Si) . . . . .	148
A.10	RTA metal on gallium nitride annealing recipes . . . . .	148
A.11	Sputter coater metal deposition recipes . . . . .	149
A.12	SCS coater parylene deposition recipes . . . . .	149
A.13	PECVD silicon dioxide deposition recipes . . . . .	150
A.14	PECVD silicon oxynitride deposition recipe . . . . .	150
A.15	Electrical resistivities of different conductors . . . . .	158
A.16	Fractions of $\mu$ LED light detected by a photodiode . . . . .	159
A.17	Minimum feature sizes for different electrode arrays . . . . .	165

# Nomenclature

$\alpha_{\text{LED,elec}}$	normal angle between an electrode and a $\mu\text{LED}$	
$\alpha_{\text{probe,LED}}$	angle of implantation of the $\mu\text{LED}$ probe	
$\Delta x$	scan distance	[m]
$\Delta z$	height difference	[m]
$\varnothing_{\text{LED}}$	LED diameter	[m]
$\lambda$	wavelength	[m]
$\mu_{\text{a}}$	absorption coefficient	$[\text{m}^{-1}]$
$\mu_{\text{s}}$	scattering coefficient	$[\text{m}^{-1}]$
$\nabla$	$\nabla = \left( \frac{\partial}{\partial x}, \frac{\partial}{\partial y}, \frac{\partial}{\partial z} \right) = \vec{e}_x \frac{\partial}{\partial x} + \vec{e}_y \frac{\partial}{\partial y} + \vec{e}_z \frac{\partial}{\partial z}$	
$\nu_{\text{s}}$	Poisson ratio of the substrate	
$\omega$	perfusion rate	$[\text{s}^{-1}]$
$\rho$	density	$[\text{kg m}^{-3}]$
$\sigma$	electrical conductivity	$[\text{S m}^{-1}]$
$\tau$	decay time constant	[s]
$\varphi$	electric field potential	[V]
$A$	frequency factor	$[\text{s}^{-1}]$
$A_{\text{elec}}$	electrode area	$[\text{m}^2]$
$C$	heat capacity	$[\text{J kg}^{-1} \text{K}^{-1}]$
$c$	speed of light ( $\sim 2.998 \cdot 10^8$ )	$[\text{m s}^{-1}]$
$C_{\text{m}}$	membrane capacitance	[F]
$D$	current source density approximation	$[\text{A m}^{-3}]$
$d_{\text{elec}}$	electrode diameter	[m]
$d_{\text{elec}}$	electrode diameter	[m]
$d_{\text{LED,elec}}$	distance between $\mu\text{LED}$ and electrode	[m]
$d_{\text{probes}}$	implantation distance between $\mu\text{LED}$ /recording probe	[m]
$E$	electric field	$[\text{V m}^{-1}]$
$e$	elementary charge ( $\sim 1.602 \cdot 10^{-19}$ )	[C]
$E_{\text{c}}$	conduction band energy	[eV]
$E_{\text{g}}$	bandgap energy	[eV]
$E_{\text{K}^+}$	equilibrium potential for potassium ions	[V]
$E_{\text{Na}^+}$	equilibrium potential for sodium ions	[V]
$E_{\text{s}}$	Young's modulus of the substrate	$[\text{N m}^{-2}]$
$E_{\text{v}}$	valence band energy	[eV]
$f$	frequency	$[\text{s}^{-1}]$
$G_{\text{K}^+}$	potassium ion conductance	[S]
$G_{\text{m}}$	leak conductance	[S]
$G_{\text{Na}^+}$	sodium ion conductance	[S]

## Nomenclature

---

$h$	Planck's constant ( $\sim 6.626 \cdot 10^{-34}$ )	$[\text{m}^2 \text{kg}^{-1} \text{s}^{-1}]$
$h$	sampling interval	$[\text{m}]$
$I$	current	$[\text{A}]$
$I$	current	$[\text{A}]$
$I$	irradiance	$[\text{W m}^{-2}]$
$I_m$	current source density	$[\text{A m}^{-3}]$
$I_{\text{plat,array}}$	platinization current for an electrode array	$[\text{A}]$
$I_{\text{plat,elec}}$	platinization current per electrode	$[\text{A}]$
$i_{\text{plat}}$	specific platinization current	$[\text{A m}^{-2}]$
$I_s$	reverse saturation current	$[\text{A}]$
$J$	current density	$[\text{A m}^{-2}]$
$k$	Boltzmann constant ( $\sim 1.381 \cdot 10^{-23}$ )	$[\text{m}^2 \text{kg s}^{-2} \text{K}^{-1}]$
$k$	correction factor	
$k$	thermal conductivity	$[\text{W m}^{-1} \text{K}^{-1}]$
$n$	number of cells that have not yet reacted	
$n_{\text{elec}}$	number of electrodes	
$p_{\text{elec}}$	electrode pitch	$[\text{m}]$
$p_{\text{elec}}$	electrode pitch	$[\text{m}]$
$P_{\text{el}}$	electrical power	$[\text{W}]$
$p_{\text{LED}}$	$\mu\text{LED}$ pitch	$[\text{m}]$
$Q$	heat source	$[\text{W m}^{-3}]$
$R$	radius of curvature after film deposition	$[\text{m}]$
$R$	resistance	$[\Omega]$
$R$	universal gas constant ( $\sim 8.315$ )	$[\text{J mol}^{-1} \text{K}^{-1}]$
$r$	depth	$[\text{m}]$
$R_0$	radius of curvature before film deposition	$[\text{m}]$
$r_{\text{black}}$	ratio of black space on platinized electrode arrays	
$T$	temperature	$[\text{K}]$
$t$	time	$[\text{s}]$
$t$	time	$[\text{s}]$
$T_0$	initial temperature	$[\text{K}]$
$t_f$	film thickness	$[\text{m}]$
$t_s$	substrate thickness	$[\text{m}]$
$V$	voltage	$[\text{V}]$
$V$	voltage	$[\text{V}]$
$V_0$	initial voltage	$[\text{V}]$
$V_{\text{excited}}$	excitable volume	$[\text{m}^3]$
$V_m$	membrane potential	$[\text{V}]$
$z_{\text{elec},1}$	distance of electrode 1 from the probe tip	$[\text{m}]$
$z_{\text{elec},n}$	position of the $n^{\text{th}}$ electrode from the probe tip	$[\text{m}]$
$z_{\text{LED},1}$	distance of $\mu\text{LED}$ 1 from the probe tip	$[\text{m}]$
$z_{\text{LED},n}$	position of the $n^{\text{th}}$ $\mu\text{LED}$ from the probe tip	$[\text{m}]$
$z_{\text{probe,elec}}$	implantation depth of the recording probe	$[\text{m}]$
$z_{\text{probe,LED}}$	implantation depth of the $\mu\text{LED}$ probe	$[\text{m}]$

”	inch (2.54 cm)	
$\Delta E$	activation energy	[J mol <sup>-1</sup> ]
$\mu$ ECoG	micro-electrocorticography	
$\mu$ LED	micro light emitting diode	
$\mu$ TP	micro transfer printing	
AAV	adeno-associated virus	
AC	alternating current	
ACR	anion channel rhodopsin	
ADP	adenosine diphosphate	
ALD	atomic layer deposition	
AlGaAs	aluminium gallium arsenide	
AlGaInP	aluminium gallium indium phosphide	
ATP	adenosine triphosphate	
Au	gold	
BOE	buffered oxide etch	
CCD	charge-coupled device	
CdSe	cadmium selenide	
ChR2	channelrhodopsin 2	
cm	centimetre (0.01 m)	
CMP	chemical mechanical polishing	
Cr	chromium	
CSD	Current source density	
CVD	chemical vapor deposition	
DAC	digital to analog converter	
DC	direct current	
DRIE	deep reactive ion etching	
e-beam	electron beam	
EBL	electron blocking layer	
eV	electronvolt ( $\sim 1.602 \cdot 10^{-19}$ J)	
FEM	finite element method	
FFC	flexible flat cable	
FIB	focussed ion beam	
fMRI	functional magnetic resonance imaging	
g	gram ( $10^{-3}$ kg)	
g	gram (0.001 kg)	
GABA	gamma-aminobutyric acid	
GaN	gallium nitride	
GaP	gallium phosphide	
GUI	graphical user interface	
h	hour	
HCL	hydrochloric acid	
HD	high-density	
HDMS	hexamethyldisilazane	
HF	hydrofluoric acid	

Hz	hertz ( $s^{-1}$ )
IBE	ion beam etching
IC	integrated circuit
ICP RIE	inductively coupled plasma reactive ion etching
ID	identification number
InGaN	indium gallium nitride
IPA	isopropanol
IrO <sub>2</sub>	iridium oxide
ITO	indium tin oxide
kbps	kilobits per second ( $10^3$ bps)
kHz	kilohertz ( $10^3$ Hz)
KOH	potassium hydroxide
LED	light emitting diode
LFP	local field potential
Li-Fi	light fidelity
LTO	low temperature oxide
Mbps	megabits per second ( $10^6$ bps)
MEA	multi electrode array
min	minute
MOVPE	metalorganic vapour phase epitaxy
MQW	multiple quantum wells
MQW	multiple quantum wells
ms	millisecond ( $10^{-3}$ s)
MUA	multiple unit activity
N <sub>2</sub>	nitrogen
nA	nanoampere ( $10^{-9}$ A)
NH <sub>4</sub> F	ammonium fluoride
Ni	nickel
nm	nanometre ( $10^{-9}$ m)
NpHR	halorhodopsin
O <sub>2</sub>	oxygen
PC	personal computer
PCA	principle component analysis
Pd	palladium
PDMS	polydimethylsiloxane
PECVD	plasma-enhanced chemical vapor deposition
PEDOT	poly(3,4-ethylenedioxythiophene)
PI	propidium iodide
pl	picolitre ( $10^{-9}$ l)
PR	photoresist
Pt	platinum
PV	parvalbumin
PVD	physical vapor deposition
PWM	pulse width modulation

RF	radio frequency
RGC	retinal ganglion cell
RIE	reactive ion etching
RPM	revolutions per minute
s	second
sccm	standard cubic centimeters per minute
SiO <sub>x</sub> N <sub>y</sub>	silicon oxynitride
SIPBS	Strathclyde Institute of Pharmacy and Biomedical Sciences
SIROF	sputtered iridium oxide film
SNF	Stanford Nanofabrication Facility
SOI	silicon-on-insulator
SPI	Serial Peripheral Interface
SST	somatostatin
TB	terabyte (10 <sup>12</sup> byte)
Ti	titanium
TiN	titanium nitride
Torr	torr (~ 133.3 Pa)
TTL	transistor-transistor logic
USB	Universal Serial Bus
VSD	voltage-sensitive dye
ZnS	zinc sulfide

# 1 Introduction

The human brain is a tremendously complex organ [1], often called the most complex object in the known universe. Understanding how it works, in terms of how the flow of electrical signals through neural circuits gives rise to the mind, is one of the biggest challenges in science. Currently, huge efforts are made to approach this problem in an interdisciplinary way. Large programs have been put in motion in the past years [2], including the Human Brain Project in Europe [3] and the BRAIN Initiative in the US [4,5]. To understand the exact wiring diagram, research has to be conducted on the neuronal level.

## 1.1 Motivation

Although the coarse structures of the brain are similar between individuals, the details are in the wiring diagram of the microcircuits. When trying to study the brain at such high resolution, it is a good idea to take an approach through first studying simpler structures and less complex model organisms. These simplifications can still provide very helpful results, since many principles of neural function and organization are conserved across different animal species [5]. In order to understand the difficulties of studying complex neural systems, one can look at one of the most popular model organisms for studying neural circuits: the roundworm *C. elegans* (see Figure 1.1). The ~1 mm-long hermaphrodite worm has



**Figure 1.1:** *Caenorhabditis elegans*, a simple model organism containing exactly 302 individually named and connectivity-mapped neurons [6]

exactly 302 neurons. Its wiring diagram, with over 7 000 synapses, is completely known [7], but until today it remains the only organism for which this mapping has been achieved. Although it is a very complicated procedure, the structure of nervous systems can now be obtained by electron microscopy integrated with tissue slicing systems. These setups are capable of producing stacks of images with high resolution in three dimensions [8].

However, even if all the morphological information of a particular nervous system is known, there is still no deep understanding of how it functions. Additional information, about how the firing patterns of all individual neurons are interrelated, is needed. The information cannot be extracted from dead tissue, but requires sophisticated technology that can probe live brain tissue [9, 10] and advanced methods for analysing the resultant datasets (can be 100s TB in size [11]).

As outlined by the BRAIN initiative, there is a strong need to “accelerate the development and application of new technologies that will enable researchers to produce dynamic pictures of the brain that show how individual brain cells and complex neural circuits interact at the speed of thought” [5]. This need for technology development is also reflected in the name of the BRAIN Initiative: “Brain Research through Advancing Innovative Neurotechnologies”. One category of tools is concerned with perturbation, more precisely activation and inhibition of neural firing. The relatively new technique of optogenetics [12–14] can be very helpful for the analysis of neural microcircuits, as it allows this on a millisecond-timescale and in a light-controlled fashion [15–18]. Cell types can be targeted genetically and neurons can be targeted individually. In this way, optogenetics can give insight into neural coding and also help further the understanding of how neural activity links to behavioural responses. It is therefore described in the BRAIN initiative as one of the key techniques, for which new tools should be developed. In order to fully exploit the technique, light needs to be delivered at high spatiotemporal resolution to regions that are often difficult to access.

Multi-photon stimulation, having good sub-cellular resolution [19–22], is limited to  $\sim 1$  mm in depth because of light absorption and scattering in the brain. One way around this problem is miniature *in vivo*-implantable probes allowing multi-point optical stimulation at resolutions approaching the cellular scale.

Just as important for neural circuit analysis is a means of fast recording of circuit responses to the induced perturbations, for which electrode arrays are a good method. It is desirable for these to have high spatial resolution and high electrode counts. At the same time, interference with the neural system has to be kept at a minimum. This means that implantable devices need to be very compact to minimize tissue damage.

New specialised tools are needed for these purposes (see review by Alivisatos *et al.* [23]), posing challenges for physicists and engineers. These problems will be addressed in this thesis, covering the development of novel photonic technologies for sophisticated optogenetic studies. The aim is for these devices and their future enhancements, to bring us one step closer to understanding neural computation and so brain malfunction.

“By exploring these patterns of activity, both spatially and temporally, and utilizing simpler systems to learn how circuits function, we can generate a more comprehensive understanding of how the brain produces complex thoughts and behaviors. This knowledge will be an essential guide to progress in diagnosing, treating, and potentially curing the neurological diseases and disorders that devastate so many lives.” [5]

## 1.2 Thesis Outline

The main concepts and techniques that allow these devices to be produced, are covered in chapters 2 and 3. This includes an introduction to the general basics of the fields involved in this interdisciplinary work, namely neurobiology, semiconductor physics and microfabrication. The subsequent chapters cover different devices for neurobiological studies. Chapters 4 and 5 concern penetrating needle-style probes for spatially precise optogenetic neuronal activation in the

brain *in vivo*, focussing on the fabrication and characterization and the *in vivo* performance, respectively. The processes for fabricating different arrays have been developed and are described in detail. Light propagation has been simulated and measured and it is shown that a wide range of tissue volumes can be stimulated with the probes. Device heating has been simulated and the model has been verified experimentally. Thermal properties are shown to be at acceptable levels. A compact system for driving the multi-channel  $\mu$ LED probes has been developed and produced and is introduced. It consists of a hardware (headstage and interface) and a software component. The probes' usefulness is then shown by activating subsets of cortical neurons in a depth-dependent manner *in vivo* in a mouse model. An advancement of this device is described in chapter 6: integrating recording electrodes makes it possible to fully exploit the probe's capabilities, as the chapter goes on to show. The described fabrication process can offer high electrode counts and densities, as shown in prototype devices. Chapter 7 describes the design, fabrication and performance of a different class of devices: transparent planar electrode arrays for (optogenetic) *in vitro* studies of the eye. Again, the design and fabrication are described, followed by characterization. It is shown how high electrode density is key for the complete recording from a volume of neurons. The following chapter outlines some directions and ideas for future work (chapter 8) after which, the overall conclusions are drawn in chapter 9.

# 2 Basics of Neuroscience and Optogenetics

This work concerns the development of novel technologies for neuroscience studies using optogenetics. This introductory chapter therefore aims to briefly describe some of the main concepts of these respective fields. The following section 2.1 touches on the basics of nervous systems. Optogenetics and other neuronal stimulation methods are then introduced in section 2.2, with section 2.3 covering neuronal recording. A summary of some key devices in this field is given in section 2.5.

## 2.1 Nervous Systems

The nervous system in vertebrate species consists of the central nervous system and the peripheral nervous system. The central nervous system includes the brain and the spinal cord. The nervous system is partly made up of nerve cells, so-called neurons. These cells can receive inputs from and relay signals to other neurons using connections called synapses. A second class of cells found in the nervous system are glial cells. These cells provide structure and metabolic support. The human brain comprises of around 86 billion ( $\sim 10^{11}$ ) neurons [24] – the same order of magnitude as the number of stars in the Milky Way. The number of neural connections is even greater, with each neuron being linked to other neurons via tens of thousands of synapses. This leads to a staggering number of synapses of around one quadrillion ( $10^{15}$ ). The next section will introduce neurons as the basic computational units of nervous systems and explain the biochemical processes underlying their function. Afterwards, the eye and the brain will be described as neural systems with large and very large integration.

### 2.1.1 Neurons

Nerve cells, or neurons, consist of a **cell body** (*soma*), **dendrites** (which are usually numerous) and an **axon**. The cell is surrounded by a membrane with a thickness of  $\sim 6\text{-}8$  nm. The *soma* contains the nucleus with the cell's genetic code. Neurons receive incoming signals through the dendrites. The signals are then integrated and when a threshold is reached, the cell itself signals. It is said to fire an action potential or spike. The cell's axon conveys the signal to downstream neurons that can be between 0.1 mm to 2 m away. Neurons create **synapses** on downstream neurons, where action potentials trigger a release of chemicals that are sensed by the postsynaptic cell. Neurons can be either **excitatory** or **inhibitory** with respect to downstream neurons [25]. Figure 2.1 shows the anatomy of a neuron.

Embedded in the cell membrane are two notable classes of membrane proteins, which are essential for neural signalling: **ion channels** and **ion pumps**. They play an important role in creating the characteristic waveform of a spike, which is unique for each neuron. When the neuron is at rest, ions are actively pumped using adenosine triphosphate (**ATP**) as an energy source. While getting hydrolysed to adenosine diphosphate (ADP), ATP provides the energy to pump three  $\text{Na}^+$ -ions out of the cell while at the same time pumping two  $\text{K}^+$ -ions in. The ions have the tendency to travel back through the ion channels, following concentration

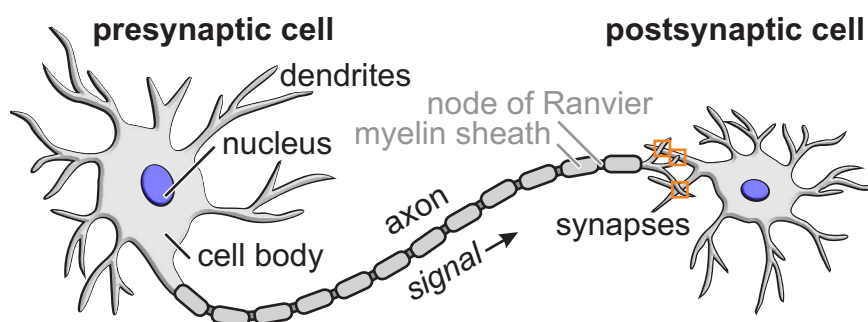


**Figure 2.1:**

Signalling between neurons (anatomy); a neuron receives inputs from upstream neurons through synapses on their dendrites, when an action potential is fired, the signal travels down the axon to downstream neurons

and electrostatic gradients, to reach equilibrium. Since this process is faster for  $K^+$ -ions than for  $Na^+$ -ions, concentrations and equilibrium potentials (shown in Figure 2.2 A) that give an overall **resting potential** of about  $-70\text{ mV}$  are reached. At rest,  $K^+$ -ions are mainly concentrated in the cell, together with anions.  $Na^+$ -,  $Cl^-$ - and  $Ca^{2+}$ -ions are mainly found extracellularly.

Also embedded in the cell membrane of a neuron are numerous **voltage-gated  $Na^+$ -channels**. These are closed when the neuron is at rest. When a certain threshold voltage is reached, following synaptic transmission, these channels open and evoke an **action potential** as depicted in Figure 2.2 B.  $Na^+$ -ions enter the cell down the chemical gradient, leading to a strong **depolarization**. As the membrane potential rises,  $K^+$ -channels also open, allowing  $K^+$ -ions to rush out

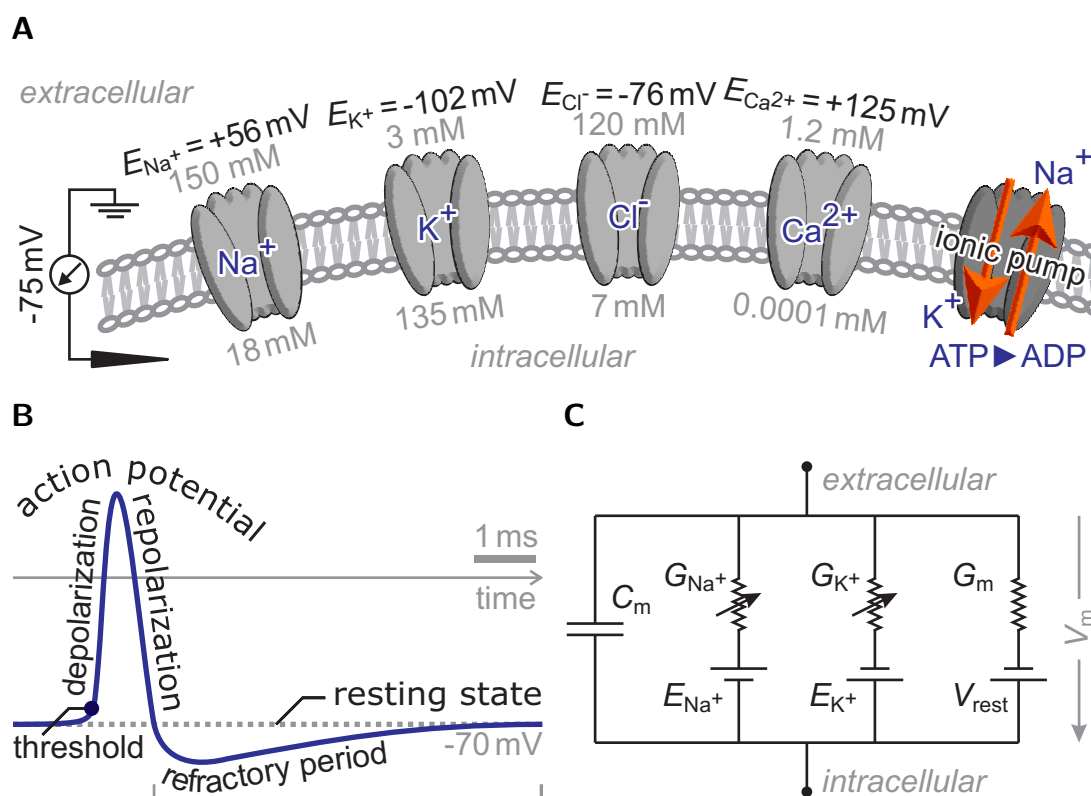


**Figure 2.2:**

Signalling between neurons (physiology); **A**) Charge carriers in a neuron at rest (modified from Squire [26, p. 95]), showing extracellular and intracellular concentrations and equilibrium potentials; **B**) Time course of an action potential, the duration of the action potential is  $\sim 1\text{ ms}$ ; **C**) Hodgkin-Huxley model of action potential generation (after Koch [27, p. 145])

of the cell. The  $\text{Na}^+$ -channels have a self-closing mechanism which is activated immediately after opening, but the  $\text{K}^+$ -channels remain open, eventually **hyperpolarizing** the cell. When they finally close, following hyperpolarization, the cell returns to its resting state. The action potential travels down the axon at a speed of  $1\text{-}100\text{ m/s}$ , depending on the thickness of the myelin sheath. The mechanism by which this happens is a chain reaction of consecutive depolarizations of neighbouring areas of the axonal cell membrane, locally opening the  $\text{Na}^+$ -channels. The signal is forced to travel unidirectionally due to the **refractory period** of the action potential (inactivation period of the  $\text{Na}^+$ -channels). The myelin sheath covering the nerve fibres leads to a rapid signal conduction since the insulated areas cannot become depolarized causing the signal to “jump” between so-called nodes of Ranvier. The low membrane capacitance and the low conductivity caused by the myelin sheath mean that, the attenuation of the potential is low, allowing it to travel further before needing to open more channels. In contrast to the electrical conduction of the action potential in the axon, the events at the synapse are chemical in nature. The presynaptic terminal contains vesicles filled with **neurotransmitters**. These are released by exocytosis when the action potential depolarises the pre-synapse and opens the voltage-dependent  $\text{Ca}^{2+}$ -channels leading to  $\text{Ca}^{2+}$ -influx. The neurotransmitters then diffuse across the synaptic cleft and bind to receptors in the postsynaptic neuron’s cell membrane, where the chemical current is converted back into an electrical one. The exact response depends on the type of receptor being activated. More information on neurophysiology can be found in a book by Squire [26].

The complete process of action potential generation and propagation can be described mathematically using the **Hodgkin-Huxley model** shown in Figure 2.2 C. Using the model, the membrane potential  $V_m$  can be described by the differential equation [27, 28, p. 151]

$$C_m \cdot \frac{dV_m}{dt} = G_{\text{Na}^+} (E_{\text{Na}^+} - V_m) + G_{\text{K}^+} (E_{\text{K}^+} - V_m) + G_m (V_{\text{rest}} - V_m) .$$

The cell membrane is modelled with a capacitance  $C_m$  and a leak conductance  $G_m$ .  $\text{Na}^+$ - and  $\text{K}^+$ -flow is modelled by the time- and voltage-dependent conductances,  $G_{\text{Na}^+}$  and  $G_{\text{K}^+}$ , respectively.  $E_{\text{Na}^+}$  and  $E_{\text{K}^+}$  are the equilibrium potentials for  $\text{Na}^+$ - and  $\text{K}^+$ -ions, respectively, and  $V_{\text{rest}}$  is the cell's resting potential.

### 2.1.2 The Eye

This thesis is about technologies for studying neural circuits. They can be applied to different neural systems, some of which have properties that make them particularly suited. A part of the brain that is easily accessible for observing neural signalling is the eye and particularly the retina. Therefore, it can be a good starting point for studying the brain's neuronal circuitry and it has long been a popular model system. The **retina** is located at the back of the eye, where light hits it through the pupil as shown in Figure 2.3 A. Like the brain, the retina itself is highly organized and has a layered structure with a thickness of  $\sim 200 \mu\text{m}$  in humans (see Figure 2.3 B). In the case of the retina, the layered structure consists of an input layer of **photoreceptor cells** and an output layer of **retinal ganglion cells** (RGCs) connected by a layer of **horizontal, bipolar** and **amacrine cells** processing the visual images so that they can be sent to the brain using the  $\sim 10^6$  RGC axons leaving the eye through a cross-sectional area of  $\sim 1 \text{ mm}^2$  (optic nerve). The number of **retinal ganglion cells** (RGCs) is only about 1% of the number of photoreceptors. Therefore, a vast amount of low-level visual processing takes place in the eye.

There are two types of photoreceptors, **rods** and **cones**, which have a distinct morphology and serve different purposes. Rods are responsible for light/dark vision. They use a receptor called rhodopsin. Cones are responsible for colour vision (using photopsin as a receptor). There are three types of cones, responding to different wavelengths of light (L: long wavelength, M: medium wavelength, S: short wavelength). The human retina contains about 100 million rods and 6 million cones, but the distribution is not uniform across the retina. Rods are

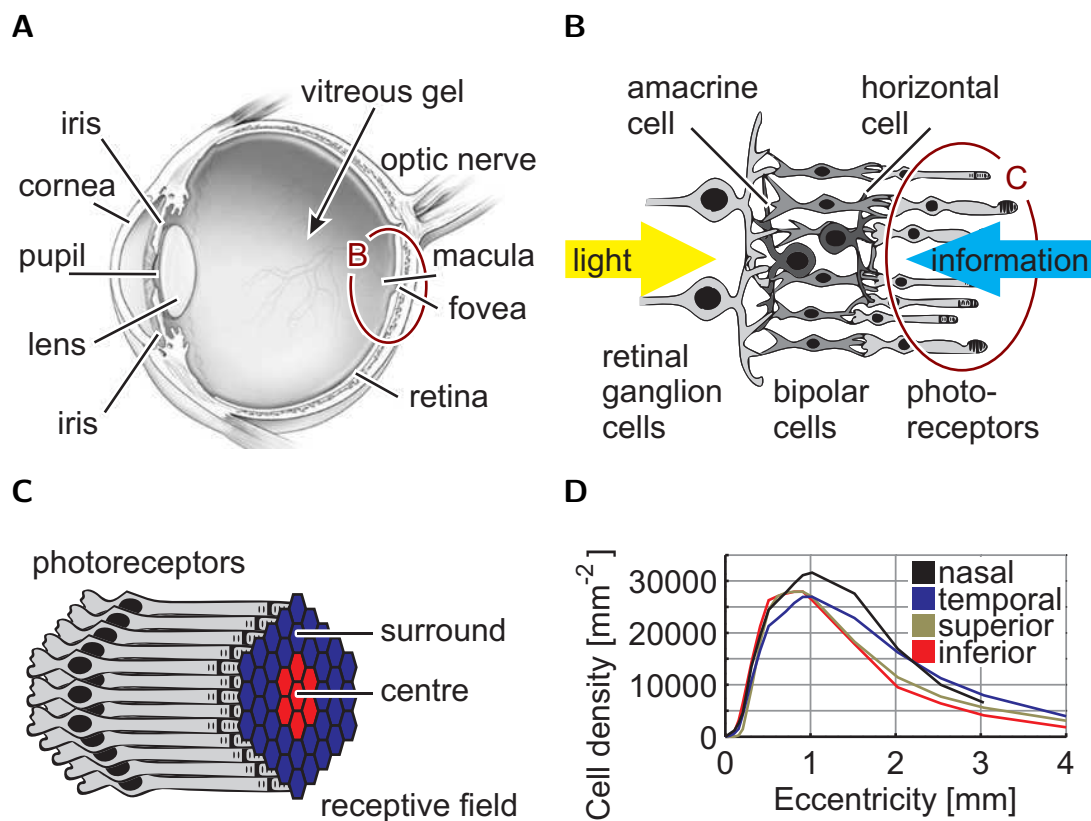


**Figure 2.3:**

The eye; **A**) Building blocks of the eye (schematic); **B**) Light and information flow in the eye; **C**) Receptive field of a retinal ganglion cell; **D**) Distribution of retinal ganglion cells across the retina; density increases when moving closer to the fovea (adapted from Curcio and Allen [29])

mainly located close to the fovea, whereas cone density is higher in the periphery. The photoreceptors give the eye some amazing capabilities. For example, cones allow us to see letters with stroke widths covering only 1-2 photoreceptors and rods allow us to sense individual photons [30].

Retinal ganglion cells come in two main functional classes called **on cells** and **off cells**. On cells fire more quickly when the eye is exposed to a brighter light stimulus, whereas off cells respond with a reduced firing rate. This mechanism helps perceive brightness changes very quickly. Furthermore, cells can be **sustained cells** or **transient cells**. Sustained cells maintain their response over the stimulus period, whereas transient cells change their firing rate only for a short period after the stimulus. Each RGC has a so-called **receptive field** – an area on the retina, that,

when exposed to a stimulus, leads to a response of the RGC (Figure 2.3 C). Usually, one can identify a centre and a surround region leading to opposite responses (on cell: centre stimulus leads to faster firing, surround stimulus decreases firing). Further information on the eye can be found elsewhere [25].

Using multi electrode arrays (MEAs), action potentials can be recorded from the RGC output layer. When the photoreceptor input layer is stimulated optically, conclusions can be drawn about the wiring of the intermediate layers. In order to allow visual stimulation without reflections from the device, and for simultaneous imaging, the MEAs need to be transparent. Current MEAs of this type have an electrode pitch of  $30\ \mu\text{m}$  [33]. In order to record closer to the fovea (the region responsible for sharp central colour vision), higher resolution arrays are needed due to the vastly increased neural density. This neural density relation is shown in Figure 2.3 D. The aim of studying the retina is to finally understand the function

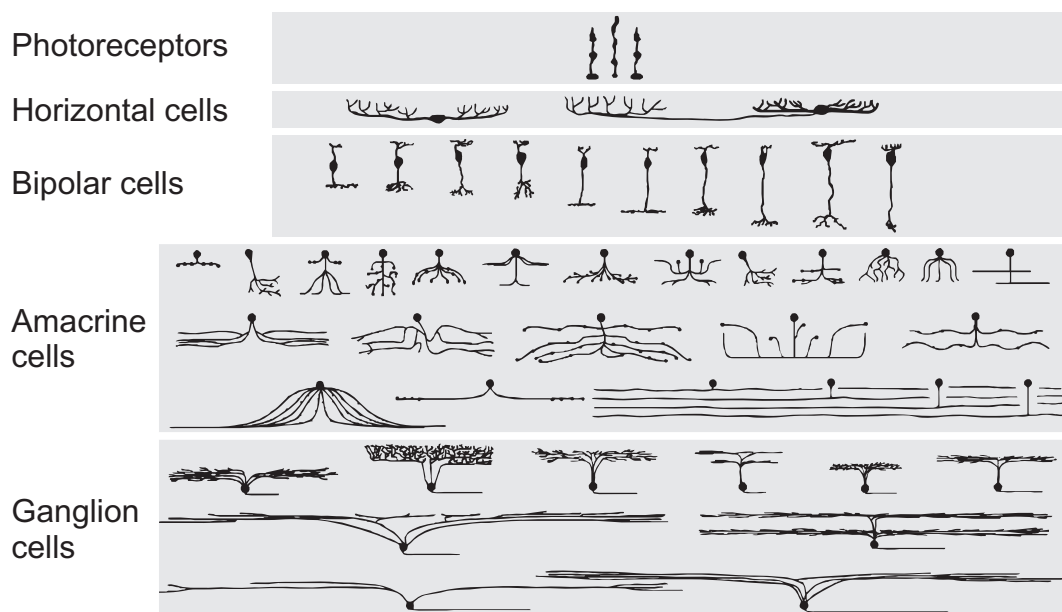


**Figure 2.4:**

Types of neurons in the retina (after Masland *et al.* [31], some wide-field amacrine cells not shown), a comprehensive morphological database covering the eye and other brain regions can also be found online [32]

of all the anatomically distinct types of neurons in the mammalian retina, of which there are ~55. The function of half of them is still unknown [34]. Figure 2.4 gives an overview of the neural subtypes; more detailed information about the retina can be found in Dowling [35] and Rodieck [36].

### 2.1.3 The Brain

The brain is the largest part of the central nervous system. It is enclosed in the skull, where it processes sensory perceptions in a highly sophisticated manner [38] and coordinates complex behaviours. It is the main place for integrating all complex information being processed by the organism. The brain contains **grey matter** and **white matter**. The white colour arises from the myelin sheath around the neurons' axons. While grey matter is present in the inner parts of the brain, the surface (**cortex**) is made up of grey matter containing mainly

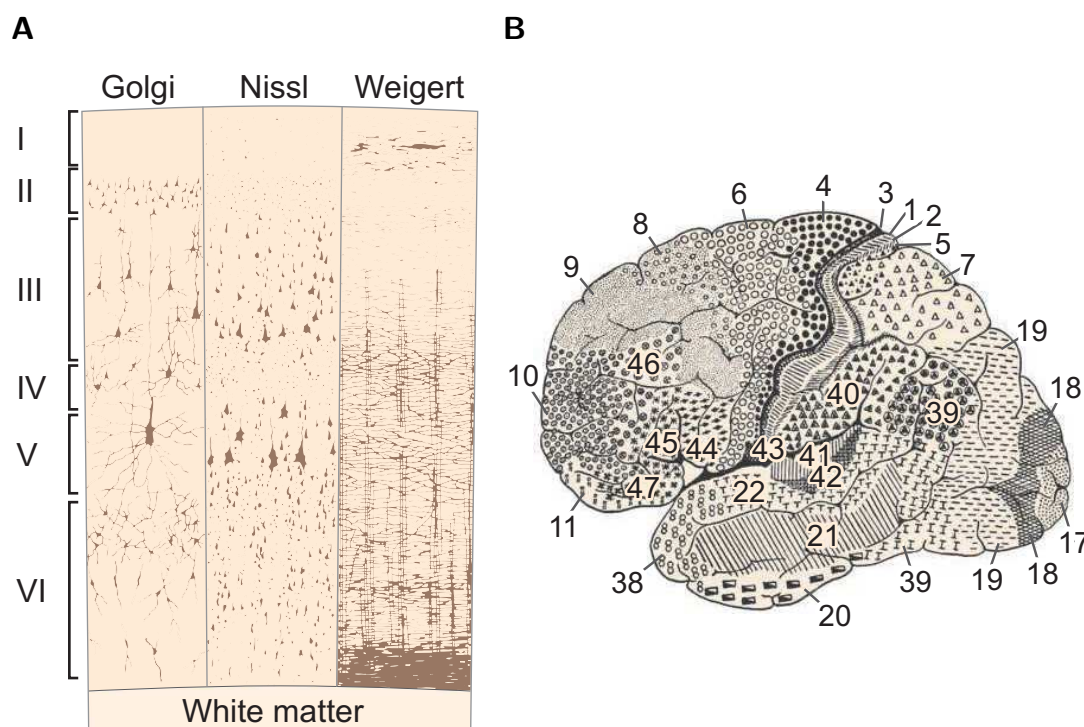


**Figure 2.5:**

Organization of the human neocortex into layers and areas; **A**) Six-layered structure of the neocortex shown using different staining methods (adapted from Heimer [37]); **B**) Brodmann areas are regions of distinct layer composition (lateral view, adapted from Kandel [25, p. 347])

neuronal cell bodies and supporting non-neuronal cells (glial cells). In humans the cortex is the largest part of the forebrain and consists of 12-15 billion neurons [24]. For mice and rats this number is about three orders of magnitude smaller (like their brains' volumes). The mouse and rat cortex contain about 4 million and 15 million neurons [39], respectively (whole brain: 71/200 million neurons, respectively, and  $\sim 10^{11}$  synapses [40,41]). In humans the biggest part of the cortex is the **neocortex**. It can also be found in all other mammals and is involved in a large range of higher functions such as sensory perception, generation of motor commands, spatial reasoning, conscious thought and (in humans) language. African elephants of all animals have the largest brain by volume, but one of the reasons their cognitive abilities are inferior compared to humans is that the vast majority (98%) of the 257 billion neurons are located not in the cortex but in the cerebellum [42]. It is thought that large cell density is another requirement for intelligence [39]. It is estimated, that the human neocortex contains about 1 000 types of neurons [43]. Like the retina, it also has a layered structure. All mammals have six **neocortical layers** (Figure 2.5 A), whose thickness depends on their position in the neocortex. The remaining part of the cortex has fewer layers and is called the allocortex. Cortical thickness does not vary a lot across species, being always around 2-4 mm [25, p. 345]. One difference is the folding of the cortex in humans (allowing greater surface area), while mice and rats have a smooth brain surface. In addition to the microscopic division into horizontal layers, the brain can be divided macroscopically into four anatomical regions: the frontal, parietal, temporal and occipital lobe. These were later found to also correlate with different brain functions. German neurologist Korbinian Brodmann further refined this by laterally dividing the human cortex into 52 so-called **Brodman areas** based on the thickness of each of its six layers (Figure 2.5 B, recently refined [44]). Many of the areas can also be linked to certain functions, such as seeing, hearing and motor control. At an even smaller level, the neocortex can be divided into **neocortical columns** that are a fraction of a millimetre in width. Neurons within columns have similar response properties, suggesting the columns constitute a local processing network [25, p. 348]. For example there is a clear

relation between neocortical columns in the visual cortex (Brodmann area 17) and the eye. Neurons within a column share the same visual receptive field and nearby columns represent nearby points in visual space [26, p. 590]. There is still a lot to be learned about the functioning of neural circuits in general. If single neurons and small groups of neurons could be switched on and off based on their type and location in the brain, conclusions could be drawn about their circuit function. Optogenetic techniques can offer this type of circuit manipulation; they will therefore be introduced in the following section.

## 2.2 Optogenetic Neural Stimulation

The conventional method to stimulate neural circuits is using electrical impulses [45]. This has the drawback, that it cannot offer control over which types of neurons are excited; every neuron in the proximity of the current source is affected. Furthermore, electrical stimulation can only excite, but not silence neurons. Fortunately, during the past decade optogenetics has developed into a useful and versatile tool for studying neural circuits and it is now widely used. Using genetically modified neurons, which as a result produce light-sensitive proteins that function as light-gated ion channels/pumps, neural signalling can be evoked or suppressed. The beginnings of optogenetics can be traced back to 1970s, when Francis Crick considered light as being a possible tool for manipulating neural circuits and overcoming the shortcomings of electrical stimulation. The first light-activated ion pump, bacteriorhodopsin, was identified in 1971 [46] and many other new members of the same family were discovered in the following decades. These pumps and channels transport various ions across cell membranes when exposed to a specific light stimulus. Halorhodopsin was discovered in 1977 [47] and channelrhodopsin followed in 2002 [48]. The genetic code for the expression of channelrhodopsin are taken from the green algae *Chlamydomonas reinhardtii*. Optogenetics began to take off as a neuroscience technique after being used successfully *in vitro* in 2002 (Zemelman *et al.* [12]) and *in vivo* in mammalian

neurons in 2005 (Boyden *et al.* [14]). With tools for **excitation** and **inhibition**, a powerful toolbox for selective neural modulation now exists. Figure 2.6 depicts the principle of cell-type specific optogenetic excitation and inhibition (panels B, C) in comparison to conventional unspecific electrical stimulation (panel A).

Optogenetics has since had a wide range of neuroscience applications. It has been used to program memories into the hippocampus [49] or to restore memories lost due to amnesia [50] or Alzheimer’s disease (in mice) [51]. It has also been shown to be useful for switching off pain [52, 53] or even turning whole-brain activity on and off [54]. In the ophthalmology community it is being investigated as a method for restoring vision in blind patients [55]. Optogenetics even has uses outside of neuroscience, where it has been used for example to precisely control the beating of the heart by stimulating cardiomyocytes [56] and for blocking tumour development [57]. Comprehensive information on optogenetics can be found in books by Yawo *et al.* [58], Kianianmomeni [59] and others [60, 61] and a review by Yizhar *et al.* [15].

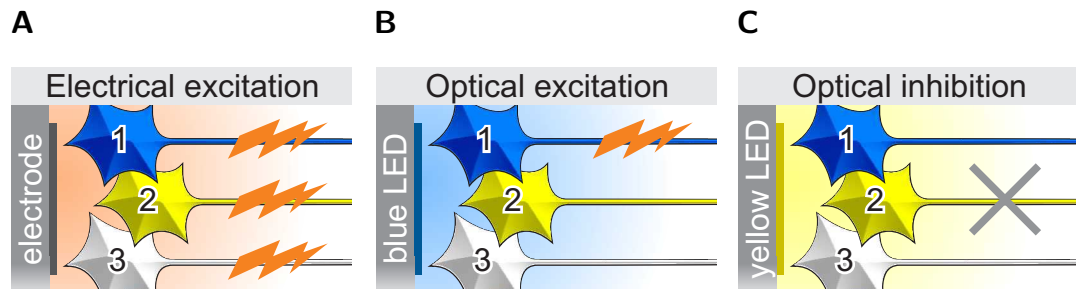


**Figure 2.6:**

Electrical and optogenetic neural modulation; neuron 1 expresses Channelrhodopsin, neuron 2 expresses Halorhodopsin, neuron 3 has not been transfected; **A**) Electrical stimulation evokes action potentials in all neurons close to the electrode; **B**) Optogenetic stimulation using a blue light source selectively activates neuron 1, other neurons fire spontaneously; **C**) Optogenetic stimulation using a yellow light source selectively silences neuron 2, other neurons fire spontaneously

### 2.2.1 Opsins

As mentioned before, optogenetic constructs have been found that can take both roles of neurotransmitters: they can evoke action potentials (excitatory, see Figure 2.2 B) or inhibit them. The most common light sensitive proteins are Channelrhodopsin, which can evoke neuronal activity if excited at  $\sim 450$  nm and Halorhodopsin, which can suppress neuronal activity if excited at  $\sim 580$  nm. Figure 2.7 illustrates the function of the two opsins. As demonstrated for example by Zhang *et al.* [62], they can be used in parallel for advanced circuit analysis.

This field is advancing rapidly, with many new opsins being identified/created. Research is focused mainly on the following parameters (among others [63]). First of all, the light-sensitivity should be high, so that significant neuronal currents can be generated with low levels of light. This also means that low power devices can be used for activation, leading to less power being converted to heat. Secondly, the peak activation wavelength and the deactivation time constant are important. It is desirable to find opsins that are activated by red light, since the attenuation length is longer in this region [64]. Especially when used for neural circuit analysis, where neural modulation at the level of individual spikes is necessary, the deactivation time constant should be small. In certain behavioural experiments, on the other hand, step opsins can be useful. They remain active after an initial exposure to

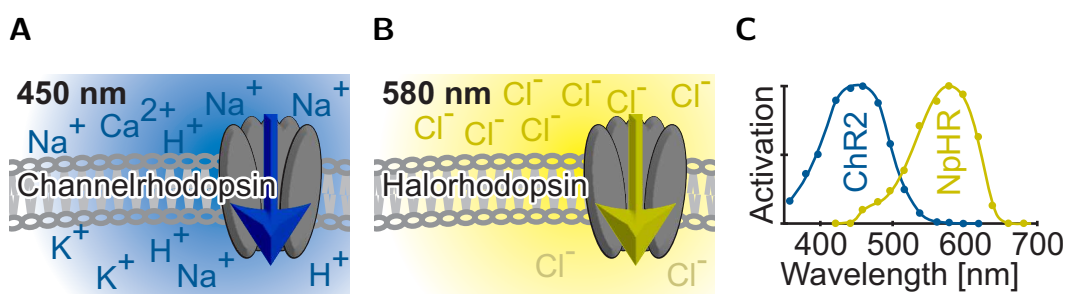


**Figure 2.7:** Optogenetic constructs; **A)** ChR2 (excitatory); **B)** NpHR (inhibitory), **C)** Absorption spectra of ChR2 and NpHR (adapted from Zhang *et al.* [62])

light. When several opsins are to be used in parallel, sharp and non-overlapping activation wavelength profiles are key. Some optogenetic constructs are mentioned below. There are many others and more detailed overviews have been given, e.g. by Wietek and Prigge [59, pp. 141-166] and Yizhar *et al.* [15].

### 2.2.1.1 Opsins for Excitation

The most widely used excitatory opsin is the cation-conducting channel **channelrhodopsin 2** (ChR2) [14]. It offers off-kinetics of 10 ms and moderate photocurrents. Important advancements have been made by engineering ChR2 to possess better kinetics, and become more sensitive to longer wavelengths. The variant used in this work with a peak absorption at 450 nm is called **H134R**. It has slightly slower off-kinetics (18 ms) but on the plus side it has a lower desensitisation (decrease in response following continued strong illumination) and its light sensitivity is increased slightly [65]. An important new variant called **Chronos** has a very short deactivation time constant of  $\sim 3$  ms and can therefore drive spikes with light pulsed up to 60 Hz. Also its light sensitivity is between one and two orders of magnitude higher than that of ChR2 [66]. Another variant is called **Chrimson**. Its benefit is that it shows a far red-shifted absorption spectrum (peak at 590 nm), allowing neurons to be activated using short pulses (5 ms) at 625 nm [66]. An example of a blue shifted (peak at 437 nm) variant is PsChR [67]. **C1V1** is a popular variant that is excitable by yellow light (540 nm). It also shows a high two-photon cross section [22]. A class of opsins called **step function rhodopsins** have a prolonged open state of several seconds to minutes [68].

### 2.2.1.2 Opsins for Inhibition

Optimized versions of the light-driven inward  $\text{Cl}^-$  pump **halorhodopsin** [69] (NpHR) and the light-driven outward proton pump **archaerhodopsin** are the most prominent of the inhibiting opsins. NpHR currently exists in its third generation. Its peak absorption is at 590 nm (yellow-red) and its off-kinetics are fast (4.2 ms) [70]. The two popular archaerhodopsin variants are the green-responsive **Arch** from *Halorubrum sodomense* [71] and **ArchT** from *Halorubrum genus* [72], where ArchT has improved ( $> 3$ -fold) light-sensitivity. In both cases the peak

absorption is in the green/yellow (566 nm) and the deactivation time constant is 9 ms. The red-shifted rhodopsin **Jaws** is an inward  $\text{Cl}^-$  pump that shows photocurrents that are three times those of the previously mentioned silencers (at  $5 \text{ mW}/\text{mm}^2$  irradiance) [73]. Light-gated anion channel rhodopsins (ACRs) are a promising tool that could replace NpHR and Arch as the standard for inhibition [74–76]. They transport many charges per photocycle and therefore require less light. Examples include the constructs slow ChloC and fast ChloC [75], where slow ChloC in particular is highly light-sensitive (irradiance  $\sim 0.1 \text{ mW}/\text{mm}^2$ ). However, temporal resolution is low, with required illumination periods of 12 seconds. This problem is being addressed as the construct **GtACR2** shows [76]. It has a peak absorption at 470 nm, a decay time constant of 0.04 s, and a very high light-sensitivity (irradiance  $\sim 0.001 \text{ mW}/\text{mm}^2$ ).

### 2.2.1.3 Opsin Expression

Subsets of neurons can be made light-sensitive using one of several approaches [77, 78]. The first option is **viral infection**, most importantly using the the small (20 nm) adeno-associated virus (AAV) carrying the optogenetic construct. In its simplest form, this leads to the transfection of neural populations that are defined by their location around the injection site. Drawbacks are tissue damage from the injection and toxicity during long-term experiments. By coating the viruses with certain proteins, they can also be forced to transfect only certain cell types or enter through defined subcellular compartments. Another option for advanced targeting makes use of the capability of certain virus combinations to transport optogenetic constructs across exactly one synapse [79]. By making the expression of the opsin dependent on the presence of so-called **site-specific recombinases** (most importantly Cre-recombinase), virus targeting can also be based on the genetic identity of a neural population, thereby only affecting a defined subclass or subtype. For many cellular phenotypes a unique gene expression pattern can be identified [80, 81]. The recombinases can be introduced through **transgenic animal lines** (animals that had a foreign gene deliberately inserted into their genome) [82]. To avoid the use of viruses, opsin expression can also be achieved by

crossing a transgenic animal carrying the optogenetic construct with a transgenic animal carrying a site-specific recombinase [83]. This is also the technique used in this work. All the described methods can be used to make relatively large populations light-sensitive. For targeting individual neurons, on the other hand, the technique of **electroporation** can be used. This technique uses a micropipette placed in close proximity to the neuron, which can then apply trains of negative voltage pulses (e.g.  $-12\text{ V}$ ) to temporarily make the cell membrane permeable for transfection [84].

### 2.2.2 Alternative Methods

Other approaches exist for enhancing the properties of nerve cells using genetic modifications. These include **chemogenetics** [85], **sonogenetics** [86] and **magnetogenetics** [87]. Chemogenetics utilises genetically engineered receptors that selectively interact with small molecules injected into the brain. The benefit is, that no further energy delivery is needed during the experiment. The technique is therefore also non-invasive. On the downside, the technique can only be used to modulate neural firing over the course of minutes or hours and cannot provide the temporal resolution necessary for the analysis of neural microcircuits. Sonogenetics uses low-pressure ultrasound that can be transduced into mechanical energy by gas-filled microbubbles to stimulate neurons by opening mechanosensitive channels. This non-invasive technique could potentially be used to overcome the problem of light delivery into the brain. However, high spatial resolution remains a difficulty. Currently volumes of a few millimetres in size can be targeted. The resolution can be improved by increasing the frequency, but this comes at the cost of penetration depth. Magnetogenetics is another approach, where neural activity is modulated by magnetic fields. The underlying mechanisms, however, are not well understood [88]. Reviews on the available techniques are available e.g. from Rajasethupathy *et al.* [89] and Park and Carmel [90].

## 2.3 Neural Recording

For optogenetics to be useful, there always needs to be a means of observing the changes that it causes. The most obvious change is a certain behaviour change of an alive animal during an experiment. This can be assessed without further equipment. If neuronal correlates of such behaviours are to be studied, or perhaps just the circuit responses without behaviour being considered, further equipment is needed. Examples of this include functional magnetic resonance imaging (**fMRI**), **fluorescent activity indicators** and **electrical recording**. fMRI lacks spatiotemporal precision for circuit analysis at the neuronal level, leaving optical methods and electrophysiology – described separately in the following sections. Several future directions for scalable high-resolution recording are outlined in Marblestone *et al.* [91].

### 2.3.1 Optical Methods

Fluorescent probes are a means to report the microenvironment within a neuron or neural compartment. There is a substantial community developing these constructs and doing very significant work. A big interest lies in using microscopy and either **Ca<sup>2+</sup> indicators** [92–94] (or H<sup>+</sup> or Cl<sup>-</sup> indicators [58, pp. 133–147]) or **voltage sensitive dyes** (VSD) [95–98] for neural recording. These can be genetically encoded and offer big advantages, such as large scale recordings at a single cell resolution. However, Ca<sup>2+</sup> indicators are slow (~50–1 000 ms), making the detection of single action impossible. The magnitude of Ca<sup>2+</sup> influx also varies between individual cells. Voltage indicators, which have also long been too slow and even cytotoxic, have recently been engineered to allow a temporal resolution of 0.2 ms [99], offering an alternative to electrical recording. Many *in vivo* experiments, however, are hard to perform. Special miniature microscope setups [100, 101] are needed. The maximum depth that can be probed is also strongly limited by absorption and scattering in the brain (extendible using multiphoton techniques [102], but only to around 1.6 mm in the most

sophisticated of cases). Making neural tissue transparent is now a possibility *ex vivo* [103–105], but only once the tissue is dead. Electrophysiology, combined with suitable implantable probes, is the standard method of choice here and will be covered in the next section.

### 2.3.2 Electrophysiology

Electrophysiology is an important method for recording from single neurons [106] and it is used throughout this work. For this, good contact has to be made with the neurons using micron-scale electrodes. The brain/electrode interface should have a large surface area to minimize the electrode's electrical impedance. Typical values for small (5  $\mu\text{m}$ -diameter) electrodes are between 200 k $\Omega$  (good) and 600 k $\Omega$  for an extracellular electrode. Low impedances for good recording can be achieved by electroplating [107] a metal such as platinum [108] (Pt) at a large current density such that it gives a very rough surface, which leads to a large contact area at the interface. Other common materials include titanium nitride [109] (TiN), iridium oxide [109] (IrO<sub>2</sub>), and the transparent polymer PEDOT [110]. Some exotic examples are carbon nanotubes [111,112], graphene [113] and boron-doped diamond [114].

The impedance of the recording system is frequency-dependent. Since the duration of an action potential is about 1 ms, the critical frequency when evaluating electrode impedances is around 1 kHz. Figure 2.8 shows the experimental setup and theory behind measuring electrode impedances. As panel A shows, a chamber is glued onto the electrode array and filled with physiological NaCl-solution. A counter electrode made of the same material as the electrode to be tested (e.g. platinum) is immersed in the solution. Contact is made with the bond pad of the array and a frequency sweep is carried out using an LCR meter recording the impedance spectrum.

A simplified equivalent circuit representing the neural interface consists of a capacitor and a resistor in parallel and a series resistor (simplified Randles cell [115], panel B). The shape of the recorded impedance curve (panel C) over the frequency ( $f$ ) spectrum can be explained by analysing the circuit. The impedance of the

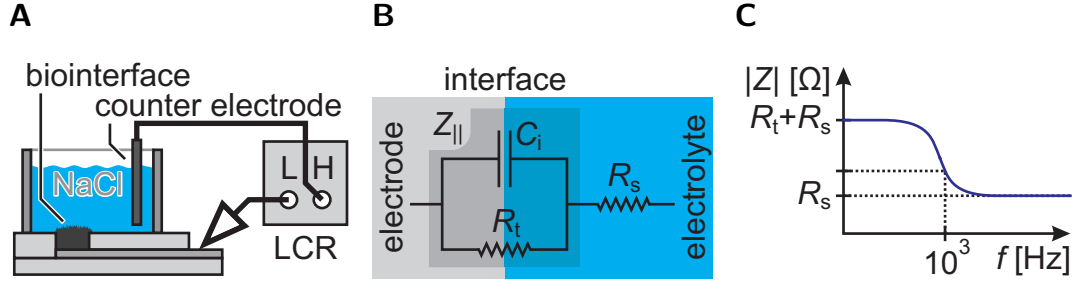


**Figure 2.8:** Brain-electrode interface; **A)** Impedance measurement setup (especially for *in vitro* MEAs); **B)** Equivalent circuit of the metal-electrolyte interface; **C)** Shape of an impedance curve of a micro-electrode

capacitor,  $Z_{C_i}$ , is equal to

$$Z_{C_i} = \frac{1}{j\omega C_i} \quad (2.1)$$

with  $\omega = 2\pi f$  and the impedance of the parallel resistor,  $Z_{R_t}$ , is equal to

$$Z_{R_t} = R_t. \quad (2.2)$$

The combined impedance of the parallel circuit,  $Z_{\parallel}$ , can be calculated as

$$\frac{1}{Z_{\parallel}} = \frac{1}{R_t} + j\omega C_i \quad (2.3)$$

and the total impedance,  $Z_{\text{Total}}$ , is the parallel circuit impedance plus the series resistance,  $R_s$ , with the following limits:

$$Z_{\text{Total}} = Z_{\parallel} + R_s, \quad (2.4)$$

$$\lim_{\omega \rightarrow 0} Z_{\text{Total}} = R_t + R_s \quad \lim_{\omega \rightarrow \infty} Z_{\text{Total}} = R_s.$$

### 2.3.3 Data Analysis

Data obtained from electrophysiological recordings is not directly useful for neural circuit analysis, since each electrode of the array records from a group of neurons. Local field potentials and current source density analyses are methods to examine neural population activity and these specific techniques will be described in more detail when needed (section 5.3). What is needed for an exact analysis of neural circuits are the spike waveforms generated from individual neurons. Obtaining this data is not an easy task, but a series of techniques have been developed over the years to facilitate this [116]. The steps used for the data analysis in this work are outlined in Figure 2.9. After a **raw data noise evaluation** has been carried out (panel A), a **spike finding** algorithm (panel B) is run to identify spikes that temporarily cross a threshold, which is set to be a multiple of the identified noise (usually 3-5). The spikes are then clustered using a (typically) five-dimensional **principle component analysis** [117] (PCA, panel C). This is

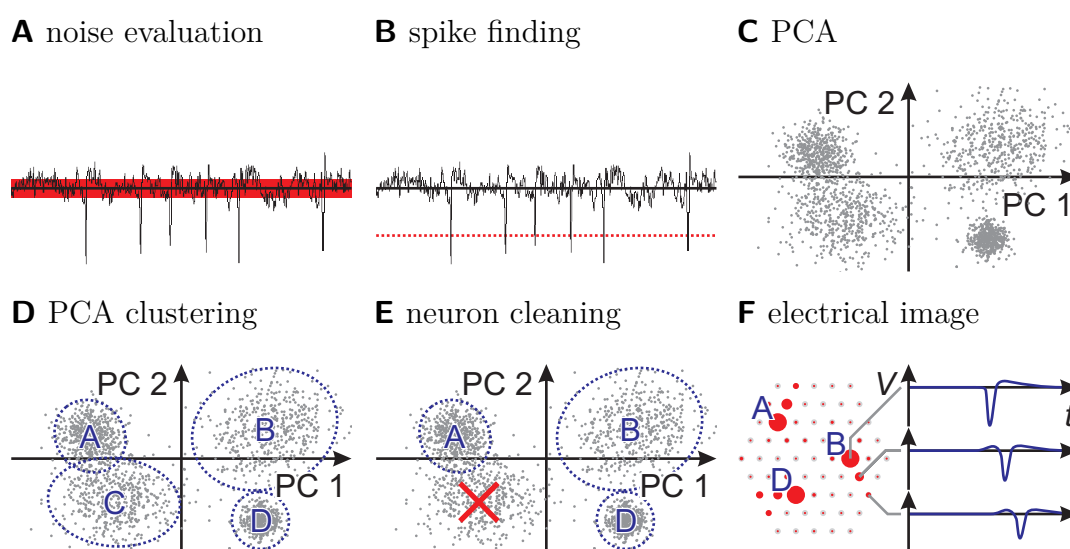


**Figure 2.9:**

Electrophysiological data analysis steps; **A)** Raw data noise evaluation; an RMS value is calculated, which can then be used to set a threshold for spike identification; **B)** Spike finding; spikes are identified using a user-defined threshold; **C)** Principle component analysis; relevant features of the spike shapes are extracted and the principle components are identified; **D)** PCA neuron finding; point clusters in PCA space are identified, belonging to the same neuron; **E)** Neuron cleaning; **F)** Electrophysiological imaging

a method commonly used to structure, simplify and visualize large datasets by approximating a large number of statistical variables by a much lower number of meaningful linear combinations (the principal components). The basis for the analysis (in the case of hexagonal arrays) are 182-dimensional vectors consisting of all analogue data points from 0.5 ms before the spike to 0.8 ms after the spike from the electrode with the highest detected peak and its six neighbours.

Each vector corresponds to one spike. The length of each vector in the first of its 182 dimensions is the respective recorded voltage on the central electrode at 0.5 ms before the spike. The length in the second dimension is the respective recorded voltage on the same electrode at 0.45 ms before the spike, and so on (sampling rate of 20 kHz). Finally, the length of each vector in the 182<sup>nd</sup> dimension is the respective recorded voltage on the 6<sup>th</sup> neighbouring electrode at 0.8 ms after the spike.

The principal component analysis now fits a 182-dimensional ellipsoid to the data points from all recorded spikes in 182-dimensional space. Each axis of the ellipsoid represents a principal component and the first principal component is set up to contain the largest possible variance in the data. Each following component has the highest possible variance while being orthogonal to all preceding components. Using this technique, individual neurons are usually clearly detectable in the first dimensions of the newly created coordinate system.

Clusters are then identified in PCA space (**PCA clustering**, panel D). The quality of this can be optimized by fine-tuning certain parameters: bins per dimension, clustering significance and min/max number of clusters. The next step is called **neuron cleaning** (panel E). The role of this step is to test for distinct neurons accidentally clustered together. The way this is done is by checking for spikes that immediately follow another spike (low inter-spike interval). Since this is physiologically impossible (refractory period), such neurons are neglected. Finally, **electrophysiological imaging** can be carried out (panel F).

The maximum signal amplitude recorded by each electrode can be plotted to show the approximate position of the neurons and the direction and velocity of signal propagation. Smooth spike waveforms for each neuron and electrode can be obtained by averaging over all spikes.

A software tool used in this work, employing this analysis framework, is called **Vision**. It was written in Java and first developed at the University of California at Santa Cruz over a decade ago [118]. Further analysis can be done using Matlab, which can interface with Java, making it relatively easy to import the data. A tool called **Cell Finder** allows manual reclustering in case the automated process was unsuccessful in detecting and separating the neurons. This process still needs to be checked by hand.

## 2.4 LED Light Sources

The first important element of applied optogenetics is the targeted genetic modification of certain neurons to make them light-sensitive. The second important element is light-delivery into the brain. For this, several technologies currently exist. As light emitting diodes (LEDs) are becoming more powerful, they not only continue to replace conventional technologies in various lighting applications, but also offer a compact and low cost alternative to conventional lasers-based light sources for optogenetics. The history of the LED [119, p. 10] dates back to the year 1907, but a practical device emitting in the visible (red) was only built in 1962. First applications included indicator lights and small calculator displays. A lot of effort was since put into broadening the available spectrum and blue emission proved particularly difficult to achieve due to high dislocation defect densities, difficulties in p-type doping, and cracking due to strain. The first such device based on InGaN was finally produced in 1994 by Shuji Nakamura, for which he received the 2014 Noble price in physics (with I. Akasaki and H. Amano). After decades of work it is now possible to build LEDs covering wavelengths in and beyond the visible spectrum using different materials and their alloys: InGaN for ultraviolet, blue and green, GaP for green and yellow, AlGaInP for yellow, orange and red and AlGaAs for red and infrared [120].

Light emitting diodes work on the principle of injection electroluminescence, which is the inverse mechanism of photodetectors and solar cells [121]. Likewise, they are made from **semiconductors**, which besides conductors and insulators represent one class of materials with respect to their electrical conductivity. While each material possesses certain energy levels, that electrons can occupy, known as conduction bands and valence bands, these bands only overlap for conductors, but are separated by a **band gap**,  $E_g$ , in the case of insulators and semiconductors. In semiconductors, the bandgap is small, which means that conduction can be achieved easily by exciting electrons to energy levels in the conduction band. The importance of the band gap in LEDs is that it defines the colour (wavelength) of the emitted light by the relationship

$$E_g = E_c - E_v \approx \frac{hc}{\lambda}. \quad (2.5)$$

Here,  $h$  represents Planck's constant,  $E_v$  and  $E_c$  are the energies of the valence and the conduction band, respectively,  $c$  is the speed of light and  $\lambda$  is the wavelength of the emitted photon. The semiconductor gallium nitride (**GaN**) has a bandgap of 3.4 eV, which corresponds to a wavelength of 366 nm [122]. The physical principle underlying radiative emission is that electrons in the conduction band can fall into the valence band and recombine with free holes, releasing energy. This energy can be emitted in the form of light and heat, where heat – generated during indirect band transitions through momentum transfer ( $\Delta k \neq 0$ , Figure 2.10 A, right) – is an unwanted phenomenon.

In the simplest LED devices, recombination and light emission happens at the interface of two regions in a material of different electron and hole concentration, induced by doping (introducing impurities). These devices are called p-n homojunctions. When no external voltage is applied across such a junction, electrons can diffuse across and recombine with holes until a space charge builds up, inhibiting further electron transfer (Figure 2.10 B, top). If a voltage is now applied in the forward direction (Figure 2.10 B, bottom), the force of the electric field helps the electrons overcome the barrier. Current flows, charge carriers can recombine

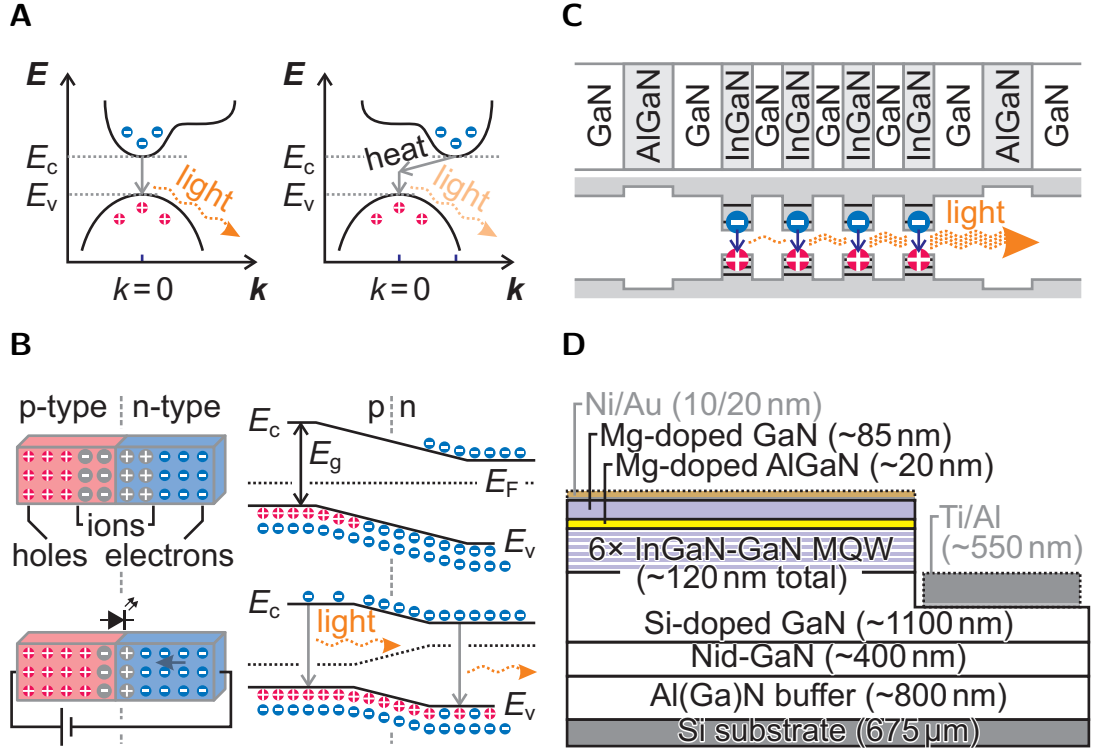


**Figure 2.10:**

LED working principles; **A)** Electronic band structure of two semiconductors; left: direct band gap, right: indirect band gap; **B)** Charge carrier concentrations and energies (adapted from Schubert [123]) in a p-n homojunction under zero bias (top) and forward bias (bottom); **C)** Example of a MQW LED structure with its associated band diagram (simplified, after Saleh and Teich [120]); **D)** GaN-on-Si LED structure of the devices fabricated in this work (epilayers patterned and contacted)

and light is generated. The resulting relationship between current  $I$  and voltage  $V$  does not follow Ohm's law ( $I = V/R$ ) like in resistors. Instead, LEDs show an exponential current-voltage relationship, which can be described by the **Shockley diode equation** [124] with the reverse saturation current  $I_s$ , the elementary charge  $e$ , the Boltzmann constant  $k$ , and the thermodynamic temperature  $T$ :

$$I = I_s \left( \exp\left(\frac{eV}{kT}\right) - 1 \right). \quad (2.6)$$

An important performance measures of high power LEDs is the **internal quantum efficiency** – the ratio of photons emitted by the active region per charge carrier injected, ideally equal to one. The second important measure is the **external quantum efficiency**, which is the ratio of photons emitted into free space per charge carrier injected. Since not all photons can escape the active region, this parameter is lower by a factor called the **extraction efficiency**. A crucial optical characteristic of light sources for optogenetics is the **irradiance** they can produce. This is measured in watts per square meter of incident surface and at the LED surface it is equal to the total optical power divided by the LED's surface area. The photometric unit corresponding to this radiometric unit is called illuminance (measured in  $\text{lm}/\text{m}^2$ ).

Improvements in LED efficiency can be made by introducing multiple quantum well (**MQW**) structures (a type of p-n heterojunction). These are thin layers of a material of relatively small bandgap sandwiched between layers of a material of larger bandgap. MQWs increase the probability of radiative recombination of the injected electrons and holes by trapping them in the active region (Figure 2.10 C). MQWs have discrete energy levels that can be approximated by the Schrödinger equation if their thicknesses is below the de Broglie wavelength of an electron. The quantum well material used in this work is indium gallium nitride (**InGaN**). This ternary material allows tuning of the LED's emission wavelength over a broad range between 366 nm (pure GaN) and 1.61  $\mu\text{m}$  (pure InN) by varying the material concentrations [120, p. 700]. All efficient blue LEDs today rely on at least one InGaN quantum well layer.

Traditionally, GaN LEDs were grown on sapphire substrates. The large lattice mismatch of 17 % and the difference in thermal expansion coefficients of 46 % made it difficult to use silicon, the otherwise standard semiconductor substrate. These problems were overcome recently, allowing the exploitation of silicon's advantages: it is cheaper, has a higher thermal conductivity (improving efficiency) and it is not brittle and therefore easier to process. Furthermore, the use of silicon allows taking advantage of decades of microfabrication research and potentially the use of silicon foundries that allow up-scaling of fabrication runs.

Growing MQW LEDs on silicon involves the formation of a layer stack such as the one shown in Figure 2.10 D (more information in Zhu *et al.* [125, 126]). In this work the composition is the following. On the **Si substrate** (675  $\mu\text{m}$  thick) an **Al(Ga)N buffer** layer (~800 nm thick) is created for stress control (by continuously grading the Al-content). An undoped layer (**Nid-GaN**, ~400 nm thick) functions as another buffer layer for improving the crystal quality of the following layers. A **Si-doped GaN** layer (~1100 nm thick) is grown, acting as the n-type semiconductor, followed by the quantum well structure (**6 $\times$  InGaN-GaN MQW region**, ~120 nm in total thickness). An electron blocking layer (EBL) is created from **Mg-doped AlGaN** (~20 nm thick). This layer has an increased bandgap, preventing energetic electrons from escaping the MQW region and thereby increasing carrier density and recombination rate. Finally, the top layer is made from **Mg-doped GaN** (~85 nm thick) – the p-type semiconductor.

When fabricating LEDs, attention must be paid to the electrical contacting of the semiconductor. The metal/semiconductor contact can be either Ohmic or diode-like (Schottky contact). For the desired formation of an **Ohmic contact**, the Schottky barrier height has to be zero or negative, which means that at the n-contact the work function of the metal must be close to or smaller than the electron affinity of the semiconductor (GaN: 4.1 eV [122]) and at the p-contact the work function of the metal must be close to or larger than the sum of the electron affinity and the bandgap energy (GaN:  $4.1 + 3.4 = 7.5$  eV [122]). Due to the high bandgap energy of GaN the choice of materials for the p-contact is very limited (commonly used: Au, Ti, Pt, Pd, Ni and Cr [127]). An annealing step is required to form the ohmic contact between the metal and the p-GaN through interfacial reactions [128, 129]. The n-contact on the other hand can be created easily and without annealing using many metals (e.g. Ti/Al) after exposing the n-semiconductor by etching. For further information on LED working principles, refer to Saleh and Teich [120] and others [119, 121, 123].

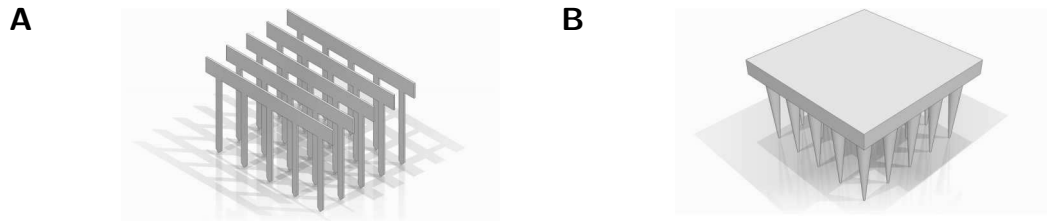
Regarding LEDs, there are different options for designing stimulating devices for optogenetics. Firstly, they can be used to replace lasers in fibre optic setups. High intensity LEDs for this purpose are commercially available (e.g. from Mightex [130] or Prizmatix [131]). However, LEDs can be made in any shape and size and can therefore also be implanted directly into the brain. For some time this approach was not adopted because of the heating of the tissue that might result, but simulations and first experiments at the Institute of Photonics show that heating can be kept within safe levels [132,133]. Some first examples of realized implantable LED probes are shown in section 2.5. A review on optical techniques in optogenetics is given by Mohanty and Lakshminarayanan [134].

## 2.5 Devices for Probing Neural Circuits

The brain is a complex network of very densely packed cells. In order to selectively stimulate it or record from it, a probe has to be brought close to the region of interest. Over the years many probes have been engineered for this purpose by different groups. In addition to the very basic microwires and arrays of the same, two paradigms in terms of microfabrication have been used over and over again, namely Michigan-style (based on K. Wise *et al.* [135]) and Utah-style arrays (based on R. Normann *et al.* [136]). Their respective designs are shown in Figure 2.11. Until recently, devices relying on these concepts were mainly electrode arrays for neural recording/stimulation, but the same concepts can also be used for optical stimulation. The following sections will introduce some key devices from the two categories (and some other approaches for implantable probes), starting with pure optical stimulation and electrical recording and finishing with an overview of integrated devices.

### 2.5.1 Optical Stimulation

A wide variety of probes for optical stimulation have recently been developed using several approaches for light-delivery.  $\mu$ LED arrays have so far been used mainly for spatially precise surface illumination *in vitro* [137–139], with OLEDs being investigated as a possible alternative [140–142]. OLEDs generally have

**Figure 2.11:**

Manufacturing approaches for implantable neural probes; **A)** Michigan-style array (2D chips, stackable); **B)** Utah-style array (fundamentally 3D)

a lower light output, but can still provide irradiances sufficient for optogenetic stimulation, depending on the application. Conventional approaches for *in vivo* optogenetics, on the other hand, utilise lasers and (non-penetrating) optical fibres to deliver light to the brain areas of interest. Two-photon techniques can also be used to achieve neural activation at increased resolution [143] and up to a depth of  $\sim 1$  mm. Problems that exist with this method are the targeting of deeper brain regions (due to the attenuation of the light) and spatially precise targeting. Figure 2.12 gives an overview of advanced devices that are aimed to address this issue among others. Deeper brain structures can be reached using penetrating optical fibres, as shown in panel A. Recently, small LED light sources have also been used with this setup (panel B, also  $3 \times 3$  arrays [161]). LEDs allow for compact and even tetherless devices. There has been resistance to direct implantation due to concerns over thermal issues, but recently groups started experimenting with implanted light sources in direct contact with the tissue allowing patterned stimulation of deep brain regions. Advantages included better scalability and the absence of coupling and transmission losses through optical fibres. Panels C-E show wireless devices with LEDs in direct tissue contact, respectively using one, four (parallel), and two individually addressable LEDs. Probe E contains more than one LED, but the shank is very invasive ( $700 \mu\text{m}$  shank width). Panel F shows a tethered device that is slightly more compact ( $400 \mu\text{m}$  shank width). Despite these developments, it is still challenging to induce rich spatiotemporal patterns of population activity at depth *in vivo*. So far, higher integration has been achieved mainly using lasers. The device shown in panel G uses six optical

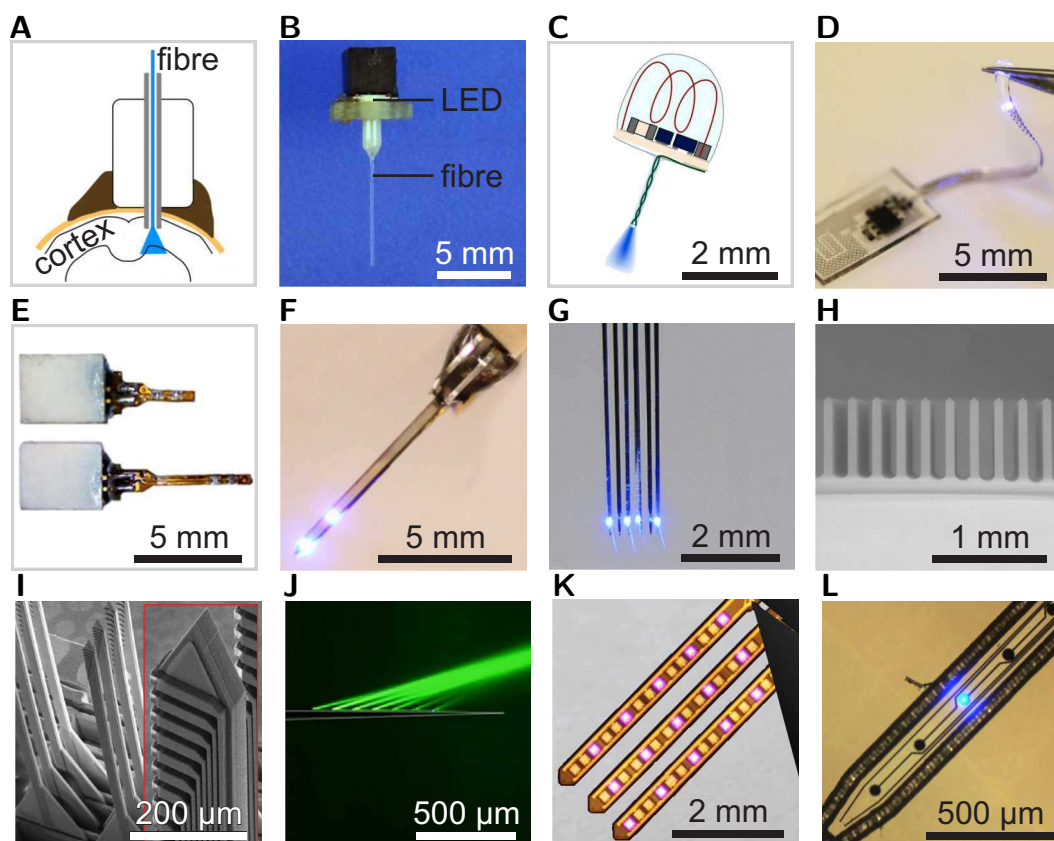


**Figure 2.12:**

Overview of devices for optogenetic stimulation; **A)** Optical fibre stimulation [144,145]; **B)** Miniature fibre-coupled wireless deep-Brain stimulator [146] (board not shown); **C)** Fully implantable wireless device using a commercial  $\mu$ LED [147]; **D)** Soft, stretchable, fully implantable, miniaturized and wireless system including several parallel transfer-printed LEDs (single channel) [132, 148, 149]; **E)** Wireless system for deep brain stimulation (two LEDs spaced at 4 mm) [150]; **F)** Probe containing two individually-addressable transfer-printed  $\mu$ LEDs [151]; **G)** Multi-waveguide probe using LEDs [152]; **H)** Utah-style glass waveguide array [153] **I)** 3D multi-waveguide array [154, 155]; **J)** Multipoint-emitting optical fibre [156, 157]; **K)** GaN-based  $\mu$ LED arrays on flexible substrates for optical cochlear implants [158, 159]; **L)** Sapphire-based micro-scale LED probe [133, 160]

fibres ( $\sim 70 \mu\text{m}$  diameter) coupled to laser sources and the device shown in panel H extends this approach to two dimensions. Impressive three dimensional arrays have been created using waveguide probes (panel I). These devices use a laser that is either scanned or deflected by a digital micromirror device to target one or several of 192 ( $6 \times 8 \times 4$ ) illumination sites. As opposed to scanning lasers, arrays of small laser diodes for coupling light in to the waveguides have also been

discussed. This would dramatically reduce the complexity of the setup [154]. Wavelength-division multiplexing can also be used to couple light in to individual waveguides by slightly varying the wavelength of a single light source, which in return can be fixed in position [162]. Another approach to obtain multiple stimulation sites on a single shank is shown in panel J. Optic fibres with openings in its cladding can be used for selection and manipulation of propagating and evanescent modes. All these are promising approaches that have demonstrated the benefits of spatiotemporal optogenetics at depth. However, they employ expensive and bulky light sources where the complexity of the optical setup becomes an issue as they are scaled up to multiple stimulation sites, making exploitation by the neuroscience community difficult. Microscale light-emitting diodes ( $\mu$ LEDs) offer a solution to this problem. One example for this is a probe developed as an optogenetic prosthesis for patients with hearing loss. The device includes three channels, each consisting of five LEDs in parallel (panel K). A solution for the brain is shown in panel L. The sapphire-based  $\mu$ LED probe was shown to activate neurons *in vivo* [160]. However, the problem with this device is that sapphire cannot be reliably thinned beyond 100  $\mu\text{m}$  making the probe invasive and susceptible to inducing damage in the surrounding neural tissue. This provides motivation for minimally invasive neural probes capable of delivering patterns of light to deep brain regions with high-density.

### 2.5.2 Electrical Recording

Various electrode arrays have been developed for *in vitro* recording from the retina or brain slices (Figure 2.13), which can survive *ex vivo* for several hours under the right conditions [163]. Planar arrays constitute one class of devices. These have been developed using different electrode arrangements (e.g. Figure 2.13 A). One way to further scale up this approach is by using integrated CMOS circuitry [164, 165]. Commercial products using 4225 electrodes with a 16  $\mu\text{m}$  pitch are available from Multi Channel Systems GmbH, Germany [166]. The disadvantage when used for retinal studies is the highly reflective substrate, which can make precise

stimulation difficult. Three dimensional electrode structures have also been used *in vitro* (Figure 2.13 B). These designs help improve the contact with the neurons or they allow contacting of deeper layers that have suffered less damage from slicing [167]. A detailed overview is given by Spira and Hai [168].

Figure 2.14 shows various devices for *in vivo* recording. These devices can be rigid or flexible with advantages on both sides. Rigid devices can be made very small and are usually easier to implant, whereas flexible devices may be more biocompatible since the mechanical properties more closely match those of the neural tissue. The most basic electrodes are microwires. They can be used individually or stacked in two or three dimensions to cover relatively large brain areas (panel A). In a miniaturized form they can be used to record from individual neurons intracellularly (panel B). Using standard microfabrication techniques, multiple electrodes can be created on one shank (“Michigan array”, panel C). NeuroNexus is a commercial manufacturer of such multichannel recording needle probes [170]. The alternative fabrication paradigm (“Utah array”) is similar to that of micro-electrocorticography ( $\mu$ ECoG) arrays (example in panel D). By producing needle structures, the electrodes are offset from the surface and can penetrate the tissue (panel E). Each needle contains exactly one electrode. Nanofabrication can be used to massively reduce the pitch (to 2  $\mu$ m, panel F), flexible options

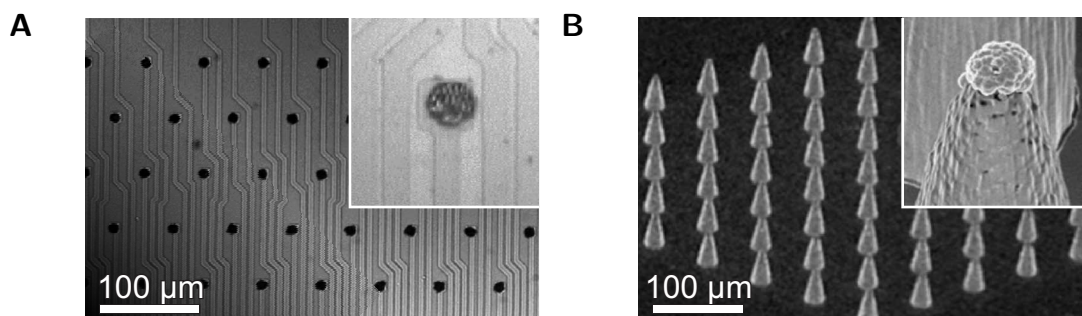


**Figure 2.13:**

Devices for electrophysiological recording *in vitro*, interface made from platinum black; **A**) Transparent (ITO on glass), planar 512 electrode array with 60  $\mu$ m electrode pitch (from Mathieson *et al.* [169]), single electroplated electrode in detail; **B**) Needle array of 61 electrodes with 60  $\mu$ m pitch (from Gunning *et al.* [167]), single electroplated electrode in detail

exist [171], and Utah-style arrays have also been equipped with a wireless option (panel G). An alternative method for creating three-dimensional arrays is stacking of Michigan-style probes (panel H). These setups can be further extended with a double-sided option (panel I). Using high-resolution fabrication techniques, narrow traces can be created leading to very high electrode counts of 16 ( $\times 6$  shanks), 32 ( $\times 8$  shanks), 64 ( $\times 1$  shank), and even 1 000 (panels J-M), which can facilitate spike sorting. When using a multi-layer fabrication process, the feature size can be larger, while keeping the same number of electrodes. This can be particularly useful on flexible substrates (panel N). Very high electrode counts can also be achieved by integrating CMOS circuitry into the probe shank (always addressing a defined subset of electrodes, panel O). Atlas Neuroengineering [172] is a company focusing on such active probes [173]. Drawbacks are the increased fabrication cost, crosstalk and the need for improved encapsulation for long-term stability of the implanted electronics. Other approaches exist, e.g. syringe-injectable nano-meshes [174]. More information on *in vivo* microelectrodes can be found in reviews, e.g. by Jorfi *et al.* [175], and a book (on neural ensemble recording) by Nicolelis [176].

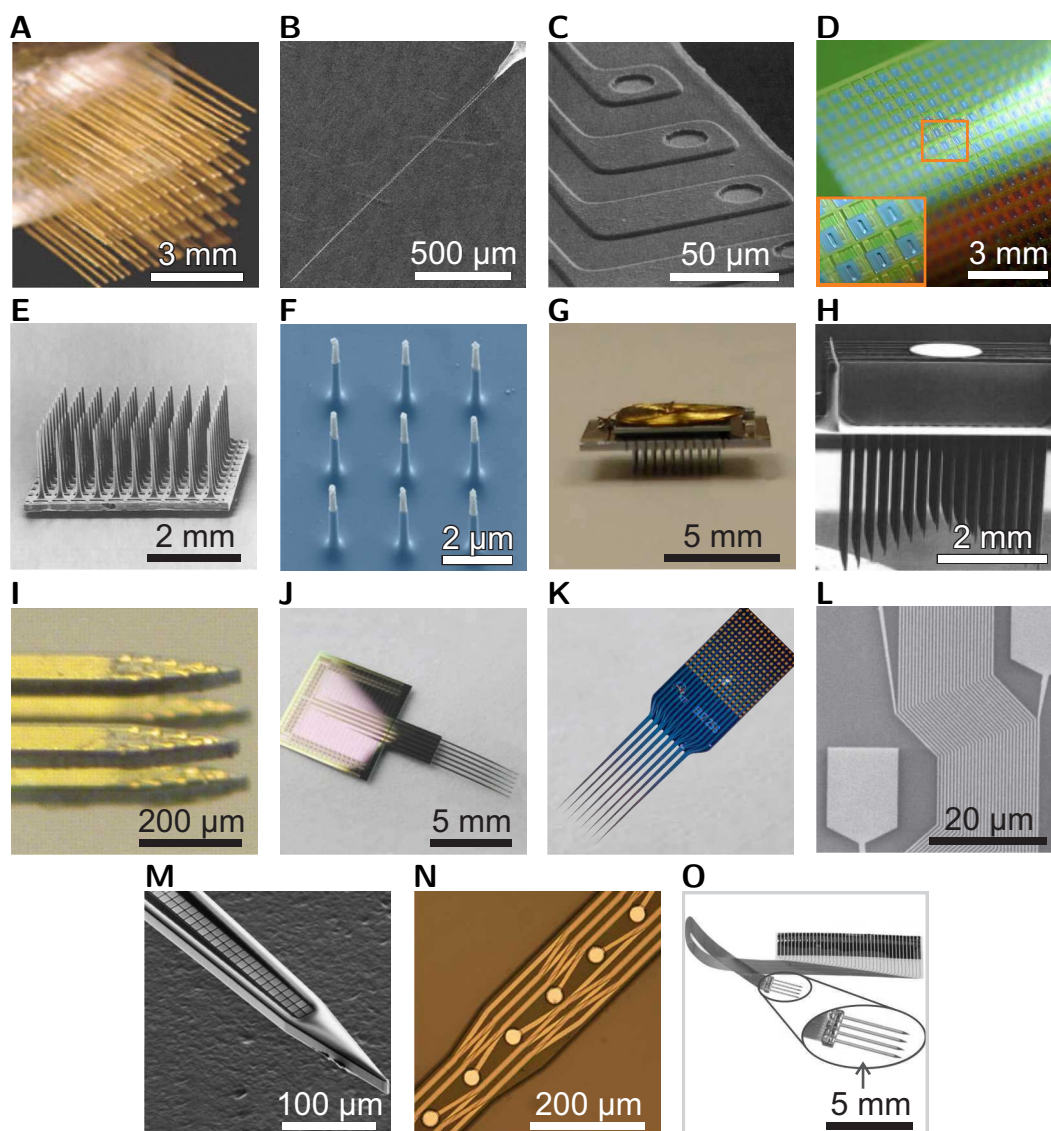


**Figure 2.14:**

Overview of devices for electrophysiological recording *in vivo*; **A**) Array of microwires (50  $\mu\text{m}$ -diameter, Teflon<sup>®</sup>-coated) stacked in 3D [177]; **B**) Intracellular pure carbon nanotube probe (5-10  $\mu\text{m}$ -diameter, parylene-coated) [178]; **C**) Four-channel linear probe (“Michigan array”) [179,180] **D**) Flexible, actively multiplexed 360 electrode ECoG array [181]; **E**) Array of 100 electrodes (“Utah array”) [182]; **F**) Vertical nanowire electrode array [183]; **G**) Wireless interface for chronic recording [184]; **H**) 8 $\times$ 16 shank 3D Michigan-style array (four sites per shank) [185]; **I**) 3D dual-side array [186]; **J**) Six-shank, 96-site probe [187]; **K**) 256-channel probe [188]; **L**) Multiplexed, nanofabricated (290 nm-traces), high-density array [189]; **M**) Nanofabricated (200 nm-traces) 1000-site single-shank probe [190]; **N**) 16-channel probe on a flexible substrate, fabricated using a two-layer process [191]; **O**) CMOS-based probe with 752 recording sites [192];

### 2.5.3 Integrated Devices

Several groups have been working on creating devices that integrate optical stimulation and electrical recording in one device in recent years. There are various approaches for fabricating such compact probes and an overview of recent accomplishments is given in Figure 2.15. First devices used an optical fibre coated with a conducting material (exposed at the tip) to be able to record from stimulated neurons (panel A). A more exotic device design makes use of thermal drawing (transforming a preform into a microfibre through heat and stress) to directly incorporate electrodes into the thin optical fibre. This makes it possible to have tens of recording sites (panel B). Microfabrication-based devices often include waveguides (e.g. from SU-8™) on a linear recording array. The device shown in panel C additionally includes a microfluidic channel for drug delivery. Other groups managed to miniaturize the basic setup by employing oxynitride waveguides on 8-channel recording probes (panel D). Multi-shank probes have been created with three electrodes and one waveguide per shank (panel E). Multiple  $\text{Si}_x\text{N}_y$  waveguides have been created on a single-shank probe together with high numbers of electrodes (panel F: 2 waveguides, 64 electrodes, panel G: 12 waveguides, 24 electrodes using a 193 nm process). Multi-shank, multi-waveguide probes have also been realized (panel H: 2 waveguides, 8 electrodes per shank). Integrated probes using LEDs as light sources include the probe shown in panel I. This very invasive piece is fabricated on a diamond substrate, showing good thermal properties. Recently, a four-shank device has been fabricated combining 3 LEDs (covering 150  $\mu\text{m}$ ) and 8 electrodes per shank (panel J). The low power consumption results in a minimal temperature increase. In addition to recording artefacts due to the Becquerel effect, capacitive coupling between the tracks in such highly integrated devices leads to artefacts when switching the LED power on and off. These have to be removed by post-processing. Integrated Utah-style arrays are also researched. In one instance a single tapered optical fibre was included in the middle of a standard recording array (panel K). Large LED arrays for *in vitro* use (as mentioned in section 2.5.1) have already been integrated with planar recording

arrays [139]. Utah-style *in vivo* devices are less common, but one example is shown in panel L. Development started with planar arrays [209] now the design includes SU-8™ needles with a conductive cladding for recording. Light from one LED is coupled in to each needle, yielding 32 ( $4 \times 4 \times 2$ ) integrated sites. The needle pitch has been further reduced to 400  $\mu\text{m}$  by another group (panel M) but instead of LEDs, their device relies on a scanning laser. Microendoscopy setups are another approach for combined lateral stimulation and recording. They provide unrivalled resolution, as shown in panel N. What becomes apparent from this multitude of devices being developed by different groups is the high demand for these advanced probes, which have been briefly summarized here. Further reviews on integrated devices are also available in the literature [210–213].

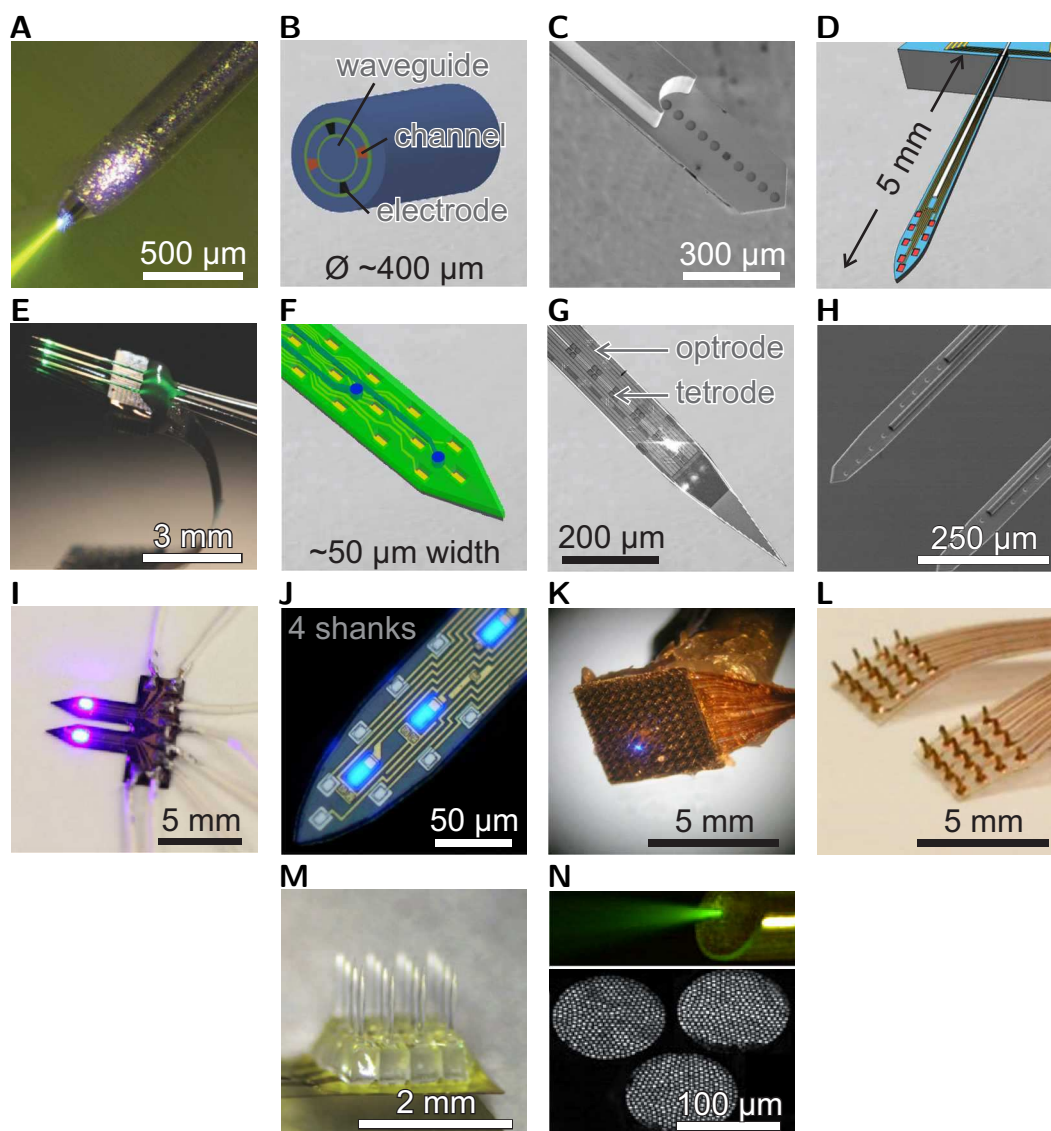


**Figure 2.15:**

Overview of devices for integrated optogenetic stimulation and electrophysiological recording; **A**) Coaxial optrode (single-site) [193]; **B**) Thermally drawn multifunctional fibres [194]; **C**) Polymer-based implant incorporating a waveguide, a fluidic channel and nine recording sites [195]; **D**) Recording probe with monolithically integrated dielectric waveguide [196]; **E**) 3D probe (recessed waveguide) with one integrated fibre per shank [197]; **F**) High-density optrode with two waveguides [198]; **G**) High-Density optrode-electrode probe using waveguides [199]; **H**) Dual-shank double-waveguide probe [200]; **I**) Diamond-based probe with one LED and two electrodes per shank [201]; **J**) Four-shank integrated GaN-on-Si probe with eight electrodes and three LEDs per shank [202]; **K**) Single waveguide integrated with Utah-style recording array [203, 204]; **L**) Slanted optrode array using  $\mu$ LEDs and waveguides [205, 206]; **M**) Transparent intracortical array (for use with external light source) [207] **N**) High-resolution fibre/electrode bundles [208]

## 2.6 Conclusion

This chapter covered basics of neurons, neuronal signalling and neural systems. Methods for stimulation and recording from these systems were introduced. Optogenetics was described as an important method for selective neural modulation with help from suitable light sources. A range of devices allowing optical stimulation and electrophysiological recording have been described. Although some of the implantable devices allow depth-dependent neural modulation, they are still limited. The waveguide probes require bulky and expensive light sources and the number of channels cannot be increased much further. Probes based on LEDs are an alternative, but the spatial resolution of probes employing commercial LEDs is low. Thermal and mechanical damage also have to be addressed, which will be done in the coming chapters. Since all the introduced devices incorporate sophisticated technology on a very small scale, it is important to first understand how they can be built. The next chapter will therefore introduce the concept of microfabrication and describe its key techniques.

## 3 Basics of Microfabrication

Microfabrication is a set of technique that is very important to this work. This chapter will therefore briefly cover the various aspects and will direct the reader to references for further information. More detailed information on microfabrication in general can be found elsewhere [214–216].

Microfabrication makes use of batch processing to create hundreds to thousands of identical devices on a substrate (usually silicon), known as a wafer. Wafers are thin slices cut from single crystal ingots (drawn from a silicon melt). The following fabrication steps are done on all devices at the same time. In the past decades a set of methods has been developed that makes it possible to fabricate devices with characteristic dimensions of less than  $100\ \mu\text{m}$  (microfabrication). The same methods can also be applied to produce even smaller systems. Nanotechnology starts with dimensions of  $100\ \text{nm}$ . As of 2016, chip designers can commercially produce integrated circuits with minimum feature sizes of only  $14\ \text{nm}$  using highly optimized processes based on the steps described in this chapter. A special environment is required to produce such small devices without contamination. All fabrication therefore takes place in a clean room containing orders of magnitude less dust particles than normal air. The clean room used for the fabrication of the devices described in this thesis, houses the tools shown in Figure 3.1. This chapter will explain each one of them and their role in the microfabrication chain. An important series of processes is known as photolithography and will be explained next.


**Figure 3.1:**

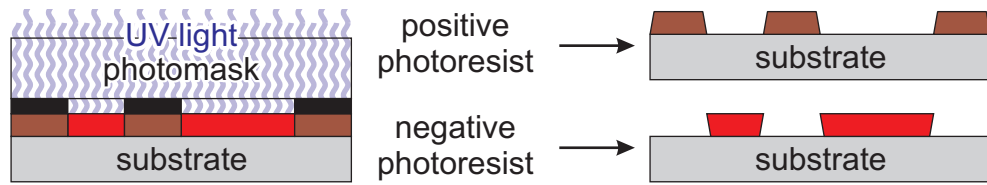
Tools used for the microfabrication in this work; **A)** Spin-coater (EMS, Model 4000) for applying photoresist; **B)** Hotplate (EMS, Model 1001-1) for photoresist baking; **C)** Mask aligner (SÜSS MicroTec, MA6) for pattern transfer to photoresist; **D)** Developer for selectively removing photoresist from an exposed film; **E)** Sputter coater (CVC, Model 601) for metal deposition; **F)** Evaporator (EDWARDS, AUTO 306) for thin metal deposition; **G)** PECVD (Oxford, Plasmalab 80 Plus) for growth of insulating layers; **H)** Rapid thermal annealer (Jipelec, JetFirst PROCESSOR) for Ohmic contact formation; **I)** RIE (Oxford, Plasmalab 80 Plus) for dry etching of thin films; **J)** ICP (STS, Multiplex ICP) for fast dry etching of thin films; **K)** Plasma asher (Matrix, SYSTEM ONE Stripper) for removing photoresist and organic contaminants; **L)** Wire bonder (K&S, Model 4526) for electrical connection to the macroworld; **M)** Parylene coater (SCS, PDS 2010 LABCOTER™ 2) for conformal biocompatible encapsulation; **N)** Stylus profilometer (Veeco, Dektak 3) for feature height measurements; **O)** Ellipsometer (Filmetrics, F20) for film thickness measurements

## 3.1 Photolithography

Photolithography is a key technique for creating microstructures. It is an optical mechanism for transferring patterns from a photomask to a light-sensitive polymer layer on a substrate by projection. The photomask is a square piece of glass usually 5" (12.7 cm) wide that is coated with chromium (it is itself created by lithography, but the pattern transfer is done by a laser or an electron beam).

The photolithography steps usually include the following. **Sample cleaning** is carried out to initially remove any surface contaminants and followed by **photoresist application**, which is usually done using spin-coating. Spin coating produces uniform layers of the light-sensitive polymer on the wafer with thicknesses usually between several hundred nanometres and several microns. The thickness can be adjusted by varying the spin speed, which is usually around several thousand RPM (dip-coating and spray-coating are alternative methods for rough surface geometries). Solvent remaining in the photoresist (PR) layer is evaporated in a **soft-bake** step (several minutes on a hot plate at around 100°C). The wafer is then ready for **exposure**. In this step, the photomask is precisely aligned with the wafer using alignment marks. It is then brought in contact and UV light coming from a mercury lamp is shone through the mask onto the resist (several seconds to minutes depending on the resist used). A **post-exposure-bake** can be used to smooth out optical interference effects. It is usually optional, except some resists require it to complete polymerization. During **development**, the soluble areas of the resist layer are removed with a developer solution (exposed sections in positive resists and unexposed sections in negative resists, see Figure 3.2), followed by rinsing with water. A **hard-bake**, as the name suggests, hardens the resist, which makes it more durable for aggressive etch processes.

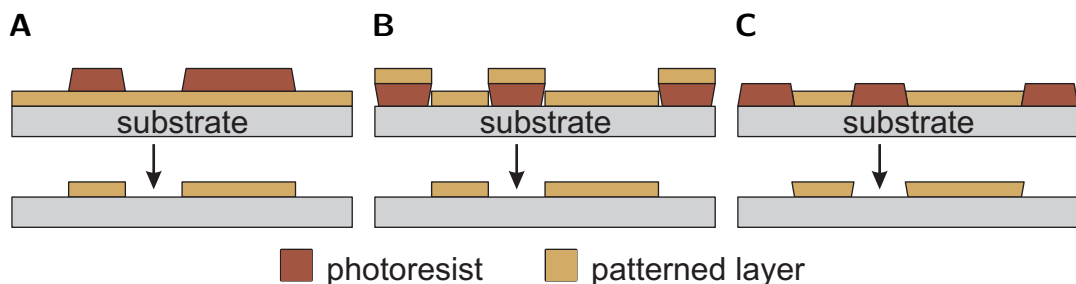
When fabricating devices with very small features (below 2  $\mu\text{m}$ ), optical steppers are typically used for the pattern transfer [217]. These machines demagnify the patterns on a photomask a certain number of times (e.g. 4 $\times$ ). Electron beam lithography is another option [218]. It can create very small features ( $\sim 10$  nm line width) and uses a focussed beam of electrons to write the pattern directly into

**Figure 3.2:**

Positive and negative types of photoresist; **positive resist**: exposed features get removed during development, **negative resist**: exposed features remain during development

a special resist. An additional advantage is that it makes photomasks obsolete. However, due to the high cost of the slow process, electron beam lithography is only an alternative when producing devices in small quantities. It is also possible to skip the photoresist step by directly writing the pattern into the substrate using a method known as focussed ion beam (FIB) [219].

Following the lithography, there are several approaches for transferring the pattern from the photoresist to the substrate. The first approach is the selective removal of material from a thin film layer through the resist mask. This can be done with various methods of dry or wet etching (Figure 3.3 A). The mask is then removed with a solvent (e.g. acetone/IPA) or by plasma ashing. Another method is to first create the mask, then deposit a film, and selectively remove it with the mask in a solvent (“lift-off”, Figure 3.3 B). Dedicated lift-off resists exist, that facilitate the process by producing an undercut that prevents material depositing on sidewalls

**Figure 3.3:**

Microtechnological structuring mechanisms; **A)** Subtractive structuring by material deposition followed by masking and etching; **B)** Additive structuring by material deposition onto a masked substrate followed by selective removal in a solvent (lift-off); **C)** Additive structuring by growing structures on a patterned substrate (e.g. electroplating)

(promotes lift-off by producing a discontinuity in the metal film). Negative resists also show this property, as do so-called image reversal resists that combine the benefits of positive and negative resists. Alternatively to lift-off, the pattern can be created by filling open areas in the resist using electroplating (Figure 3.3 C). Material deposition will be further explained in the next section.

## 3.2 Material Deposition

Thin film deposition mechanisms can be classified as being either physical (e.g. physical vapour deposition, PVD) or chemical (e.g. chemical vapour deposition, CVD). **Sputtering** is a quick PVD method for a wide range of materials. For the fabrication of the devices in this work, titanium, gold and aluminium were deposited by sputtering, with titanium acting as an adhesion layer. Figure 3.4 A illustrates the working principle: A target is bombarded with argon ions at low pressure. The ejected atoms travel towards the substrate and get deposited as a thin film. When RF-sputtering is used, even insulating materials can be deposited, since the technique avoids the build-up of positive charge on the target.

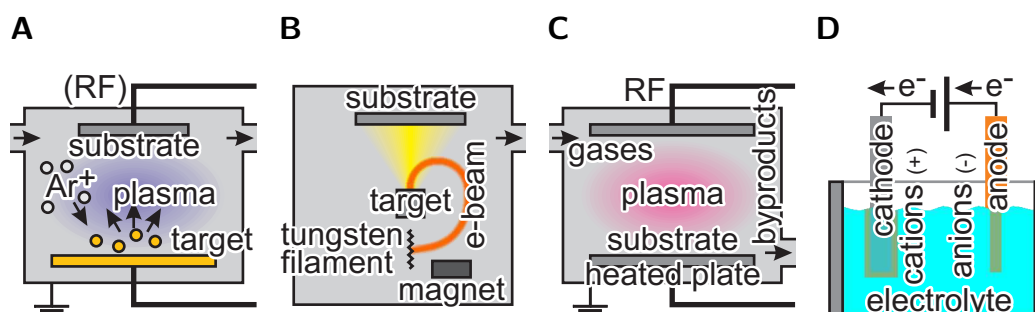


**Figure 3.4:**

Material deposition mechanisms used in microfabrication; **A)** Sputtering; **B)** Electron beam evaporation; **C)** PECVD; **D)** Electroplating; the cathode is covered with a layer made up of the anode material; charged particles are transported through the electrolyte when a voltage is applied between cathode and anode

Another PVD technology that is used in this work is **electron beam evaporation** (e-beam, Figure 3.4 B). In this case, a target is heated using an electron gun. The material evaporates and atoms travel towards the substrate (in high vacuum). The deposition rate is relatively slow compared to sputtering, but results in very uniform and pure films while keeping the temperature of the wafer at room temperature.

Plasma-enhanced chemical vapour deposition (**PECVD**, Figure 3.4 C) is a type of chemical vapour deposition that is frequently used during the fabrication of microsystems to create thin films of materials such as oxides, nitrides and carbides. For this, reaction gases are introduced into the chamber, where electrons in a plasma (as opposed to external heat) lead to the dissociation of the molecules. There are various ways for depositing silicon dioxide and silicon nitride. The reaction equations describing the deposition used here are given below (for silicon dioxide and silicon nitride, respectively). Using the same chemicals as for SiO<sub>2</sub> deposition in different proportions, it is also possible to create silicon oxynitride compounds.



A wide range of metals can be deposited using a process called **electroplating** [107] (Figure 3.4 D). For this process, the substrate must have a conductive surface, which is connected to the cathode of a current/voltage source with the target material connected to the anode. Both are immersed in an electrolyte solution and current flow leads to a material deposition on the substrate. Very thick structures can be created this way. The resulting surface is relatively rough but it can be smoothed by using additives in the electrolyte. In the case of platinum deposition, chlorine builds up on the anode and platinum is formed on the cathode as a result

of the following chemical reactions [108]:

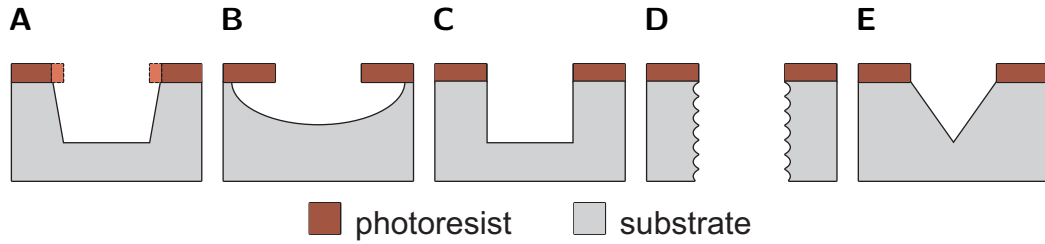


## 3.3 Annealing

In this work annealing is used during the LED fabrication for creating an ohmic contact between the semiconductor material and a previously evaporated metal layer (see section 2.4). This can be achieved through chemical reactions at the interface at elevated temperatures. Using the equipment, rapid temperature changes of up to 200°C/s and peak temperatures of over 1000°C can be reached using infrared radiation from a tungsten-halogen lamp. Special environments can be created during the process using O<sub>2</sub> and N<sub>2</sub>.

## 3.4 Etching

Etching is an important microfabrication method as it offers selective removal of material. Usually, etches are developed to obtain a high preference for a certain material. Etches are often also directional (anisotropic), which can be a helpful way to create sophisticated three-dimensional structures. Etching can be done using dry and wet etching methods, which will be addressed separately below. The different etch profiles that can be obtained are summarised in Figure 3.5. Important parameters are the etch rate of the material, the selectivity over the masking material used and the anisotropy of the etch. A good summary of etch rates is given by Williams *et al.* [220, 221]. One can distinguish between bulk and surface micromachining. While in surface micromachining thin films are deposited and selectively etched, in bulk micromachining structures are defined by selectively etching inside a substrate.

**Figure 3.5:**

Etch profiles resulting from different dry and wet etch processes; **A)** Physical dry etch; relatively good depth-selectivity, slopes on sidewalls due to mask etching at the pattern edges; **B)** Chemical etch (wet or dry); typically highly isotropic etch profile; **C)** Physical-chemical dry etch; leads to best etch profile (low undercut), profile created due to etch products being removed from surface by ion bombardment; **D)** Deep reactive ion etch (Bosch process); sidewall profile due to cyclic process, very high aspect ratios possible; **E)** Anisotropic wet etch (slow and fast etching crystal planes), profile depends on wafer orientation

### 3.4.1 Wet Etching

Wet etching methods use chemical reactions to create structures on a sample. They are usually characterized by a very isotropic etch profile, which makes them less suitable for small features. On the plus side, they tend to offer a high selectivity between materials. An overview of chemicals used for wet etching in this work is given in Table 3.1. Most commonly used is silicon dioxide etching using BOE (buffered oxide etch), which consists of hydrofluoric acid (HF) buffered with ammonium fluoride ( $\text{NH}_4\text{F}$ ) for a more controlled etch rate. BOE removes PECVD oxides following the reaction



Some wet etches are also highly anisotropic because they favour certain crystal planes. This can be exploited when creating 3D structures. Vertical sidewalls, pyramidal structures or underetched features can be created by changing the crystal orientation of the substrate material with respect to the wafer surface. A popular etchant for silicon is potassium hydroxide (KOH) with the crystal plane-dependent etch rates shown in Table 3.1.

### 3.4 Etching

Chemical	Material	Etch rate [nm/min]
BOE (7:1), 21°C	SiO <sub>2</sub> (PECVD) ITO	290 0.7
KOH (34 %), 70°C	Si <100> Si <110> Si <111> SiO <sub>2</sub> (PECVD)	629 [222] 1292 [222] 9 [222] 15 [221]
I <sub>2</sub> :KI:H <sub>2</sub> O (1 g:4 g:40 ml), 21°C	Au	~1000
HCl (40 %):H <sub>2</sub> O (1:1), 21°C	surface oxides	tens
NH <sub>4</sub> OH (30 %):H <sub>2</sub> O <sub>2</sub> (30 %):H <sub>2</sub> O (1:1:5), 70°C	organics, metals (Ti)	not measured, used for cleaning

**Table 3.1:**

Chemicals used for wet etching and their etch rates on different materials

#### 3.4.2 Dry Etching

Dry etching methods include ion beam etching (IBE) and reactive ion etching (RIE). Inductively coupled plasma reactive ion etching (ICP RIE, short ICP) and deep reactive ion etching (DRIE) are special forms of RIE. A comprehensive review is given by Nojiri [223]. **Ion beam etching** is a dry etch method that acts like an atomic sand blaster. Electrons emitted by a heated cathode are used to ionize argon atoms (or other heavy ion species) in a high vacuum. These ions are then accelerated towards the sample which leads to a unselective evaporation of the target materials. The process is particularly suited for materials that are hard to etch chemically. **RIE** uses a setup similar to RF-sputtering systems, but a mix of reactive gases are introduced in the chamber. The etch mechanism is a combination of physical etching by energetic ions and chemical etching from plasma radicals. **ICP RIE** systems are RIE systems in which the conventional parallel plate setup is modified. An RF coil is responsible for creating the plasma far away from the sample. A second power supply is used to create an electric field between the coil and the wafer, causing ion bombardment. This setup makes it possible to achieve high etch rates while minimizing damage. Among various other processes, ICP systems can be used to run the **Bosch process**, which is a

highly directional DRIE process for silicon. It allows trenches with aspect ratios of up to 90:1 to be created by continuously cycling between two steps: the etch step itself (using  $\text{SF}_6$ ) and a sidewall passivation step (using  $\text{C}_4\text{F}_8$ ), during which a fluoropolymer protective film is created.

### 3.5 Testing

Many microfabrication steps can be assessed under an optical microscope and lateral dimensions can be measured. Film thicknesses can be measured using a profilometer. Methods include **stylus profilometry** [224], where a sharp tip is moved over a patterned surface, and **ellipsometry** [225], where film thickness is determined by measuring the polarisation of light reflected from the surface. White light interferometry is an alternative for visualizing three dimensional surfaces. Electrical testing is done using probe stations (e.g. Wentworth 280X with HP 4155A), where set voltages or current can be applied through a set of needles attached to micro-manipulators.

### 3.6 Substrate Thinning

With an increasing demand of ever smaller chips, substrate thickness has become an issue that is being industrially addressed. Companies now offer to thin silicon substrates down to  $7\mu\text{m}$  (DISCO HI TEC EUROPE GmbH, Germany) using **mechanical grinding** [226]. An alternative to grinding is to use **silicon-on-insulator** (SOI) wafers. Here, a thin silicon device layer and a thick silicon substrate are separated by a thin insulating layer (usually  $\text{SiO}_2$ ), which allows device release by a selective wet etch process [227]. Chemical mechanical polishing (CMP) is an alternative method for thinning and planarizing a range of materials, where mechanical polishing is assisted by chemical etching. It is relatively slow, but can produce very flat surfaces, making it still very popular in industry [228].

## 3.7 Dicing

After the fabrication is complete, the individual devices created in parallel on the wafer usually have to be separated from each other. This singulation is called dicing. The most common method uses a **circular saw** to cut the wafer into rectangular shapes with a blade usually a few hundred microns wide. An alternative crude method is to scribe and break the wafer. This works when trying to dice the wafer along its crystal planes. **Laser dicing** [229] is another alternative, which makes it possible to create more complex geometries.

## 3.8 Bonding

**Die bonding** [230] is the attachment of the device onto a substrate. This can be a lead frame or even just a PCB. A specialised resin is used and the device is then precisely picked and placed. **Wire bonding** is a technique used to make electrical contact with the microsystem. Using a wire with a typical diameter of 25  $\mu\text{m}$  made from materials such as aluminium, with a low content of silicon, a robust bond is created both on the device's and on the substrate's contact pad. Wire bonders use ultrasound and pressure to achieve this. Wire bonds come in different shapes, namely wedge and ball bonds [231].

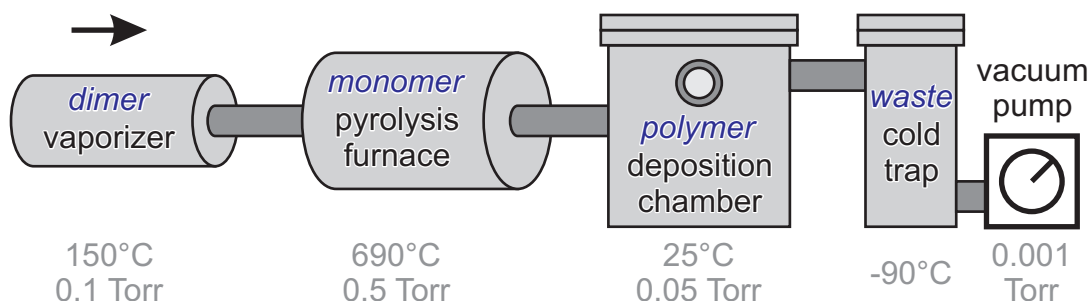
## 3.9 Encapsulation

When dealing with microdevices for biological environments, encapsulation is often necessary to ensure **biocompatibility** (“the ability of a material to perform with an appropriate host response in a specific situation” [232]). One popular option for this are parylene polymers. Parylene is deposited from a gaseous monomer. It can be viewed as a condensation process taking place at room temperature. Unlike other deposition mechanisms, the process produces conformal coatings, meaning that sidewalls are coated with the same thickness as surfaces (see 3.6). A lot of care has to be taken to create good adhesion between parylene and the substrate. This can be achieved with adhesion promoters, which have to be applied before the deposition (see Table A.12).

**Figure 3.6:**

Encapsulation quality; **A)** Non-conformal coating using previously described processes; **B)** Conformal coating (e.g. parylene), all sides of the sample evenly covered

Figure 3.7 shows a schematic of the deposition process. The granular monomer is first loaded into the vaporizer, where it then sublimates under heat and vacuum. Cleaving of the dimer into a monomer is achieved in a furnace at 690°C. At room temperature the monomer polymerizes and forms the desired film on the substrate. Waste products condense in the cold trap so they do not enter the vacuum pump. The chamber and vaporizer form a control loop: the chamber pressure is measured and used to adjust the temperature of the vaporizer, which in turn controls the rate at which the monomer is created and enters the chamber. The amount of monomer in the chamber affects the pressure. The process ends automatically when the dimer has sublimated completely. It leads to a drop in chamber pressure and a surge in vaporizer temperature above threshold.

**Figure 3.7:**

Parylene deposition (schematic); material flow is from a vaporizer over a furnace into the process chamber, where the deposition takes place, waste products are collected in a cold trap

## **3.10 Conclusion**

This chapter covered basics of microfabrication. Photolithography was explained as a key technique for building very small scale devices. Methods for creating and removing thin films were summarized. The next section will focus on the engineering of a group of devices employing these microfabrication techniques. The devices allow spatiotemporally precise optical stimulation in live animals (rodents), in order to further understanding of neural processing in the brain (see chapter 2).

## 4 $\mu$ LED Needle Probes for Depth-Specific Optogenetic Control of the Brain *In Vivo*

As demonstrated by other groups [233–235], controlling neural circuits is a powerful approach to uncover a causal link between neural activity and behaviour. Optogenetics – offering cell-type-specific perturbation with millisecond precision – has been widely adopted by the neuroscience community [236]. However, optogenetic studies require light delivery in complex patterns with cellular-scale resolution, while covering a large volume of tissue at depth *in vivo*, which is impossible with conventional methods. Penetrating arrays offer a solution by moving the light source into the brain, as shown in Figure 4.1 A. This chapter introduces novel silicon-based light-emitting diode ( $\mu$ LED) arrays (see Figure 4.1 B) for *in vivo* optogenetics, offering an inexpensive novel tool for the precise manipulation of neural activity. The devices consist of up to ninety-six 25  $\mu$ m-diameter  $\mu$ LEDs

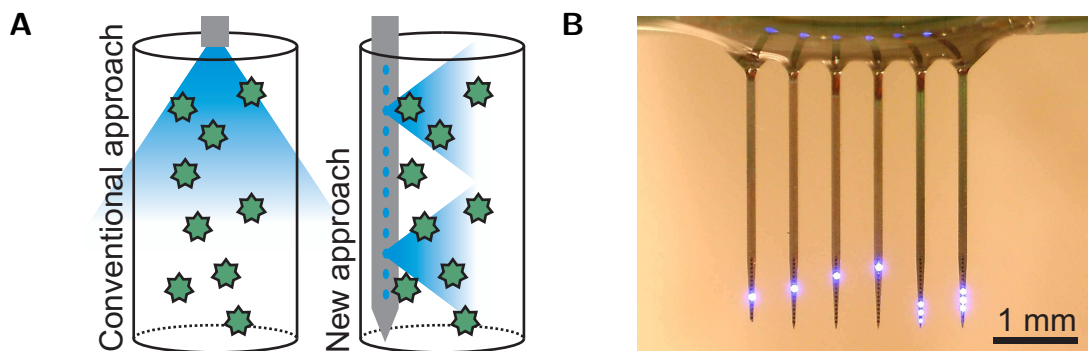


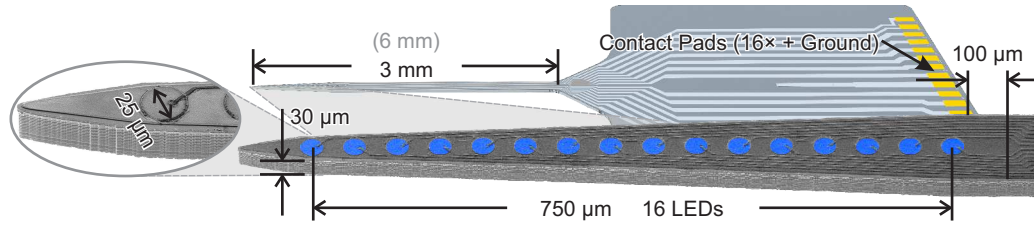
**Figure 4.1:**

Working principle of LED needle probes; **A)** LED needle probe compared to conventional approach using fibre optics: the probe penetrates the brain and illuminates neurons at different depths with light propagating sideways; **B)** Arrays of needle probes allow for complex stimulation patterns using 96  $\mu$ LEDs distributed over six shanks

emitting at a wavelength of 450 nm with a peak irradiance of  $400 \text{ mW/mm}^2$ . A width of  $100 \mu\text{m}$ , tapering to  $1 \mu\text{m}$  at the tip, and a  $\sim 40 \mu\text{m}$  thickness help minimize tissue damage during insertion; thermal properties permit optogenetic operating regimes and average temperature increases below  $0.5^\circ\text{C}$ . The following sections will cover the probe design, fabrication, simulation, characterization and control.

### 4.1 Design

GaN-on-Si LEDs can be fabricated in almost any size and shape. The fact that the active layers just need to be patterned by lithography and an etch makes high density arrays possible. Silicon can be easily patterned as well to create the needle-shaped structure. Design restrictions arise from the minimum fabricable feature sizes and the fact that the probes should be as compact as possible to minimize tissue damage. The  $\mu\text{LEDs}$  should be in the order of a neuronal cell body in size. On the other hand,  $\mu\text{LEDs}$  with dimensions of  $\sim 10 \mu\text{m}$  diameter are difficult to fabricate reliably. If the design layout is only considered then the shank widths should be in the order of  $100 \mu\text{m}$  and the device thickness should be below  $50 \mu\text{m}$  to keep tissue damage at an acceptable level. However, this ignores the optical (light emission profile) and thermal properties (probe/tissue heating), which play a significant role in constraining the design and are explored in this chapter. Further design criteria are that the  $\mu\text{LEDs}$  should be able to cover all the layers of the mouse cortex and that it should be possible as well to target deeper brain structures. The  $\mu\text{LEDs}$  are therefore spaced out over  $750 \mu\text{m}$  and the shank length was chosen to be at least 3 mm. Given the maximum width of  $100 \mu\text{m}$  and a minimum fabricable track and gap width of  $2 \mu\text{m}$ , a maximum number of 16  $\mu\text{LEDs}$  can be fitted onto a single shank. Bond pads should be around  $100 \mu\text{m}$  in width. The currently established minimum track width and separation values for commercially available printed circuit boards are  $100 \mu\text{m}$ . To facilitate wire bonding, the same values were chosen for the bond pads on the

**Figure 4.2:**

1D single-shank  $\mu$ LED array; SEM image of the tip (before parylene deposition, which adds  $\sim 6 \mu\text{m}$  to each side) in front of a schematic of the whole probe, 16  $\mu$ LEDs in a linear arrangement with a pitch of  $50 \mu\text{m}$ ,  $\mu$ LED diameter is  $25 \mu\text{m}$  as shown in detail, shank length is either 3 mm or 6 mm, individual tracks lead to the p-contact of each  $\mu$ LED

device. All these constraints lead to a probe design with the dimensions shown in Figure 4.2. In Table 4.1 an overview of the designed and fabricated needle probes is given, showing numbers of stimulation sites and dimensions (the naming of the probes is explained in section A.2.1); Figure 4.3 shows images and schematics.

In preparation for electrode integration (see chapter 6), slightly wider probes have also been fabricated (Table 4.1, device b) that can accommodate the additional metal tracks required. The microfabrication approach adopted here can be easily scaled to 100s of sites and beyond. To demonstrate this advantage, four- and

	Name	Shanks			LEDs				Electrodes
		# []	width [ $\mu\text{m}$ ]	length [mm]	# per shank []	# 2D []	# 3D (4x) []	pitch [ $\mu\text{m}$ ]	
a	<b><math>1 \times 16(\text{S/L})^1</math></b>	1	102	3/6	16			50	0
b	<b><math>1 \times 16\text{W}(\text{S/L})</math></b>	1	171	3/6	16			50	0
c	<b><math>4 \times 8(\text{S})</math></b>	4	102	3	8	32	128	100	0
d	<b><math>6 \times 16(\text{S})</math></b>	6	102	3	16	96	384	50	0
e	Spacer	0							

<sup>1</sup> S=short (3 mm), L=long (6 mm)

**Table 4.1:**

Overview of designed and fabricated  $\mu$ LED needle probes showing number of shanks and LEDs, as well as basic dimensions for various designs (values for 3D designs assume stacking of four die); fabricated devices in bold; a-d)  $\mu$ LED devices, e) spacer for 3D integration

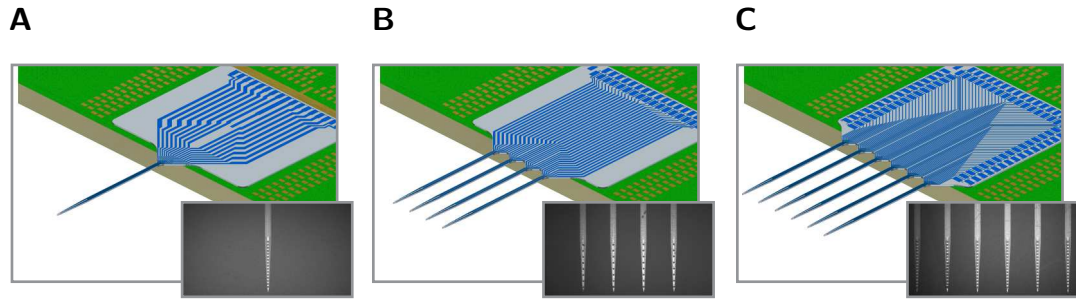


**Figure 4.3:**

Overview of designed and fabricated  $\mu$ LED needle probes (images in front of schematics on PCBs); **A**) 1D single-shank, 16  $\mu$ LEDs (Table 4.1 a); **B**) 2D quad-shank, 32  $\mu$ LEDs (Table 4.1 c); **C**) 2D hex-shank, 96  $\mu$ LEDs (Table 4.1 d)

six-shank probes with up to 96  $\mu$ LEDs were fabricated in addition to the single shank devices (Table 4.1, devices c-d). Furthermore, these fabrication techniques permit batch fabrication of devices on a single substrate and with correct mask design, it is possible to create future 3D systems using stacked devices (Table 4.1, device e).

Figure 4.4 shows other available stimulating devices (introduced in section 2.5) assessed by their ability to stimulate over a wide range, their spatial precision and their invasiveness. The new  $\mu$ LED devices just described are assessed by the same criteria. What can be seen is that the devices introduced in this work offer both high spatial coverage and resolution, which was previously unavailable. At the same time the invasiveness is kept low, minimizing brain damage. Probe stacking could eventually produce devices that can have a similar coverage and resolution as those shown by Zorzos *et al.* [154, 155] (Figure 4.4 C), but with a smaller cross section. A notable advantage is ease of use, since  $\mu$ LED based probes do not require expensive laser setups.

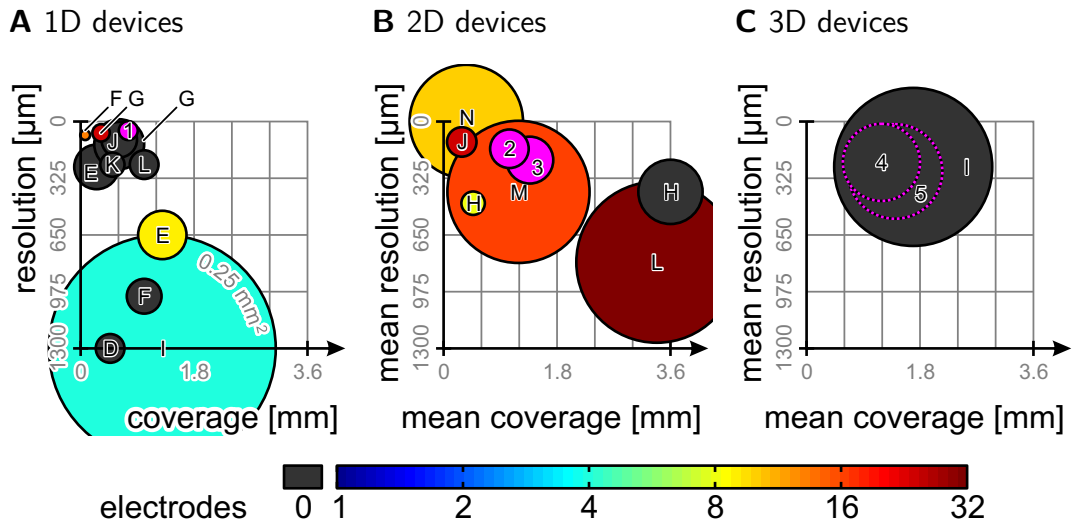


**Figure 4.4:**

Comparison of optogenetic stimulation devices (cf. sections 2.5.1 and 2.5.3, single-source devices not shown), assessed by their spatial coverage and resolution (location of the centre points of the circles) in one (panel A), two (panel B) and three (panel C) dimensions; resolution and coverage are averaged for multi-dimensional probes; the circular area is proportional to probe invasiveness (cross section); devices fabricated within the scope of this work are highlighted in pink, other stimulating probes (no electrodes) are shown in grey (letters correspond to the devices shown in Figure 2.12); integrated recording probes are colour-coded to show the number of electrodes (letters correspond to the devices shown in Figure 2.15); **A**) 1D-probes, ①: single-shank probe from this work (Figure 4.3 A); **B**) 2D-probes, ②: quad-shank probe from this work (Figure 4.3 B), ③: hex-shank probe (Figure 4.3 C); **C**) 3D-probes, ④: 4× quad-shank probe from this work, stacked (future device, Figure 8.4 A), ⑤: 4× hex-shank probe from this work, stacked (future device, Figure 8.4 B)

## 4.2 Fabrication

This section covers the fabrication of the  $\mu$ LED probes. The process is divided into the front-end, meaning the monolithic microfabrication using techniques described in chapter 3, and the back-end, referring to the following system integration steps. A quick summary is given here, followed by a detailed step by step description in sections 4.2.1 and 4.2.2.

The fabrication started with a 6-inch GaN-on-Si wafer with LED layers grown on Si(111) by metalorganic vapour phase epitaxy (MOVPE). The wafers are supplied by Plessey Ltd.; further details of growth and the epitaxial layer sequence are available in section 2.4 and elsewhere [125]. In brief, the epistuctures consist of an AlN nucleation layer, an AlGaN strain management layer, and a Si-doped GaN layer, followed by InGaN/GaN multiple quantum wells (MQW), an AlGaN current blocking layer, and a p-type GaN layer.

The material was diced into samples by scribing the back side and cleaving (see Figure A.4 for schematic). All the following steps of the fabrication process are pictured in Figure 4.5. The top panel in each of the itemised steps shows a schematic cross-section, while the lower panel shows a plan view image of the actual device. A thin layer of Ni/Au was electron-beam evaporated onto the surface of the wafer and forms a current spreading contact to the p-type GaN. This metal layer was then photolithographically patterned and reactive-ion etched, followed by an inductively coupled plasma (ICP) etch of the p-type GaN that exposed the n-type layer. This creates isolated 25  $\mu\text{m}$ -diameter mesa structures that form the  $\mu\text{LEDs}$ . The wafer was then thermally annealed to ensure good electrical contact between the Ni/Au layer and the p-type GaN. A Ti/Al metal layer was sputter-deposited to serve as a contact to the n-GaN, covering the whole sample except the  $\mu\text{LED}$  sites. After this, an insulating bilayer of  $\text{SiO}_2$  was deposited using PECVD and selectively etched on the  $\mu\text{LEDs}$  to allow contact through to the current spreading layer. A Ti/Al metal stack was deposited to create the sixteen tracks for the  $\mu\text{LEDs}$  and ICP etched. These connect to the current spreading contact and are electrically insulated by the deposition of another  $\text{SiO}_2$  bilayer. Contact pad vias were etched and Ti/Au contact pads were deposited to facilitate wire bonding. Trenches around each device were created by deep reactive ion etching and defined the final probe shape. The devices were thinned from the back side to a final thickness of 30  $\mu\text{m}$ , which also singulates each probe. Probes were then separated from the frame and die and wire bonded to a custom-designed PCB. The wire bonds were potted using a UV-curable epoxy.

A thick layer of parylene C was conformally deposited on the probe for insulation and to improve biocompatibility. The whole process has been developed to the point where yields of 75 % in terms of individually addressable  $\mu$ LEDs are being achieved, with electrical shorts and breaks being the dominant sources of failure.

### 4.2.1 Front-End

The fabrication process is described in more detail below. Each step (1-17) links to the corresponding panel in Figure 4.5.

**Step 1** After scribing an ID on the back of each sample, they were cleaned in acetone and isopropanol for five minutes. Any surface oxides were removed by immersing them in a solution of hydrochloric acid (HCL) and deionized water (1:1) for two minutes. The samples were cleaned with deionized water and blow-dried using nitrogen. They were then taped to a silicon carrier wafer using Kapton® tape over the corners of the samples. They were loaded into the electron beam evaporator for metal deposition. Care was taken to minimize exposure time to the environment. A 10/20 nm bilayer of nickel/gold (Ni/Au) was then deposited using deposition rates of  $\sim 0.05$  nm/s and  $\sim 0.15$  nm/s, respectively. Ni/Au has a higher translucence compared to the alternative, palladium (Pd). It is therefore the choice for top-emitting LED devices.

**Step 2** A photoresist mask was created using (MICROPOSIT®) S1818® (spun at 4000 RPM for 30 s, with prior HDMS prime). The samples were soft-baked at 115°C for 2 min. The samples were then exposed for 7.5 s using photomask 1.1. Development was done using diluted (1:1 with deionized water) MICROPOSIT® developer concentrate (Shibley, USA) for 40 s.

**Step 3** The current spreading metal layer was etched using RIE 2 recipe *niautest* (using Ar/O<sub>2</sub>, Table A.5) for 4 min. The samples were transferred to a silicon carrier wafer and fixed using wax. The p-GaN was then etched using ICP 2 recipe *GaN\_David* (using Cl<sub>2</sub>, Table A.8) for 60 s. After the etch the samples were cleaned using (MICROPOSIT® REMOVER) 1165 (heated on a hotplate at 115°C

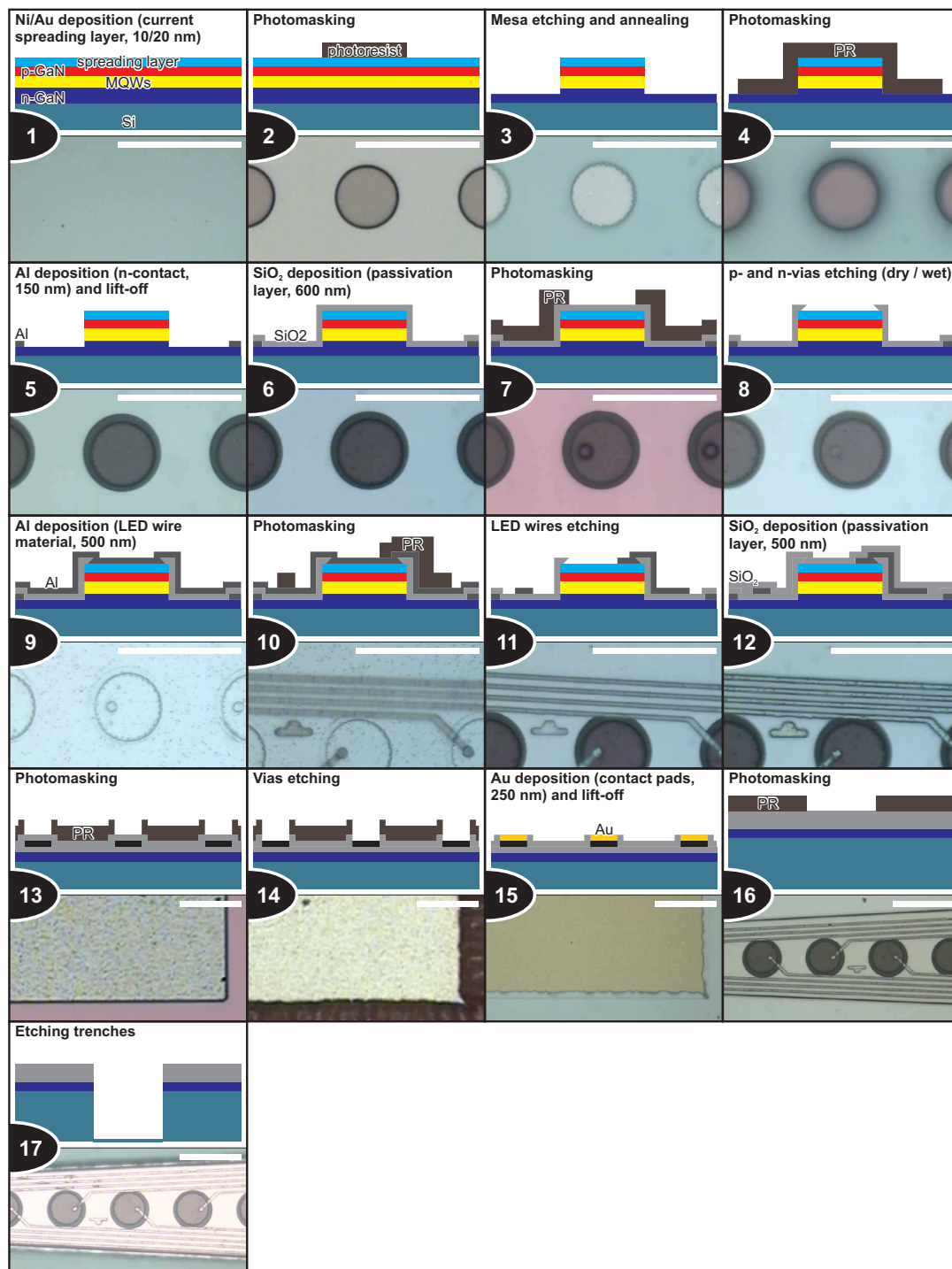


**Figure 4.5:**

Fabrication steps of  $\mu$ LED needle probes (front-end); mesa structures are etched into GaN-on-Si material, aluminium tracks are created to contact the p-GaN and the n-GaN, separated by an insulating  $\text{SiO}_2$  layer, trenches are etched for consequent device separation, scale bars are  $50\ \mu\text{m}$

for about one hour), followed by a five-second ultrasound clean. The samples were cleaned in water and dried. Annealing was done on a silicon carrier wafer (samples loosely placed) using program 3 on the RTA (Figure 3.1).

⚡ long ultrasound exposure can damage the current spreading layer

**Step 4** A thick (7  $\mu\text{m}$ ) photoresist mask was created using (MEGAPOSIT®) SPR®220-7 photoresist spun at 4000 RPM for 30 s (with prior HDMS prime). The resist was baked at 115°C for 2 min. The samples were then exposed for 40 s using photomask 1.2. Development using diluted MICROPOSIT® developer concentrate (1:1 with deionized water) took about one minute (agitate samples strongly).

**Step 5** A bilayer of titanium and aluminium was deposited by sputtering (Figure 3.1). For this, the samples were fixed to a silicon carrier wafer using Kapton® tape. Titanium was deposited for 2:51 min and aluminium was deposited for 4:33 min leading to a layer thickness of 50/100 nm. A lift-off was performed overnight using acetone followed by a 15 s ultrasound clean and a 5 min clean in isopropanol.

**Step 6** A SiO<sub>2</sub> bilayer of 300/300 nm was deposited using PECVD (Figure 3.1). The deposition rate was checked using a Filmetrics ellipsometer and a blank piece of silicon loaded in the machine with the samples. The deposition time of the second run was adjusted accordingly. Samples were also cleaned using acetone and isopropanol for five minutes each between the two runs. Bilayers are used to avoid pinhole formation.

**Step 7** A photoresist mask was created using S1828® (spun at 4000 RPM for 30 s, with prior HDMS prime). The samples were soft-baked at 115°C for 2 min. The samples were then exposed for 12 s using photomask 1.3. Development was done using diluted MICROPOSIT® developer concentrate (1:1 with deionized water) for 40 s followed by 3 s in pure developer (overdevelopment facilitates remasking).

**Step 8** Vias were etched using RIE 1 recipe *mlesio2* (using  $\text{CHF}_3/\text{Ar}$ , Table A.1) for 14:00 min (halfway through the oxide layer). Resist was then stripped using acetone (30 min) and isopropanol (5 min) and the samples were remasked using S1828® (process as outlined before). This was done to avoid defects in the resist mask being transferred, etching the oxide mask out of place. Samples were etched further using RIE 1 recipe *mlesio2* (using  $\text{CHF}_3/\text{Ar}$ , Table A.1) until ~50 nm of the oxide film remained. The final etch was done using a buffered oxide etch (BOE, diluted 7:1). A plastic beaker was used, the etch time was 90 s. After the etch, samples were cleaned in deionized water, acetone (overnight) and isopropanol (5 min).

 BOE is a dangerous chemical, extreme care must be taken

**Step 9** A bilayer of titanium and aluminium was deposited by sputtering (samples on carrier wafer with Kapton® tape). Titanium was deposited for 2:51 min and aluminium was deposited for 22:45 min leading to a layer thickness of 50/500 nm.

**Step 10** A photoresist mask was created using S1818® (spun at 4000 RPM for 30 s, with prior HDMS prime). The samples were soft-baked at 115°C for 2 min. They were then exposed for 7.5 s using photomask 1.4. Development was done using diluted MICROPOSIT® developer concentrate (1:1 with deionized water) for 20 s.

**Step 11**  $\mu\text{LED}$  tracks were etched using ICP 1 recipe *AlRobert* (using  $\text{Cl}_2/\text{BCl}_3$ , Table A.6) for 3:30 min (colour change was visible after ~2:40 min indicating a complete etch). Resist was then stripped using acetone and isopropanol (5 min each).

**Step 12** A SiO<sub>2</sub> layer of ~500 nm was deposited using PECVD (Figure 3.1). A bilayer might be used in the future to help protect the devices *in vivo*. The deposition rate was checked using the Filmetrics ellipsometer on a blank piece of silicon loaded in the machine with the samples.

**Step 13** A thick (7 μm) photoresist mask was created using SPR®220-7 photoresist spun at 4000 RPM for 30 s (with prior HDMS prime). The resist was baked at 115°C for 2 min. The samples were then exposed for 40 s using photomask 2.6. Development using diluted MICROPOSIT® developer concentrate (1:1 with de-ionized water) took about one minute (agitate samples strongly).

**Step 14** Contact pad vias were etched using RIE 1 recipe *iopsio2* (using CHF<sub>3</sub>/Ar, Table A.1) for ~14:00 min (10 % overetch). A one-minute oxygen plasma clean was performed to remove any resist residues on the contact pads (RIE 1 recipe *o2ash*, using O<sub>2</sub>, Table A.4).

**Step 15** Contact pads were sputtered using a titanium/gold layer stack (50/250 nm). Titanium was deposited for 2:51 min and gold was deposited for 2:00 min. A lift-off was performed in heated 1165 (hotplate at 115°C) for 30 min followed by a 10 s ultrasound clean. Samples were then cleaned in water and blow-dried.

**Step 16** A thick (7 μm) photoresist mask was created using SPR®220-7 photoresist spun at 4000 RPM for 30 s (with prior HDMS prime). The resist was baked at 115°C for 2 min. The samples were then exposed for 20 s using photomask 2.9. Development using diluted MICROPOSIT® developer concentrate (1:1 with de-ionized water) took about three minutes (agitate samples strongly).

**Step 17** The etching of the trenches consisted of the consecutive removal of several layers. SiO<sub>2</sub> was first removed using RIE 1 recipe *iopsio2* (using CHF<sub>3</sub>/Ar, 42:18 min, 10 % overetch, Table A.1). Titanium and aluminium were then removed using ICP 1 recipe *AlRobert* (using Cl<sub>2</sub>/BCl<sub>3</sub>, Table A.6) for ~3 min (one minute

after completion of colour change). The photoresist burns in the process. It was therefore removed (using 1165) and the samples were remasked (see step Step 16). The GaN epistructures were etched using ICP 2 recipe *GaN\_David* (using  $\text{Cl}_2$ , Table A.8) for 2:30 min. Trenches in silicon were etched using DRIE recipe *hptest4* (using  $\text{SF}_6$ ) for 10:00 min, which leads to trenches approximately 45  $\mu\text{m}$  deep. The resist was subsequently removed.

### 4.2.2 Back-End

The following steps (18-20) correspond to the panels in Figure 4.6.

**Step 18** (Figure 4.6) The samples were transferred to a carrier wafer face down. A photoresist layer (S1828®) was used for adhesion. The resist was baked with the samples securing them in place. The wafers were then thinned to a final thickness of 30  $\mu\text{m}$  using mechanical grinding (DISCO HI TEC EUROPE GmbH, Germany). The single probes were removed from the carrier wafer by washing with acetone and filtration through filter paper. The fragile devices can be moved using their property to adhere via surface tension to a wet cotton bud.

Wet etching with KOH could replace this approach and reduce costs. The crystal plane orientation of the used material ( $\langle 111 \rangle$  wafer) makes horizontal underetching ( $\langle 100 \rangle$  and  $\langle 110 \rangle$  planes) possible, but great care must be taken to protect the devices during this aggressive etch.

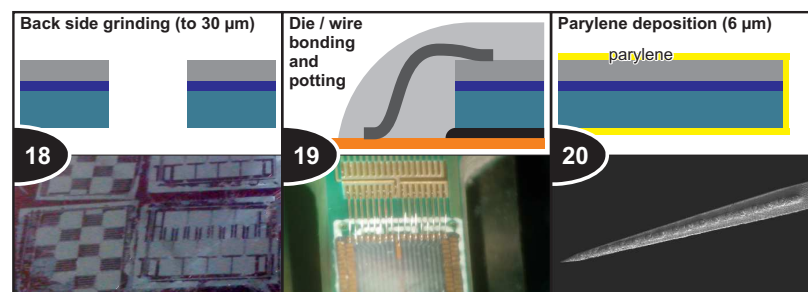


**Figure 4.6:**

Fabrication steps of LED needle probes (back-end); devices are separated by back side grinding and passivated with parylene C on a PCB

**Step 19** Two-layer PCBs were designed using CadSoft EAGLE layout editor [237] and fabricated by Eurocircuits N.V., Belgium [238]. The PCBs were then populated using reflow soldering. For **die bonding**, an adhesive was first applied to the PCBs. The devices were then picked up with a wet cotton swab stick and transferred to the PCB. They were manually aligned and pushed into the glue. **Wire bonding** was done manually with a K&S Model 4526 wire bonder. The wire was 25  $\mu\text{m}$  in diameter and made from Al wire with 1% Si. The contact pads were protected by **potting** with NOA68 epoxy (Norland), which was then cured by UV radiation ( $\sim 15$  min at  $5 \text{ W}/\text{m}^2$ ). A plastic box was fitted with metal inlays for safely storing the probes (Figure A.7).

**Step 20** Parylene C deposition was the final step in the fabrication process. The polymer was deposited conformally onto the device (see Figure 3.7). A layer thickness of  $\sim 6 \mu\text{m}$  was used. A-174 silane adhesion promoter was used in vapour form by wetting the chamber walls.

## 4.3 Simulation

In order to predict the behaviour of the  $\mu\text{LED}$  probes *in vivo*, various simulations have been conducted examining optical and thermal characteristics. Monte Carlo simulations for light propagation can give an estimate for the maximum penetration depth of the light into the tissue for a given optical power at the  $\mu\text{LED}$  surface, paired with the known activation levels of the optogenetic opsins. A Joule heating and transient heat transfer simulation can give insight into the pulse waveforms that such an operation would permit, keeping the peak or average temperature below a certain threshold that is safe for the cells.

### 4.3.1 Light Propagation

When thinking about the spatial resolution of the probes, it is important to consider not only the separation of the light sources, but also how light propagates through brain tissue from the  $\mu$ LED surface. Monte Carlo simulations have therefore been conducted to assess the expected light propagation in brain tissue (code modified from Jacques [239]). The  $\mu$ LED was treated as a Lambertian

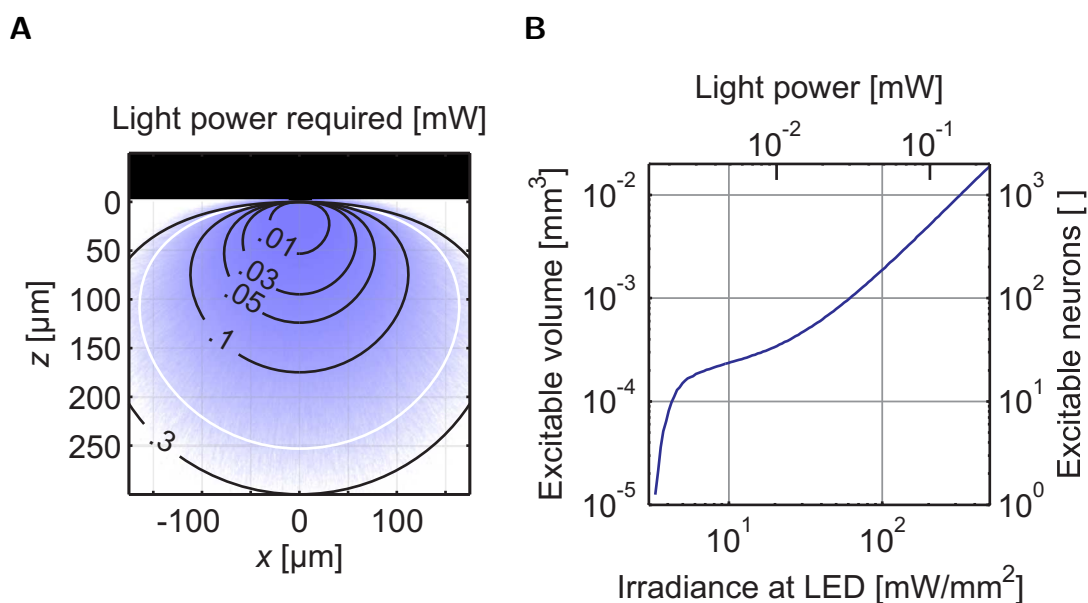


**Figure 4.7:**

Simulated light propagation in brain tissue; **A)** Light power output required to excite channelrhodopsin at various locations from the LED ( $I > 1 \text{ mW/mm}^2$ ), the white line shows the volume that an average  $\mu$ LED with electrical characteristics as shown in Figure 4.14 can excite at 5 mA; **B)** Estimation of the number of neurons excitable with a given light power or irradiance (volume data extracted from panel A,  $10^5 \text{ neurons/mm}^3$  assumed [27,240] with all neurons expressing ChR2)

source and coefficients for scattering ( $\mu_s$ ) and absorption ( $\mu_a$ ) were assumed to be  $117\text{ cm}^{-1}$  and  $0.7\text{ cm}^{-1}$ , respectively (grey matter [64]). Figure 4.7 A shows the simulation results – light powers required for ChR2 excitation ( $I > 1\text{ mW}/\text{mm}^2$ ) at various points within the irradiated tissue.

If the neuron density is taken as  $10^5\text{ mm}^{-3}$  (mouse cortex) [27, 240], a rough estimate of the number of affected units can be calculated. This demonstrates that each  $\mu\text{LED}$  has a dynamic range that can target very few neurons on the one end, and up to  $\sim 1500$  neurons at 5 mA (Figure 4.7 B). More neurons can be recruited at higher drive currents; however, the limiting factor becomes the dissipation of electrical power as heat at the surface of the  $\mu\text{LED}$ . This is an important factor when implanting optoelectronic devices, such as this, into the brain and will be discussed further in the next section.

Monte Carlo simulations can also provide information about the resolution that can be achieved using the  $\mu\text{LED}$  probes. The results are shown in Figure 4.8. Panels A-C illustrate how the optical field spreads through simulated brain tissue for varying  $\mu\text{LED}$  sizes (50, 25, 10 and 5  $\mu\text{m}$  diameters) and at different  $\mu\text{LED}$

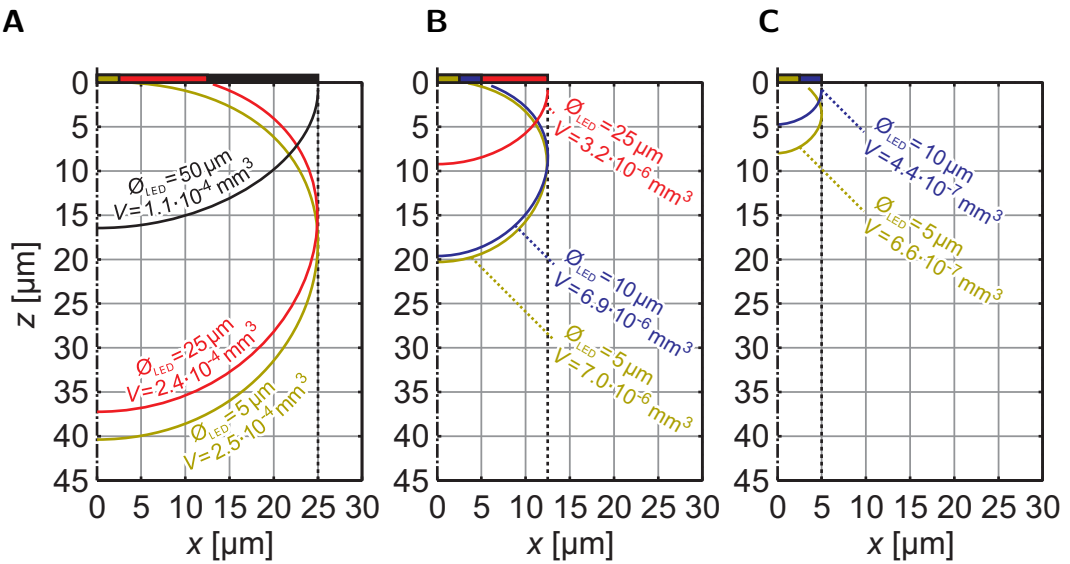


**Figure 4.8:**

Simulated  $\mu\text{LED}$  resolution during optogenetic stimulation of brain tissue; contour lines represent activation thresholds (arbitrary value), values for excitable volume are shown; **A)** 50  $\mu\text{m}$  lateral resolution ( $\text{LED diameter } \text{O}_{\text{LED}} < 50\text{ }\mu\text{m}$ ); ; **B)** 25  $\mu\text{m}$  resolution ( $\text{O}_{\text{LED}} < 25\text{ }\mu\text{m}$ ); **C)** 10  $\mu\text{m}$  resolution ( $\text{O}_{\text{LED}} < 10\text{ }\mu\text{m}$ )

separations (50, 25 and 10  $\mu\text{m}$  pitch). In panel A it can be seen that if the optical field is restricted to a 25  $\mu\text{m}$  lateral spread (so that it does not interfere with an identical neighbouring  $\mu\text{LED}$  50  $\mu\text{m}$  away), the depth penetration normal to the surface for 50  $\mu\text{m}$  diameter  $\mu\text{LEDs}$  is small ( $< 15 \mu\text{m}$ ). Decreasing the  $\mu\text{LED}$  size to 25  $\mu\text{m}$  diameter, but maintaining the pitch and resolution restriction, increases the maximum depth penetration to  $\sim 40 \mu\text{m}$ . However, decreasing the  $\mu\text{LED}$  size further, to 5  $\mu\text{m}$ , does not substantially increase the volume of tissue illuminated ( $V_{\text{excited}}$ ). This indicates that at a  $\mu\text{LED}$  pitch of 50  $\mu\text{m}$ , 25  $\mu\text{m}$ -diameter  $\mu\text{LEDs}$  offer a resolution similar to that of much smaller diameter  $\mu\text{LEDs}$ , mainly due to the Lambertian emission profile of the light source. If higher resolution is required (reduction in  $\mu\text{LED}$  pitch), the size of the  $\mu\text{LEDs}$  can be decreased, as shown in panels B, C for a 25  $\mu\text{m}$  and 10  $\mu\text{m}$   $\mu\text{LED}$  pitch, respectively.  $\mu\text{LEDs}$  with 10  $\mu\text{m}$  diameter were fabricated to demonstrate smaller  $\mu\text{LEDs}$  are possible using the techniques outlined in this thesis (see Table A.13 in the appendix). If neighbouring  $\text{LEDs}$  are on at the same time, the profiles change as shown in Figure A.10.

### 4.3.2 Device Heating

The major drawback of implantable LED devices, such as this, is the inefficiency of electrical current conversion to light, meaning that heat is generated at the LED surface (see section 2.4). This is particularly relevant when directly inserting a probe into the tissue, positioning the light source next to the neurons. It opens up the possibility of the temperature change itself modulating biological function. Neurons are known to be very sensitive to thermal fluctuations, though exact quantitative data is varied and difficult to interpret [241,242]. The aim of this section is to show that with the correct design criteria, each  $\mu\text{LED}$  is capable of perturbing neurons in optogenetic experiments, without excessive tissue heating. The key point is that the thermal properties of the silicon/tissue interface mean that pulse widths and repetition rates can be realized that are well suited to optogenetic activation.

In order to understand the heat produced in the  $\mu$ LED probe and its surrounding medium, a COMSOL Multiphysics® model was created. COMSOL uses the finite element method (FEM) to approximate heat distribution (and potentially a variety of other physical phenomena) by splitting up the model geometry into a finite number of partial bodies. In the case of heat transfer COMSOL then numerically solves the heat equation

$$\rho C \frac{\partial T}{\partial t} - \nabla \cdot (k \nabla T) = Q \quad (4.1)$$

for the temperature  $T$  (in K). Material properties needed are the density  $\rho$  (in  $\text{kg}/\text{m}^3$ ), the heat capacity  $C$  (in  $\text{J}/\text{kg}\cdot\text{K}$ ) and the thermal conductivity  $k$  (in  $\text{W}/\text{m}\cdot\text{K}$ ). Values for these are summarized in Table 4.2. Heat sources or sinks are represented by the power density term,  $Q$  (in  $\text{W}/\text{m}^3$ ). The basic model can be extended in several ways, for example by incorporating cooling through blood perfusion. This is done by adding an additional heat source term  $\omega \rho_b C_b (T_a - T)$  with the arterial blood temperature  $T_a$ , the density of blood  $\rho_b$ , heat capacity  $C_b$  and perfusion rate  $\omega$  (in  $\text{s}^{-1}$ ). If the rate of metabolic heat generation was considered as well, one would arrive at Pennes' famous bioheat transfer equation [245], popular in thermal modelling.

The probe was included in the model with its original geometry. To make use of its symmetry, only one half was modelled with the boundary condition at this symmetry interface being defined as a reflecting (Neumann) boundary – a standard technique in modelling of this sort (see Figure 4.9 A). The core material was assumed to be pure silicon. The  $\mu$ LEDs were modelled as half cylinders

	Si *	Brain [243]	Parylene C [244]	Air *
Density $\rho$ [ $\text{kg}/\text{m}^3$ ]	2329	1040	1289	
Heat capacity $C$ [ $\text{J}/\text{kg}\cdot\text{K}$ ]	700	3650	712	temperature-
Thermal conductivity $k$ [ $\text{W}/\text{m}\cdot\text{K}$ ]	130	0.527	0.084	dependant

\* from COMSOL materials library

**Table 4.2:** Material properties used in thermal simulations

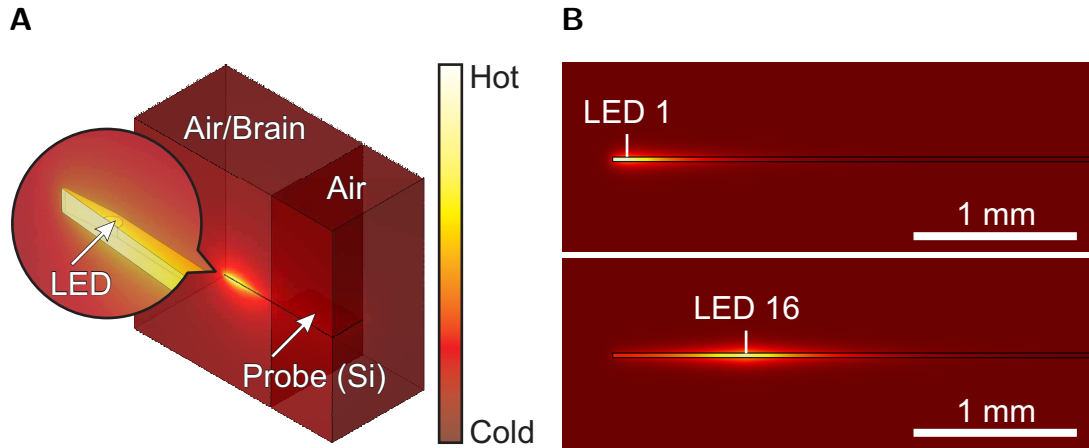


**Figure 4.9:**

COMSOL model of heat transfer in  $\mu$ LED probe and environment; **A)** Model geometry showing half of the  $\mu$ LED probe with the shank immersed in either air or brain tissue and the contact pad area surrounded by air, temperature increase due to Joule heating during a light pulse is shown with colour; **B)** Temperature profile around probe shank immersed in brain tissue following a 20 ms pulse on  $\mu$ LED 1 and  $\mu$ LED 16

with  $1\ \mu\text{m}$  height and  $25\ \mu\text{m}$  diameter. The whole probe was surrounded with a  $6\ \mu\text{m}$  thin layer of parylene C. A cuboid surrounded the tip of the probe and the material was chosen to be either brain tissue or air. The distal end of the probe was always surrounded by a cuboid of air. The boundaries of the media were held at a constant temperature  $T_0$ . Heating of the probe was simulated using boundary heat sources at the  $\mu$ LED/parylene C interface, where the  $\mu$ LED was assumed to be perfectly inefficient (all input electrical power converted to heat). The real wall plug efficiency is around 1%). The simulated electrical power of the boundary heat source was extracted from a typical (shown in section 4.4.1) IV-curve ( $P_{\text{el}} = V \cdot I$ ). Similar models have been created by Wu *et al.* [202], Smith *et al.* [246] and Li *et al.* [247].

Results from the simulation show that the heat transfer occurs primarily along the silicon shank. This is due to the high thermal conductivity of silicon with respect to the neural tissue. The effect of the silicon substrate acting as a heat sink results in the peak temperature varying with  $\mu$ LED position (Figure 4.9B), due to heat flow being strongly limited in one direction when the  $\mu$ LED is located close to the probe tip. In the experiments covered in chapter 5, irradiance values of up to

### 4.3 Simulation

150 mW/mm<sup>2</sup> (1 mA drive current) were used. Temperature changes induced by this mode of operation can be predicted by the COMSOL model and are summarized in Figure 4.10. Panel A quantifies the dependence between peak temperature and  $\mu$ LED position. Now let us consider the furthest  $\mu$ LED from the tip ( $\mu$ LED 16, cf. Figure A.8 for  $\mu$ LED 1). The peak temperature change at the surface of the

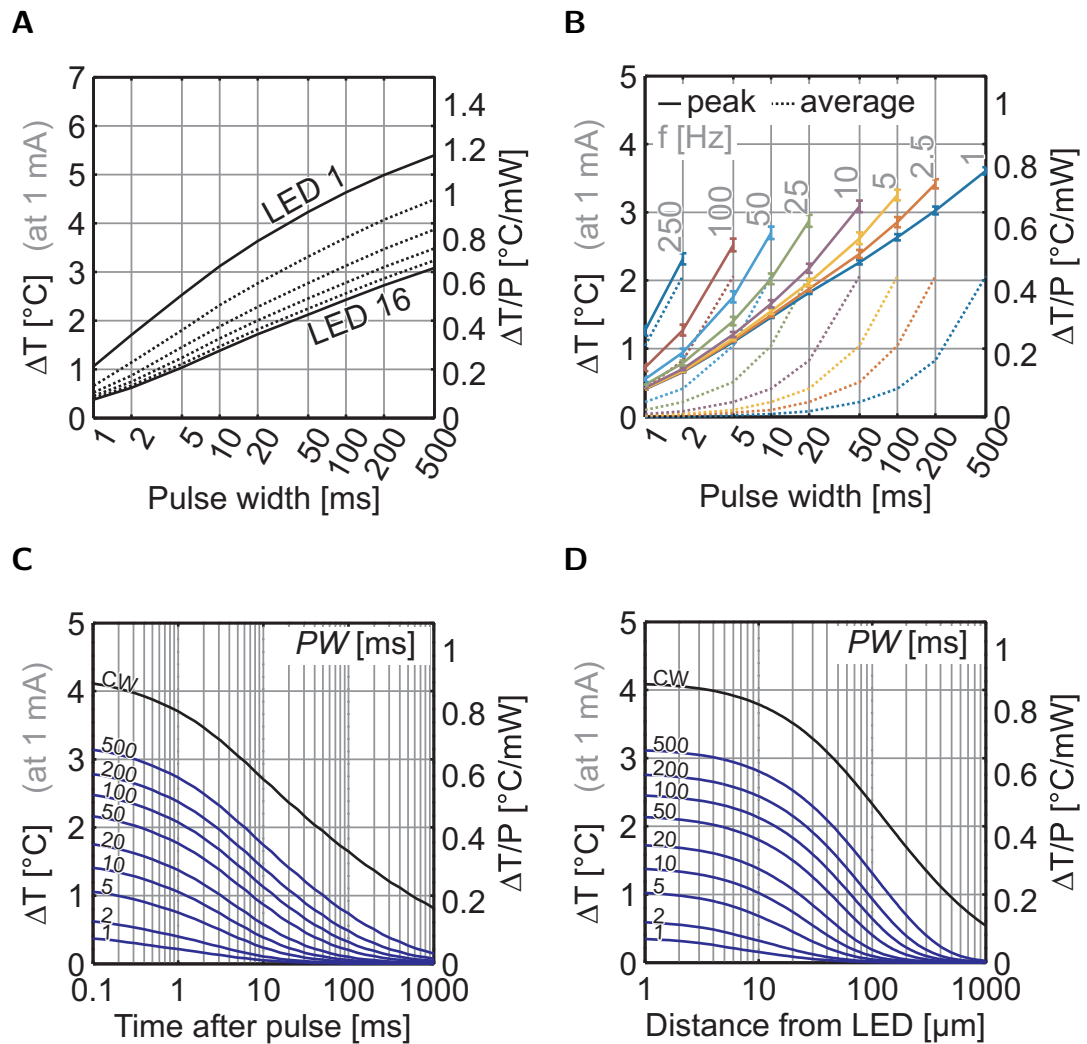


**Figure 4.10:**

Simulated tissue temperatures during LED probe operation ( $I = 150$  mW/mm<sup>2</sup>, LED 16, cf. A.8 for LED 1); **A)** Temperature depends on the LED position; **B)** Peak and average temperatures during continuous operation in pulsed mode for various combinations of pulse width and repetition rate; **C)** Temperature dissipation over time following a pulse of certain pulse width (blue) or a continuous pulse (black); **D)** Maximum temperature at various distances from the LED following a pulse of certain pulse width (blue) or a continuous pulse (black);

$\mu$ LED varies from 0.4 to 4°C depending on pulse width (1 ms to CW). This decays with time after the pulse and distance into the brain (Figure 4.10 C,D). It is important to note that the temperatures scale linearly with electrical input power, as shown on the secondary ordinate (right-hand y-axis). This is interesting as a predictive tool when devices have been characterized electrically (IV/LI). It is also important to note that the average temperature is considerably lower than the peak temperature that occurs during operation. At this irradiance level, the thermal characteristics of the neural probe permit duty cycles of ~10 % without the average temperature rise extending beyond 0.5°C (Figure 4.10 B). Peak temperature increases for continuous pulsed operation are also shown in Figure 4.10 B. and lie between ~0.5-4°C.

During experiments, light pulses of 50 ms duration at a repetition rate of 2.8 Hz were used. The peak temperature increase during this continuous pulsed operation is ~2.5°C at the  $\mu$ LED surface and occurs at the end of each pulse. As mentioned before, this drops off quickly in time and space, with 50 ms pulses taking ~30 ms to cool below 0.5°C (Figure 4.10 C). At the same time, neurons that are ~70  $\mu$ m away from the  $\mu$ LED never get exposed to these temperatures (Figure 4.10 D). The average temperature increase at these parameters is predicted to be around 0.5°C, which is often taken as a threshold for safe operation. Control experiments detailed in chapter 5 show that there is no visible thermally-induced change in neural firing rate with the parameters used (Figure 5.6 N), giving credence to the predicted average temperature increase of around 0.5°C.

Thermal damage in biological systems is complicated. It is usually a result of increased temperature level and duration [248,249]. Quantifying the maximum settings for safe operation considering magnitude and duration of heat exposure is an essential goal. One possible way of predicting the impact of the increased temperature on the neurons is by looking at the Arrhenius damage integral. The Arrhenius equation describes the temperature dependence of reaction rates and it

can be written in its differential form as

$$\frac{dn}{dt} = -nA \exp\left(\frac{-\Delta E}{RT}\right), \quad (4.2)$$

with the number  $n$  of cells that have not yet reacted, time  $t$ , the universal gas constant  $R$ , thermodynamic temperature  $T$ , and the two reaction parameters  $A$  (pre-exponential factor, a measure of the effective collision frequency between reacting molecules) and  $\Delta E$  (activation energy, the minimum energy needed for the reaction to occur) [250,251]. The equation has the solution

$$\frac{n(\tau)}{n_0} = \exp(-\Omega(\tau)), \quad (4.3)$$

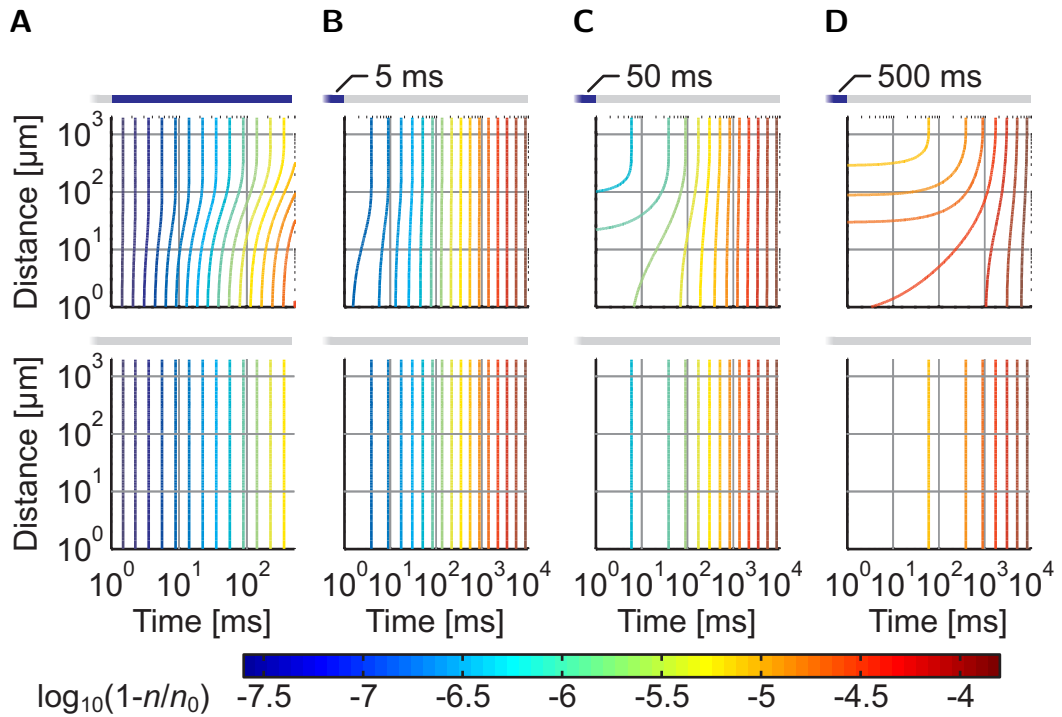
where  $n_0$  is the total number of cells and

$$\Omega(\tau) = A \int_{t=0}^{\tau} \exp\left(\frac{-\Delta E}{RT(t)}\right) dt. \quad (4.4)$$

The integral can be solved by using the trapezoidal rule, which is given as

$$\int_a^b f(x) dx \approx (b-a) \left[ \frac{f(a) + f(b)}{2} \right], \quad (4.5)$$

and temperature distributions at many points in time provided by the solution of the COMSOL simulation. Fractions of affected cells regarding cell death ( $A = 2.98 \cdot 10^{80} \text{ s}^{-1}$ ,  $\Delta E = 5.06 \cdot 10^5 \text{ J mol}^{-1}$  [252]) are shown in Figure 4.11. What can be seen is that even long pulses do not cause cell death of large fractions of the population. The rate of cell death caused by increased temperature from the LEDs is increased slightly during LED operation. However, the natural rate of cell death remains the main cause of cell death, which can be seen when comparing the top and bottom plots during the time frame after the LED is switched off. Neurons could still change their behaviour, but the reaction parameters regarding these more subtle cell perturbations are not known. If they could be identified accurately (Figure A.9), it might be possible to give more precise limits for  $\mu$ LED stimulation with respect to increased temperature.

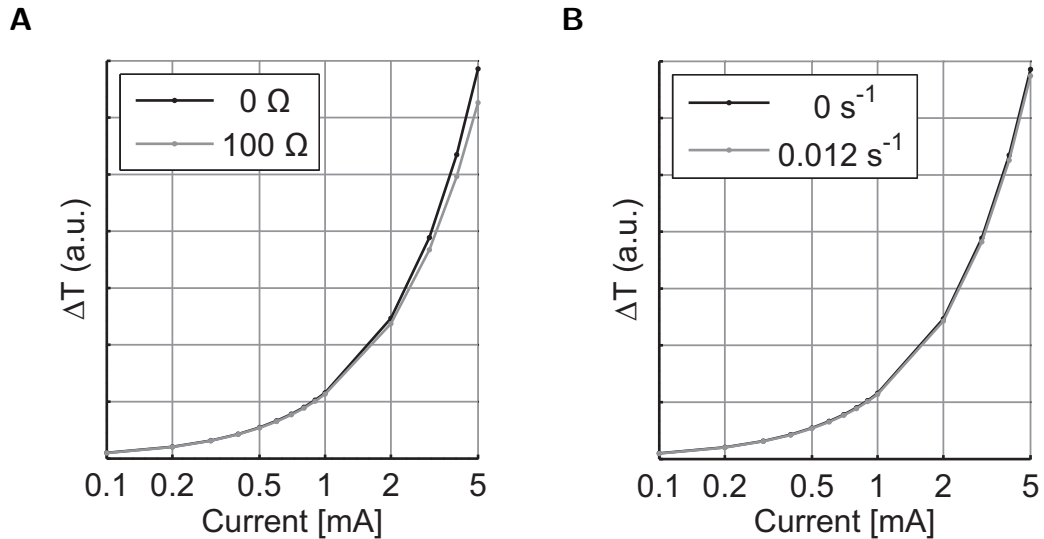


**Figure 4.11:**

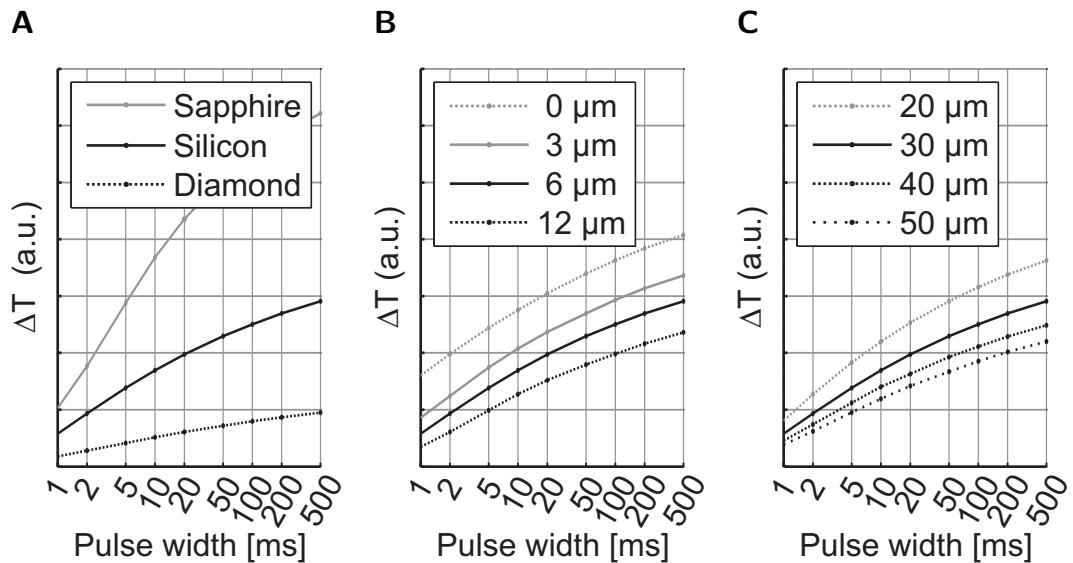
Arrhenius damage integrals for  $\mu$ LEDs, comparing damage induced by  $\mu$ LED heat (top) and damage occurring at base temperature (bottom); blue: LED on, grey: LED off; fractions of damaged cells ( $1 - n/n_0$ ) are colour-coded; **A)** top: LED on at 5 mA, bottom: LED off; **B)** Top: LED off after 5 ms pulse at 5 mA, bottom: LED remaining off after 5 ms off-period; **C)** Top: LED off after 50 ms pulse at 5 mA, bottom: LED remaining off after 50 ms off-period; **D)** Top: LED off after 500 ms pulse at 5 mA, bottom: LED remaining off after 500 ms off-period

Further simulations have been performed taking into account the series resistance of the tracks leading up to the  $\mu$ LED sites (Figure 4.12 A, a value of  $100 \Omega$  has been chosen as an upper boundary, cf. section A.2.3.3) as well as cooling by blood perfusion of the brain (Figure 4.12 B). Since their effect is observed to be small, they can be neglected in the models.

Figure 4.13 shows the influence of some other modelling parameters on the temperature development in the system. Panel A shows the effects of a change in substrate material on the maximum temperature. Silicon is contrasted to sapphire and diamond. The thermal benefit of moving away from the conventional LED substrate, sapphire, can be seen clearly: the result is a reduction in peak temperature by about 50%. Diamond is an interesting future substitute for silicon.

**Figure 4.12:**

Influence of various model parameters on the simulated maximum temperature (at surface of LED 1 during static operation); **A**) Track resistance in series with LED ( $100 \Omega$ ); **B**) Blood perfusion ( $0.012 \text{ s}^{-1}$ )

**Figure 4.13:**

Influence of various model parameters on the simulated maximum temperature (at surface of LED 1 after one pulse at  $I = 5 \text{ mA}$ ); **A**) Different substrate materials (silicon vs. diamond and sapphire); **B**) Parylene C coating with different thicknesses ( $0\text{-}12 \mu\text{m}$ ); **C**) Thickness of the silicon substrate ( $20\text{-}50 \mu\text{m}$ )

Being one of the best known thermal conductors (Table 8.1), it can help reduce the peak temperature by roughly another  $2/3$ . Panel B shows the influence of the thickness of the insulating parylene layer on the peak temperature (at the interface

between the probe and the tissue along the LED normal). A 6  $\mu\text{m}$  parylene C layer, as used on the probes introduced here, helps reduce the peak temperature by about 25 % compared to an uncoated probe. Increasing the parylene thickness can help further reduce the temperature as shown. Panel C shows the effect of the probe thickness on the temperature. The probe substrate plays an important role in transferring away excess heat, since its thermal conductivity is much higher than that of brain tissue. As apparent in the plot, consideration should be given to thermodynamic aspects, when thinking about producing thinner probes that could help minimize tissue damage. Table 4.3 shows peak temperature increases for the case that all 16  $\mu\text{LEDs}$  are on simultaneously (worst case). When using long pulses, the peak temperature increase can be around twice as high as when using single LEDs (cf. Figure 4.10 A). Such parallel stimulation is therefore only possible with lower powers. This requires opsins with increased sensitivity or accepting more locally confined stimulation.

$\Delta T$ [°C]	$PW$ [ms]								
	1	2	5	10	20	50	100	200	500
1	0.9	1.8	3.4	4.4	5.5	6.8	7.7	8.6	9.6
2	0.9	1.9	3.5	4.7	5.8	7.2	8.2	9.1	10.2
3	0.9	1.9	3.6	4.8	5.9	7.4	8.4	9.4	10.5
4	0.9	1.9	3.6	4.8	5.9	7.5	8.5	9.5	10.7
5	0.8	1.8	3.5	4.8	5.9	7.5	8.5	9.6	10.7
6	0.8	1.7	3.4	4.7	5.9	7.4	8.5	9.5	10.7
7	0.8	1.7	3.3	4.6	5.8	7.3	8.4	9.4	10.6
8	0.7	1.6	3.2	4.5	5.6	7.1	8.2	9.3	10.5
9	0.7	1.5	3.1	4.3	5.5	7.0	8.0	9.1	10.2
10	0.6	1.4	3.0	4.1	5.3	6.8	7.8	8.8	10.0
11	0.6	1.3	2.8	4.0	5.1	6.5	7.5	8.5	9.7
12	0.6	1.2	2.6	3.7	4.8	6.2	7.2	8.2	9.3
13	0.5	1.1	2.4	3.5	4.6	5.9	6.9	7.8	8.9
14	0.5	1.0	2.2	3.3	4.3	5.6	6.5	7.4	8.5
15	0.4	0.9	2.0	3.0	4.0	5.2	6.1	7.0	8.1
16	0.3	0.8	1.8	2.7	3.6	4.8	5.7	6.5	7.6

**Table 4.3:**

Peak temperature increase (per  $\mu\text{LED}$ ) following a simultaneous pulse ( $I = 150 \text{ mW}/\text{mm}^2$ ) with a defined pulse width on 16  $\mu\text{LEDs}$

## 4.4 Characterization

The inputs of the models require experimental parameters and the probes described in section 4.2 have been characterized electrically, optically and thermally. Precise electrical and optical data is essential for driving the probes towards a desired output. Thermal characterization was used to verify the models that have been covered above.

### 4.4.1 Electrical Characteristics and Light Output

Electrical and optical characterization have been carried out using a programmable current source (GS610, Yokogawa) and an optical power meter (PM100A with detector S120VC, Thorlabs). Unlike an integrating sphere, the simple optical power meter does not give absolute power values, since not all the light can be recorded from a Lambertian emitter. A correction factor therefore has to be applied to the measured value depending on the position of the detector. For a distance of 6 mm and an angle of  $45^\circ$  of the  $\mu$ LED centred in front of the detector, the correction factor is  $k \approx 3.68$  (detector radius 4.75 mm, additional values in section A.2.4.1). An integrating sphere was used to check this approximation and values agreed well ( $\pm 10\%$ ). A previously developed LabVIEW program can simultaneously interface with both the current source and the optical power meter. The output voltage is then swept typically from  $-3\text{ V}$  to  $+8\text{ V}$  in steps of  $0.1\text{ V}$ , while the electrical current and the optical power are recorded. Figures 4.14 A,B show the electrical and optical characteristics of a typical  $\mu$ LED on a fabricated probe. The average voltage at  $5\text{ mA}$  current is  $6.56\text{ V}$  with a standard deviation of  $0.57\text{ V}$  and the average light output at  $5\text{ mA}$  current is  $0.19\text{ mW}$  with a standard deviation of  $0.01\text{ mW}$  ( $n = 20$  functional LEDs).

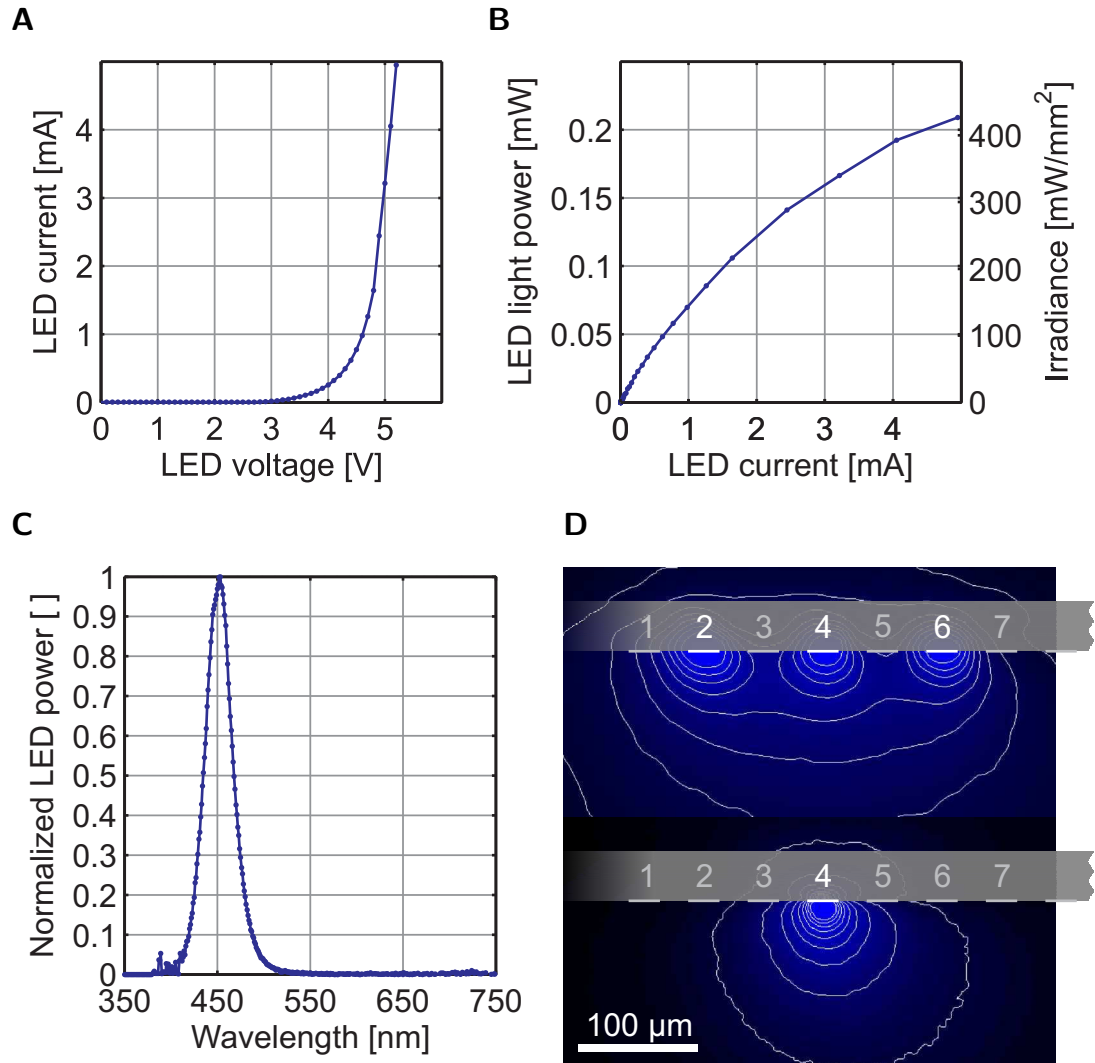


**Figure 4.14:**

Characterization of electrical and optical  $\mu$ LED power; **A)** Electrical characteristic curve showing forward current in relation to forward voltage (IV); **B)** Optical characteristic curve showing light output in relation to forward current (LI); **C)**  $\mu$ LED emission spectrum (spectral line half-width is 33 nm); **D)**  $\mu$ LED emission profiles from probe immersed in fluorescein solution (top: single  $\mu$ LED, bottom: three  $\mu$ LEDs), isocontours show the Lambertian emission profile

The  $\mu$ LED emission is further characterized in Figures 4.14 C,D, with panel C showing the emission spectrum of a typical  $\mu$ LED on the probe. The peak wavelength is 452 nm and the spectral line half-width is 33 nm. Panel D shows  $\mu$ LEDs simultaneously emitting in fluorescein solution (fluorescein concentration is

0.1  $\mu\text{M}$ ), highlighting the Lambertian emission profile underlying the Monte Carlo simulations (Figure 4.7). The plot was produced by imaging the probe from the side using a CCD camera. Isocontours of fluorescence were then identified in the image.

### 4.4.2 Device Heating

Thermal imaging (FLIR SC7000 Series) was used to assess device heating. A calibration curve was first recorded to obtain the temperature-dependent emissivity of the parylene-coated GaN-on-Si probes. This was done using a type E thermocouple attached via thermal paste to the bonding area of the probe. The probe was heated to  $100^\circ\text{C}$  using a heat gun and then left to cool down to room temperature, while thermocouple readings were recorded and thermal images simultaneously acquired at 2 Hz. This was repeated five times to generate the data shown in Figure 4.15 A. A linear fit was applied to the scatter plot of detector count values against measured temperature. The gradient links relative changes in detector counts to changes in temperature. This thermal camera and calibration curve can then be used to record the probe temperature under a variety of operating conditions. This experimentally obtained probe temperature is compared to simulation results in Figure 4.15 B. Considering that the model and the measurement are done completely independent from each other, the match between the two is very good. Differences can be explained by slight deviations of the real thermal properties and geometry from those used in the model. Peak temperature and temperature offset were measured for various combinations of  $\mu\text{LED}$ , current, pulse width and repetition rate. Figures 4.15 C,D show examples of thermal imaging data recorded (black line). A more accurate future alternative method, that could be used to obtain data in physiological solution is described by Shrestha *et al.*. The approach makes use of a micropipette [253], which can have dimensions small enough to record temperature changes around individual  $\mu\text{LED}$ s, while

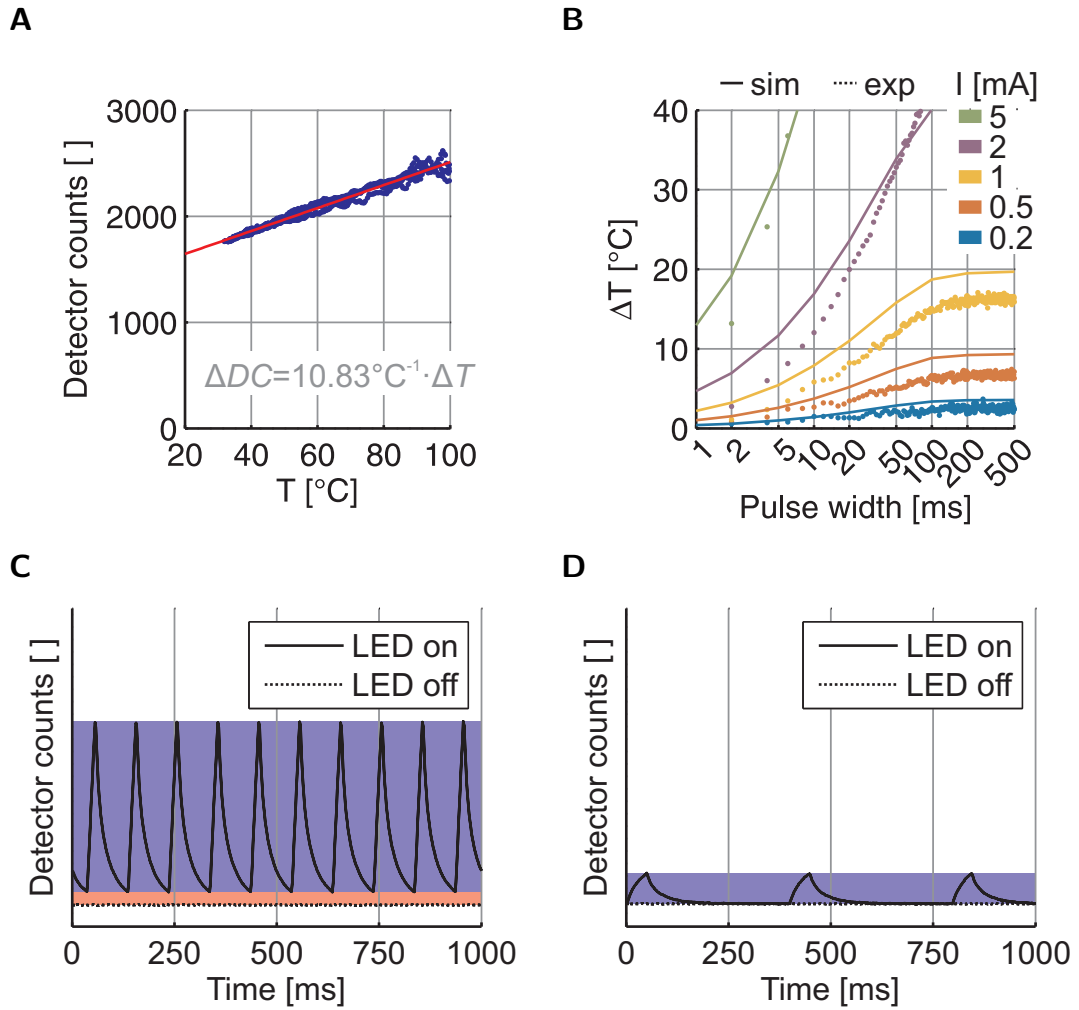


**Figure 4.15:**

Probe heating as detected by a thermal camera; **A)** Calibration curve recorded on LED 9 (middle of the shank) using thermal imaging and a thermocouple; **B)** Calibration factor from A) applied to thermal imaging values recorded during one light pulse of LED 9 (sampled at 500 Hz) at different currents; **C)** Temporal profile of camera detector counts during continuous pulsed operation,  $I = 5$  mA,  $PW = 20$  ms,  $f = 10$  Hz; temperature offset is shaded in red; fluctuating temperature is shaded in blue; peak temperature is the sum of the two;  $t_{1/e} = 20$  ms; **D)** Another temperature trace example for pulsed LED operation (50 ms pulses at 2.5 Hz, 1 mA), note: rate is low enough that offset is not generated

offering millisecond resolution. This method seems relatively easy to use, since no complicated thermal camera calibration has to be carried out. It is also expected to give more accurate results, since the measurements can be done directly in an environment that closely matches the *in vivo* conditions.

## 4.5 Probe Controlling

In order to control the  $\mu$ LED probes, additional hardware and software is required. The hardware connects the  $\mu$ LED probe to a PC through a set of control electronics. The software sends control commands to the hardware. In the following sections each component will be described individually.

### 4.5.1 Control Hardware

The developed control hardware consists of several parts. A headstage includes electronics for  $\mu$ LED addressing. The headstage is then connected to an external interface board containing a programmable LED sink driver (cf. section A.2.7) and a microcontroller, which is connected to a PC via a USB interface. The microcontroller accepts triggers from external hardware and can use them to produce a certain output from the  $\mu$ LED probe. Triggers are particularly useful when coupling the  $\mu$ LED probe with recording hardware. Figure 4.16 gives an overview of the control hardware. The individual components are further described below.

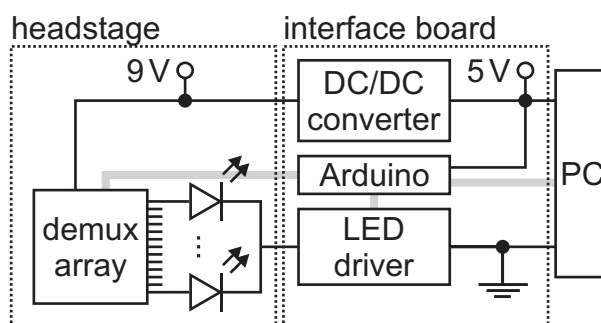


**Figure 4.16:**

Simplified schematic of  $\mu$ LED probe control hardware, showing the circuit to power the  $\mu$ LEDs and the signal flow (grey lines)

### 4.5.1.1 Headstages

Two different PCBs, acting as headstages, were designed and produced (Eurocircuits N.V., Belgium [238]). They allow the control of the different probes by addressing one  $\mu$ LED at a time using several 16-channel low-cost demultiplexers (HC4067). The small PCB shown in Figure 4.17 A can either be fitted with one or three of these ICs to drive 16- or 32-channel probes, respectively. The PCB shown in Figure 4.17 B shows a 96-channel version using a switching matrix of seven demultiplexer ICs. Apart from the probe, the other component on the boards is a 12-way micro USB-style socket with a small footprint. The 12-wire interface is used for supplying power, demultiplexer addressing, and for connecting the n-contact of the  $\mu$ LED probe to the output of the LED sink driver. The weights of the populated 16-, 32- and 96-channel headstages are 1.6 g, 1.9 g and 3.6 g, respectively, allowing them to be used in small rodents. A connection to the interface board is made using a screened miniature (1.72 mm diameter) 12-core cable (Rotronik 08.301.12.36/PFA) and a 12-pin USB-style connector at each end.

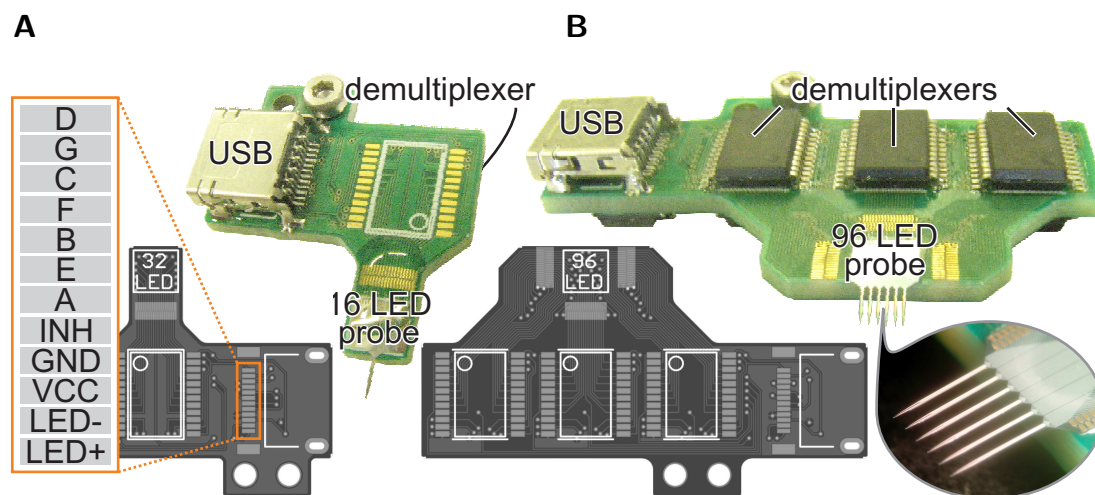


**Figure 4.17:**

$\mu$ LED probe headstages (schematics and populated boards), pin configuration shown in detail (cascaded demultiplexer select lines E-G (highest bit) for first stage and A-D (highest bit) for second stage, INH = inhibit, GND = ground, VCC = supply voltage, LED+ = LED anode voltage, LED- = LED cathode voltage); **A**) 16- or 32-channel board using one or three demultiplexers, respectively; **B**) 96-channel board using seven demultiplexer ICs

### 4.5.1.2 Interface Board

An interface board has been designed consisting of an Arduino Nano microcontroller and a custom-built LED driver board (cf. Figures A.5 and A.6). The boards (and the attached headstage/ $\mu$ LED probe) are powered via USB through a 9 V DC/DC converter on the LED driver board (Murata, MEV1S0509SC). In addition to the the driver itself, the driver board contains a shift register for outputting the (headstage) demultiplexer channel select signals (7 select lines and 1 enable line, allowing control of up to  $2^7 = 128$   $\mu$ LEDs). The final purpose of the driver board is to lead out 10 I/O lines from the Arduino through a USB-style 12-pin connector. The driver board is connected to the Arduino as a shield, allowing control of both the LED driver and the shift register, and resulting in a very compact setup, as shown in Figure 4.18 A. Furthermore, a miniature enclosure has been designed to house the interface electronics (outer dimensions  $46 \text{ mm} \times 22 \text{ mm} \times 25.5 \text{ mm}$ ). It was machined from aluminium and the complete final system is shown in Figure 4.18 B.

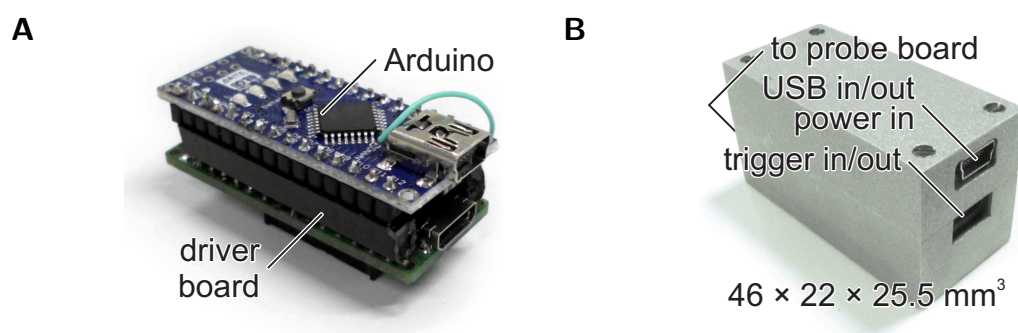


**Figure 4.18:**

$\mu$ LED probe interface board; **A**) Assembly consisting of Arduino Nano microcontroller board and a custom-designed LED driver board, power is provided and data can be sent through USB, several triggers can be input/output via a 12-pin USB-style connector, the probe board is attached using the same connector on the back side of the board; **B**) Interface board in a custom-designed enclosure

## 4.5.2 Control Software

Control software was developed using Visual Basic .NET (PC interface, Figure 4.19) and C (Arduino sketch). The PC software offers a graphical user interface (GUI) showing relevant electrical, optical and thermal information and it allows the selection of the  $\mu$ LED channel and current. The software communicates with the Arduino Nano microcontroller via its serial interface. It sends command strings consisting of the command name (one character) followed by the command parameters (one or more bytes). The basic commands are the following: “C” to set the channel, followed by 3 bytes ( $3 \times 0-255 \hat{=} \mu$ LED x-, y-, z-position, cf. Figure A.15), “E” to enable the output followed by 1 byte ( $1 \hat{=} \text{enabled}$ ,  $0 \hat{=} \text{disabled}$ ), “I” to set the current followed by 1 byte ( $0-255 \hat{=} \text{minimum to maximum current}$ , which depends on resistor value) and “T” to enable the external trigger followed by 1 byte ( $1 \hat{=} \text{enabled}$ ,  $0 \hat{=} \text{disabled/override}$ ).

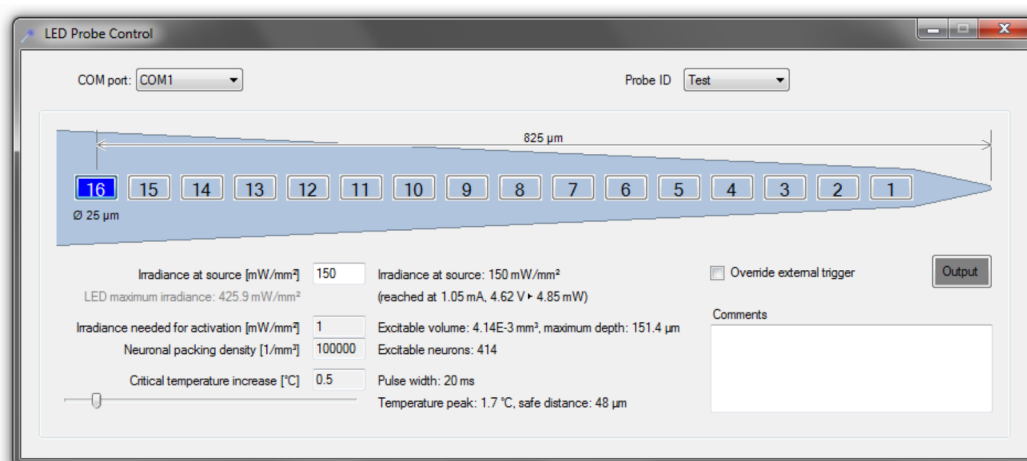


**Figure 4.19:**

Control software (screenshot); Software loads probe profiles including IV- and LI-data and allows selection of  $\mu$ LED channel and source irradiance, simulations for light emission and heat propagation are then interpolated for the selected stimulation case, showing excitable tissue volume, number of neurons, peak temperature and safe distance (if above a preset threshold)

The commands are interpreted by the Arduino sketch running in a continuous loop. The demultiplexer select lines, corresponding to a  $\mu$ LED channel, are taken from a table and the correct values are then output through the shift register on the driver board. The byte values proportional to the desired  $\mu$ LED current are replaced by values to set the current gain of the LED driver (taken from a table) and shifted out using the three-wire interface. If enabled, an external trigger pulse is used to switch the LED driver on or off (the trigger is continuously monitored). Otherwise, this is done when the respective command is received from the PC software. The Arduino sketch can easily be extended for example to allow additional trigger inputs or outputs. When a more complicated stimulation pattern is required (fast switching between  $\mu$ LEDs), the easiest way could be to bypass the PC software, and instead include all stimulation patterns in the Arduino sketch, which can then be selectively executed using the different trigger lines.

## 4.6 Conclusion

In this chapter the design, fabrication, simulation, characterization and control of needle-shaped  $\mu$ LED probes were outlined. The probes have been predicted to be useful for *in vivo* optogenetics. The following chapter will demonstrate the functionality of the finished devices, showing how they can be used to stimulate neural populations in the cortex in a layer-specific manner.

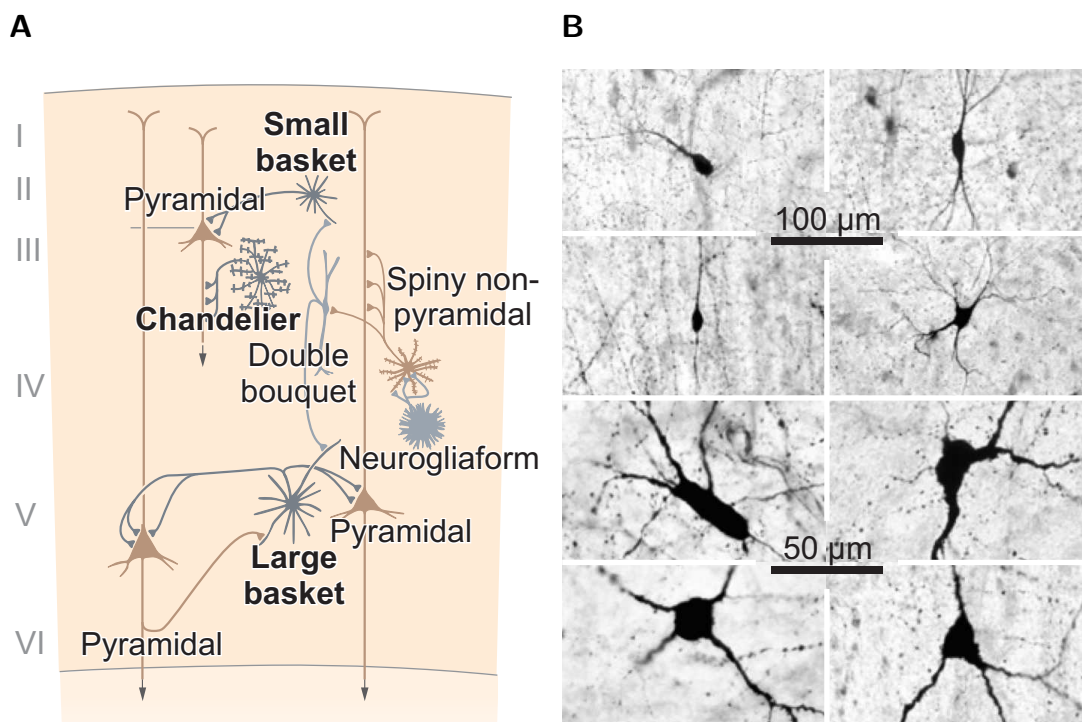
# 5 Optogenetic Perturbations *In Vivo* Using $\mu$ LED Needle Probes

The previous chapter covered the design and fabrication of  $\mu$ LED probes for *in vivo* optogenetics. The aim of this chapter is to demonstrate their functionality and performance. In order to show depth-dependent neural activation, the mouse neocortex was chosen (detailed in section 2.1.3). Here the probe is expected to have a resolution approaching the cellular scale, while covering the full depth. In the neocortex the six-layered structure is the most prominent anatomical feature with distinct functional properties [254]. The thickness of each layer is sub-millimetre with many cell types distributed across layers. Depth-dependent neural activation would be tremendously helpful in understanding this circuit, but this is challenging with conventional approaches.

Two novel optogenetic experiments have therefore been carried out and are covered below. The first experiment is the depth-specific activation of a certain neural subtype present across cortical layers. The second experiment is the induction of various spatiotemporal patterns of neural population activity with a simple pan-neuronal expression of opsins in the cortex. The general idea behind the first experiment is to pick a certain type of neuron and to understand something new about it in terms of its function. In this case, a subtype of GABAergic interneurons was chosen. The next section will therefore give a brief introduction to GABAergic interneurons in the cortex before a detailed experimental description.

## 5.1 GABAergic Interneurons in the Cortex

In the human brain about 20-30% of all neurons are interneurons (or local circuit neurons) [255]. In rodents this number lies between 10-20% [256]. As opposed to projection neurons, interneurons have short axons and relay information between neighbouring neurons (Figure 5.1). Interneurons in the central nervous system are mainly inhibitory and use the neurotransmitter Gamma-Aminobutyric acid (**GABA**). These neurons are sparsely distributed across layers with recent evidence of functional variations [259–261]. In the cortex there are mainly three types of GABAergic interneurons: neurons expressing the  $\text{Ca}^{2+}$ -binding protein **parvalbumin** (PV), the neuropeptide somatostatin (SST), and the ionotropic serotonin receptor 5HT3a (5HT3aR). In this study, the focus lies on parvalbumin expressing (PV+) neurons. These neurons account for ~40% of GABAergic interneurons and can be found in layers II-VI. PV-expression has been associated

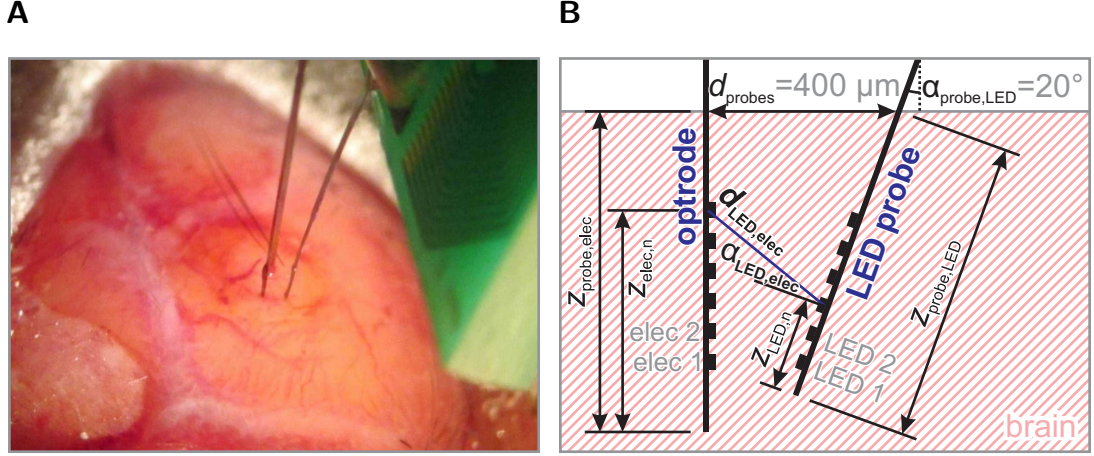


**Figure 5.1:** GABAergic interneurons in the cortex (after Houser *et al.* [257]); **A)** parvalbumin expression has been associated with basket cells and chandelier cells (bold); **B)** Examples of GABAergic interneurons with different somatic and dendritic morphology (after Ascoli *et al.* [258])

with the fast-spiking firing pattern, with fast spiking **basket cells** and **chandelier cells** being the two morphologically distinct subgroups (Figure 5.1 A). These groups, however, can be further divided into functionally distinct subgroups, which are not well-defined yet [256,258]. Optogenetic probes with high spatial resolution could be a helpful tool to further study the different types. Being able to optically excite individual GABAergic interneurons – in this case using single-cell transfection – has already been shown to be a very helpful tool [262].

## 5.2 Experimental Setup

The following *in vivo* experiments and data analysis were done by Dr Shuzo Sakata and Dr Tomomi Tsunematsu at SIPBS (University of Strathclyde). The setup used was the following. Anaesthetized mice were placed in a stereotaxic frame and body temperature was retained at 37°C. After incision, the bone above the right sensorimotor cortices was removed and the cavity was filled with warm saline during the entire recording session. A  $\mu$ LED probe was slowly inserted into the cortex with a 20° angle and penetrated 1.1-1.5 mm. A silicon-based optrode, containing 32 microelectrodes and an optical fibre (A1x32-10mm-50-177-A32OA, NeuroNexus, see Figure 5.2 A) was inserted slowly and penetrated 1.0-1.1 mm. Figure 5.2 B shows a schematic of the setup after parallel implantation of the two probes. The distance between the  $\mu$ LED probe and optrode was 400  $\mu$ m at the cortical surface. For histological verification of tracks, the rear of both probes was coated with the molecular tracer DiI. Once both probes were inserted into the target depth, recording sessions were initiated. Each recording session typically consisted of a **non-stimulation period** (at least 2 min), the **intensity testing period** and another **non-stimulation period** (up to 2 min). The non-stimulation period was for assessing spontaneous neural activity. In the intensity testing period, optical stimulation from an **optic fibre** of the optrode ( $86.6 \text{ mW/mm}^2$ ) was applied at the beginning, followed by  **$\mu$ LED** stimulation with varied irradiances ( $0.1\text{-}150 \text{ mW/mm}^2$ ) and a repeat **optic fibre** stimulation. Each


**Figure 5.2:**

Parallel implantation of  $\mu$ LED probe and NeuroNexus optrode; **A**)  $\mu$ LED probe (right) at an angle of  $20^\circ$  and NeuroNexus optrode (left), separated by  $400 \mu\text{m}$  at the surface of the cortex (under surgical microscope); **B**) Schematic showing the distance and angle between stimulation and recording sites

optical stimulation consisted of 50 ms pulses at 2.8 Hz repetition rate (300 ms interval) with 100 repetitions. For electrophysiological recording, broadband signals were amplified relative to a cerebellar bone screw and were digitized at 20 kHz.

The distance  $d_{\text{LED,elec}}$  between any stimulating  $\mu$ LED and any recording electrode from the arrays used in the experimental setup can be calculated as

$$d_{\text{LED,elec}} = (d_{\text{probes}} + (z_{\text{LED},n} - z_{\text{probe,LED}}) \cdot \sin \alpha_{\text{probe,LED}}) \cdot \sqrt{1 + \frac{((z_{\text{LED},n} - z_{\text{probe,LED}}) \cdot \cos \alpha_{\text{probe,LED}} - z_{\text{elec},n} + z_{\text{probe,elec}})^2}{(d_{\text{probes}} + (z_{\text{LED},n} - z_{\text{probe,LED}}) \cdot \sin \alpha_{\text{probe,LED}})^2}}, \quad (5.1)$$

where  $z_{\text{LED},n}$  is the position of the  $n^{\text{th}}$   $\mu$ LED from the probe tip and  $z_{\text{elec},n}$  is the position of the  $n^{\text{th}}$  recording electrode from the tip,  $z_{\text{probe,LED}}$  and  $z_{\text{probe,elec}}$  are the implantation depths of the  $\mu$ LED probe and the recording probe, respectively,  $\alpha_{\text{probe,LED}}$  is the angle of implantation of the  $\mu$ LED probe, and  $d_{\text{probes}}$  is the separation distance between the probes on the cortical surface. The position of the  $n^{\text{th}}$  LED and electrode (respectively) can be calculated as

$$z_{(\text{LED}/\text{elec}),n} = z_{(\text{LED}/\text{elec}),1} + (n - 1) \cdot p_{(\text{LED}/\text{elec})} \quad (5.2)$$

## 5.2 Experimental Setup

with the distance  $z_{(\text{LED}/\text{elec}),1}$  of the first site from the tip and the pitch  $p_{(\text{LED}/\text{elec})}$  between two sites. The normal angle  $\alpha_{\text{LED},\text{elec}}$  between an electrode and a  $\mu\text{LED}$  on the  $\mu\text{LED}$  probe can be calculated as

$$\alpha_{\text{LED},\text{elec}} = -\alpha_{\text{probe,LED}} - \arctan\left(\frac{(z_{\text{LED},n} - z_{\text{probe,LED}}) \cdot \cos \alpha_{\text{probe,LED}} - z_{\text{elec},n} + z_{\text{probe,elec}}}{d_{\text{probes}} + (z_{\text{LED},n} - z_{\text{probe,LED}}) \cdot \sin \alpha_{\text{probe,LED}}}\right). \quad (5.3)$$

Using these values and the results from the Monte Carlo simulations from section 4.3.1, an estimate of the light power at each electrode site can be obtained. Figure 5.3 shows this for the parameters used in the *in vivo* experiments described here.

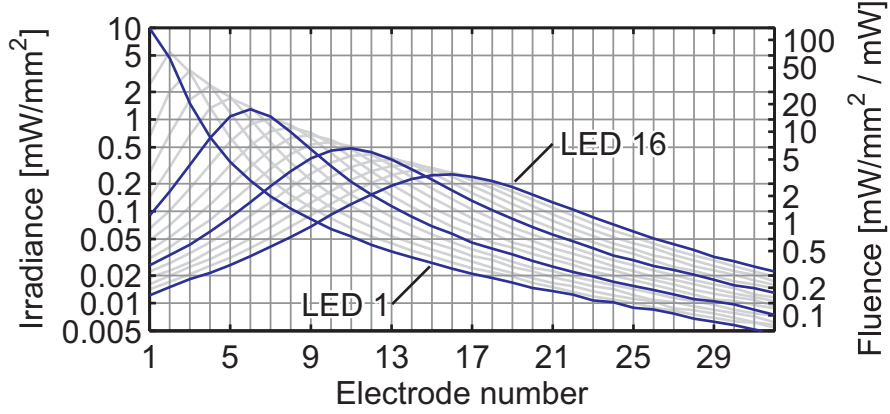


**Figure 5.3:**

Irradiance values on electrode sites when simultaneously implanted with a  $\mu\text{LED}$  probe at an angle;  $d_{\text{probes}} = 400 \mu\text{m}$ ,  $\alpha_{\text{probe,LED}} = 20^\circ$ ,  $z_{\text{probe,LED}} = 1.1 \text{ mm}$  and  $z_{\text{probe,elec}} = 1 \text{ mm}$ ,  $p_{\text{LED}} = p_{\text{elec}} = 50 \mu\text{m}$ ,  $z_{\text{LED},1} = 87 \mu\text{m}$ ,  $z_{\text{elec},1} = 50 \mu\text{m}$ , simulated irradiance profile taken from section 4.3.1; irradiance is proportional to LED light output power (right ordinate), the left ordinate shows the values for one specific case (current of 1 mA leads to an irradiance of  $150 \text{ mW}/\text{mm}^2$  on the LED)

## 5.3 Signal Processing

The next sections describe the techniques used for signal processing. Each data analysis step will be addressed separately. Some background information will be given where necessary.

### 5.3.1 Spike Sorting

All spike detection and sorting took place offline. The recorded data (see Figure 5.4) was bandpass filtered, a threshold was picked, and PCA was performed on waveforms over threshold (cf. section 2.3.3). For this process, freely available software (KlustaSuite [263]) was used. In the experiment in the PV-IRES-Cre::Ai32 mouse, only single units which fulfilled the following two conditions were analysed: 1) with isolation distance [264] values  $\geq 20$  and 2) with response probability values  $> 0.7$  to optical stimulation from the cortical surface. Isolation distance is defined as the Mahalanobis distance from the identified cluster within which as many spikes belong to the specified cluster as to others and quantifies how well-separated the spikes of the cluster are from other spikes recorded simultaneously. In the Emx1-IRES-Cre::Ai32 mouse experiments there was excessive spike overlap during optical stimulation, making spike sorting difficult and so spike events were simply treated as multi-unit activity (MUA). All spike train and LFP analysis was performed using Matlab (Mathworks).

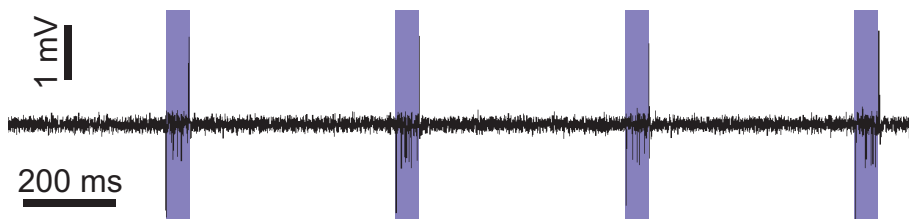


**Figure 5.4:**

Example of a voltage trace recorded from a microelectrode during optogenetic stimulation (stimulation periods highlighted in blue)

### 5.3.2 Depth Estimation of Single Units

As described elsewhere [265,266], the depth of spike-sorted units was estimated from the stereotaxically measured depth of the electrode tip and spike waveform profiles. These waveforms allow estimation of the somatic position by attributing location to the recording site with the maximum peak-to-trough amplitude on an averaged signal.

### 5.3.3 Local Field Potentials

Local field potentials (LFPs) refer to the electric potentials in the extracellular space around neurons generated by the summed electrical current flowing from multiple neurons close to a recording site [267]. Despite their name, LFPs are therefore quite non-local compared to spikes. The physiological significance of LFPs has recently seen a revival as it was realized that they may contain information about the outside world, which cannot be extracted from spiking data alone [268]. Action potentials represent the output of the computation performed by individual neurons. LFPs, on the other hand, reflect the input of a given cortical area and processing by local neurons (excitatory and inhibitory), which manifest as slow waveforms [38]. In the present case, LFPs were extracted from the broadband signal after low pass ( $< 800$  Hz) filtering and re-sampling at 1 kHz across channels.

### 5.3.4 Current Source Density Analysis

Neuronal transmembrane currents, resulting from synaptic activity and action potentials, establish an ensemble of current sources and sinks with respect to the conductive extracellular medium. Current flowing between sources and sinks leads to potential differences (field potentials), which can be recorded using electrode arrays. However, the generated potentials always add algebraically, which makes interpretation ambiguous. It is therefore desirable to compute directly the distribution of current sources and sinks, which provides superior resolution of neuronal events. Current source density (CSD) analysis was first introduced by Pitts in 1952 [269]. It measures the amplitude of source or sink

current at any point. The CSD ( $I_m$ ) is related to the current density  $J$  (a vector quantity measuring amplitude and direction of current flow) through a divergence operation and the current density is related to the electric field  $E$  through Ohm's law (with the conductivity tensor  $\sigma$ ). When magnetic effects are neglected ( $\nabla \times E = 0$ ), the electric field can be related to the gradient of the field potential  $\varphi$ . In summary, the CSD is a scalar quantity related to the second spatial derivative of the LFP [38, 270, 271]:

$$I_m = \nabla J = \nabla(\sigma E) = \nabla(\sigma(-\nabla\varphi)). \quad (5.4)$$

When the conductivity is isotropic and homogeneous, this simplifies to  $I_m = -\sigma\nabla^2\varphi$  (Poisson's equation). To produce the CSD depth profiles shown in Figure 5.6 using previously described methods [265, 272], LFPs corresponding to the uppermost and lowermost channels were first duplicated (to be able to apply equation 5.5). LFPs were then smoothed across spatially adjacent channels to reduce high spatial-frequency noise components:

$$\bar{\varphi}(r) = \frac{1}{4} [\varphi(r+h) + 2\varphi(r) + \varphi(r-h)], \quad (5.5)$$

where  $\varphi(r)$  is the LFP at depth  $r$ , and  $h$  is the sampling interval (50  $\mu\text{m}$ ). Next, the current source density distribution was approximated by calculating the second derivative  $D$  (proportional to the CSD) using finite differences:

$$\frac{I_m}{\sigma} = -\nabla^2\varphi \approx D = \frac{1}{h^2} [\bar{\varphi}(r+h) - 2\bar{\varphi}(r) + \bar{\varphi}(r-h)]. \quad (5.6)$$

For visualization purposes, data were linearly interpolated and plotted as pseudo-colour images, with red (current sink, negative  $D$ ) and blue (current source, positive  $D$ ).

### 5.3.5 Classification Analysis

If we want to assess the difference in the neural response to the different stimulation cases, two data processing steps have to be carried out. First, a principal component analysis (PCA, see section 2.3.3) with singular value decomposition has to be applied to reduce the dimensionality of CSD depth profiles on a single trial basis. In this case, signals from the bottom 17 or 19 channels were used. To eliminate optical and electrical artefacts, a time window from 4-49 ms from the onset of optical stimulation was taken. Each CSD map was treated as a single vector and then a PCA (Matlab *pca* function) was applied. Secondly, for classification analysis, 10-fold cross validation for linear discriminant analysis (Matlab *crossval* function) has to be performed with the first three PCs mentioned above, then the overall successful classification rate across all tests can be computed.  $k$ -fold cross validation randomly break the dataset into  $k$  partitions, clusters the data based on all of them except one, and then tests the clustering using the remaining data. This is repeated for all  $k$  and the results are averaged.

## 5.4 Depth-Specific Activation of Cortical GABAergic Neurons *In Vivo*

A  $\mu$ LED probe was inserted in the anaesthetised mouse neocortex, expressing Channelrhodopsin 2 (ChR2) in parvalbumin positive (PV+) neurons, which is a major type of cortical GABAergic interneuron [255, 256, 258]. To demonstrate depth specificity, three  $\mu$ LED sites were selected, located at 525, 675, and 775  $\mu$ m from the probe tip. To evaluate effects of  $\mu$ LED stimulation on PV+ neuron activity and to compare the performance of the  $\mu$ LED probe with a conventional optic fibre approach, a silicon-based 32-channel electrode probe with an optic fibre (silicon optrode, Figure 5.5) was also inserted. The two probes were separated by 400  $\mu$ m at the cortical surface with a 20° angle. As shown in Figure 5.5 A, optic

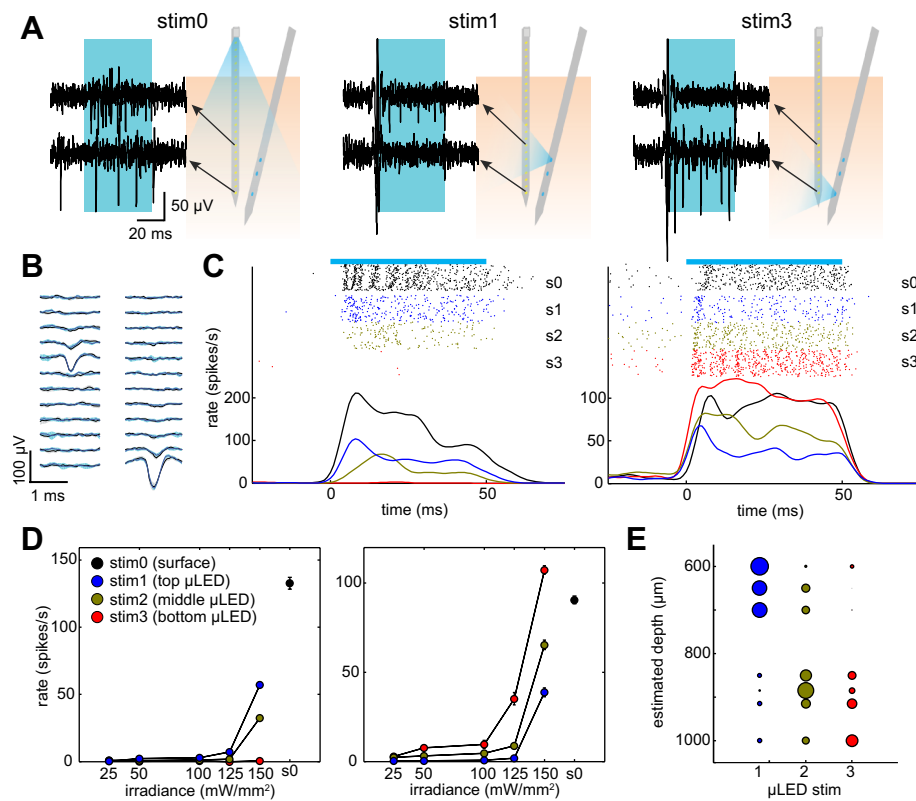


**Figure 5.5:**

Depth-dependent activation of PV+ neurons *in vivo*; **A**) Schematic of probe insertion and high-pass filtered (800 Hz) signals from two separate recording channels, which were separated by 350  $\mu\text{m}$ ; stim0: optical fibre stimulation from cortical surface (86.6  $\text{mW}/\text{mm}^2$ ), stim1 and stim3 (150  $\text{mW}/\text{mm}^2$ ): light stimulation from top and bottom  $\mu\text{LED}$ s; **B**) Average spike waveforms of two exemplary PV+ cells across channels, black: spontaneous spikes, blue: optically evoked spikes, errors indicate the 95% confidence interval **C**) Peristimulus time histograms of two PV+ cells, s0: surface stimulation (stim0, 86.6  $\text{mW}/\text{mm}^2$ ), s1-3:  $\mu\text{LED}$  stimulations (stim1-3, 150  $\text{mW}/\text{mm}^2$ ); blue bar indicates light stimulus and the ticks indicate spike times across 100 trials for each stimulation case **D**) Average light evoked responses across different stimulus conditions and irradiances; effects of  $\mu\text{LED}$  stimulation sites and irradiance were highly significant in both cells (top:  $F_{2,8} = 342.5$ ,  $F_{4,8} = 1153.9$ ,  $p < 0.00001$ , bottom:  $F_{2,8} = 191.98$ ,  $F_{4,9} = 2395.2$ ,  $p < 0.0001$ , two-way ANOVA); error bars indicate SEM **E**) Depth profiles of normalized responses across simultaneously recorded PV+ cells and across stimulus conditions;  $\mu\text{LED}$  number corresponds to stimulus location (stim1-3, 150  $\text{mW}/\text{mm}^2$ ); circle size represents light evoked responses normalized by sum of responses across three conditions

fibre stimulation from the cortical surface elicited spikes in two different channels, separated by 350  $\mu\text{m}$  – suggesting different cortical layers. When light illumination (50 ms, 150  $\text{mW}/\text{mm}^2$ ) was provided by the  $\mu\text{LED}$  probe, spikes were preferentially elicited in one of those channels depending upon which  $\mu\text{LED}$  was used.

To quantify this tendency, single units were isolated and spike rates were measured over 100 trials across different irradiances (25-150  $\text{mW}/\text{mm}^2$ , Figures 5.5 B-E). In the examples in Figures 5.5 B-D, two simultaneously recorded neurons were located at different cortical depths based on the position of the peak amplitude of the spike waveforms (Figure 5.5 B). While the surface illumination elicited robust responses in these neurons,  $\mu\text{LED}$  stimulations evoked distinct responses: deeper  $\mu\text{LED}$  stimulation (stim3) elicited larger responses in the deeper neuron, whereas upper  $\mu\text{LED}$  stimulation (stim1) evoked more spikes from the superficial neuron. This tendency was quantified across different irradiance levels, by showing statistically significant effects on spiking activity dependent on stimulus location ( $p < 0.00001$ , two-way ANOVA). Further confirmation of this tendency came from analysing simultaneously recorded PV+ neurons ( $n = 7$ ) across layers (Figure 5.5 E), which showed a different magnitude of activation across PV+ neurons depending on stimulation depth. This demonstrates that  $\mu\text{LED}$  stimulation induces neural activation, at sub-millimetre resolution, across neocortical layers.

### **5.5 Induction of Distinct Spatiotemporal Population Activity across Cortical Layers**

Another strength of the  $\mu\text{LED}$  probes is the ability to induce distinct spatiotemporal patterns of neural population activity *in vivo*, even in the case where an animal has dense expression of ChR2 across cell populations. To demonstrate this capability, a similar experiment was performed in another transgenic line expressing ChR2 across all cortical layers (Emx1-IRES-Cre::Ai32,  $n = 5$ ). Optically evoked responses across different stimulation conditions were compared again. First, evoked local field potentials (LFPs) across channels were assessed

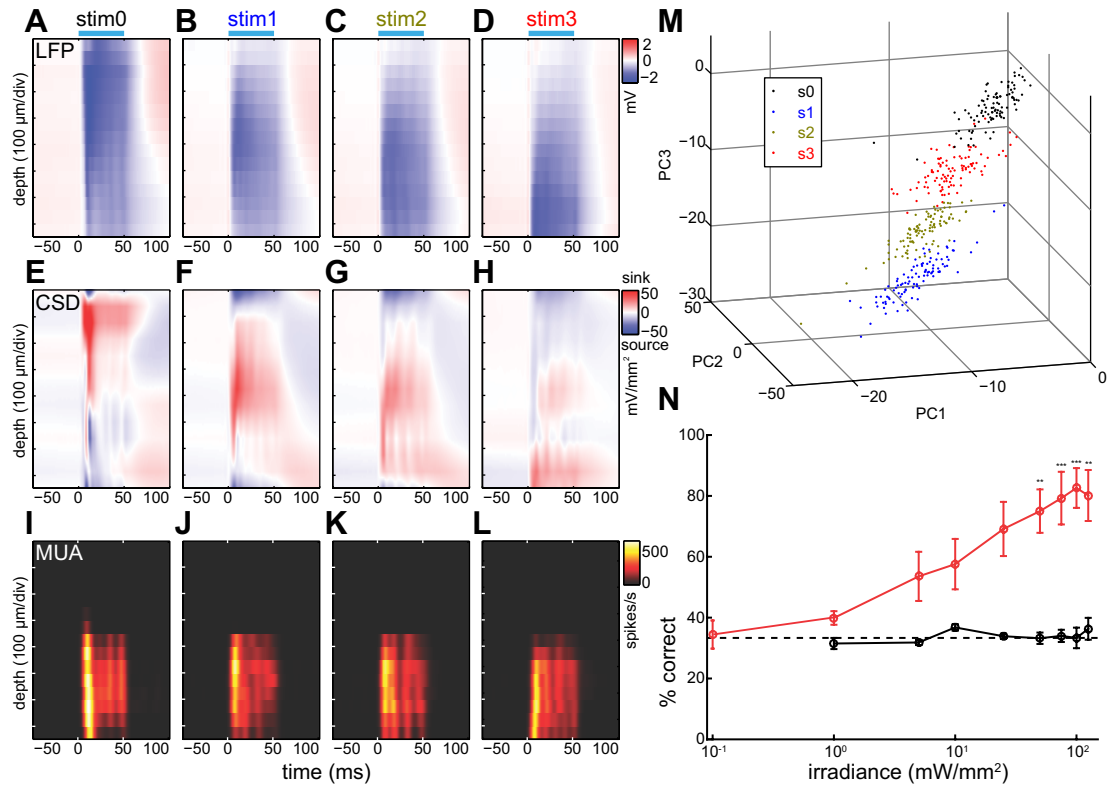


**Figure 5.6:**

Distinct spatiotemporal patterns of neural population activity induced by  $\mu$ LED stimulation *in vivo*; **A-D**) Depth profile of optically evoked local field potentials (LFPs); the average LFP ( $n = 100$ ) in each channel is shown as a function of time (light on at time  $t = 0$ , blue bars indicate light stimulus); note that the biggest deflection ( $\sim -2$  mV) was observed close to the stimulation site; stim0: optical fibre stimulation from cortical surface ( $86.6$  mW/mm<sup>2</sup>), stim1-3: light stimulation from top, middle and bottom  $\mu$ LEDs respectively ( $150$  mW/mm<sup>2</sup>); **E-H**) Depth profile of current source density (CSD) as a function of time; **I-L**) Depth profile of multiunit activities (MUAs); **M**) Principal component analysis (PCA) of CSD profiles; each dot represents a CSD profile for a single trial ( $n = 100$ ) and each stimulation condition; **N**) Percentage of successful CSD profile classifications (after PCA) as a function of irradiance for the three  $\mu$ LED stimulations; Emx1-IRES-Cre::Ai32 shown in red ( $n = 5$ ) and Ai32 mice in black ( $n = 3$ ); dotted line is the chance level (three  $\mu$ LEDs); error bars indicate SEM; \*\*:  $p < 0.005$ , \*\*\*:  $p < 0.001$  (two-way ANOVA with post-hoc Tukey's honest significant difference)

(Figures 5.6 A-D). As expected, conventional surface illumination elicited the largest deflection in superficial layers (Figure 5.6 A). For stimulation with the  $\mu$ LED probe, a different depth profile of LFPs was observed, with larger deflection at deeper channels corresponding to deeper  $\mu$ LED stimulation (Figure 5.6 D).

The current source density (CSD, Figures 5.6 E-H) was computed to determine the net extracellular current flow into and out of neocortical circuits as a function of distance [272]. This reinforces the differences between the two stimulation paradigms, with surface illumination inducing the largest current sink superficially and the  $\mu$ LED probe creating distinct spatiotemporal patterns of activation dependent on stimulus locations. To quantify these activation patterns on a single trial basis, the data dimensionality was first reduced by applying a principle component analysis (PCA, Figure 5.6 M), with the first three principle components explaining 94 % of the variance. Importantly, these CSD depth profiles showed clear clusters depending on stimulus conditions, indicating different patterns of activity. Each activation pattern was then classified under the three  $\mu$ LED stimulation conditions, applying a linear classifier with ten-fold cross validation (Figure 5.6 N). As irradiance of  $\mu$ LED stimulation increased, the classification rate significantly improved from a chance level of 33 %. This indicates that the clusters separate in PC-space, i.e. the induced CSD depth profiles become more distinctive.

The same procedure was applied in control animals without ChR2 expression (Ai32 mice,  $n = 3$ ), to confirm that the classification rate remained around the chance level (black line in Figure 5.6 N). The significant difference ( $F_{1,7} = 75.69$ ,  $p < 0.0001$ , two-way ANOVA) between induced neural patterns in the control and ChR2 expressing mice demonstrates that the observations are due to ChR2 activation, rather than effects from localised light stimulation alone. Finally, the observations were confirmed based on multi-unit activities (MUAs) across channels (Figures 5.6 I-L). Depending on stimulus conditions, the location of peak activity and activity propagation patterns differed. Thus, using the  $\mu$ LED probes even without a complex genetic approach, various spatiotemporal patterns of neural population activity can be induced *in vivo*.

## 5.6 Histological Assessment of $\mu$ LED Probe Invasiveness

For the histological assessment of invasiveness of the  $\mu$ LED probes (Figure 5.7), a mechanical probe was used. It had the same properties as the functional probes in terms of dimensions and materials and was implanted in two *Emx1-IRES-Cre::Ai32* mice under urethane anaesthesia (1.5 g/kg). Surgical procedures were the same as previously described. Before insertion, the mechanical probe was painted with propidium iodide. The probe was inserted in the sensorimotor area at three different penetration speeds (2, 5, 20  $\mu\text{m/s}$ ). The penetration speed was controlled by a motorized manipulator. The probe was penetrated up to 3 mm from the cortical surface and left for an hour. It was then withdrawn at 2  $\mu\text{m/s}$  to compare acute damage between different insertion speeds. After the experiments, the animals were perfused transcardially with physiological saline followed by 4% paraformaldehyde/0.1 M phosphate buffer, pH 7.4. After an overnight post-fixation in the same fixative, brains were immersed into 30% sucrose/phosphate buffer saline, cut into 80 coronal sections with 100  $\mu\text{m}$  thickness using a sliding microtome (SM2010R, Leica), and the sections were mounted on gelatin-coated slides and cover-slipped with a mounting media. Sections were observed under an epifluorescent upright microscope. Propidium iodide is not permeant to live cells and can therefore be used to detect dead cells in a population, whereas EYFP is used to stain all cells. When looking at the overlay of the fluorescence images of the two dyes, one can see that the dead cells make up a fraction of the whole cell population and they are confined to a small volume around the probe. This result is very typical for commonly used silicon-based multi-site electrodes, where the maximum thickness of commercially available probes is 50  $\mu\text{m}$ .

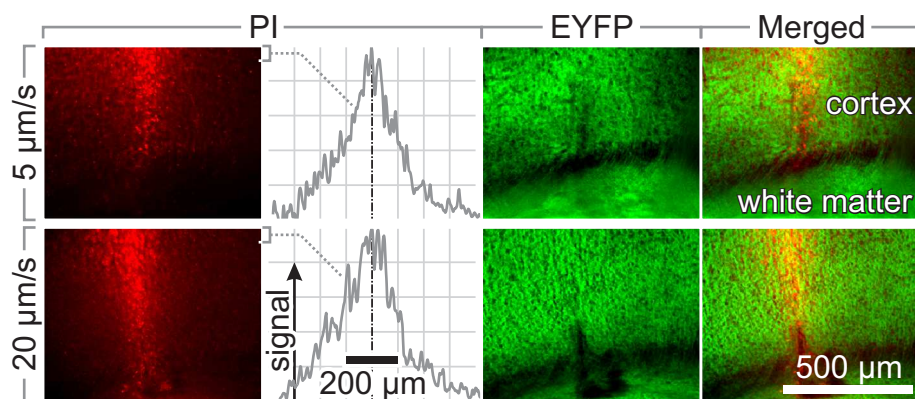


**Figure 5.7:**

Histological assessment of  $\mu$ LED probe invasiveness; The probe was inserted in an *Emx1-IRES-Cre::Ai32* mouse with  $5 \mu\text{m/s}$  and  $20 \mu\text{m/s}$ , cell degeneration was assessed by propidium iodide (PI) staining, normalized PI intensity spectrum created from top  $50 \mu\text{m}$  of PI image

## 5.7 Discussion and Outlook

Microstimulation of neural populations has been a tremendously influential approach for investigating causal links between neural activity and behaviour [273]. The new  $\mu$ LED devices introduced in this work are powerful tools to optogenetically stimulate the brain in a depth-dependent and cell-type specific manner. Although electrophysiological and optical recording of neural population activity has been performed in many brain areas and species with cellular resolution (even in freely behaving conditions), technologies for neural control still remain in their infancy. An important goal in this field is to develop technologies to deliver light in large volumes of biological tissue with high spatiotemporal resolution. The  $\mu$ LED probes can overcome several technical challenges toward this end.

Firstly, they can deliver light even in **deep brain regions** with **micro-millimetre resolution** in a **minimally invasive** fashion. Since silicon-based electrodes can be implanted in the brain chronically for months, it will be interesting to investigate long-lasting effects of our device in freely behaving animals in the future. As the design is similar to silicon-based multi-site electrodes, which have been used over the past decades [186–188, 265, 274], the  $\mu$ LED devices make it possible to

perform a wide range of experiments with respect to optogenetic microstimulation. Secondly, the devices are **scalable** due to integration of light sources on the probe and the adoption of wafer-scale silicon microfabrication. Once microfabricated, the probes are easy to integrate into conventional biology labs with minimal costs. As demonstrated here, there are several immediate applications of the  $\mu$ LED probe. One particularly useful application is when optical illumination is required at higher spatial resolution in a deep brain area compared to conventional optical fibre stimulations. An ideal target is a cell class distributed across functionally distinct sub-regions in a small volume of brain tissue, such as cortical GABAergic neurons. This application offers an opportunity to perform *in vivo* activation of a particular genetically defined cell-type in a depth dependent manner at a resolution of 10s-100s of microns. Activating a sub-cellular component of a particular cell-type (such as the apical dendrites of pyramidal cells or axonal terminals in different input layers in a single brain area) is an interesting application (however, this is still limited by the available opsin technologies [202]). It is also feasible to activate a specific group of neurons within a topographically organized brain area, such as the tonotopic map in the auditory system.

Another application is one where various spatiotemporal patterns of neural activity need to be induced without employing complex genetic manipulations. While in this work transgenic mice were used to demonstrate the technology, in many species it is a challenge to express opsins in a cell-type-specific manner. The  $\mu$ LED probe offers the opportunity to perform new types of optogenetic experiments with a conventional molecular biological approach. In addition, a caveat of conventional optogenetic activation is to generate unnatural, excessive synchronous responses in a large number of neurons. Even though spatiotemporally organized neural population activity is a fundamental ingredient of neural coding [265, 275–277]. The  $\mu$ LED probe can open up possibilities to artificially mimic the dynamic nature of neural population activity at high spatiotemporal resolution *in vivo*. This will enhance efforts to understand neural function and to develop new strategies to treat brain disorders.

### **5.8 Conclusion**

This chapter showed how the  $\mu$ LED probes introduced in chapter 4 can be a useful tool for neuroscience. Neurons can be optically stimulated locally at different depths of the cortex, as shown exemplary using two different classes of neurons. As opposed to parallel implantation of a separate device, integration of electrode sites on the same probe can allow more localized stimulation and recording of circuit responses. The  $\mu$ LED devices were therefore upgraded with this feature and the next chapter will cover the fabrication and characterization in full detail.

## 6 $\mu$ LED Needle Probes with Integrated Recording Electrodes for Precise Analysis of Neural Circuits

In order to use optogenetics as a powerful tool for circuit analysis, optical stimulation has to be paired with a means of feedback. The method of choice for this is electrophysiological recording. As shown in the previous chapter, the  $\mu$ LED probes introduced in chapter Chapter 4 can be used in combination with standard needle-shaped recording probes (commercially available from companies such as NeuroNexus). In order to achieve more precise feedback when activating relatively small local populations, this method of a second implanted device is not ideal. The separation distance is either too large, or, when the probes are implanted very close to each other, tissue damage becomes a big problem. Typically, recording probes can only record from and accurately cluster neurons up to  $\sim 50\ \mu\text{m}$  away [267]. It is therefore desirable to have electrodes as close to the stimulating  $\mu$ LED as possible. To achieve this, they were integrated onto the same device in this work (devices are still early prototypes). Wu *et al.* also recently demonstrated this capability [202]. Although their device contains 3  $\mu$ LEDs per shank, the present work demonstrates the scalability of this approach with having 16  $\mu$ LEDs per shank. This chapter covers the design, fabrication, characterization and performance of these integrated probes.

## 6.1 Device Overview

The design of the integrated recording probes is based on the stimulating probes presented in chapter 4, with different electrode designs added on a separate layer. In Table 6.1 an overview of all recording needle probes is given. Figure 6.1 shows schematics and images of designed and fabricated devices. Numbers of stimulation and recording sites and basic dimensions are summarized. The naming of the probes is explained in section A.2.1.

	Name	Shanks			LEDs				Electrodes				arrangement <sup>2</sup>
		# []	width [ $\mu\text{m}$ ]	length [mm]	# per shank []	# 2D []	# 3D (4 $\times$ ) []	pitch [ $\mu\text{m}$ ]	# per shank []	# 2D []	# 3D (4 $\times$ ) []	pitch [ $\mu\text{m}$ ]	
a	<b>1<math>\times</math>16+16L(S/L)</b> <sup>1</sup>		102	3/6	16			50	16			50	L
b	<b>1<math>\times</math>16+32T(S/L)</b>	1	171	3/6	16			50	32			[25/75], 25 <sup>3</sup>	T
c	1 $\times$ 16+64T(S/L)		102	3/6	16			50	64			25, 25	T
d	<b>4<math>\times</math>8+16L(S)</b>	4	102	3	8	32	128	100	16	64	256	50	L
e	<b>4<math>\times</math>8+16T(S)</b>		102	3	8	32	128	100	16	64	256	[25/175], 25	T
f	<b>6<math>\times</math>0+16L(S)</b>	6	102	3					16	96	384	50	L
g	Spacer	0											

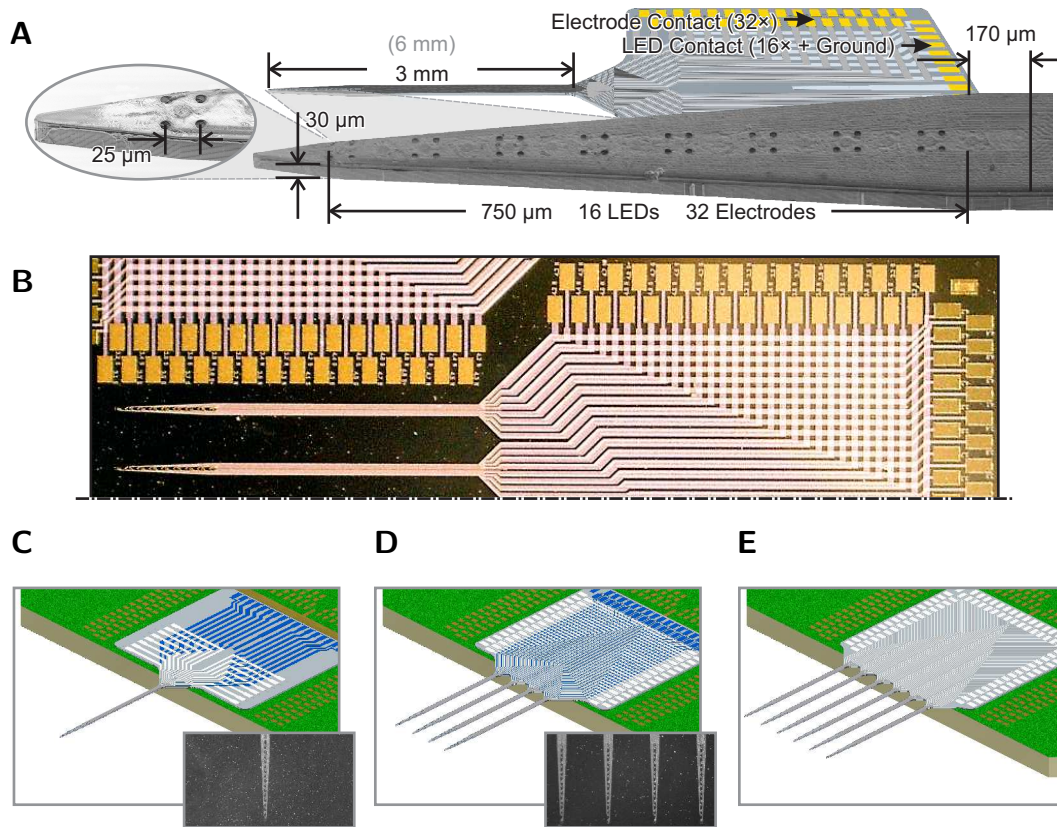
<sup>1</sup> S=short (3 mm), L=long (6 mm)

<sup>2</sup> L=linear , T=tetrode 

<sup>3</sup> [x pitch between electrodes / x pitch between tetrodes], y pitch between electrodes

**Table 6.1:**

Overview of designed and fabricated recording  $\mu\text{LED}$  needle probes (also see Table 4.1) showing number of shanks, LEDs and electrodes, as well as basic dimensions for various designs (values for 3D designs assume stacking of four dice); fabricated devices in bold; a-e) integrated devices for stimulation and recording (the narrow width of the 64-channel devices arises from the anticipated move to advanced lithography techniques), f) recording-only device (could be stacked with stimulation-only devices), g) spacer for 3D integration

**Figure 6.1:**

$\mu$ LED arrays with integrated electrodes; **A)** SEM of a single-shank device in front of a schematic, 16  $\mu$ LEDs in a linear arrangement with a pitch of 50  $\mu$ m, shank length is either 3 mm or 6 mm, individual tracks lead to the p-contact of each LED and each electrode, 49 bond pads are located on the right hand side of the device (including one common n-contact), electrode pitch is 25  $\mu$ m, tetrode pitch is 100  $\mu$ m; **B)** Picture of a four-shank device during fabrication (prior to device release); **C-E)** Overview of designed (and fabricated) probes (images in front of schematics on PCBs): 1D single-shank, 16  $\mu$ LEDs/16 linear electrodes (Table 6.1 a), 2D quad-shank, 32  $\mu$ LEDs/64 tetrode electrodes (Table 6.1 e), and 2D hex-shank, no  $\mu$ LEDs/96 electrodes Table 6.1 f)

## 6.2 Fabrication

The integrated probes are an upgrade of the probes introduced in chapter 4. The fabrication process is therefore very similar up to a point (cf. Figure 4.5, where some of the following steps have also been explained in more detail). After the creation of the LED tracks (step 11 in the fabrication of the  $\mu$ LED probes, Figure 4.5) the fabrication differs as follows. A 1  $\mu$ m-thick SiO<sub>2</sub> layer was deposited using PECVD to decouple the two track layers from each other

(Figure 6.2, **step i1**). A second Ti/Al (50/500 nm) layer stack was then sputtered to form the electrode tracks (**step i2**). It was patterned using S1805® photoresist. Resist was spun at 2000 RPM for 30 s, baked at 115°C for 1:30 min, exposed for 2.8 s, post-exposure-baked at 115°C for 1:30 min, developed for ~30 s (developer diluted 1:1) and hard-baked at 115°C for 2 min (**step i3**). The tracks were etched (ICP 1 recipe *AlRobert*, ~1 min overetch after colour change, ~4 min total). The samples were subsequently cleaned using acetone and IPA for 5 min each (**step i4**).

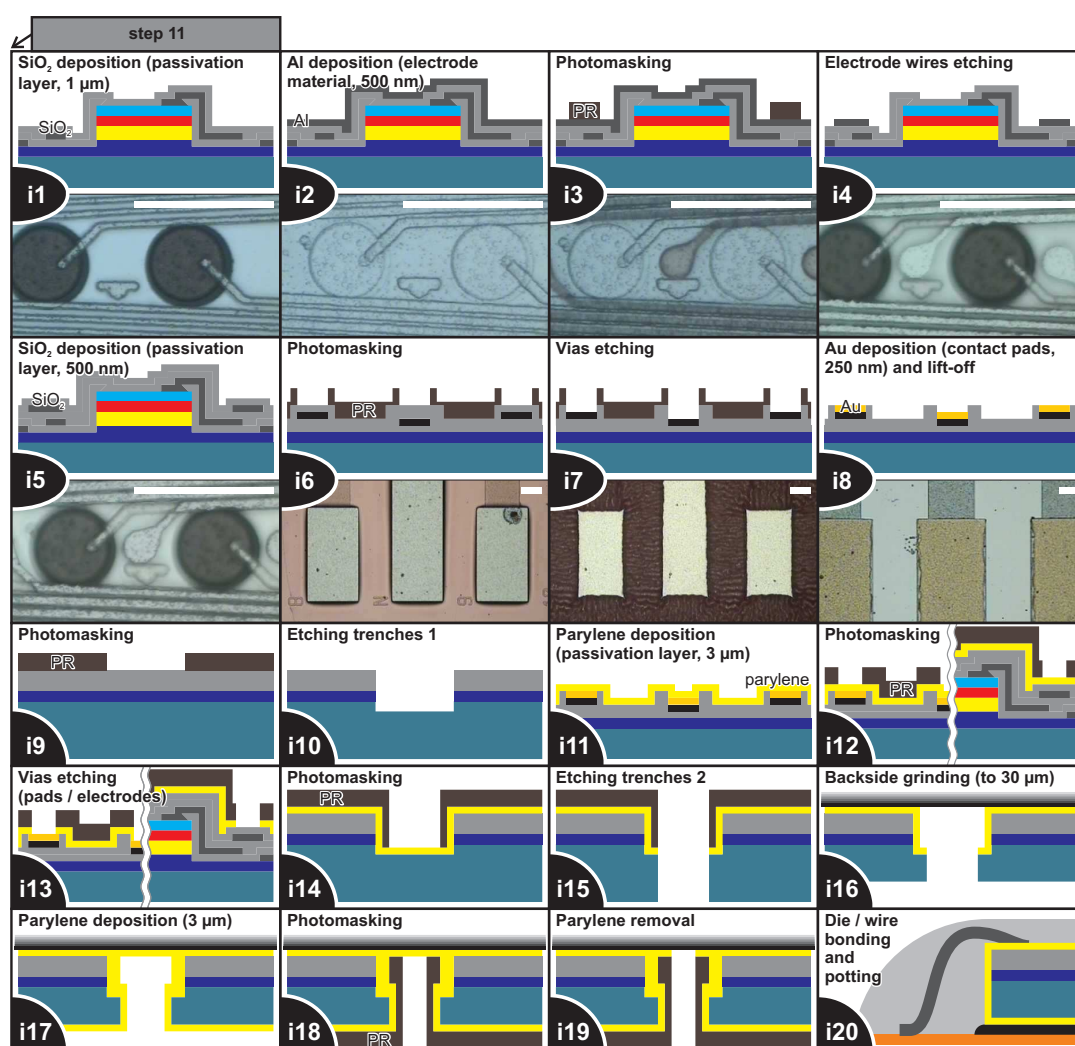


**Figure 6.2:**

Fabrication steps of  $\mu$ LED needle probe with integrated electrodes; additional steps to the  $\mu$ LED needle probe fabrication are required to monolithically create the electrode structures (following step 11 in Figure 4.5); electrode tracks are made from aluminium, vias are opened through the insulating parylene layer and the electrode interface is created through platinum black electroplating

A bilayer of SiO<sub>2</sub> (500 nm total) was deposited (**step i5**) and photomasked using SPR®220-7 photoresist (**step i6**). Contact pad vias (~1.5 μm deep) were etched using RIE 1 recipe *iopsio2* followed by a one minute oxygen plasma clean using RIE 1 recipe *o2ash* (**step i7**). Contact pads were created by sputtering of a 50/250 nm titanium/gold layer stack followed by a lift-off process (**step i8**).

The devices were characterized at this point (see section 6.3) and it was found that further process optimization of the described steps is necessary to improve the yield of functional electrodes. After that, the following steps are anticipated to be necessary to eventually finish the fabrication. First, the samples will have to be masked using SPR®220-7 photoresist (**step i9**) and trenches will have to be etched by consecutive removal of the SiO<sub>2</sub>, Ti/Al and GaN layers (**step i10**). The samples will have to be cleaned and a 3 μm-thick layer of parylene C will have to be deposited conformally (**step i11**). The samples will then have to be photomasked using SPR®220-7 photoresist (**step i12**) and plasma etched (RIE 1) to open electrode and contact pad vias (**step i13**). The samples will have to be cleaned and photomasked again using SPR®220-7 photoresist (**step i14**). The trench etch, which consists of parylene removal followed by a deep reactive ion etch of ~45 μm, will have to be continued (**step i15**). The samples will have to be attached to a carrier wafer and thinned to 30 μm from the back side (**step i16**). The remaining surfaces will have to be coated with 3 μm of parylene (**step i17**). This step is necessary to protect the silicon substrate from getting attacked by the physiological environment during chronic implantation. Another lithography step (**step i18**) will have to be done to remove parylene from the trenches (**step i19**) before bonding and potting (**step i20**).

Parylene processing is difficult and obtaining a complete and stable passivation is expected to be difficult. The approach taken by Wu *et al.* [202] could be an alternative. They have coated just the top side of the probe using SiO<sub>2</sub> and Al<sub>2</sub>O<sub>3</sub> formed by atomic layer deposition (ALD).

## 6.3 Characterization

For preliminary testing purposes, vias were opened in the  $\text{SiO}_2$  layer after fabrication step i8 (Figure 6.3 A). The probes were characterized by measuring crosstalk between layers. They were then electroplated in order to measure electrode impedance. Platinization underlined the need for a high quality  $\text{SiO}_2$  layer. Platinum black formed in many places on the probe indicating pinholes in the passivation layer.

On a second sample a 1  $\mu\text{m}$ -thick parylene layer was deposited before opening the vias in order to cover pinholes in the  $\text{SiO}_2$  layer. In this case an individually addressable electrode could be identified and platinized, as shown in Figure 6.3 B. Impedance testing was consequently carried out and a value of 1.04  $\text{M}\Omega$  at 1 kHz was measured. This is still in the expected range, but could be reduced by electroplating for a longer time or at a different current density in order to increase the surface area of the electrode. The rough surface topography of the electrode track underlayer arising from the two-layer fabrication process made the lithography of the electrode tracks difficult and resulted in discontinuities in the electrode tracks. The yield of individually addressable electrodes was therefore

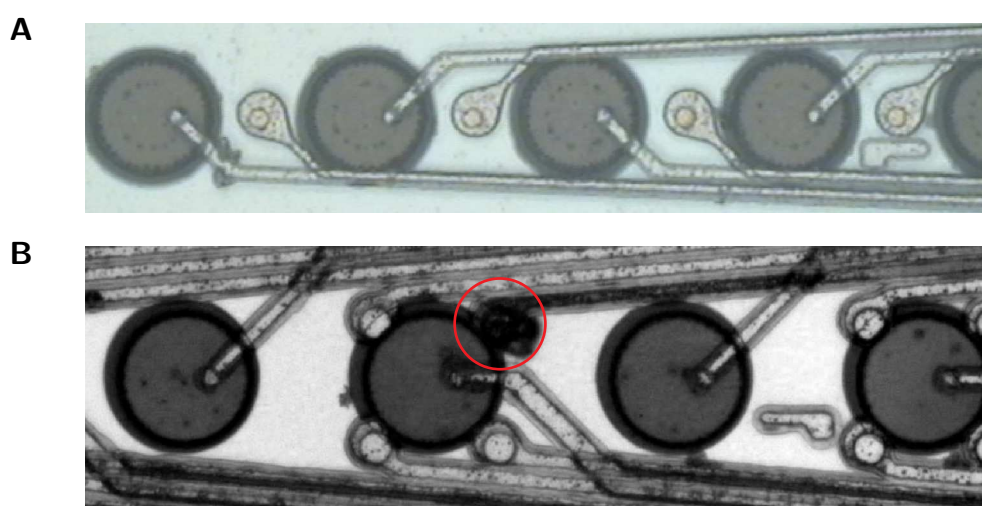


**Figure 6.3:**

Recording  $\mu\text{LED}$  probe with electrode via through an insulating layer, electrode diameter is  $\sim 5 \mu\text{m}$ ; **A)** Vias through  $\text{SiO}_2$  layer before platinization; **B)** Vias through  $\text{SiO}_2$ /parylene layers after successful platinization (individual channel)

very low, which could potentially be addressed by adding a planarization step (e.g. CMP) after the LED track passivation in the future. Sputtered iridium oxide films (SIROFs) could be used as an alternative material for the electrode interface in the future. In this case a lift-off process can be used instead of electroplating. Crosstalk between the LED tracks and the recording electrodes was assessed by measuring the inter-track capacitance. LED track 1 was tested with electrode tracks 1-32 (Figure 6.4 A). Capacitance values in the range of 1-3 pF were found (6.4 B), with the middle tracks having the highest values. This was expected, due to the distance of the tracks running parallel being longer. When turning on the  $\mu$ LEDs, crosstalk will raise the voltage of the electrode tracks temporarily. This voltage will then decay (discharging capacitor) following the relationship

$$V(t) = V_0 \exp\left(-\frac{t}{\tau}\right) \quad (6.1)$$

with the initial voltage  $V_0$ , time  $t$  and the decay time constant  $\tau$ , depending mainly on the resistance to ground through the physiological solution,  $R_{\text{solution}}$  (Intan amplifier input resistance is high at  $\sim 1.3 \text{ G}\Omega$ ), and the inter-track capacitance,  $C_{\text{tracks}}$ :

$$\tau = R_{\text{solution}} \cdot C_{\text{tracks}} \cdot \quad (6.2)$$

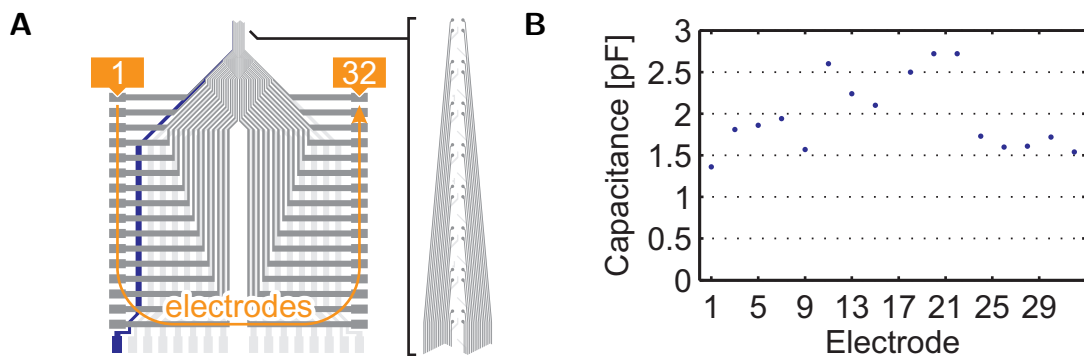


**Figure 6.4:**

Crosstalk between LED and electrode tracks in integrated  $\mu$ LED needle probes; **A)** Schematic showing electrode track numbers and highlighting LED track 1; **B)** Capacitance between LED track 1 and electrode tracks 1-32 (cf. panel A, shorted neighbours were excluded)

In order to prevent the amplifier from being saturated, which would make the detection of spikes impossible, an amplifier circuit could be used, which can temporarily ground the electrodes after the stimulation pulse. Such circuits have been developed in the past for electrical stimulation, for example by Hottowy *et al.* [278] and cope with very large artefacts, allowing the recording of action potentials 50  $\mu$ s after electrical stimulation on the same electrode.

## 6.4 Probe Controlling

Several alternatives for establishing a bidirectional connection to the integrated probes in the future have been designed and are shown below (Figure 6.5).

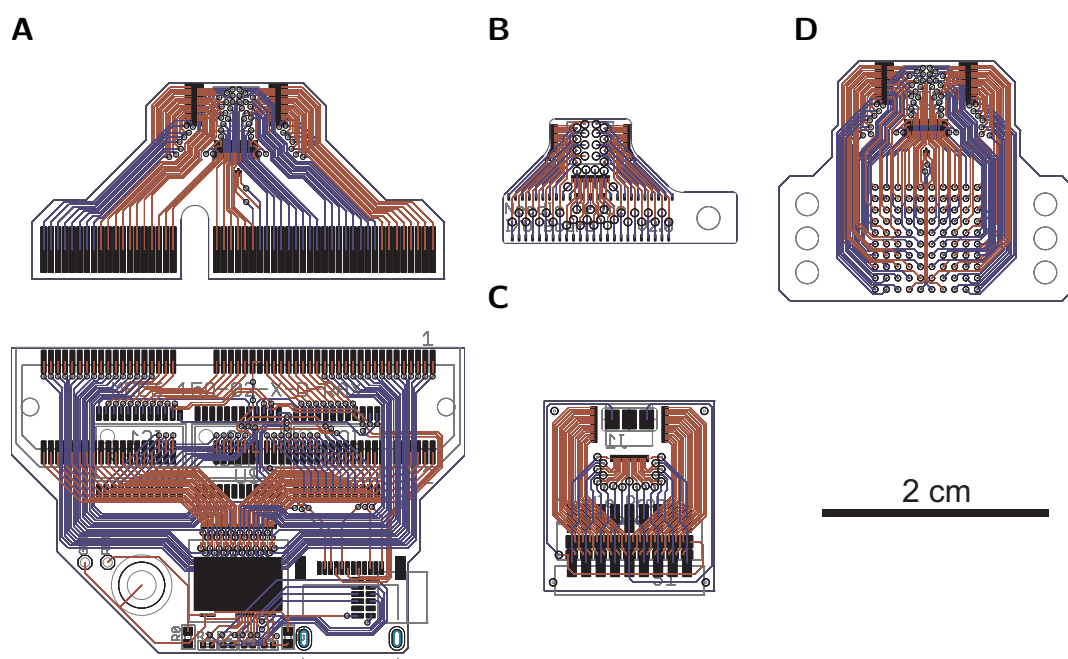


**Figure 6.5:**

Interface hardware for recording  $\mu$ LED probes with up to 32  $\mu$ LEDs and 64 electrodes; **A**) Probe board (top) without components and with an edge connector to interface with a control board (bottom) including demultiplexers for  $\mu$ LED addressing (32  $\mu$ LEDs) and an IC (Intan RHD2132) for recording of neural signals (64 electrodes); **B**) A compact 48-channel ( $\mu$ LEDs/electrodes) board with an FFC connector (Hirose FH35-49S-0.3SHW); **C**) An alternative 16- $\mu$ LEDs/32-electrodes board with Omnetics connector to interface with Intan recording hardware and pin header to interface with an external LED driver; **D**) Probe board with an alternative connector to the one shown in panel A (Samtec ZA1 Series low profile micro array interposer), matching control board not shown

PCBs based on these designs could be fabricated in the future. The designs make use of different miniature connector systems. There are convenient options now for off-the-shelf multi-channel electrophysiological miniature amplifiers. With the RHD2000 series, Intan Technologies LLC [279] offers 16-, 32-, and 64-channel amplifiers with a maximum bare die size of  $7.3\text{ mm} \times 4.2\text{ mm}$ . These include analogue to digital converters and the output of the digitized data is via an SPI interface. Since the amplifiers are relatively expensive and the implantable probes should be considered as wear and tear items, it is not preferable to combine them on a single PCB. Considering the high number of connections required and the limited space this complicates the PCB design. Figure 6.5 A (bottom) shows a design, where a 64-channel amplifier has been combined with the 32-channel demultiplexer array for  $\mu\text{LED}$  addressing from section 4.5.1.1, together with a probe board that can be connected to this controller board. Figure 6.5 B-D show alternative designs for probe boards making use of different connector systems.

## 6.5 Conclusion

In this chapter the further development of  $\mu\text{LED}$  needle probes (chapter 4) towards integrated devices for stimulation and recording was described. The adjustments and additional steps of the fabrication were detailed. Preliminary electrode characterization was carried out. Further optimization is necessary to allow use in *in vivo* experiments and control hardware will have to be fabricated. The devices will open up possibilities for a wide range of optogenetic circuit analyses. Penetrating devices are limited by their number of recording sites, but in order to fully understand a neural circuit it is necessary to have relatively large and dense arrays of electrodes. This is easier to achieve for devices, that do not penetrate the brain, but record from the surface. The following chapter covers such arrays, that can be paired with optogenetics to dissect circuits of the retina *in vitro*.

## 7 Transparent Planar Electrode Arrays for Studying the Retina *In Vitro*

As shown in the previous chapters, MEAs offer high temporal resolution electrophysiological recording from many cells simultaneously. They are therefore also used extensively to study neural systems, such as that in the retina, *in vitro*. An open question is, what resolution is required for recording from all neurons in a population. This can be studied with the new arrays presented in this chapter, which have a resolution that is four times higher compared to current devices. The results from these studies also have implications for future layouts of integrated  $\mu$ LED neural probes (chapter 6).

When trying to understand the wiring diagram of the brain, the eye is a good place to start for various reasons. It is relatively easy to approach and it has a planar, layered structure, which makes it easy to probe. It is possible to stimulate input cells naturally using light and the output cells lie at the surface, which makes it easy to record responses. Furthermore, retinal tissue can stay alive for hours *in vitro*. As shown in section 2.1.2, the RGC density is a function of eccentricity (Figure 2.3D). In high-density regions close to the fovea there is a maximum neural packing density of  $30\,000\text{ mm}^{-2}$  and conventional electrode arrays fail to provide the resolution necessary to study the wiring in sufficient detail. A lot of work has been done on 512 electrode arrays in the past and the number of detected neurons was always around 300. This was true whether the pitch was  $60\text{ }\mu\text{m}$  or  $30\text{ }\mu\text{m}$ , meaning that many neurons were missed in the recording. High-density multi-electrode arrays (HD MEA) are therefore needed for getting a more detailed glimpse into the computational inner workings of this highly sophisticated organ. Several electrode arrays with different channel counts based on centred hexagon

arrangements have been developed in the past [118]. The layouts are based on centred hexagons, containing a number of  $3n(n - 1) + 1$  electrodes (with an integer  $n \geq 1$ ). A layout example of a 61 electrode array is shown in Figure 7.1. The arrays had detection areas of  $0.173 \text{ mm}^2$  and  $0.043 \text{ mm}^2$  (61 electrode arrays with  $60 \mu\text{m}$  and  $30 \mu\text{m}$  pitch, respectively), meaning each electrode had to record from 85 or 21.2 neurons to achieve 100% detection, which is not feasible. If the electrode pitch was reduced  $15 \mu\text{m}$ , the detection area would be only  $0.011 \text{ mm}^2$ , with each electrode having to record from just 5.3 neurons, which is step towards complete recording of all neurons.

Another ongoing difficulty with MEA recordings is the attribution of identified neural spiking patterns to specific neurons, since conventional triangulation techniques fail to provide the accuracy necessary in densely packed retinal tissue. This is where the combination of electrophysiological recording and high-resolution optogenetic stimulation can be useful. For example, by co-expressing an opsin and a fluorescent protein in a subset of RGCs, they can be activated by **optical stimulation**, giving an electrical footprint of a genetically targeted neuron that

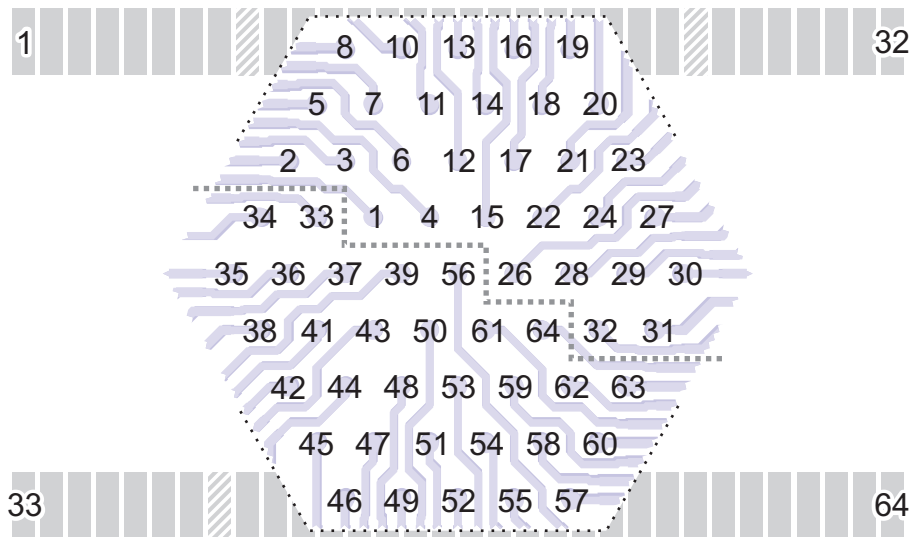


**Figure 7.1:** 61 electrode array channel map; schematic showing connections between electrode position in a hexagonal array and contact pad position (central section not to scale)

can be matched to the fluorescent signal. Subsequent functional studies then allow the identification of the neural type with morphology. Spike waveforms can be recorded and matched to waveforms recorded from hundreds of RGCs during **visual stimulation** and fluorescence imaging data.

## 7.1 61 Electrode Arrays

The first fabricated device is a 61-channel array, the mask layout, fabrication and characterization of which are detailed below.

### 7.1.1 Mask Layout

The mask layout is based on the mask layout of previously fabricated 61 electrode arrays [280]; only the central section was changed. Figure 7.2 shows the design of the first and second generation device with  $60\ \mu\text{m}$  and  $30\ \mu\text{m}$  electrode pitch, respectively (panels A, B) and compares it to the new design having an electrode

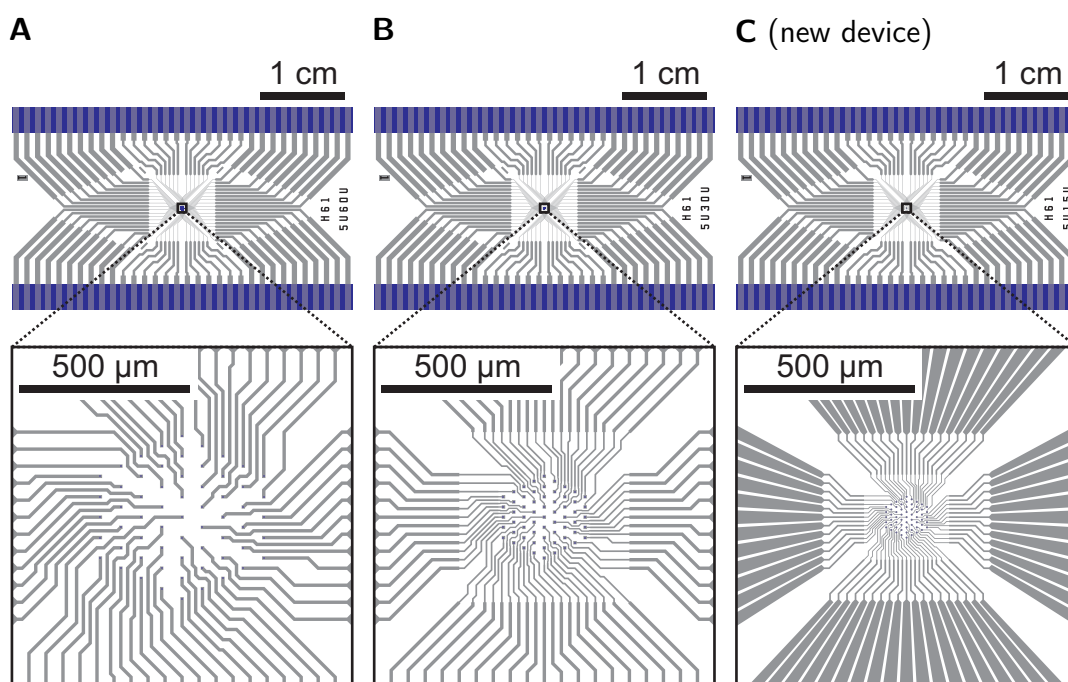


**Figure 7.2:** 61 electrode arrays (schematic); **A**)  $60\ \mu\text{m}$  electrode pitch (cf. Gunning [280]); **B**)  $30\ \mu\text{m}$  electrode pitch (cf. Gunning [280]); **C**)  $15\ \mu\text{m}$  electrode pitch

pitch of  $15\ \mu\text{m}$  (panel C). The inner section was basically scaled down by a factor of two. The size of the electrode sites was kept at  $5\ \mu\text{m}$ . The underlying ITO electrodes are  $6\ \mu\text{m}$  in diameter, leading to a minimum track separation of  $1.5\ \mu\text{m}$  (localized around electrode sites,  $2\ \mu\text{m}$  elsewhere, see section A.4.2). Two 5" photomasks were designed for fabricating three devices per 4" wafer in parallel. The masks contain the electrode tracks and vias, respectively. Marks for wafer dicing are also present.

### 7.1.2 Fabrication

The fabrication of the 61 electrode arrays consists of three main steps: the patterning of the ITO electrode tracks, the deposition of a passivation layer on top of the array, and via-etching through this layer to create the electrode sites. The devices are then separated by wafer dicing and after electroplating the electrode sites (using platinum black to create a good electric interface with the neurons), the arrays are ready to use. On the surface, the fabrication process appears

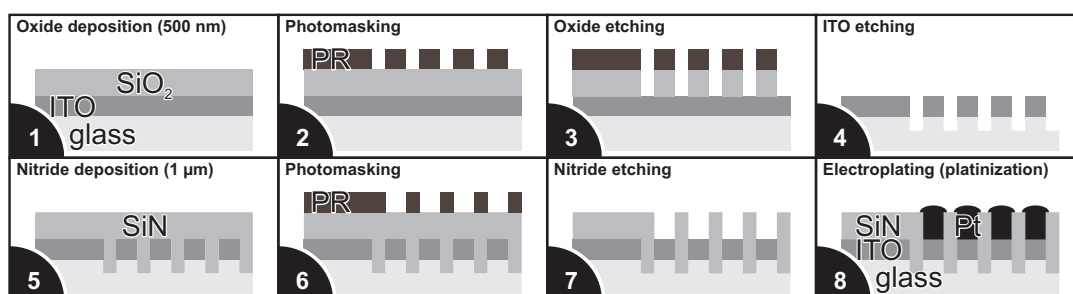


**Figure 7.3:**

Fabrication of 61 electrode arrays with  $15\ \mu\text{m}$  electrode pitch; fabrication consists of etching of ITO tracks (with  $\text{SiO}_2$  hard mask) and deposition of an insulating layer ( $\text{SiN}_x$ ) followed by etching of vias and electroplating using platinum black

straightforward. However, the production of high-quality arrays, needed for retinal studies, is complicated. Figure 7.3 shows the basic steps in the fabrication of the 61 electrode arrays. Figure 7.4 shows the central section of an array during the fabrication.

Wafers were purchased from Thin Film Devices Inc., USA. The substrate material was Corning® EAGLE XG® display glass. The diameter was 100 mm (~4 inch) and the thickness was 1.1 mm. ITO was sputter-coated with a thickness of  $145 \pm 10$  nm and a sheet resistance of  $20 \pm 2 \Omega/\square$  by the supplier. The coated wafers had a transmission of 88 % at 550 nm. Masks for photolithography were obtained from Delta Mask B.V., The Netherlands.

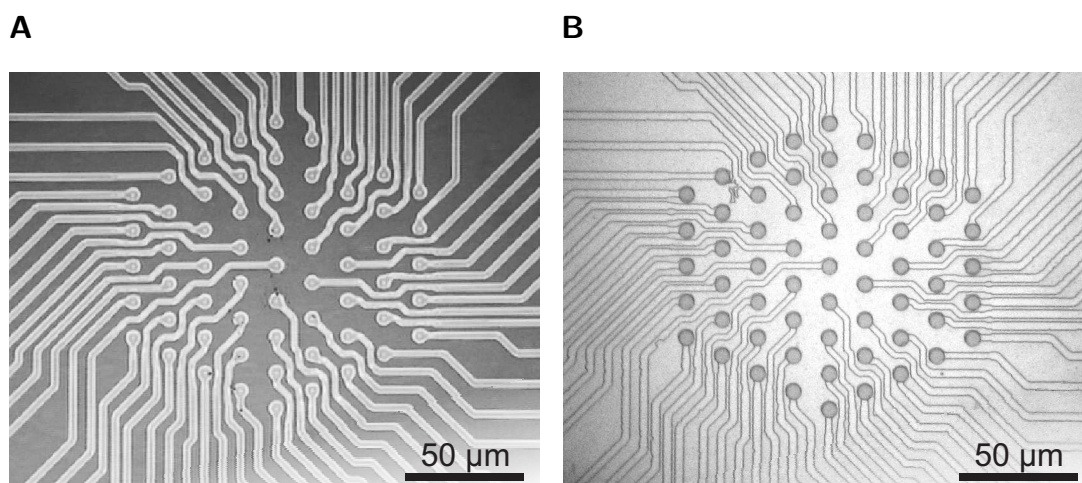


**Figure 7.4:**  
61 electrode array with 15  $\mu\text{m}$  pitch; **A)** After patterning of the electrode tracks;  
**B)** After passivation and vias etching

### 7.1.2.1 ITO Etching

After the wafers were scribed with an ID on the back side, they were cleaned in acetone and isopropanol for five minutes. A silicon dioxide hardmask was then created using PECVD (section 3.2) recipe *ox200* (Table A.13). This is necessary, since photoresist etches quickly using the ITO etch recipe. Standard S1828® resist is too thin and lithography of the 2  $\mu\text{m}$  features is already difficult using S1828®. For the deposition of the hard mask, the wafers were loaded into a cold chamber (100°C) to avoid shattering of the glass and 500 nm of oxide was deposited at 300°C.

This oxide layer was then patterned using a photomask. 500 nm-thick S1805® photoresist was spun at 4000 RPM for 30 s with prior HDMS prime. A soft bake was performed for one minute at 115°C and the resist was exposed with mask 1 (*WIRES*) for 3 s. The resist was developed in diluted developer (MICROPOSIT® developer concentrate, 50 % deionized water) for approximately 30 s. The hard mask was etched using RIE 1 recipe *iopsio2* (Table A.1) for 18 min (40 % overetch). The ITO layer was consequently etched using ICP 1 recipe *ITOetch2* (Table A.7) for 11 min (50 % overetch). The remaining hardmask was removed using RIE 1 recipe *iopsio2* (15 min).

### 7.1.2.2 Passivation

Coating the high-density electrode arrays with an appropriate passivation layer is not straightforward. The layer needs to be thick enough to capacitively decouple the ITO tracks from the conducting solution on top of the layer. It must also survive in a heated electrolytic solution (34°C Ames' Medium) without dissolving. The thick layer (~1 µm), coupled to the small pitch between the electrode vias, requires a very low-stress film (see section A.4.1 for background theory). Otherwise, cracks can develop in the passivation layer after the etching of the vias. The dicing process also requires a high-quality passivation layer as cracking and delamination can occur at this stage. A 1 µm-thick, low-temperature (200°C), low-stress film (<250 MPa tensile) of SiN<sub>x</sub> was therefore deposited using PECVD (Rogue Valley Microdevices, USA). Ammonia-free PECVD silicon (oxy-)nitride (SiO<sub>x</sub>N<sub>y</sub>) layers could be a potential alternative that can be fabricated with the available tools (Figure 3.1). Layers produced by the current recipe (Table A.14), however, showed poor adhesion, leading to peeling during wafer dicing.

### 7.1.2.3 Vias Etching

A photomask was created using ~2 µm-thick ma-N 1420 photoresist (spun at 3000 RPM for 30 s). A soft bake was performed for two minutes at 100°C and the resist was exposed with mask 2 (*VIAS*) for 20 s. The resist was then developed (ma-D 533/S) for ~30 s. The resist was hard baked for 30 min at 100°C (ramped-up

from room temperature) to increase etch resistance. Vias were etched using RIE 1 recipe *SiN-RS* (Table A.2) for 30 min (40 % overetch). The wafers were then cleaned using acetone and isopropanol, followed by a piranha etch ( $\text{H}_2\text{SO}_4$  and  $\text{H}_2\text{O}_2$ , 3:1).

There is still room for optimization of this process. Firstly, mask alignment with the necessary precision was very difficult. Ideally, alignment marks would be formed in the same layer as the electrode tracks. However, the transparency of the ITO layer makes this challenging. A separate alignment marks mask can be used, but leads to accumulated registration errors that add up to an unacceptable level. The vias were therefore finally aligned directly over the tracks in the central section of the arrays using a negative photomask (mostly clear/glass). A problem with this approach is that particulates on the mask can lead to out-of-place etching, destroying the device. A positive photomask, used with a tracks mask with alignment marks, is expected to help prevent this in the future. In order to improve the visibility of the alignment marks, a thin reflective metal layer sputtered over these features (lift-off process) could help improve contrast and masks have been designed to this effect. Another issue is the SiN etch recipe, which was found to etch ITO unexpectedly quickly. Also the etch rate was found to be non-uniform between the large bond pad vias and the small electrode vias. A process based on  $\text{SF}_6$  is expected to solve these problems, but the process still needs optimization.

#### 7.1.2.4 Electroplating

The procedure for electroplating the electrode arrays with platinum black is to apply a current of 80 nA/electrode ( $4\text{ nA}/\mu\text{m}^2$ , see section A.4.3) for  $\sim 20$  s and until a drop in resistance or a growth of the black platinum spots, indicating an “overflow” of the electrode vias, can be observed. The platinum solution consists of 1 % **platinic chloride**, 0.08 % **lead acetate** (for improved adhesion [108]) and 98.92 % **water**.

#### 7.1.2.5 Alternative Methods for Passivation

Several alternative materials exist, that could be used for insulation. These include low temperature oxide (LTO), silicon carbide (SiC) and parylene C. SiC has been used for similar devices by Lei *et al.* [281]) and, in comparison to  $\text{SiO}_2$  and  $\text{SiN}_x$ , proved to be a very good insulator, due to low stress and low dissolution rate. One drawback is the relatively high refractive index of  $\sim 2.5$  [282] that may affect the optical transparency required for retinal studies. LTO requires higher temperatures ( $425^\circ\text{C}$ ) than PECVD  $\text{SiO}_2$  and is a standard process in many cleanrooms using silane and oxygen [214, p. 51] to deposit. It offers a higher density film than the PECVD counterpart and so may be more resistant to dissolution. Parylene C has a slightly better refractive index of  $\sim 1.6$  [244] compared to PECVD  $\text{SiN}_x$  ( $\sim 1.9$  [283]). Its electrical properties are also better with an electrical resistivity of  $\sim 10^{15}\ \Omega\cdot\text{m}$  [244] compared to  $\sim 10^{10}\ \Omega\cdot\text{m}$  [283] and a dielectric constant of  $\sim 3.1$  [244] compared to  $\sim 7$  [283]. The low dielectric constant of parylene C allows for thinner passivation layers. While  $\text{SiN}_x$  layers have previously been produced with a thickness of  $1\ \mu\text{m}$ , the inversely proportional relationship between film thickness and capacitance means that this number could theoretically be halved.

First tests showed that parylene C might be a possible future replacement for  $\text{SiN}_x$  (Figure 7.5). Difficulties persist regarding etching and adhesion. Parylene can only be etched in oxygen plasmas, which have no selectivity over photoresist. A thick photoresist is therefore needed. For testing purposes,  $1.5\ \mu\text{m}$  of parylene C were deposited conformally on the wafers (see Table A.12). The wafers were then masked with a  $\sim 2.5\ \mu\text{m}$ -thick photoresist (ma-N 1420 spun at 1500 RPM for 60 s

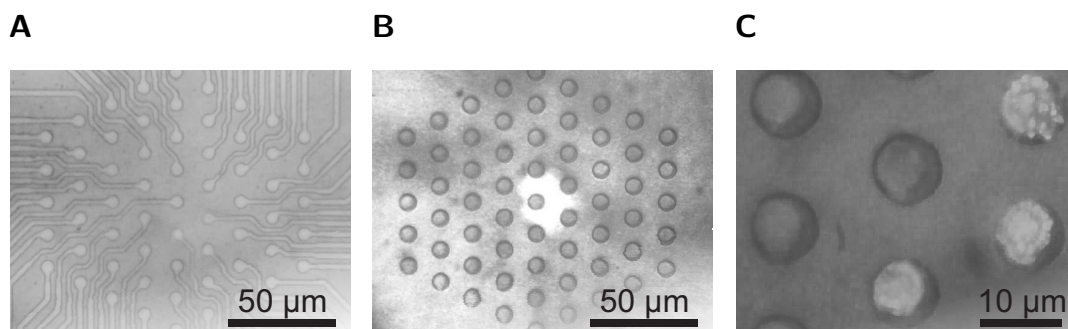


**Figure 7.5:**

Parylene passivation of electrode arrays; **A)** After conformal deposition of 1.5 μm of parylene on the electrode tracks; **B)** After etching of vias through the parylene passivation layer (delamination visible in the centre); **C)** After electroplating using platinum black (two electrodes on right hand side and centre bottom)

and baked at 100°C for 3 min). The thick layers lead to the underlying structures being invisible during mask alignment. The resist was therefore removed from the alignment mark sections using isopropanol. After exposure of 20 s and development of ~30 s using ma-D 533/S, parylene vias were etched using RIE 1 recipe *paryl-RS* (Table A.3) for a total of 7 min (40% overetch) in two runs (to avoid excessive heating). The photoresist mask was subsequently removed using acetone and isopropanol. Figure 7.5 B shows delamination in the central section occurring during photolithography. A soft bake at reduced temperature might help solve this issue. This adhesion of parylene seems to be the major issue with its use and is likely due to the physical nature of the deposition technique (i.e. no chemical bonds are formed at the intermediate surface).

### 7.1.3 Characterization

Inter-channel capacitance was measured using an LCR meter (LCR-821, ISO-TECH) to confirm that electrical recording will be possible with low crosstalk between channels. Figure 7.6 shows the results from this experiment.

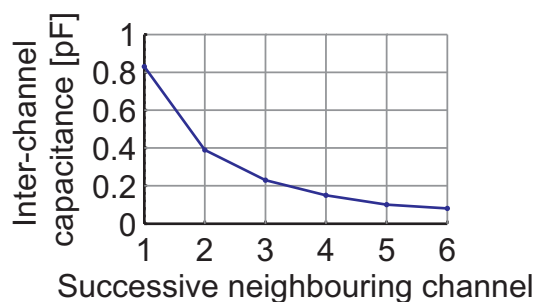


**Figure 7.6:**

Inter-channel capacitance of a 61 electrode array with 15  $\mu\text{m}$  electrode pitch (channel 1 and neighbouring channels)

Inter-channel capacitance was found to be low with values very similar to those of the large-pitch arrays [280]. As expected, the inter-channel capacitance exhibits an inversely proportional relationship to the channel separation distance.

## 7.2 519 Electrode Arrays

Arrays with high electrode counts have been successfully fabricated previously. They consisted of either 512 electrodes in a rectangular arrangement [169] or 519 electrodes with 30  $\mu\text{m}$  pitch in a hexagonal arrangement [280, 284]. In this work, the fabrication design (Figure 7.7) and process flow for the 519 electrode arrays was adapted to the available tools (chapter 3) and processes have been modified to improve yield and fabrication cost. Part of the process had been successfully tested in the fabrication of the 61 electrode arrays (section 7.1.2) and could therefore be reused for the fabrication of larger area high-density electrode arrays.

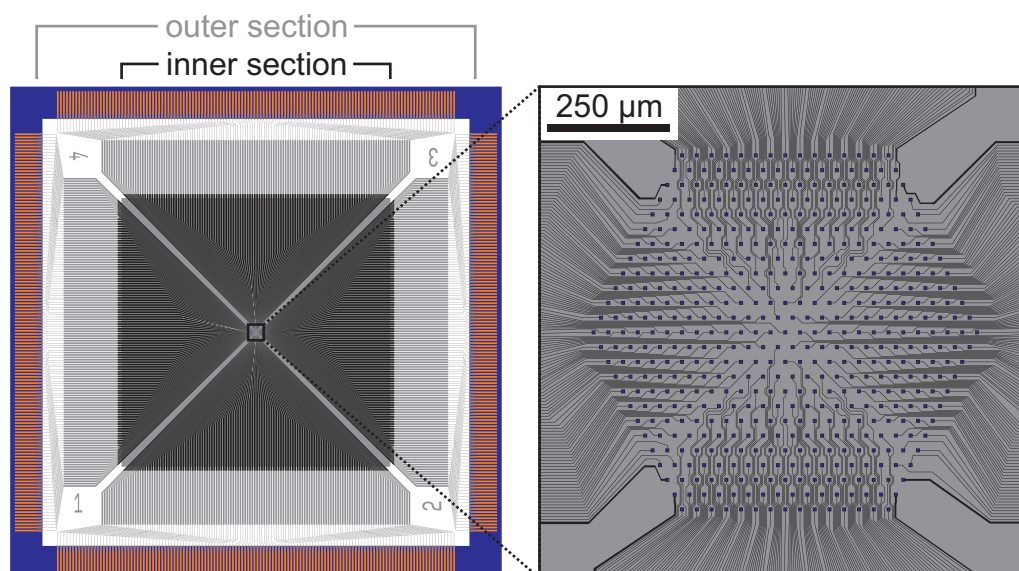


**Figure 7.7:** 519 electrode array with  $30\ \mu\text{m}$  electrode pitch (schematic), central section in detail, electrode tracks are patterned using a two-step process (high resolution inner section and low resolution outer section)

The titanium hard mask previously used in the fabrication [169] was found to be not well-suited. Titanium particulates deposited during sputtering, leading to points of increased layer thickness, which translates to high numbers of shorts between neighbouring tracks after etching (81% shorts measured,  $n = 3$  wafers). In order to reduce this number, a  $\text{SiO}_2$  hardmask (cf. 61 electrode array fabrication) was chosen. This was possible, since the revised fabrication no longer relies on electron beam lithography, which required a reflective substrate to ensure accurate mapping of the surface needed to stitch electron beam field of views together. ITO on glass wafers were consequently coated with  $500\ \text{nm}$  of  $\text{SiO}_2$  (Figure 7.8, **step 1**) using a low-temperature deposition (Table A.13). They were then coated with photoresist and the inner section of the arrays (Figure 7.7, four on each wafer, high resolution,  $1\ \mu\text{m}$  minimum feature size) was patterned by an optical stepper at the Stanford Nanofabrication Facility, USA (SNF, **step 2**). The move away from electron beam lithography helped significantly reduce time and cost of the fabrication. However, the maximum size of the pattern that can be exposed is  $18\ \text{mm} \times 18\ \text{mm}$ , meaning a second (low resolution) lithography step is required to pattern the outer section of the arrays. After the lithography, the  $\text{SiO}_2$  hard

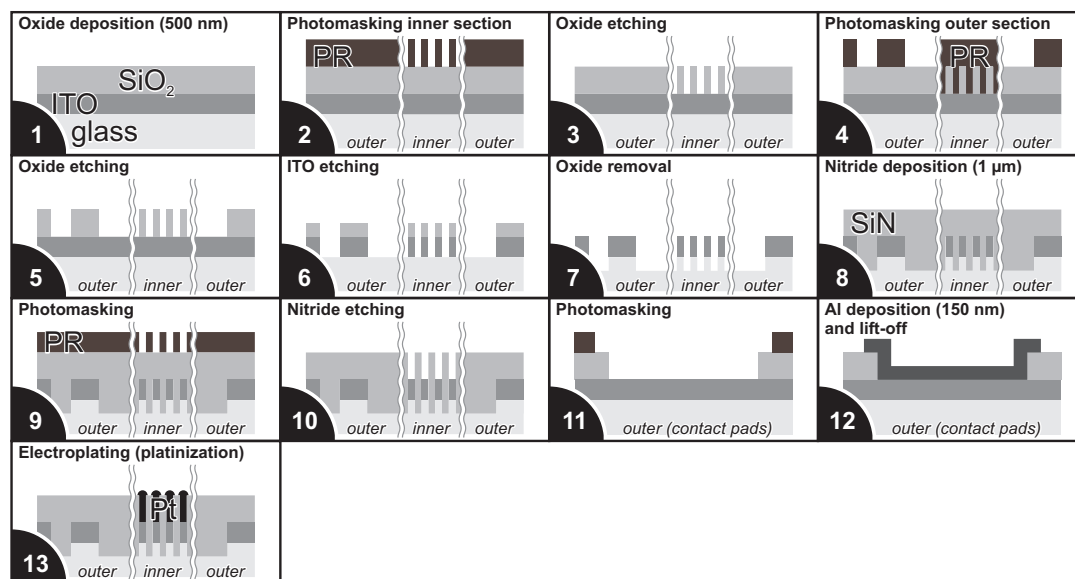


**Figure 7.8:** Fabrication of 61 electrode arrays with 15  $\mu\text{m}$  electrode pitch; fabrication consists of etching of ITO tracks (with  $\text{SiO}_2$  hard mask) and deposition of an insulating layer ( $\text{SiN}_x$ ) followed by etching of vias and electroplating using platinum black

mask was etched (**step 3**). A 5" photomask for creating the outer section of the MEAs was designed and purchased from Delta Mask B.V., The Netherlands. The mask covers the central section of the arrays with a square ( $17.5\text{ mm} \times 17.5\text{ mm}$ ), leading to an overlap between the electrode pattern on the mask and the patterned central section on the wafer of  $250\text{ }\mu\text{m}$  on each side. Using  $2.8\text{ }\mu\text{m}$ -thick S1828® photoresist, the outer section was patterned photolithographically (**step 4**) and the  $\text{SiO}_2$  layer was etched using the same process as for the inner section (**step 5**). The photoresist was removed using acetone and isopropanol and the ITO tracks were etched on the whole arrays (**step 6**), followed by the removal of the remaining  $\text{SiO}_2$  (**step 7**).

This process improved the quality of the arrays, but the level of shorts is still unacceptably high at 15% ( $n = 3$  wafers). In order to achieve acceptable yields in the future (>97% functioning electrodes), two changes will be made. Firstly, the  $\text{SiO}_2$  hardmask will be deposited externally (Rogue Valley Microdevices, USA) to improve film quality. Secondly, wafers with extra high flatness (peak to valley variation across wafer) will be used. The standard product from Thin Film Devices

is specified at  $5\lambda$  (at 632 nm), corresponding to a flatness of  $3.16\ \mu\text{m}$ . Wafers with a flatness of 158 nm ( $\lambda/4$ , the highest quality available) are expected to increase yield by improving the photolithography process using the optical stepper. Another issue has been the wafer thickness, for which 1.1 mm is just at the limit of the lithography tool. Wafers with a thickness of 0.8 mm will therefore be used. The radius of curvature of the wafers must be kept high ( $>30\ \text{m}$ , cf. section A.4.1), requiring low stress in the deposited layer stack. The mask design has been changed to include alignment marks in the ITO pattern of the central section (for aligning the outer section and the vias). As with the 61 electrode arrays, selectively adding a sputtered metal layer over these features could furthermore help improve the poor contrast when aligning.

### 7.3 Readout Hardware

The multi-channel miniature amplifiers introduced in chapter 6 offer a compact, low-cost and easy-to-use alternative to previous custom-built hardware. In order to interface with the miniature amplifiers systems, (RHD2164, Intan Technologies LLC, USA), an adapter board was designed using EAGLE PCB design software [237] (Figure 7.9 A). The fabrication was done by Eurocircuits N.V., Belgium [238]. The adapter board allows insertion of a 61 electrode array in the middle section. It can be clamped with the previously-used standard custom-built clamp (Figure 7.9 B). The contact pads are connected to two Omnetics Nano-Strip connectors (one on each side of the board) mating with the amplifier board.

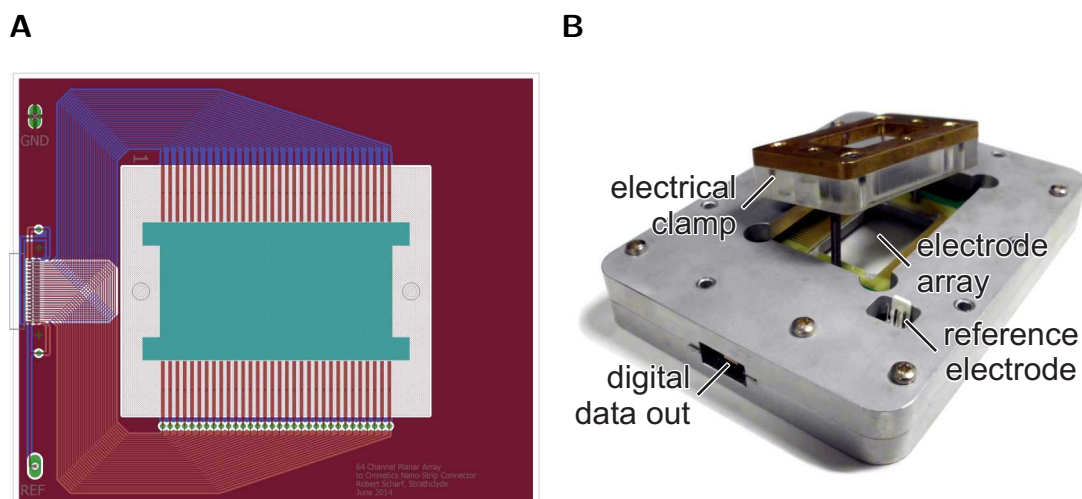


**Figure 7.9:** 61 electrode array adapter board; **A)** Schematic of 61 electrode array adapter for interfacing with a miniature amplifier system (RHD2164, Intan Technologies LLC, USA) using Omnetics Nano-Strip connectors; **B)** Machined array holder

## 7.4 Outlook

In order to study larger sections of the retina at high spatial resolution, a new generation of electrode arrays is needed. Since all electrode tracks need to be routed out individually, the fabrication becomes increasingly difficult. The next sections shows mask designs that have been created, demonstrating scalability of the devices, but bordering on the limits of what can be fabricated with the conventional tools.

### 7.4.1 512 Electrode Arrays, Second Generation

In the second generation of 512 electrode arrays the electrode pitch is reduced from  $30\ \mu\text{m}$  to  $15\ \mu\text{m}$ . Additionally, the mask design is optimised, so that only one mask is required for patterning the ITO tracks (see Figure 7.10). This is achieved by designing the array rotationally symmetric. The mask therefore has to hold just one quarter of the track pattern. The whole image is created by a stepwise shift and rotation of the mask by  $90^\circ$ . The minimum feature size in this design is  $0.5\ \mu\text{m}$  and the diameter of the area covered by the electrodes is  $0.375\ \text{mm}$ . The excellent alignment accuracy of current optical stepper models,

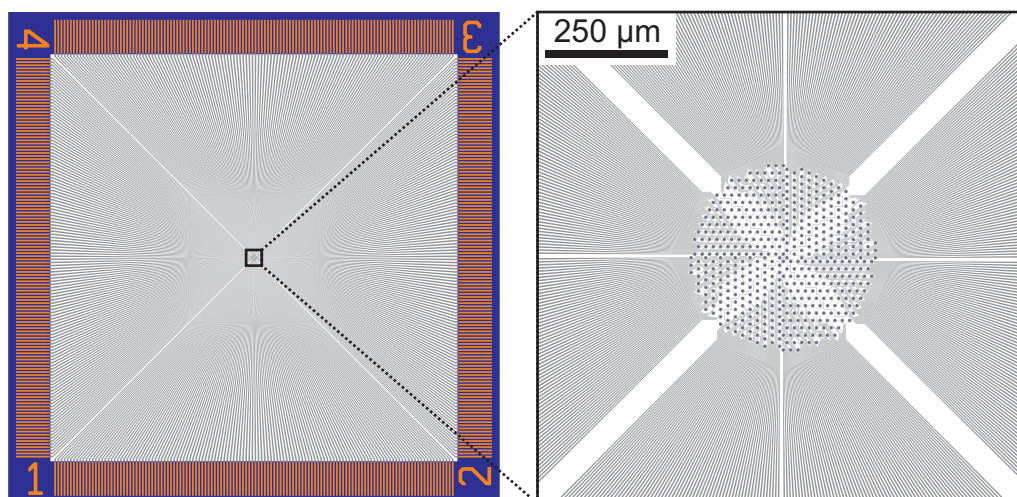


**Figure 7.10:**

High density 512 electrode array (schematic) with  $15\ \mu\text{m}$  electrode pitch, central section in detail

which is in the range of nanometres, means that devices can easily be produced using a stitching method such as the one described here. Multi-layer lithography could be investigated as an alternative for future designs in order to increase the line width and therefore reduce the possibility of breaks in the electrode tracks, but it has its own disadvantages. These include increased layer stress, which might lead to cracks, difficult lithography due to a rough surface topography of underlayers (unless CMP is used), crosstalk between layers, and a decrease in optical transparency.

### 7.4.2 2048 Electrode Arrays

In this configuration the number of electrodes is increased by a factor of four. Once again the design makes use of rotational symmetry (cf. section 7.4.1). Masks are designed for two electrode pitches:  $60\ \mu\text{m}$  and  $30\ \mu\text{m}$ , leading to minimum feature sizes of  $1.5\ \mu\text{m}$  and  $0.75\ \mu\text{m}$ , respectively. The diameter of the area covered by the electrodes is  $3.0\ \text{mm}$  and  $1.5\ \text{mm}$ , respectively (see Figure 7.11).

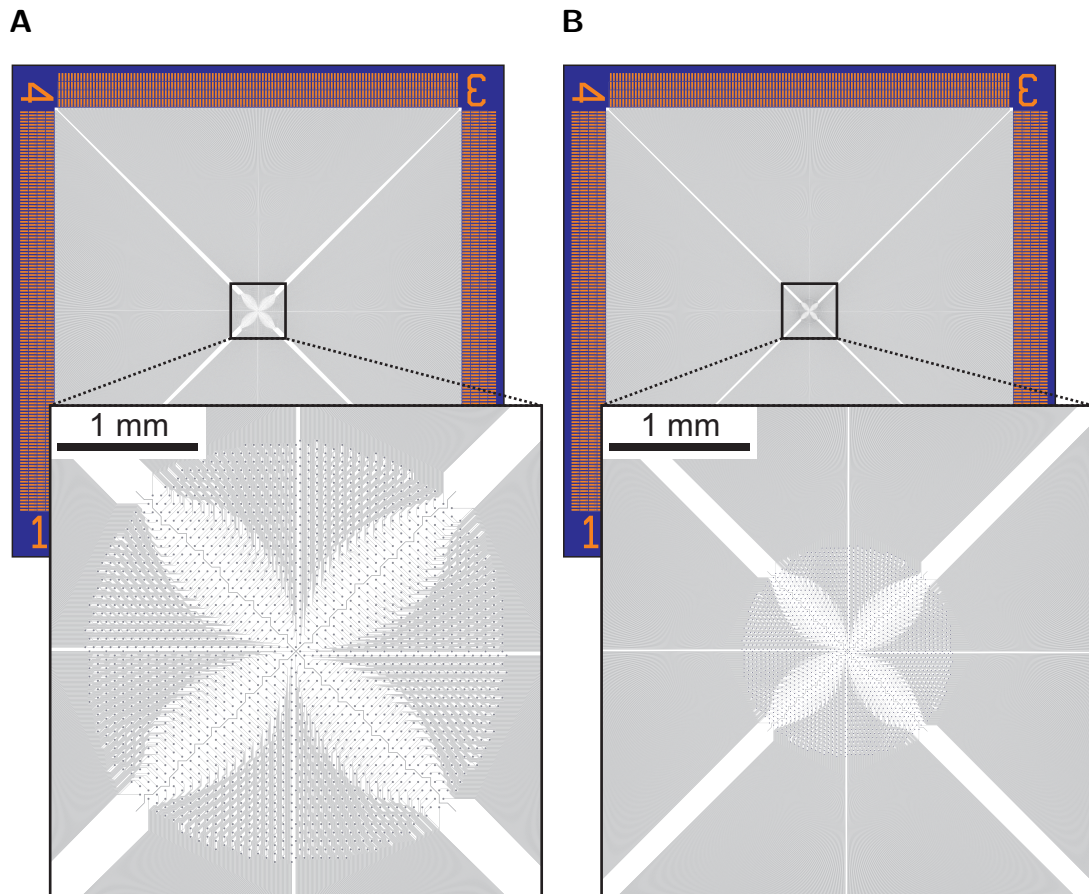


**Figure 7.11:**

High density 2048 electrode arrays (schematic), central section in detail;  
A) 60  $\mu\text{m}$  electrode pitch, B) 30  $\mu\text{m}$  electrode pitch

## 7.5 Conclusion

This chapter covered the adjustment of established planar array designs to allow studies of the retina in regions of high neural packing density. The electrode pitch was reduced by 50 %, approaching the limits of what can be fabricated with the available fabrication tools. New electrode arrays have been designed. High-density electrode integration is essential when trying to record from closely-packed neurons. This concludes the main experimental part. The next section will focus on future developments on the presented devices.

## 8 Future Work

As shown in the previous chapters, optogenetics is a powerful tool for neuroscience and microfabricated devices can be very helpful for optical stimulation and electrical recording. In order to fully exploit the opportunities offered by the biological toolkit, various features can be envisaged, that could be implemented in future devices. Some of these features will be described below.

### 8.1 $\mu$ LED Needle Probes

$\mu$ LED probes have been shown to be a useful tool for neural circuit analysis. Other (or more advanced) experiments require certain modifications. These include wireless, chronic implants, multi-colour stimulation and high-density probes, scaled up in three dimensions.

#### 8.1.1 Wireless Probes

A major goal in neuroscience has been to establish how networks of neurons link to behavioural responses. This has proven extremely challenging due to the complexity of the problem. In order to have the best chance of success, experiments are designed where the measurement equipment has the minimal effect on the behaviour of the animal. In terms of technology development, this often requires wireless power delivery and communication with an implanted probe to allow *in vivo* experiments to be carried out not only in a head-fixed configuration, but also in freely moving animals. Apart from using batteries [285], a range of different methods for energy transfer already exist for optogenetic devices. These include photovoltaics [286] and radio frequency transmission [147, 148].

Kendall Research Systems offers commercial wirelessly-powered current sources that can be combined with any multichannel LED stimulation system (up to four channels) [287]. Limitations arise from weight restrictions. When batteries are used, this also puts a limit on the duration of the experiment.

### 8.1.2 Multi-Colour Probes

A big interest lies in using advanced optogenetic stimulation, where two or more opsins are used in parallel, for example to study how different synapses or pathways interact to encode information in the brain [66], or for bidirectional control of locomotion [62] using excitation and inhibition. Multi-colour probes could be a very useful tool for these purposes. There are several different approaches that can be taken for their fabrication. The probes can either be made monolithically, which means that all the  $\mu$ LEDs initially emit at the same wavelength and some additional processing is required to selectively change the colour on a defined subset. The alternative is to separately fabricate  $\mu$ LEDs of different colour and to then combine them by transferring them to the probe. These options will be examined below.

#### 8.1.2.1 Colour-Tunable LEDs

Colour-tunable  $\mu$ LEDs would be the ideal solution since they allow stimulation using different wavelengths at any fixed location. Colour-tunable devices have been made (among others) by Zhang *et al.*. They describe the fabrication of a device that changes its emission wavelength from 600 nm to 550 nm depending on the current flowing through the LED (0.1 mA to 80 mA) [288]. The drawback of this method is that the colour is linked to a certain brightness through the current density. The only way to get around this is by using pulse width modulation, which is expected to lead to artefacts in the electrophysiological recordings. Furthermore, the wavelength shift is relatively small to be useful. Stacked RGB OLEDs can also offer colour tuning and could be investigated as an alternative.

### 8.1.2.2 Colour Converters

Colour converters are another method for obtaining single-substrate probes capable of multi-colour stimulation. Colour converters are coatings, that absorb up to 100 % of the light emitted by the  $\mu$ LEDs (depending on the thickness) and then re-emit light at a different wavelength. The technology is widely used. Yellow phosphors on blue LEDs are the standard method for producing white LEDs for lighting applications. At present, colour converters have efficiencies that are high enough to be suitable for optogenetic probes (maximum efficiency  $\sim$ 15 %).

The colour-converting films are difficult to pattern lithographically, which is why other methods for selective deposition have to be found. One possible method is ink-jet printing. Commercial ink-jet printers (e.g. FUJIFILM Dimatix DMP-2800 Series) can precisely eject droplets with volumes as low as 1 pl (corresponding to a hemispherical droplet with a diameter of  $\sim$ 16  $\mu$ m). Another approach makes use of the  $\mu$ LED light sources themselves (Figure 8.1 A).

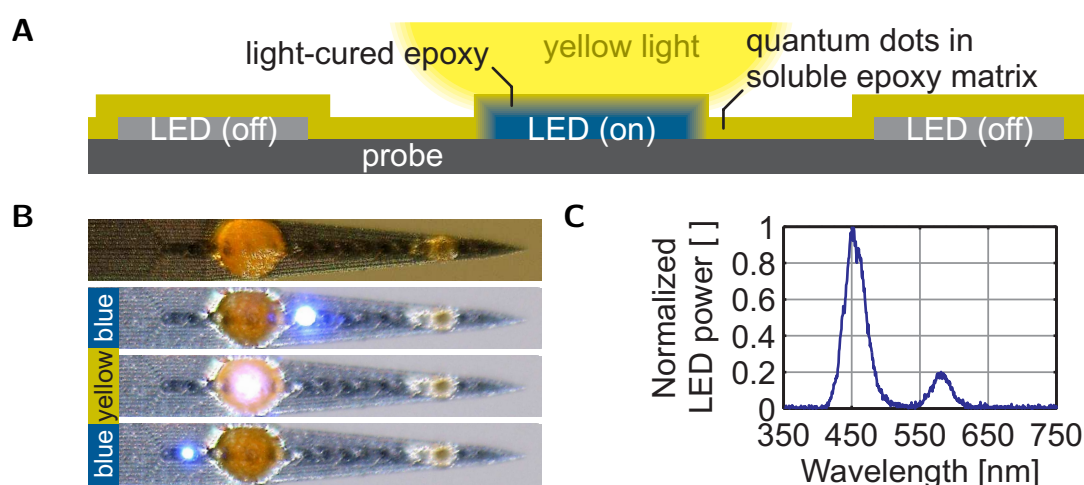


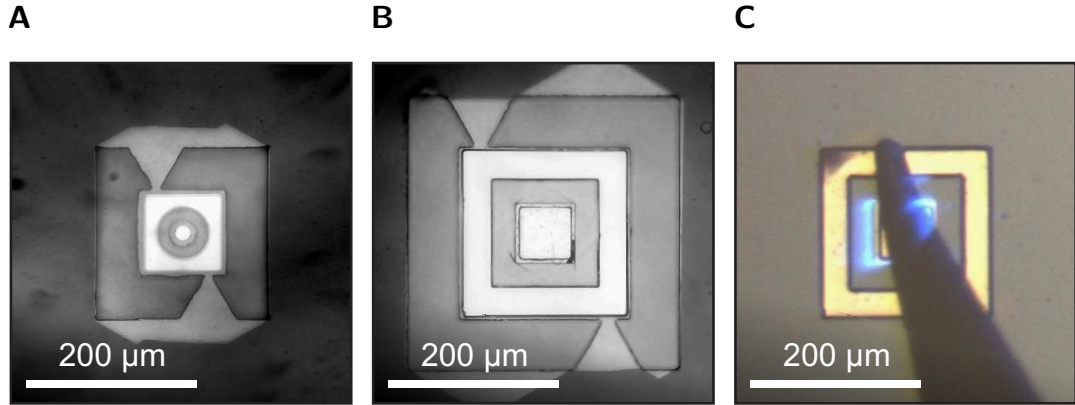
**Figure 8.1:**

Selective deposition of colour converters on  $\mu$ LED probes; **A)** Schematic; quantum dots embedded in a epoxy matrix act as colour converters; after dip-coating the probe, the epoxy can be cured by light emitted from individually selected  $\mu$ LEDs and their quantum dot coating; uncured epoxy can then be removed using solvents; **B)** Image of a processed probe, blue and yellow  $\mu$ LEDs turned on; **C)** Emission spectrum of a  $\mu$ LED after deposition of the colour converter

By using a light-curable epoxy mixed with the active material, the probes can be dip-coated completely, followed by a selective curing using the  $\mu$ LEDs. To demonstrate the feasibility of the process, colloidal quantum dots (alloyed CdSe/ZnS, 5.5-6.5 nm diameter, Cytodiagnosics, Canada) were mixed in an epoxy (E131, Ossila, UK) using a concentration of 100 mg/ml. A  $\mu$ LED probe was immersed in the solution and selected  $\mu$ LEDs were turned on for  $\sim$ 4 min using at an irradiance of  $\sim$ 250 mW/mm<sup>2</sup>, which cured the epoxy. Excess epoxy was removed using toluene. The performance of the resulting device is shown in Figure 8.1 B (image of the multi-colour device) and Figure 8.1 C (emission spectrum). As apparent, the quantum dot concentration was too low for full colour conversion. Higher concentrations were also used, but led to the epoxy becoming incurable. Further experiments will have to be carried out. Using different solvents, fully absorbing layers with thicknesses of 100s of nanometres can currently be fabricated at the institute. A wide variety of colours could potentially be produced this way, opening up possibilities for advanced optogenetic control.

### 8.1.2.3 Transfer Printing

In order to obtain more efficient devices, a technique called micro transfer printing ( $\mu$ TP) can be used. One example of transfer-printable  $\mu$ LEDs fabricated within the scope of this thesis is shown in Figure 8.2 (additional information in section A.3). Transfer printing allows the separate fabrication of thin microdevices (in this case  $\mu$ LEDs) and a target substrate (in this case micro-needles). Using a stamp made of a polymer such as polydimethylsiloxane (PDMS), the  $\mu$ LEDs can be picked up. They are then transferred to the target substrate using a micro- or nano-positioner. The technology makes use of the different adhesion strength of the printable device to the elastomer stamp and the target substrate depending on the stamp velocity.  $\mu$ TP was first developed by Rogers *et al.* [289] and then commercialized by X-Celeprint, now offering transfer printing of up to 48,000 devices with an accuracy of 1.5  $\mu$ m using a highly automated process [290]). The technology has also been adopted at the Institute of Photonics and refined to allow nanoscale positioning [291] of 50  $\mu$ m wide  $\mu$ LEDs [292]. When moving to

**Figure 8.2:**

Transfer-printable  $\mu$ LEDs attached to the substrate by narrow ( $12\ \mu\text{m}$ ) anchors, contacted with a gold anode and a surrounding cathode; **A**)  $100\ \mu\text{m}$  wide square-shaped  $\mu$ LED,  $30\ \mu\text{m}$ -diameter circular mesa; **B**)  $200\ \mu\text{m}$  wide square-shaped  $\mu$ LED,  $65\ \mu\text{m}$ -wide square mesa; **C**) Device from panel B probed during fabrication, light is mainly emitted through the back side

other substrates, on which LED epistructures cannot be grown, transfer printing becomes necessary. The move is useful for improving thermal management, as described in the following section. Preliminary work on neural probes been done at the Institute of Photonics [293]. Others have also recently begun working on needle probes based on LED transfer technology [294].

### 8.1.3 Thermal Management

As shown in section 4.3.2, the thermal properties of the silicon substrate limit the operating range of the  $\mu$ LED devices. Highly heat conductive substrates, such as diamond, can be used to enhance this range. With a thermal conductivity of  $990\ \text{W}/\text{m}\cdot\text{K}$  (compared to  $130\ \text{W}/\text{m}\cdot\text{K}$  for silicon, see Table 8.1), higher power operation

	Silicon	Diamond
Density $\rho$ [ $\text{kg}/\text{m}^3$ ]	2329	3515
Heat capacity $C_P$ [ $\text{J}/\text{kg}\cdot\text{K}$ ]	700	520
Thermal conductivity $k$ [ $\text{W}/\text{m}\cdot\text{K}$ ]	130	990

**Table 8.1:**

Thermal properties of silicon and diamond (from COMSOL materials library)

becomes possible allowing light penetration further into the tissue. Diamonds are commercially available either on silicon substrates [295] or as thin (i.e. 50  $\mu\text{m}$ ) free-standing platelets or membranes with diameters of up to 80  $\mu\text{m}$  [296]. These platelets can be processed after capillary bonding them onto a silicon carrier wafer. Graphene [297] based coatings have also been shown to improve thermal conductivity significantly [298] and could be investigated.

As apparent in the thermal simulation results, temperatures along  $\mu$ LEDs close to the probe tip are considerably higher compared to those further down on the shank (Figure 4.9 B). To overcome this problem, the probe shanks in future designs can be extended so that heat from all LEDs can be conducted away from the source. There is a trade-off between shank extension and tissue damage, which has to be considered in the design.

Thermal restrictions can be eased further by employing other opsins [66, 76], which are more sensitive than commonly used ChR2 and allow activation with irradiances that are orders of magnitude lower. This means that the peak irradiances needed to excite a certain volume also drop by orders of magnitude. For example, to replicate the results from chapter 5 using the opsin Chronos, we would require only 15  $\text{mW}/\text{mm}^2$  (compared to 150  $\text{mW}/\text{mm}^2$ ) to excite the same volume and the resulting reduction in electrical power means almost any combination of pulse duration and duty cycle keeps the peak temperature below 0.5°C (cf. Figure 4.10). New opsins will open up new possibilities for complex, massively parallel optogenetic stimulation patterns using multiple  $\mu$ LEDs.

### 8.1.4 LED Addressing

Apart from opening up the possibility to employ improved heat-sinks, the move to transfer-printed  $\mu$ LEDs also allows the use of a variety of advanced addressing mechanisms. Since the transfer-printed  $\mu$ LEDs do not have to have a common cathode, matrix addressing becomes available. This can dramatically reduce the number of tracks needed, which would otherwise soon become a bottleneck when scaling up the number of stimulation sites (see Table 8.2). Monolithic devices could also be addressed this way by etching off the p-GaN and thereby

insulating the mesas, but a highly resistive (silicon) substrate is needed. Using charlieplexing [299], which makes use of the fact that current flow in LEDs can only be in one direction, an even higher number of  $\mu$ LEDs can be addressed using very few tracks. This could be very helpful particularly when using hard-to-pattern flexible substrates. Figure 8.3 shows a possible future design making use of matrix addressing. By having 16 tracks on each shank (as on the devices fabricated before, introduced in chapter 4), up to 64  $\mu$ LEDs per shank could be controlled individually. When multiple shanks are used, the number of bond pads required can be kept low (e.g. 48 pads for 576  $\mu$ LEDs) by also addressing the shanks in a

	Number of tracks								
	1	2	4	8	16	32	64	128	$n$
Common cathode	0	1	3	7	15	31	63	127	$n - 1$
Matrix addressing	0	1	4	16	64	256	1024	4096	$\lfloor n/2 \rfloor \cdot \lceil n/2 \rceil$
Charlieplexing	0	2	12	56	240	992	4032	16256	$n^2 - n$

**Table 8.2:**

LED addressing schemes; number of addressable LEDs using a certain number of tracks and wiring methods; multiplexing can help overcome fabrication problems arising from standard addressing

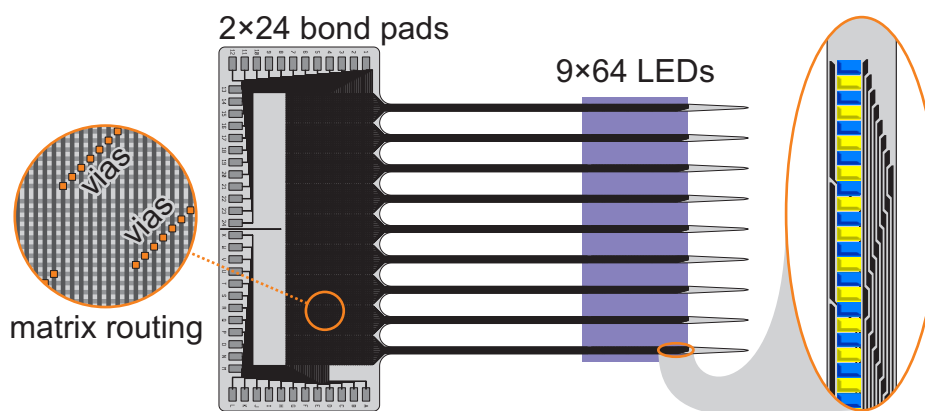


**Figure 8.3:**

Nine-shank multiplexed probe containing 576  $\mu$ LEDs (schematic); tracks can be routed in a way that allows to have 64  $\mu$ LEDs on each shank (controlled by 16 (8+8) tracks, keeping the shank width small), matrix routing is detailed, showing two perpendicular layers of tracks connected through vias; a total number of 48 (24+24) contact pads is needed on the far end of the probe; the substrate can be diamond for better heat transfer and the  $\mu$ LEDs can have multiple colours (blue/yellow shown)

matrix fashion. As shown, this routing can be done on the far end of the probe. Matrix addressing has the problem that it reduces flexibility in the biological experiments. For example in some cases it might be necessary to simultaneously activate certain layers in the cortex, whereas with matrix addressing the possible combinations of LEDs are strongly limited. Fast switching between LEDs could instead be used, but this also strongly increases crosstalk artefacts.

A further alternative is to include active addressing circuitry including current sources/sinks on the silicon shank.  $\mu$ LEDs could then be transfer-printed directly onto their dedicated drivers. The advantage of this approach is the ability to turn on several  $\mu$ LEDs at a time without the need for fast switching. One limitation is the need to use silicon as a substrate to be able to use commercial semiconductor foundry services. This removes the possibility of using substrates, such as diamond, to mitigate thermal issues.

### 8.1.5 3D $\mu$ LED Arrays

Chip stacking is a standard process in industry now [300] (Figure 8.4 A). Therefore it is expected to be relatively straightforward to produce three-dimensional devices based on the probes that have already been fabricated. Figures 8.4 B, C show how chip stacking could be used. Several 2D multi-shank arrays could be stacked on top of each other separated by a spacer (photomasks have been made for producing the spacers, see Figure A.3). Using thin (e.g. 0.5 mm) double-sided

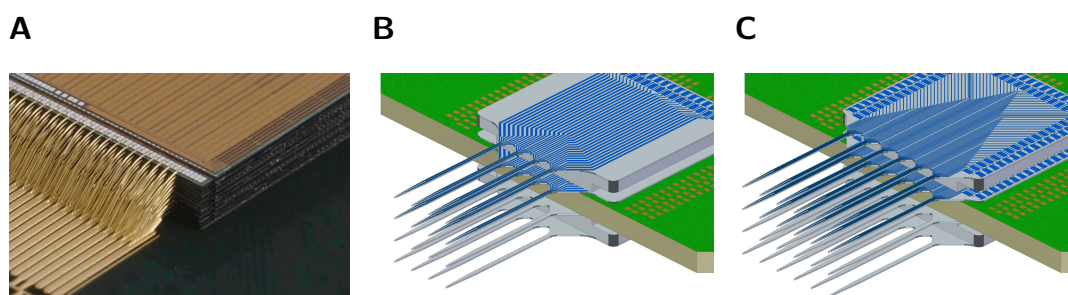


**Figure 8.4:**

3D chip stacking; **A)** Example from 2007: stack of 20 chips, each with a thickness of  $30\ \mu\text{m}$  [301]; **B, C)** Multi-shank  $\mu$ LED arrays (schematic), probes die-bonded to both sides of a thin double-sided PCB and stacked, separated by a spacer, **B)** 16-shank 3D device ( $4\times 4$  shanks), **C)** 24-shank 3D device ( $4\times 6$  shanks)

PCBs, probes could be placed on both sides with the PCB itself acting as a spacer. Since the individual chips can be electrically isolated, a multitude with e.g. 384 ( $4 \times 96$ )  $\mu$ LEDs could be controlled easily using multiplexing between chips and just minor modifications to existing control hardware (include four current sinks).

### 8.1.6 Further Improvements

**Passivation** The passivation could be improved to allow long-term use. Oxide/nitride stacks [302, p. 211] or silicon carbide [281] could be used as a stable diffusion barrier to improve chronic *in vivo* stability of the devices.

**Micro-Lensing** Micro-lenses could be utilized for focusing the light emitted by the  $\mu$ LEDs. The technology has been developed at the Institute of Photonics in the past [303]. The diameter of the lenses can be close to the diameter of the  $\mu$ LEDs, but the thickness of the probes will increase. Furthermore, the separate fabrication of micro-lenses with the required shape using suitable materials and integration with the probes is expected to be difficult.

**LED driver** The LED driver can potentially be improved by using a circuit based on an operational amplifier, which is expected to give better control over the current over a wider range. Since only one current source is required when multiplexing, a simple circuit (as shown in Figure A.16) could be realized using only few components.

## 8.2 $\mu$ LED Probes *In Vivo*

Using the high-density two-dimensional  $\mu$ LED arrays, one interesting feature, that could be studied, is the receptive field of a neuron. Receptive field mapping has been carried out extensively for retinal ganglion cells in the past [33]. Using optogenetics and 96-Channel hex-shank probes, similar experiments can be conceived in the cortex (shown in Figure 8.5).

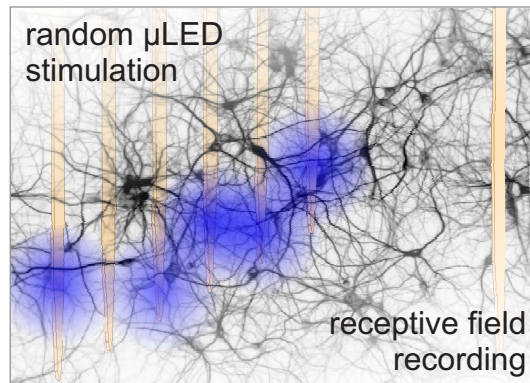


**Figure 8.5:**

Optogenetic receptive field mapping *in vivo*; a two-dimensional  $\mu$ LED array is implanted alongside a single-shank recording probe; receptive fields can be studied by randomly switching through all  $\mu$ LED channels; non-correlated neuronal firing averages out, whereas correlated firing can be detected

## 8.3 Recording $\mu$ LED Needle Probes

Similar improvements to the ones described before can also be made to the recording  $\mu$ LED probes. Two future directions are outlined below. These are wireless probes and on-chip electronics.

### 8.3.1 Wireless Probes

As mentioned in chapter 6, wireless probes are very useful for the neuroscience community. Probes that offer both stimulation and recording capabilities, however, pose further challenges to the interface due to the very high amount of electrophysiological data produced. One option would be to save all data locally and only read it out after the experiment. This, however, would provide no means of direct feedback of the recording quality. A wireless interface, on the other hand, would have to have a high bandwidth. Assuming a sampling rate of 20 kHz and a resolution of 12 bit, the interface needs to be able to transfer 240 kbps per channel, or 7.68 Mbps using 32 channels. One possibility to transfer this data is by using an optical link consisting of a transmitting LED and a receiving photodiode (visible light communication, the basis of Li-Fi technology [304]). This is currently under

development. The power consumption in addition to the power consumed by the  $\mu$ LED probe (depending on irradiance required) is expected to be around 40 mW. This is to power a 32-channel amplifier ( $\sim 18.5$  mW), an LED for transmitting the digitized data stream ( $\sim 6.5$  mW) and a microcontroller unit ( $\sim 15$  mW).

#### 8.3.2 Electronics On-Chip

Including the electronics for  $\mu$ LED control (current sources) and electrode readout (amplifier and serializer) onto the probe will be a necessary move when scaling up the number of stimulation sites and especially recording sites. Once again, this would entail the move to transfer-printed  $\mu$ LEDs, so that all the circuitry could be fabricated using conventional CMOS processes at a standard foundry. One limiting factor in this case is the power consumption of the integrated circuits. Assuming a PCB can dissipate heat at a rate of  $10 \text{ W/K}\cdot\text{m}^2$  [305, p. 348] and it has a size of  $1 \text{ cm}^2$ , the PCB would be able to dissipate (on two sides)  $2 \text{ mW/K}$ . If the PCB is allowed to heat from room temperature to body temperature ( $\sim 10^\circ\text{C}$  increase), the electrical power of the integrated circuitry will have to be below 20 mW (100 mW if a  $5 \text{ cm}^2$  PCB is considered).

#### 8.3.3 3D LED / Electrode Arrays

As detailed for the (stimulation only)  $\mu$ LED needle probes (section 8.1.5), advanced devices incorporating recording electrodes can be created by stacking of two or more chips. In this way, three dimensional arrays of integrated  $\mu$ LED/electrode probes could be made as shown in Figure 8.6 A (e.g. using four of device  $4 \times 8 + 16L(S)$ ). Electrode-only probes (i.e device  $6 \times 0 + 16L(S)$ ) could also be combined with  $\mu$ LED-only probes (i.e device  $6 \times 16(S)$ ) to produce devices as shown in Figure 8.6 B and similar to what was used in *in vivo* experiments described in chapter 5. Additional effort will have to be put into designing matching high-density PCBs that contain demultiplexer switching circuitry and several amplifier chips (cf. Berényi *et al.* [188]).

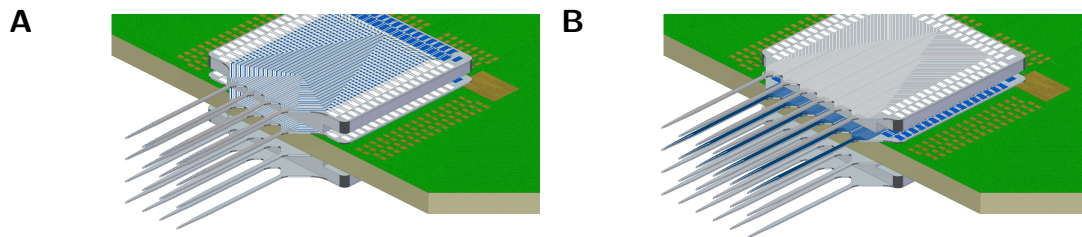


**Figure 8.6:** 3D multi-shank  $\mu$ LED/electrode arrays (schematic); **A)** 16-shank 3D device ( $4 \times 4$  shanks); **B)** 24-shank 3D device ( $4 \times 6$  shanks)

## 8.4 Planar *In Vitro* Electrode Arrays

Next generation high-density (cf. section 7.1) and very high-density (cf. sections 7.4.1 and 7.4.2) transparent planar electrode arrays for *in vitro* use have been designed.

The impact of the reduced electrode pitch on the neural recordings will now be evaluated. For the  $15\ \mu\text{m}$ -pitch 61 electrode arrays this can be done by spatial undersampling (Figure 8.7). Selectively masking a part of the electrodes produces arrays with equivalent pitches of  $30\ \mu\text{m}$  and  $60\ \mu\text{m}$ , respectively, just like in previously-fabricated lower-density arrays.

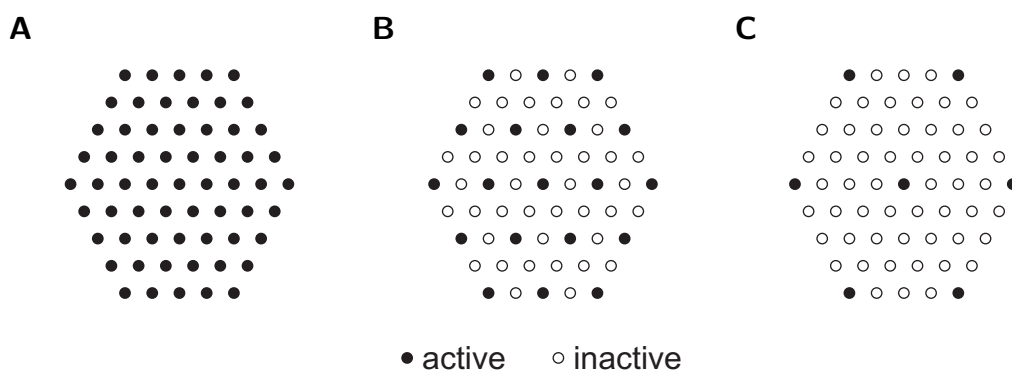


**Figure 8.7:** Spatial undersampling of electrophysiological data recorded using a 61 electrode array ( $15\ \mu\text{m}$  pitch), active channels in black; **A)** All 61 channels active ( $15\ \mu\text{m}$  pitch); **B)** 19 out of 61 channels active (every 2<sup>nd</sup>, equivalent to  $30\ \mu\text{m}$  pitch); **C)** 7 out of 61 channels active (every 4<sup>th</sup>, equivalent to  $60\ \mu\text{m}$  pitch)

One thing to note is that when reducing the electrode pitch, the ratio of black space (platinized electrodes)  $r_{\text{black}}$  on the array increases. It can be calculated as

$$r_{\text{black}} = \frac{\pi d_{\text{elec}}^2}{4p_{\text{elec}}^2} \quad (8.1)$$

with the electrode diameter  $d_{\text{elec}}$  and the electrode pitch  $p_{\text{elec}}$ . While the ratio is only 0.5% at a 60  $\mu\text{m}$  pitch, this number increases to 8.7% when the pitch is reduced to 15  $\mu\text{m}$ . Conductive hydrogels (e.g. PEDOT [110]) could be investigated as alternative materials to maintain transparency.

## 9 Conclusion

The brain is a tremendously complex system with its  $10^{11}$  neurons and  $10^{15}$  synapses. Optogenetics, can be a helpful tool to untangle the brain's neural circuits and understand the underlying functional mechanisms by allowing selective light-mediated control of neural subtypes. Further improvements in the biological constructs are constantly being made, leading to higher light-sensitivity and more discrete excitation spectra. The biological tools by themselves, however, are not sufficient. Disruptive advances are needed in the field of microsystems engineering to non-destructively interface with the brain's building blocks for both stimulation and recording. In this work several different optoelectronic microdevices were introduced that will hopefully prove useful on the way to developing a deeper understanding of the functioning of the brain. The new devices focus on different parts of the brain that can be studied *in vivo* and *in vitro*.

Implantable  $\mu$ LED probes were developed, fabricated, characterized and tested *in vivo* in the mouse cortex. Unlike many other devices (LED- or fibre-based), the presented probes allow optical stimulation of deep brain structures in a site-specific fashion. The density and coverage of the the light sources is higher than in competing systems (multipoint-emitting optical fibres [156, 157] and integrated GaN-on-Si  $\mu$ LED probes [202]) and previously fabricated sapphire-based  $\mu$ LED probes (McAlinden *et al.* [133, 160]).  $\mu$ LEDs have been shown to be good light sources for multi-point stimulation due to their relatively low implantation damage (cf. waveguide-based approaches, Zorzos *et al.* [154, 155]) and their scalability (unlike fibre-based technology).  $\mu$ LEDs have a sharp emission profile and light output that can be tuned over a wide optical power range. Notably, thermal properties have also been shown to be at acceptable levels, with a  $0.5^{\circ}\text{C}$  increase in brain temperature still allowing optogenetic stimulation of neurons at relevant

frequencies and pulse widths. While waveguide-based probes suffer from incoupling, outcoupling and transmission losses, in  $\mu$ LED devices the outcoupling of the light is the only concern. To address this, a thin metal film could be used as a mirror which directs light out through the LED's front surface. This technique, however, can only be employed easily when working with transfer-printed membrane-like  $\mu$ LEDs. In the case of GaN-on-Si, a lot of development would have to go into changing the growth process of the material. One other measure that could be taken is to create a roughened  $\mu$ LED surface – for example by wet etching – to counteract internal reflections.  $\mu$ LEDs can be the basis of many future advancements, several of which have been sketched out.  $\mu$ LEDs could be used to further scale up the number of light sources and allow advanced experiments including combined excitation and silencing of neurons, as well as those involving chronic implantation and freely behaving animals. Behavioural experiments seem relatively straightforward with  $\mu$ LED-based devices, compared to laser-based probes due to the compactness of the setup. However, the long-term tissue reactions still have to be studied.

Although significantly large neural populations can be excited using  $\mu$ LED-based implantable probes, the maximum tissue volume that can be targeted at high spatiotemporal resolution is still limited. Depending on the experiment, multiphoton techniques could offer more flexibility. Optogenetic perturbations can be carried out, superficially covering the whole brain. Behavioural experiments, however, are limited due to the to the complex setup and the maximum light penetration depth is a problem that the  $\mu$ LED probes presented here can overcome. Since a large interest lies in getting a deep understanding of small subsystems of the brain, these probes remain a very useful tool. A different, very scalable technique, that aims to combine the invasive and non-invasive approaches is currently being developed by Chamanzar *et al.*: tetherless microdevices that can be positioned at various locations in the brain, absorb light at wavelengths that can propagate well through tissue, and emit at wavelength relevant for optogenetics [306], similar to neural dust [307, 308]. Results from future experiments remain to be seen.

Recording probes consisting of linearly arrayed electrodes on a needle-shaped silicon substrate are a standard tool used in neuroscience experiments. This concept can be integrated into the design of the  $\mu$ LED devices, as demonstrated by first fabrication tests. When state-of-the-art microfabrication techniques are used, high-density tetrode structures fully covering large distances could also be created, allowing the parallel recording of large populations at the resolution of individual neurons. Competing probes use a single-layer process (Wu *et al.* [202]), which means the number of stimulation and recording sites is very limited. Also, integrating high-density electrodes onto waveguide probes is problematic, since the waveguides occupy a lot of space and require high-density lithography. There is also no straightforward method for incorporating electrodes onto multipoint-emitting optical fibres [156, 157], whose fabrication is based on standard methods. Thermally drawn fibres are one approach that can include electrodes. Depth-specificity, however, still remains to be shown. The approach taken here is therefore expected to give very positive results in the future. It is competing with optical methods, which are getting better very rapidly [99], but again are limited by a maximum depth and complicated setup.

In order to demonstrate how high electrode density is necessary to understand highly complex wiring diagrams in certain neural systems, a different type of device was developed in the scope of this thesis: electrode arrays for *in vitro* monitoring of retinal ganglion cell responses to optogenetic stimulation of retinal neurons. For this, several new fabrication processes were examined and employed. New designs with four times the resolution of previous devices were created and devices are being fabricated. It will be interesting to see how the recording devices perform in biological experiments in the future. It is expected that spike sorting will be facilitated dramatically, allowing good identification of single neurons and observation of their individual electrophysiological properties.

# A Appendix

## A.1 Microfabrication Recipes

This section lists recipes used for the microfabrication of the devices that have been introduced. The recipes are valid for the very tools used in this work.

### A.1.1 RIE 1 Recipes

**Note** both recipes can severely burn photoresist thicker than S1818®

		<b>iopsio2.rec</b>	<b>mlesio2.rec</b>	
Process pressure		0.03	0.03	Torr
Fluoroform (CHF <sub>3</sub> ) flow		5	5	sccm
Argon (Ar) flow		15	15	sccm
RF forward power		200	120	W
Etch rate	SiO <sub>2</sub>	~39	~23	nm/min
	glass	~9		
	ITO	~0.3		
	SiN	~21	~15	

**Table A.1:** RIE 1 silicon dioxide etch recipes; **iopsio2**: standard etch; **mlesio2**: reduced power etch

		<b>SiN-RS.rec</b>	
Process pressure		0.03	Torr
Fluoroform (CHF <sub>3</sub> ) flow		5	sccm
Oxygen (O <sub>2</sub> ) flow		10	sccm
Methane (CH <sub>4</sub> ) flow		20	sccm
RF forward power		75	W
Etch rate	SiN	~49	nm/min
	photoresist	~48	nm/min

**Table A.2:** RIE 1 silicon nitride etch recipe

		<b>paryl-RS.rec</b>	
Process pressure		0.08	Torr
Oxygen (O <sub>2</sub> ) flow		50	sccm
RF forward power		200	W
Etch rate	parylene C photoresist	~380 *	nm/min

\* etch rate of small features is lower by ~20 %

**Table A.3:** RIE 1 parylene C etch recipe

		<b>o2ash.rec</b>	<b>o2clean.rec</b>	
Process pressure		0.05	0.1	Torr
Oxygen (O <sub>2</sub> ) flow		30	50	sccm
RF forward power		120	200	W

**Table A.4:** RIE 1 oxygen clean; **o2ash**: wafer descum; **o2clean**: chamber clean

### A.1.2 RIE 2 Recipes

		<b>niautest.rec</b>	
Argon (Ar) flow		40	sccm
Oxygen (O <sub>2</sub> ) flow		4	sccm
Process pressure		0.045	Torr
RF forward power		300	W
Etch rate (Ni/Au)		>7.5	nm/min

**Table A.5:** RIE 2 nickel/gold (Ni/Au) current spreading metal layer etch

### A.1.3 ICP 1 Recipes

		AlRobert.set	
Chlorine (Cl <sub>2</sub> ) flow		4	sccm
Boron trichloride (BCl <sub>3</sub> ) flow		16	sccm
Process pressure		0.02	Torr
RF mode		platen only	
Platen power		50	W
Etch rate	Ti/Al	~550/2.75 *	nm/min
	SiO <sub>2</sub>	~6.6	

\* etch rate is not uniform, a longer etch is required to etch through any surface oxide layer, etch rates for pure titanium and aluminium have not been tested

**Table A.6:** ICP 1 titanium/aluminium (Ti/Al) etch (quick and low-power with high selectivity)

		ITOetch2.set	
Argon (Ar) flow		6	sccm
Chlorine (Cl <sub>2</sub> ) flow		4	sccm
Boron trichloride (BCl <sub>3</sub> ) flow		16	sccm
Process pressure		0.02	Torr
RF mode		simultaneous	
Platen power		100	W
Coil power		600	W
Etch rate	ITO	~21	nm/min
	SiO <sub>2</sub>	~22	

**Table A.7:** ICP 1 indium tin oxide (ITO) etch

### A.1.4 ICP 2 Recipes

	GaN_David	
Chlorine (Cl <sub>2</sub> ) flow	50	sccm
Process pressure	0.005	Torr
Coil power	700	W
Platen power	300	W
Etch rate (GaN)	~1 000	nm/min

**Table A.8:** ICP 2 gallium nitride (GaN) etch

### A.1.5 DRIE Recipes

**Note** the DRIE etch tool is located at Glasgow University

	hptest4	
Etch rate (Si)	~4.4	nm/min

**Table A.9:** Deep reactive ion etch (Bosch process) for silicon (Si)

### A.1.6 RTA Recipes

	recipe 3 (Ni/Au)	recipe 5 (Pd)
Gas used	air	N <sub>2</sub>
Temperature sequence	0, 90, 315, 510, 510, 315, 90, 0	0, 95, 300, 300, 95, 0 °C
Time sequence	30, 30, 30, 30, 30, 30, 30	60, 40, 180, 40, 40 s

**Table A.10:** RTA nickel/gold (Ni/Au) and Palladium (Pd) on gallium nitride (GaN) annealing recipes

### A.1.7 Sputter Coater Recipes

	Ti	Al	Au	
Current	6	6	4	A
Deposition rate	17.5	22	125	nm/min

**Table A.11:** Sputter coater metal deposition recipes (titanium, aluminium, gold)

### A.1.8 Parylene Coater Recipes

**Note** moisten the chamber walls with ~1 ml of A-174 silane (gamma-methacryloxypropyltrimethoxy silane) prior to deposition to improve parylene adhesion to the substrate

		Parylene C	Parylene N	
Deposition rate		~5	~0.75	μm/h
Dimer required	small samples	~1.36	?	g/μm
	large samples	$\sim 1.36 \cdot \left(1 + \frac{A}{5800 \text{ cm}^2}\right)^*$	?	

\* with the sample surface area  $A$  in  $\text{cm}^2$  (e.g.  $162 \text{ cm}^2$  for a 4" wafer)

**Table A.12:** SCS coater parylene deposition recipes (parylene C, parylene N)

### A.1.9 PECVD Recipes

	oxide200.rec	lowsio2d.rec	
Silane (SiH <sub>4</sub> ) flow	170	1000	sccm
Nitrous oxide (N <sub>2</sub> O) flow	710	500	sccm
HF forward power	70	70	W
RF mode	continuous	continuous	
RF first pulse	HF	HF	
Process pressure	1	0.5	Torr
Substrate temperature	300	100	°C
Deposition rate (SiO <sub>2</sub> )	~36	~18-19	nm/min

**Table A.13:** PECVD silicon dioxide deposition recipes; **oxide200**: standard deposition; **lowsio2d**: low temperature deposition

	nhfreepu.rec	
Silane (SiH <sub>4</sub> ) flow	40	sccm
Nitrogen (N <sub>2</sub> ) flow	1250	sccm
HF forward power	200	W
LF power	20	W
RF mode	pulsed	
RF first pulse	HF	
HF pulse time	13	s
LF pulse time	7	s
Process pressure	0.65	Torr
Substrate temperature	100-300	°C
Deposition rate (SiO <sub>x</sub> N <sub>y</sub> )	100°C	~9.3
	300°C	~7

**Table A.14:** PECVD silicon oxynitride deposition recipe

## A.2 $\mu$ LED Needle Probes

### A.2.1 Device Naming

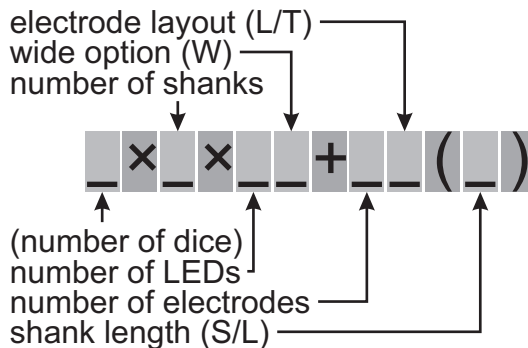


**Figure A.1:** Explanation of device codes for fabricated  $\mu$ LED probes and integrated recording devices

### A.2.2 Fabrication

#### Mask 1

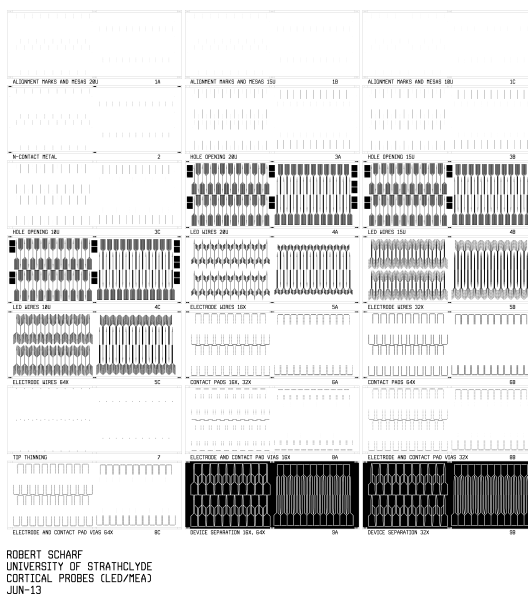


**Figure A.2:** Photomasks for LED probe fabrication (Set 1), mask size is 5", dimensions of each submask are 29.5 mm  $\times$  11.6 mm

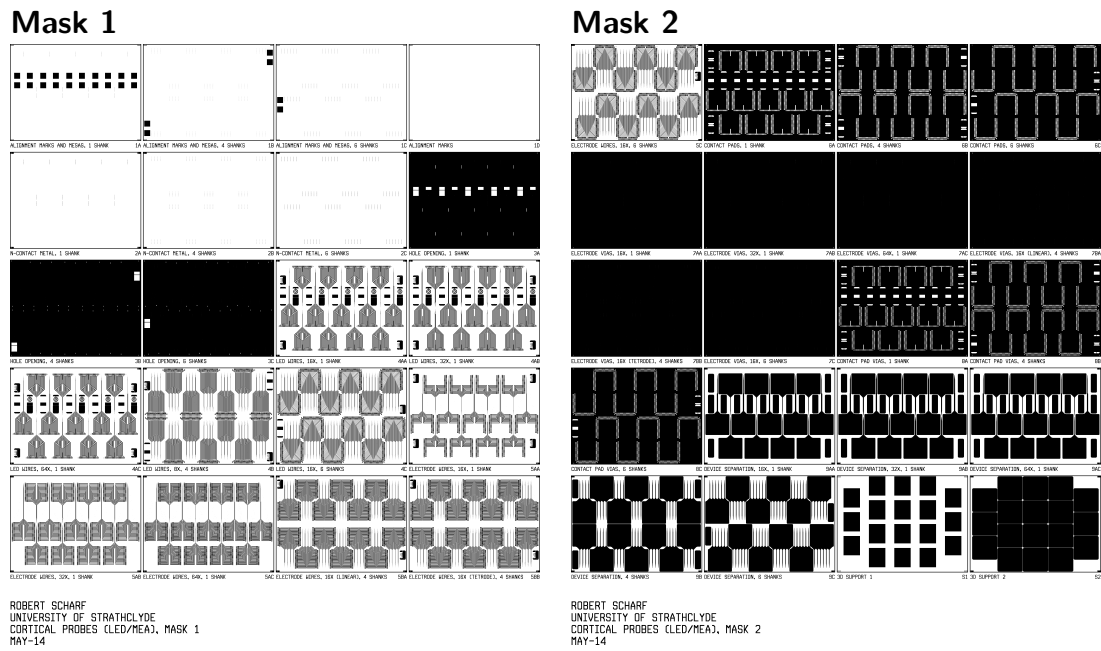


**Figure A.3:** Photomasks for LED probe fabrication (Set 2), mask size is 5", dimensions of each submask are 22.2 mm  $\times$  16.4 mm

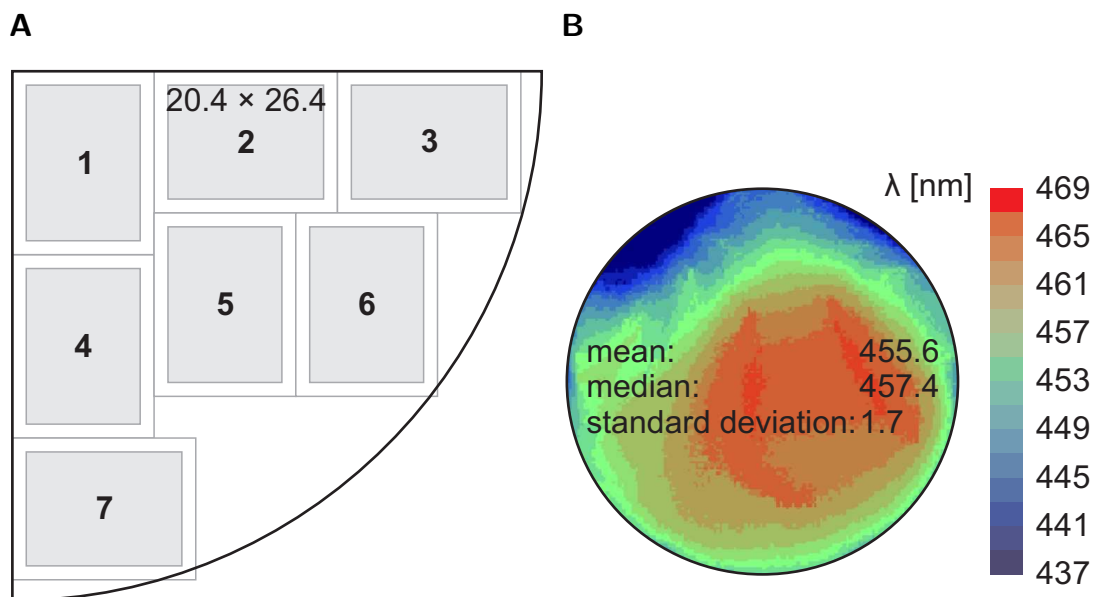


**Figure A.4:** Material for LED needle probe fabrication; **A)** Diced wafer (schematic, looking at back surface); samples are 20.4  $\times$  26.4 mm<sup>2</sup>, this includes a  $\sim$ 2 mm border on each side; **B)** Photoluminescence map showing wavelength distribution across the wafer surface



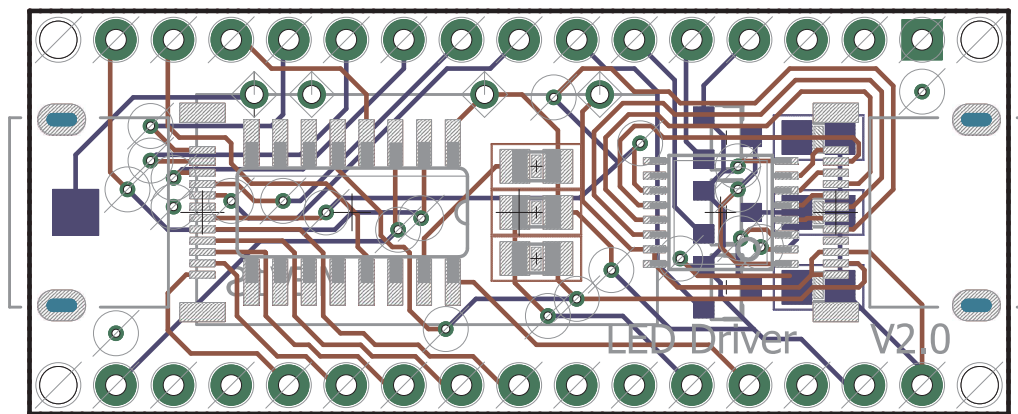
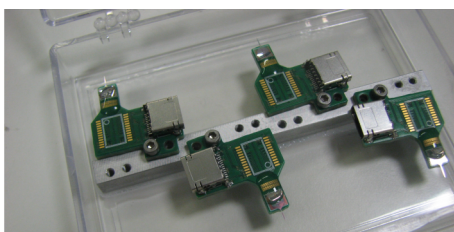


**Figure A.6:** LED driver printed circuit board

**A**



**B**

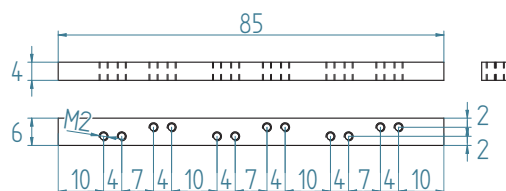


**Figure A.7:** LED probe holder; **A)** Holder inside a storage box (BCW 1-HB25); **B)** Schematic of machined aluminium bar for holding the PCBs

### A.2.3 Simulation

#### A.2.3.1 Device Heating

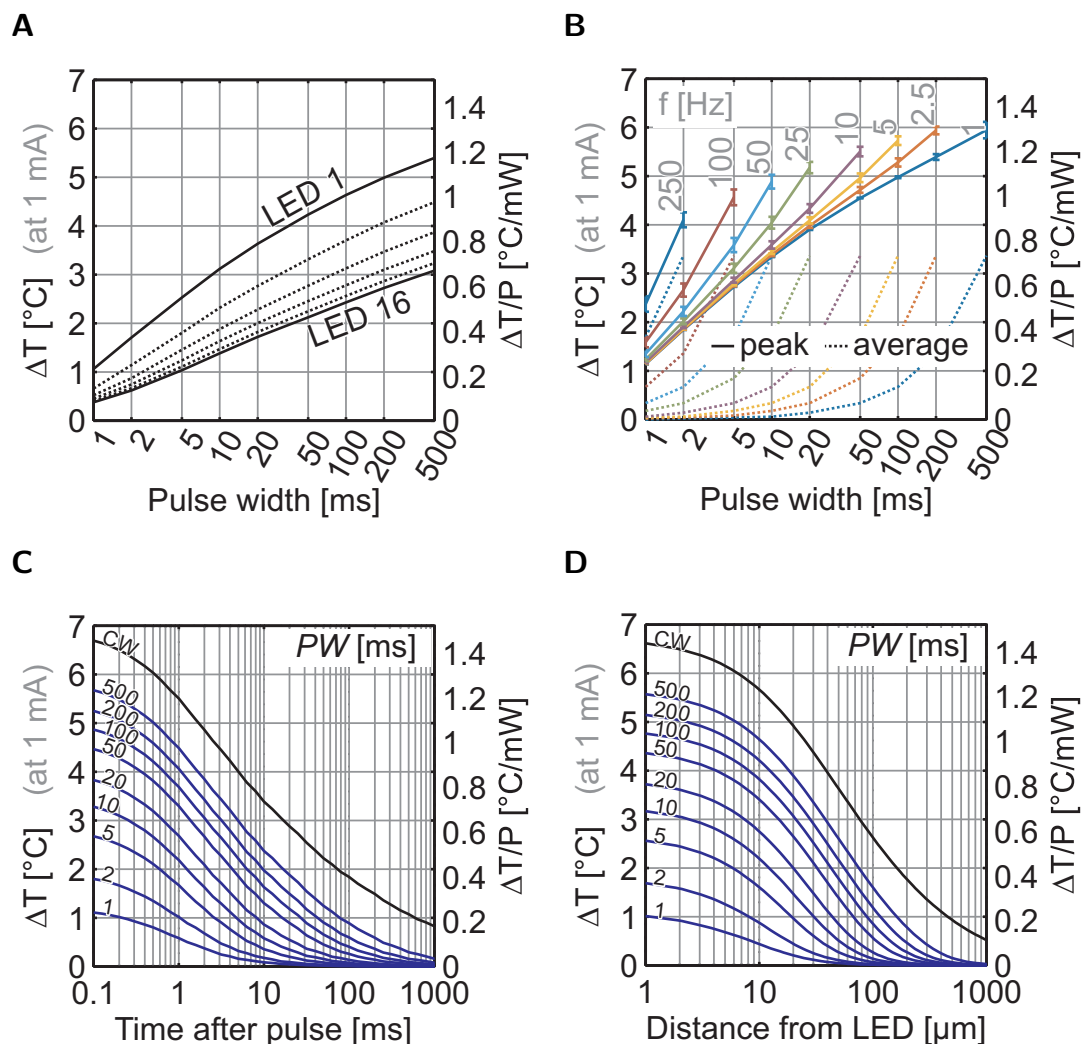


**Figure A.8:** Simulated tissue temperatures during LED probe operation ( $I = 150 \text{ mW}/\text{mm}^2$ , LED 1, cf. Figure 4.10 for LED 16); **A)** Temperature depends on the LED position; **B)** Peak and average temperatures during continuous operation in pulsed mode for various combinations of pulse width and repetition rate; **C)** Temperature dissipation over time following a pulse of certain pulse width (blue) or a continuous pulse (black); **D)** Maximum temperature at various distances from the LED following a pulse of certain pulse width (blue) or a continuous pulse (black)

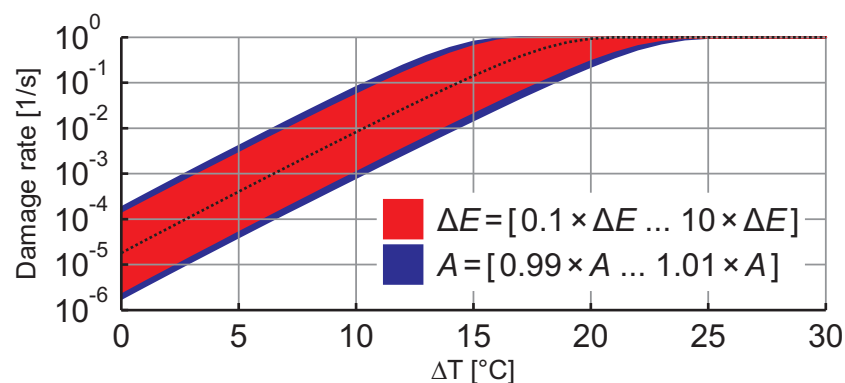


**Figure A.9:** Effect of reaction parameter uncertainties on Arrhenius damage rate; a change of  $\Delta E$  of one order of magnitude or a change of  $A$  of 1% leads to a change of the damage rate (at constant temperature) of approximately one order of magnitude

### A.2.3.2 Light Propagation

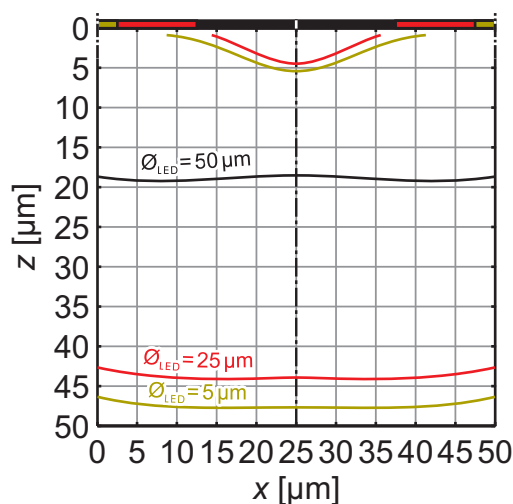


**Figure A.10:** Simulated  $\mu$ LED resolution during optogenetic stimulation of brain tissue, simultaneously using two neighbouring  $\mu$ LEDs; contour lines represent activation thresholds (arbitrary value)

### A.2.3.3 Resistance of a Conductor

The relatively long and narrow metal tracks on the LED needle probe devices dissipate some heat. When turning up the current, this can become significant. The resistance of the tracks has therefore been estimated as follows. The resistance of a long conductor with a rectangular cross-section illustrated in Figure A.11 is given as

$$R = \frac{\rho l}{A} = \frac{\rho l}{wh}. \quad (\text{A.1})$$

When working with sputtered thin films, usually one can encounter metal bilayers, which are two conductors with different thicknesses ( $h_1$  and  $h_2$ ) in parallel. The combined resistance can be calculated as

$$\frac{1}{R} = \frac{1}{R_1} + \frac{1}{R_2} \quad (\text{A.2})$$

$$R = \frac{\rho_1 \rho_2}{h_1 \rho_2 + h_2 \rho_1} \cdot \frac{l}{w}. \quad (\text{A.3})$$

When using a simplified geometry of this device and the material resistivities from Table A.15, the total resistance for the 50/500 nm-thick p- and the 50/100 nm-thick n-tracks leading to LED 1 ( $R_p$  and  $R_n$ , respectively) can be estimated as follows ( $R_p \approx 46 \Omega$  and  $R_n \approx 7 \Omega$  for LED 16):

$$R_p \approx 0.056 \Omega \cdot \left( \frac{3000 \mu\text{m}}{80 \mu\text{m}} + \frac{2200 \mu\text{m}}{3 \mu\text{m}} + \frac{850 \mu\text{m}}{2.2 \mu\text{m}} \right) = 65 \Omega \quad (\text{A.4})$$

$$R_n \approx 0.273 \Omega \cdot \left( \frac{3000 \mu\text{m}}{3000 \mu\text{m}} + \frac{2200 \mu\text{m}}{100 \mu\text{m}} + \frac{850 \mu\text{m}}{70 \mu\text{m}} \right) = 10 \Omega. \quad (\text{A.5})$$

The series resistance of p- and n-tracks then lies between  $53 \Omega$  and  $75 \Omega$  (LED 16 and LED 1, respectively).

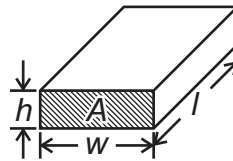


**Figure A.11:** Cross-section of a conductor (schematic)

	Ti	Al	Au
$\rho$ [ $\Omega\text{m}$ ]	$4.20 \cdot 10^{-7}$	$2.82 \cdot 10^{-8}$	$2.44 \cdot 10^{-8}$

**Table A.15:** Electrical resistivities of different conductors used in the fabrication of neural microdevices

## A.2.4 Characterization

### A.2.4.1 Light Output

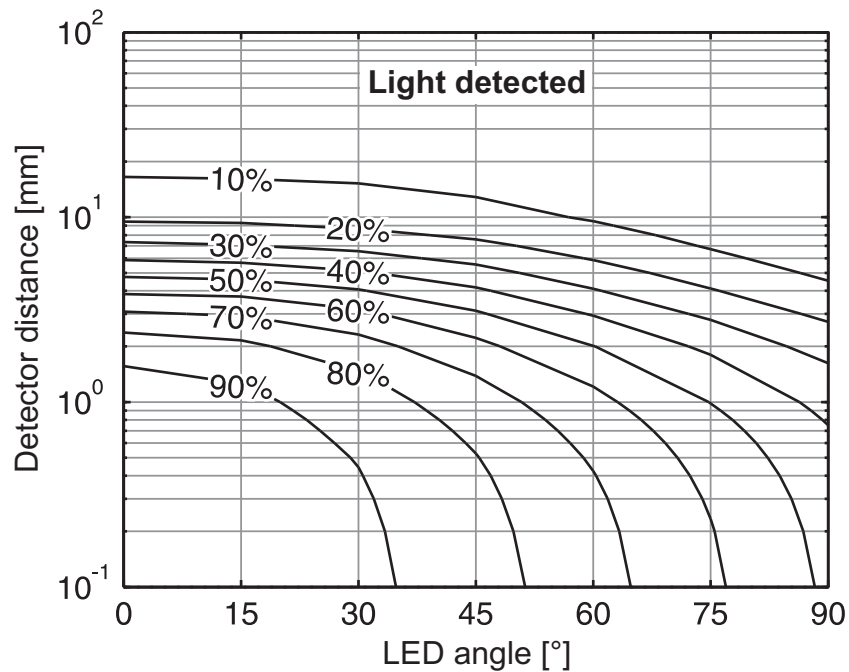
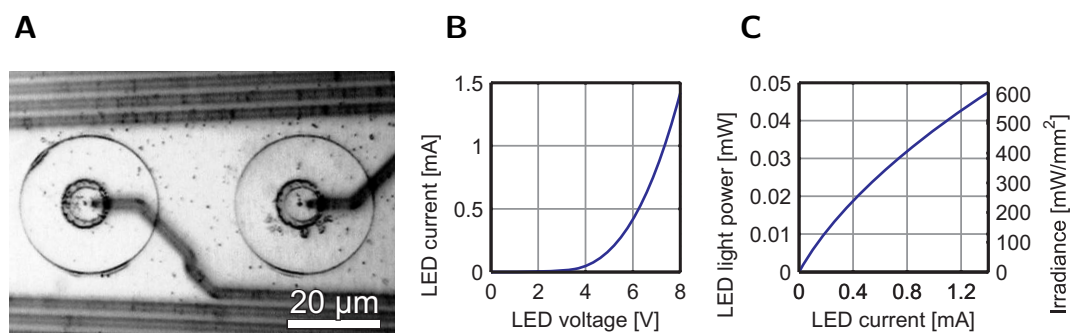


**Figure A.12:** Fractions of  $\mu$ LED light detected by a photodiode during  $\mu$ LED optical power characterization; detector radius  $r = 4.75$  mm, distance from detector  $d = 0..100$  mm, probe angle  $\alpha = 0..90^\circ$ ; light powers detected from LED when centred in front of the detector

[%]	Light detected from LED															
	1	2	3	4	5	6	7	8	9	10	11	12	13	14	15	16
1	27	27	27	26	26	26	26	25	25	25	24	24	24	24	23	23
2	27	27	27	27	26	26	26	26	25	25	25	24	24	24	24	23
3	28	27	27	27	27	26	26	26	26	25	25	25	24	24	24	24
4	28	28	27	27	27	27	26	26	26	26	25	25	25	24	24	24
5	28	28	28	27	27	27	27	26	26	26	26	25	25	25	24	24
6	29	28	28	28	27	27	27	27	26	26	26	26	25	25	25	24
7	29	29	28	28	28	27	27	27	27	26	26	26	26	25	25	25
8	29	29	29	28	28	28	27	27	27	27	26	26	26	26	25	25
9	30	29	29	29	28	28	28	27	27	27	27	26	26	26	26	25
10	30	30	29	29	29	28	28	28	27	27	27	27	26	26	26	26
11	30	30	30	29	29	29	28	28	28	27	27	27	27	26	26	26
12	31	30	30	30	29	29	29	28	28	28	27	27	27	27	26	26
13	31	31	30	30	30	29	29	29	28	28	28	27	27	27	27	26
14	31	31	31	30	30	30	29	29	29	28	28	28	27	27	27	27
15	32	31	31	31	30	30	30	29	29	29	28	28	28	27	27	27
16	32	32	31	31	31	30	30	30	29	29	29	28	28	28	27	27

**Table A.16:** Fractions of light detected by a photodiode during  $\mu$ LED optical power characterization; detector radius  $r = 4.75$  mm, distance from detector  $d = 6$  mm, probe angle  $\alpha = 45^\circ$ ; light powers detected from all 16 LEDs as a fraction of total LED light power when any particular LED is centred in front of the detector

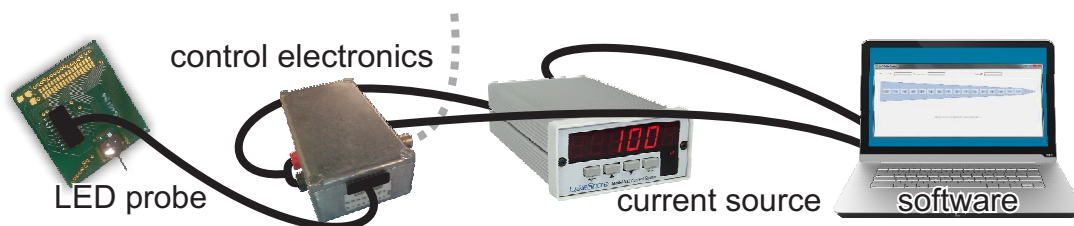
#### A.2.4.2 Smaller LEDs



**Figure A.13:** LEDs with 10  $\mu$ m diameter; **A)** Image of a probe containing 10  $\mu$ m-diameter LEDs; **B)** IV-curve of the device shown; **C)** LI-curve of the device shown

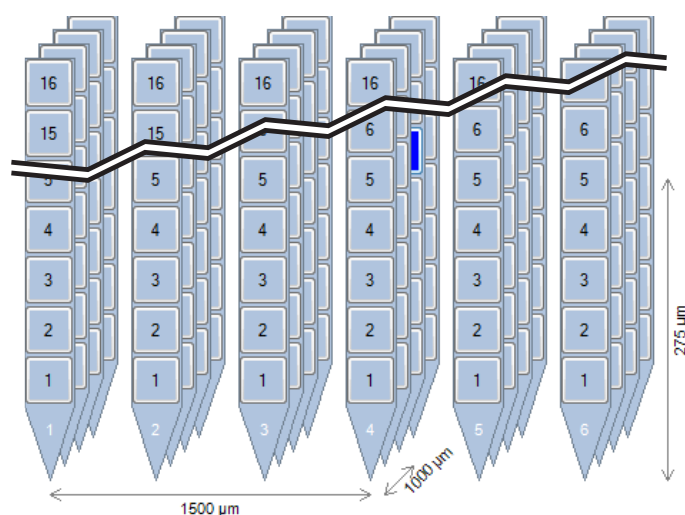
### A.2.5 First Generation Control Hardware

Figure A.14 shows the first generation of the LED probe control hardware designed for 16-channel LED probes. It consisted of the probe on a custom-designed PCB, control electronics (Arduino and demultiplexer) and a current source (LakeShore Model 121). The control hardware was connected to a PC with custom-designed software.



**Figure A.14:** First generation control hardware; a current source and a channel switch consisting of an Arduino and a demultiplexer are connected to a PC vis USB; the output of the current source is connected to the switch circuit; the output of the switch circuit is connected to the LED probe using a 17-way cable; the channel and the target irradiance can be selected using the software; the LED can be turned on and off using either the software or by an external trigger (TTL pulse) going into the switching circuit

### A.2.6 Advanced Control Software



**Figure A.15:** Control software for 3D  $\mu$ LED arrays (screenshot of the channel selection interface)

### A.2.7 LED Drivers

A multitude of LED drivers currently exist on the market allowing different numbers of LEDs to be driven with a defined current, that can be either set statically or be programmable. The physical design of the LED probes, however, heavily restricts the choice. There are AC (including a rectifier) and DC drivers. There are also boost and buck drivers creating an output voltage that is, respectively, higher or lower than the supply voltage. Often they offer dimming by pulse width modulation (PWM). Overviews are given by Winder [309] and by Khanna [119].

Almost all available options are so-called **sink drivers**, which means that they allow current flow into the driver IC. These drivers can only be used with individually wired common anode (common p) LEDs. Therefore, in order to be useful for the monolithically fabricated GaN-on-Si needle probes, wafer polarity would have to be reversed. This, however, is not easy to achieve, due to p-GaN diffusion caused by heating during following growth steps. A popular example for a 16-channel driver with programmable current output is the TLC5940 (TI). The TLC5916 (TI) is a programmable 8-channel driver. TI offers linear dimming under the name dot correction.

**Source drivers** can be used for common cathode (common n) LEDs, but they are rare. One option offering eight channels but no adjustable current is the UDN2982 (Allegro Microsystems). When driving multiple LEDs, an alternative is to use shift registers such as the 8-channel 74HC595 (NXP), which can source or sink current.

When **multiplexing** is used, drivers with only one current output can be sufficient for controlling a high number of LEDs. The current path can then be adjusted by a series of demultiplexers acting as switches. In the case of the 16-channel probe, only one 16-channel IC (e.g. HC4067) is sufficient. This approach was taken here.

Alternatives to dedicated LED drivers include operational amplifier circuits. A basic transconductance amplifier is shown in Figure A.16. Other designs can be found elsewhere [310]. Using a digital to analogue converter (DAC), the digital output of a microprocessor (such as the one used in the Arduino boards) could be used to provide the input for this amplifier circuit.

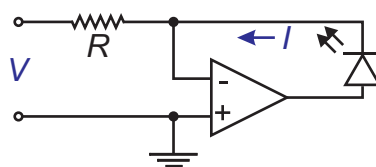


**Figure A.16:** Transconductance amplifier (voltage-controlled current source) [311, p. 297]; the circuit produces a current  $I$  proportional to a voltage  $V$  ( $I = -V/R$ )

## A.3 Transfer-Printed LEDs

Figure A.17 shows a photomask for the fabrication of individual transfer-printable  $\mu$ LEDs for optogenetics. The mask steps are the following: **1**) mesa patterning ( $30\ \mu\text{m}$  round and  $65\ \mu\text{m}$  square), **2**) p- and n-metal deposition (negative masks included as alternatives), **3**) underetch for creating micron-thick  $100\ \mu\text{m}$  and  $190\ \mu\text{m}$  square dies, and **4**) singulation of groups of  $4\times 4$  LEDs.

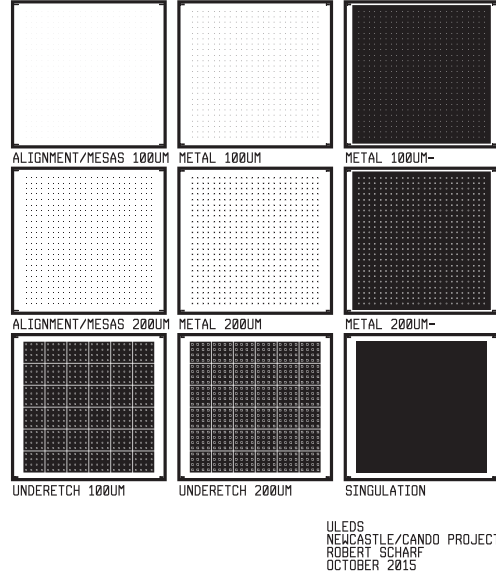


**Figure A.17:** Photomask for fabrication of individual transfer-printable  $\mu$ LEDs, mask size is 4”, dimensions of each submask are 20.6 mm  $\times$  19.6 mm

## A.4 Planar *In Vitro* Arrays

### A.4.1 Thin Film Stress and Wafer Curvature

Low stress passivation layers are required for the fabrication of the planar *in vitro* arrays to avoid cracking and peeling of the film. Film stress is given by the Stoney formula

$$\sigma = \frac{E_s}{6(1-\nu_s)} \frac{t_s^2}{t_f} \left( \frac{1}{R} - \frac{1}{R_0} \right), \quad (\text{A.6})$$

where  $E_s$  is the Young’s modulus of the substrate and  $\nu_s$  is the Poisson ratio,  $t_s$  is the thickness of the substrate and  $t_f$  is the thickness of the film,  $R$  is the radius of curvature of the wafer after deposition of the film and  $R_0$  is the radius of curvature of the wafer before the deposition [214]. The radii of curvature can be obtained from stylus profilometer (i.e. Dektak) measurements or optical profilometry and calculated from the scan distance  $\Delta x$  and the height difference  $\Delta z$  as (circular

segment)

$$R = \frac{4(\Delta z)^2 + (\Delta x)^2}{8\Delta z}. \quad (\text{A.7})$$

### A.4.2 Minimum Feature Size Calculation

The critical features appear at the outer ring of electrodes of the array, where all the tracks leading to the inner electrodes have to be squeezed in the slots (see Figure A.17). The width of the slots  $w_{\text{slot}}$  can be calculated as

$$w_{\text{slot}} = p_{\text{elec}} - d_{\text{elec}}, \quad (\text{A.8})$$

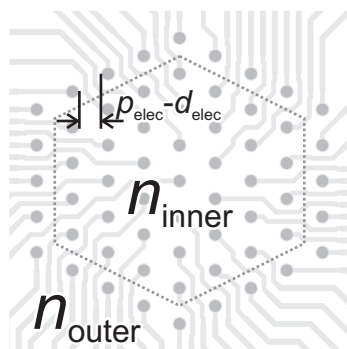
where  $p_{\text{elec}}$  is the electrode pitch and  $d_{\text{elec}}$  is the electrode diameter. Each slot has to accommodate  $n_{\text{tracks}}$  tracks and  $n_{\text{tracks}} + 1$  gaps of equal width  $w_{\text{track}}$

$$(2 \cdot n_{\text{tracks}} + 1) \cdot w_{\text{track}} = w_{\text{slot}}, \quad (\text{A.9})$$

where the number of tracks  $n_{\text{tracks}}$  is the number of central electrodes  $n_{\text{inner}}$  divided by the number of peripheral electrodes (or gaps)  $n_{\text{outer}}$ :

$$n_{\text{tracks}} = \left\lceil \frac{n_{\text{inner}}}{n_{\text{outer}}} \right\rceil. \quad (\text{A.10})$$

Track widths required for the fabrication of arrays of different size and pitch are summarized in Figure A.17. The minimum feature size can be increased by optimizing (shrinking) the electrode diameter.



			number of electrodes		
			61	519	2053
		$n_{\text{outer}}$	24	76	154
		$n_{\text{inner}}$	37	443	1899
		$d_{\text{elec}}$		7.5	
		$n_{\text{tracks}}$	2	6	13
elec-	60	$w_{\text{slot}}$ [ $\mu\text{m}$ ]		52.5	
		$w_{\text{track}}$ [ $\mu\text{m}$ ]	10.5	4.03	1.94
trode	30	$w_{\text{slot}}$ [ $\mu\text{m}$ ]		22.5	
		$w_{\text{track}}$ [ $\mu\text{m}$ ]	4.5	1.73	0.83
pitch	15	$w_{\text{slot}}$ [ $\mu\text{m}$ ]		7.5	
		$w_{\text{track}}$ [ $\mu\text{m}$ ]	1.5	0.57	0.27

**Table A.17:** Minimum feature sizes for different electrode arrays

### A.4.3 Platinization

The platinization current for an electrode array  $I_{\text{plat,array}}$  can be calculated as

$$I_{\text{plat,array}} = n_{\text{elec}} \cdot I_{\text{plat,elec}}, \quad (\text{A.11})$$

where  $n_{\text{elec}}$  is the number of electrodes and  $I_{\text{plat,elec}}$  is the platinization current per electrode. The platinization current per electrode can be calculated using the electrode area  $A_{\text{elec}}$  and the specific platinization current  $i_{\text{plat}}$ :

$$I_{\text{plat,elec}} = A_{\text{elec}} \cdot i_{\text{plat}} = \pi \left( \frac{d_{\text{elec}}}{2} \right)^2 \cdot i_{\text{plat}}, \quad (\text{A.12})$$

where  $d_{\text{elec}}$  is the electrode diameter. The electrode diameter in this case is equal to  $5 \mu\text{m}$ . The optimum specific platinization current has been determined to be  $4 \text{ nA}/\mu\text{m}^2$  by Gunning [280]. For the 61 electrode arrays fabricated here, the total platinization current is therefore equal to

$$I_{\text{plat,array}} = 61 \cdot \pi \left( \frac{5 \mu\text{m}}{2} \right)^2 \cdot 4 \frac{\text{nA}}{\mu\text{m}^2} = \underline{\underline{4.79 \mu\text{A}}}. \quad (\text{A.13})$$

# Bibliography

- [1] Tononi, G., Edelman, G. M. & Sporns, O. Complexity and coherency: integrating information in the brain. *Trends in Cognitive Sciences* **2**, 474–484 (1998).
- [2] Abbott, A. Neuroscience: Solving the brain. *Nature* **499**, 272–274 (2013).
- [3] The Human Brain Project - Human Brain Project (2014). URL <https://www.humanbrainproject.eu/>.
- [4] Obama, B. BRAIN Initiative | The White House (2014). URL <http://www.whitehouse.gov/share/brain-initiative>.
- [5] BRAIN 2025: A scientific vision. Brain Research through Advancing Innovative Neurotechnologies (BRAIN) Working Group Report to the Advisory Committee to the Director, NIH (2014). URL [http://braininitiative.nih.gov/pdf/BRAIN2025\\_508C.pdf](http://braininitiative.nih.gov/pdf/BRAIN2025_508C.pdf).
- [6] Herman Lab. URL <https://www.k-state.edu/hermanlab/>.
- [7] White, J. G., Southgate, E., Thomson, J. N. & Brenner, S. The structure of the nervous system of the nematode *Caenorhabditis elegans*. *Philos. Trans. R. Soc. Lond., B, Biol. Sci.* **314**, 1–340 (1986).
- [8] Denk, W. & Horstmann, H. Serial Block-Face Scanning Electron Microscopy to Reconstruct Three-Dimensional Tissue Nanostructure. *PLoS Biol* **2**, e329 (2004).
- [9] Alivisatos, A. P. *et al.* The Brain Activity Map Project and the Challenge of Functional Connectomics. *Neuron* **74**, 970–974 (2012).
- [10] Ullo, S. *et al.* Functional connectivity estimation over large networks at cellular resolution based on electrophysiological recordings and structural prior. *Front Neuroanat* **8** (2014).
- [11] Lee, W.-C. A. *et al.* Anatomy and function of an excitatory network in the visual cortex. *Nature advance online publication* (2016).
- [12] Zemelman, B. V., Lee, G. A., Ng, M. & Miesenböck, G. Selective Photostimulation of Genetically ChARGed Neurons. *Neuron* **33**, 15–22 (2002).
- [13] Nagel, G. *et al.* Channelrhodopsin-2, a directly light-gated cation-selective membrane channel. *PNAS* **100**, 13940–13945 (2003).
- [14] Boyden, E. S., Zhang, F., Bamberg, E., Nagel, G. & Deisseroth, K. Millisecond-timescale, genetically targeted optical control of neural activity. *Nat Neurosci* **8**, 1263–1268 (2005).
- [15] Yizhar, O., Fenno, L., Davidson, T., Mogri, M. & Deisseroth, K. Optogenetics in neural systems. *Neuron* **71**, 9–34 (2011).
- [16] Miesenböck, G. Optogenetic control of cells and circuits. *Annu. Rev. Cell Dev. Biol.* **27**, 731–758 (2011).
- [17] Dugué, G. P., Akemann, W. & Knöpfel, T. A comprehensive concept of optogenetics. *Prog. Brain Res.* **196**, 1–28 (2012).
- [18] Häusser, M. Optogenetics: the age of light. *Nat Meth* **11**, 1012–1014 (2014).
- [19] Rickgauer, J. P. & Tank, D. W. Two-photon excitation of channelrhodopsin-2 at saturation. *PNAS* **106**, 15025–15030 (2009).
- [20] Rickgauer, J. P., Deisseroth, K. & Tank, D. W. Simultaneous cellular-resolution optical perturbation and imaging of place cell firing fields. *Nat Neurosci* **17**, 1816–1824 (2014).

- [21] Szabo, V., Ventalon, C., De Sars, V., Bradley, J. & Emiliani, V. Spatially Selective Holographic Photoactivation and Functional Fluorescence Imaging in Freely Behaving Mice with a Fiberscope. *Neuron* **84**, 1157–1169 (2014).
- [22] Packer, A. M., Russell, L. E., Dalgleish, H. W. P. & Häusser, M. Simultaneous all-optical manipulation and recording of neural circuit activity with cellular resolution in vivo. *Nat Meth* **12**, 140–146 (2015).
- [23] Alivisatos, A. P. *et al.* Nanotools for Neuroscience and Brain Activity Mapping. *ACS Nano* **7**, 1850–1866 (2013).
- [24] Azevedo, F. A. *et al.* Equal numbers of neuronal and nonneuronal cells make the human brain an isometrically scaled-up primate brain. *J. Comp. Neurol.* **513**, 532–541 (2009).
- [25] Kandel, E. R., Schwartz, J. H., Jessell, T. M., Siegelbaum, S. A. & Hudspeth, A. J. *Principles of Neural Science, Fifth Edition* (McGraw-Hill Medical, New York, 2012), 5 edition edn.
- [26] Squire, L. R. *Fundamental Neuroscience, Fourth Edition* (Academic Press, 2012), 4 edition edn.
- [27] Koch, C. *Biophysics of computation information processing in single neurons* (Oxford University Press, New York, 1999).
- [28] Hodgkin, A. L. & Huxley, A. F. A quantitative description of membrane current and its application to conduction and excitation in nerve. *J Physiol* **117**, 500–544 (1952).
- [29] Curcio, C. A. & Allen, K. A. Topography of ganglion cells in human retina. *J. Comp. Neurol.* **300**, 5–25 (1990).
- [30] Tinsley, J. N. *et al.* Direct detection of a single photon by humans. *Nat Commun* **7**, 12172 (2016).
- [31] Masland, R. *et al.* The fundamental plan of the retina. *Nature neuroscience* **4**, 877–886 (2001).
- [32] NeuroMorpho.Org. URL <http://neuromorpho.org/index.jsp>.
- [33] Field, G. D. *et al.* Functional connectivity in the retina at the resolution of photoreceptors. *Nature* **467**, 673–677 (2010).
- [34] Masland, R. H. Neuronal diversity in the retina. *Current Opinion in Neurobiology* **11**, 431–436 (2001).
- [35] Dowling, J. E. *The Retina: An Approachable Part of the Brain* (Harvard University Press, 1987).
- [36] Rodieck, R. W. *The first steps in seeing* (Sinauer Associates, Sunderland, Mass., 1998).
- [37] Heimer, L. *The Human Brain and Spinal Cord: Functional Neuroanatomy and Dissection Guide* (Springer, New York, 1995), 2nd ed. 1995 edition edn.
- [38] Quiroga, R. Q. & Panzeri, S. (eds.) *Principles of Neural Coding* (CRC Press, Boca Raton, 2013), 1 edition edn.
- [39] Roth, G. & Dicke, U. Evolution of the brain and intelligence. *Trends in Cognitive Sciences* **9**, 250–257 (2005).
- [40] Herculano-Houzel, S. & Lent, R. Isotropic Fractionator: A Simple, Rapid Method for the Quantification of Total Cell and Neuron Numbers in the Brain. *J. Neurosci.* **25**, 2518–2521 (2005).
- [41] Herculano-Houzel, S., Mota, B. & Lent, R. Cellular scaling rules for rodent brains. *PNAS* **103**, 12138–12143 (2006).
- [42] Herculano-Houzel, S. *et al.* The elephant brain in numbers. *Front. Neuroanat* **8**, 46 (2014).

- [43] Koch, C. *The Quest for Consciousness: A Neurobiological Approach* (Roberts & Co, Denver, Colo, 2004).
- [44] Glasser, M. F. *et al.* A multi-modal parcellation of human cerebral cortex. *Nature advance online publication* (2016).
- [45] Merrill, D. R., Bikson, M. & Jefferys, J. G. Electrical stimulation of excitable tissue: design of efficacious and safe protocols. *Journal of Neuroscience Methods* **141**, 171–198 (2005).
- [46] Oesterhelt, D. & Stoerkenius, W. Rhodopsin-like Protein from the Purple Membrane of Halobacterium halobium. *Nature* **233**, 149–152 (1971).
- [47] Matsuno-Yagi, A. & Mukohata, Y. Two possible roles of bacteriorhodopsin; a comparative study of strains of Halobacterium halobium differing in pigmentation. *Biochemical and Biophysical Research Communications* **78**, 237–243 (1977).
- [48] Nagel, G. *et al.* Channelrhodopsin-1: A Light-Gated Proton Channel in Green Algae. *Science* **296**, 2395–2398 (2002).
- [49] Ramirez, S. *et al.* Creating a False Memory in the Hippocampus. *Science* **341**, 387–391 (2013).
- [50] Ryan, T. J., Roy, D. S., Pignatelli, M., Arons, A. & Tonegawa, S. Engram cells retain memory under retrograde amnesia. *Science* **348**, 1007–1013 (2015).
- [51] Shrestha, P. & Klann, E. Alzheimer’s disease: Lost memories found. *Nature advance online publication* (2016).
- [52] Iyer, S. M. *et al.* Virally mediated optogenetic excitation and inhibition of pain in freely moving nontransgenic mice. *Nat Biotech* **32**, 274–278 (2014).
- [53] Gu, L. *et al.* Pain Inhibition by Optogenetic Activation of Specific Anterior Cingulate Cortical Neurons. *PLOS ONE* **10**, e0117746 (2015).
- [54] Liu, J. *et al.* Frequency-selective control of cortical and subcortical networks by central thalamus. *eLife* **4**, e09215 (2015).
- [55] Pan, Z.-H., Lu, Q., Bi, A., Dizhoor, A. M. & Abrams, G. W. Optogenetic Approaches to Restoring Vision. *Annual Review of Vision Science* **1**, 185–210 (2015).
- [56] Burton, R. A. B. *et al.* Optical control of excitation waves in cardiac tissue. *Nat Photon* **9**, 813–816 (2015).
- [57] Chernet, B. T., Adams, D. S., Lobikin, M. & Levin, M. Use of genetically encoded, light-gated ion translocators to control tumorigenesis. *Oncotarget* (2016).
- [58] Yawo, H., Kandori, H. & Koizumi, A. *Optogenetics: Light-Sensing Proteins and Their Applications* (Springer Japan, 2015).
- [59] Kianianmomeni, A. (ed.) *Optogenetics*, vol. 1408 of *Methods in Molecular Biology* (Springer New York, New York, NY, 2016). URL <http://link.springer.com/10.1007/978-1-4939-3512-3>.
- [60] Knöpfel, T. & Boyden, E. S. *Optogenetics: Tools for Controlling and Monitoring Neuronal Activity*. Progress in Brain Research (Book 196) (Elsevier, Amsterdam, 2012), 1 edition edn.
- [61] Hegemann, P. & Sigrist, S. *Optogenetics* (Walter de Gruyter, 2013).
- [62] Zhang, F. *et al.* Multimodal fast optical interrogation of neural circuitry. *Nature* **446**, 633–639 (2007).
- [63] Lin, J. Y. A User’s Guide to Channelrhodopsin Variants: Features, Limitations and Future Developments. *Exp Physiol* **96**, 19–25 (2011).

- [64] Yaroslavsky, A. N. *et al.* Optical properties of selected native and coagulated human brain tissues in vitro in the visible and near infrared spectral range. *Phys. Med. Biol.* **47**, 2059 (2002).
- [65] Lin, J. Y., Lin, M. Z., Steinbach, P. & Tsien, R. Y. Characterization of Engineered Channelrhodopsin Variants with Improved Properties and Kinetics. *Biophysical Journal* **96**, 1803–1814 (2009).
- [66] Klapoetke, N. C. *et al.* Independent optical excitation of distinct neural populations. *Nat Meth* **11**, 338–346 (2014).
- [67] Govorunova, E. G., Sineshchekov, O. A., Li, H., Janz, R. & Spudich, J. L. Characterization of a Highly Efficient Blue-shifted Channelrhodopsin from the Marine Alga *Platymonas subcordiformis*. *J. Biol. Chem.* jbc.M113.505495 (2013).
- [68] Berndt, A., Yizhar, O., Gunaydin, L. A., Hegemann, P. & Deisseroth, K. Bi-stable neural state switches. *Nat Neurosci* **12**, 229–234 (2009).
- [69] Han, X. & Boyden, E. S. Multiple-Color Optical Activation, Silencing, and Desynchronization of Neural Activity, with Single-Spike Temporal Resolution. *PLOS ONE* **2**, e299 (2007).
- [70] Gradinaru, V. *et al.* Molecular and Cellular Approaches for Diversifying and Extending Optogenetics. *Cell* **141**, 154–165 (2010).
- [71] Chow, B. Y. *et al.* High-performance genetically targetable optical neural silencing by light-driven proton pumps. *Nature* **463**, 98–102 (2010).
- [72] Han, X. *et al.* A high-light sensitivity optical neural silencer: development and application to optogenetic control of non-human primate cortex. *Front. Syst. Neurosci.* **5**, 18 (2011).
- [73] Chuong, A. S. *et al.* Noninvasive optical inhibition with a red-shifted microbial rhodopsin. *Nat Neurosci* **17**, 1123–1129 (2014).
- [74] Berndt, A., Lee, S. Y., Ramakrishnan, C. & Deisseroth, K. Structure-Guided Transformation of Channelrhodopsin into a Light-Activated Chloride Channel. *Science* **344**, 420–424 (2014).
- [75] Wietek, J. *et al.* Conversion of Channelrhodopsin into a Light-Gated Chloride Channel. *Science* **344**, 409–412 (2014).
- [76] Govorunova, E. G., Sineshchekov, O. A., Janz, R., Liu, X. & Spudich, J. L. Natural light-gated anion channels: A family of microbial rhodopsins for advanced optogenetics. *Science* **349**, 647–650 (2015).
- [77] Packer, A. M., Roska, B. & Häusser, M. Targeting neurons and photons for optogenetics. *Nat Neurosci* **16**, 805–815 (2013).
- [78] Zhang, F. *et al.* Optogenetic interrogation of neural circuits: technology for probing mammalian brain structures. *Nature Protocols* **5**, 439–456 (2010).
- [79] Wall, N. R., Wickersham, I. R., Cetin, A., Parra, M. D. L. & Callaway, E. M. Monosynaptic circuit tracing in vivo through Cre-dependent targeting and complementation of modified rabies virus. *PNAS* **107**, 21848–21853 (2010).
- [80] Sugino, K. *et al.* Molecular taxonomy of major neuronal classes in the adult mouse forebrain. *Nat Neurosci* **9**, 99–107 (2006).
- [81] Fishell, G. & Heintz, N. The Neuron Identity Problem: Form Meets Function. *Neuron* **80**, 602–612 (2013).
- [82] Kuhlman, S. J. & Huang, Z. J. High-Resolution Labeling and Functional Manipulation of Specific Neuron Types in Mouse Brain by Cre-Activated Viral Gene Expression. *PLOS ONE* **3**, e2005 (2008).

- [83] Madisen, L. *et al.* A toolbox of Cre-dependent optogenetic transgenic mice for light-induced activation and silencing. *Nat Neurosci* **15**, 793–802 (2012).
- [84] Judkewitz, B., Rizzi, M., Kitamura, K. & Häusser, M. Targeted single-cell electroporation of mammalian neurons in vivo. *Nat. Protocols* **4**, 862–869 (2009).
- [85] Sternson, S. M. & Roth, B. L. Chemogenetic Tools to Interrogate Brain Functions. *Annual Review of Neuroscience* **37**, 387–407 (2014).
- [86] Ibsen, S., Tong, A., Schutt, C., Esener, S. & Chalasani, S. H. Sonogenetics is a non-invasive approach to activating neurons in *Caenorhabditis elegans*. *Nat Commun* **6** (2015).
- [87] Wheeler, M. A. *et al.* Genetically targeted magnetic control of the nervous system. *Nat Neurosci* **advance online publication** (2016).
- [88] Meister, M. Physical limits to magnetogenetics. *arXiv:1604.01359 [q-bio]* (2016). ArXiv: 1604.01359.
- [89] Rajasethupathy, P., Ferenczi, E. & Deisseroth, K. Targeting Neural Circuits. *Cell* **165**, 524–534 (2016).
- [90] Park, H. G. & Carmel, J. B. Selective Manipulation of Neural Circuits. *Neurotherapeutics* 1–14 (2016).
- [91] Marblestone, A. H. *et al.* Physical principles for scalable neural recording. *Front. Comput. Neurosci* **7**, 137 (2013).
- [92] Miyawaki, A. *et al.* Fluorescent indicators for Ca<sup>2+</sup> based on green fluorescent proteins and calmodulin. *Nature* **388**, 882–887 (1997).
- [93] Ohkura, M. *et al.* Genetically Encoded Green Fluorescent Ca<sup>2+</sup> Indicators with Improved Detectability for Neuronal Ca<sup>2+</sup> Signals. *PLOS ONE* **7**, e51286 (2012).
- [94] Nguyen, J. P. *et al.* Whole-brain calcium imaging with cellular resolution in freely behaving *Caenorhabditis elegans*. *PNAS* 201507110 (2015).
- [95] Peterka, D. S., Takahashi, H. & Yuste, R. Imaging voltage in neurons. *Neuron* **69**, 9–21 (2011).
- [96] Baker, B. J. *et al.* Imaging brain activity with voltage- and calcium-sensitive dyes. *Cell. Mol. Neurobiol.* **25**, 245–282 (2005).
- [97] Knöpfel, T. Genetically encoded optical indicators for the analysis of neuronal circuits. *Nat Rev Neurosci* **13**, 687–700 (2012).
- [98] Hochbaum, D. R. *et al.* All-optical electrophysiology in mammalian neurons using engineered microbial rhodopsins. *Nat Meth* **11**, 825–833 (2014).
- [99] Gong, Y. *et al.* High-speed recording of neural spikes in awake mice and flies with a fluorescent voltage sensor. *Science* **350**, 1361–1366 (2015).
- [100] Ghosh, K. K. *et al.* Miniaturized integration of a fluorescence microscope. *Nat Meth* **8**, 871–878 (2011).
- [101] Jennings, J. H. *et al.* Visualizing Hypothalamic Network Dynamics for Appetitive and Consummatory Behaviors. *Cell* **160**, 516–527 (2015).
- [102] Wang, K., Horton, N. G. & Xu, C. Going Deep: Brain Imaging with Multi-Photon Microscopy. *Opt. Photon. News* **24**, 32–39 (2013).
- [103] Chung, K. *et al.* Structural and molecular interrogation of intact biological systems. *Nature* **advance online publication** (2013).
- [104] Susaki, E. A. *et al.* Whole-Brain Imaging with Single-Cell Resolution Using Chemical Cocktails and Computational Analysis. *Cell* **157**, 726–739 (2014).
- [105] Silvestri, L., Allegra Mascaro, A. L., Costantini, I., Sacconi, L. & Pavone, F. S. Correlative two-photon and light sheet microscopy. *Methods* **66**, 268–272 (2014).

- [106] Marx, V. Neurobiology: rethinking the electrode. *Nat Meth* **11**, 1099–1103 (2014).
- [107] Kanani, N. *Electroplating: Basic Principles, Processes and Practice* (Elsevier, 2004).
- [108] Feltham, A. M. & Spiro, M. Platinized platinum electrodes. *Chem. Rev.* **71**, 177–193 (1971).
- [109] Weiland, J. D., Anderson, D. J. & Humayun, M. S. In vitro electrical properties for iridium oxide versus titanium nitride stimulating electrodes. *IEEE Transactions on Biomedical Engineering* **49**, 1574–1579 (2002).
- [110] Venkatraman, S. *et al.* In Vitro and In Vivo Evaluation of PEDOT Microelectrodes for Neural Stimulation and Recording. *IEEE Transactions on Neural Systems and Rehabilitation Engineering* **19**, 307–316 (2011).
- [111] Giugliano, M., Gambazzi, L., Ballerini, L., Prato, M. & Campidelli, S. Carbon Nanotubes as Electrical Interfaces to Neurons. In Silva, G. A. & Parpura, V. (eds.) *Nanotechnology for Biology and Medicine*, Fundamental Biomedical Technologies, 187–207 (Springer New York, 2012). URL [http://link.springer.com/chapter/10.1007/978-0-387-31296-5\\_9](http://link.springer.com/chapter/10.1007/978-0-387-31296-5_9). DOI: 10.1007/978-0-387-31296-5\_9.
- [112] Bareket-Keren, L. & Hanein, Y. Carbon nanotube-based multi electrode arrays for neuronal interfacing: progress and prospects. *Front Neural Circuits* **6** (2013).
- [113] Fabbro, A. *et al.* Graphene-Based Interfaces Do Not Alter Target Nerve Cells. *ACS Nano* **10**, 615–623 (2016).
- [114] Piret, G. *et al.* 3d-nanostructured boron-doped diamond for microelectrode array neural interfacing. *Biomaterials* **53**, 173–183 (2015).
- [115] Randles, J. E. B. Kinetics of rapid electrode reactions. *Discuss. Faraday Soc.* **1**, 11–19 (1947).
- [116] Lewicki, M. S. A review of methods for spike sorting: the detection and classification of neural action potentials. *Network: Computation in Neural Systems* **9**, R53–R78 (1998).
- [117] Jolliffe, I. T. *Principal Component Analysis* (Springer, New York, 2002), 2nd edition edn.
- [118] Litke, A. *et al.* What does the eye tell the brain?: Development of a system for the large-scale recording of retinal output activity. *IEEE Transactions on Nuclear Science* **51**, 1434–1440 (2004).
- [119] Khanna, V. K. *Fundamentals of Solid-State Lighting: LEDs, OLEDs, and Their Applications in Illumination and Displays* (CRC Press, Boca Raton, 2014).
- [120] Saleh, B. E. A. & Teich, M. C. *Fundamentals of Photonics* (Wiley-Interscience, Hoboken, N.J, 2007), 2 edition edn.
- [121] Neamen, D. A. *Semiconductor Physics And Devices* (McGraw-Hill Higher Education, New York, NY, 2011), 4 edition edn.
- [122] Levinshtein, M. E., Rumyantsev, S. L. & Shur, M. S. (eds.) *Properties of Advanced Semiconductor Materials: GaN, AlN, InN, BN, SiC, SiGe* (Wiley-Blackwell, New York, 2001), 1 edition edn.
- [123] Schubert, E. F. *Light-emitting diodes* (Cambridge University Press, Cambridge; New York, 2006).
- [124] Shockley, W. The Theory of p-n Junctions in Semiconductors and p-n Junction Transistors. *Bell System Technical Journal* **28**, 435–489 (1949).
- [125] Zhu, D. *et al.* High-efficiency InGaN/GaN quantum well structures on large area silicon substrates. *Phys. Status Solidi A* **209**, 13–16 (2012).
- [126] Humphreys, C., McAleese, C., Kappers, M., Liu, Z. & Zhu, D. Semiconductor wafer comprising gallium nitride layer having one or more silicon nitride interlayer therein (2013). URL <http://www.google.co.uk/patents/US20130270575>.

- [127] Liu, Q. Z. & Lau, S. S. A review of the metal–GaN contact technology. *Solid-State Electronics* **42**, 677–691 (1998).
- [128] Lee, C.-T., Lin, Y.-J. & Lee, T.-H. Mechanism investigation of NiOx in Au/Ni/p-type GaN ohmic contacts annealed in air. *Journal of Elec Materi* **32**, 341–345 (2003).
- [129] Song, J. O., Ha, J. S. & Seong, T. Y. Ohmic-Contact Technology for GaN-Based Light-Emitting Diodes: Role of P-Type Contact. *IEEE Transactions on Electron Devices* **57**, 42–59 (2010).
- [130] Mightex Systems. URL [http://www.mightexsystems.com/family\\_info.php?cPath=256\\_260\\_261&categories\\_id=261](http://www.mightexsystems.com/family_info.php?cPath=256_260_261&categories_id=261).
- [131] Prizmatix - Ultra High Power LEDs and Fiber optic products for R&D. URL <http://www.prizmatix.com/>.
- [132] Kim, T.-i. *et al.* Injectable, Cellular-Scale Optoelectronics with Applications for Wireless Optogenetics. *Science* **340**, 211–216 (2013).
- [133] McAlinden, N. *et al.* Thermal and optical characterization of micro-LED probes for in vivo optogenetic neural stimulation. *Opt. Lett.* **38**, 992–994 (2013).
- [134] Mohanty, S. K. & Lakshminarayanan, V. Optical techniques in optogenetics. *Journal of Modern Optics* **62**, 949–970 (2015).
- [135] Wise, K. D., Angell, J. B. & Starr, A. An Integrated-Circuit Approach to Extracellular Microelectrodes. *IEEE Transactions on Biomedical Engineering* **BME-17**, 238–247 (1970).
- [136] Normann, R. A., Campbell, P. K. & Li, W. P. Silicon based microstructures suitable for intracortical electrical stimulation (visual prosthesis application). In *Proceedings of the Annual International Conference of the IEEE Engineering in Medicine and Biology Society*, 714–715 vol.2 (1988).
- [137] Poher, V. *et al.* Micro-LED arrays: a tool for two-dimensional neuron stimulation. *J. Phys. D: Appl. Phys.* **41**, 094014 (2008).
- [138] Grossman, N. *et al.* Multi-site optical excitation using ChR2 and micro-LED array. *J. Neural Eng.* **7**, 016004 (2010).
- [139] Nakajima, A. *et al.* CMOS image sensor integrated with micro-LED and multielectrode arrays for the patterned photostimulation and multichannel recording of neuronal tissue. *Opt. Express* **20**, 6097–6108 (2012).
- [140] Smith, J., O’Brien, B., Lee, Y.-K., Bawolek, E. & Christen, J. Application of Flexible OLED Display Technology for Electro-Optical Stimulation and/or Silencing of Neural Activity. *Journal of Display Technology* **10**, 514–520 (2014).
- [141] Steude, A. & Gather, M. C. OLED microdisplays as biophotonics platform. FTh2B.4 (OSA, 2014).
- [142] Morton, A., Murawski, C., Pulver, S. R. & Gather, M. C. High-brightness organic light-emitting diodes for optogenetic control of *Drosophila* locomotor behaviour. *Scientific Reports* **6**, 31117 (2016).
- [143] Dhakal, K., Gu, L., Black, B. & Mohanty, S. K. Fiber-optic two-photon optogenetic stimulation. *Opt. Lett.* **38**, 1927–1929 (2013).
- [144] Aravanis, A. M. *et al.* An optical neural interface: in vivo control of rodent motor cortex with integrated fiberoptic and optogenetic technology. *J. Neural Eng.* **4**, S143 (2007).
- [145] Adamantidis, A. R., Zhang, F., Aravanis, A. M., Deisseroth, K. & de Lecea, L. Neural substrates of awakening probed with optogenetic control of hypocretin neurons. *Nature* **450**, 420–424 (2007).

- [146] Lee, S. *et al.* A Miniature, Fiber-Coupled, Wireless, Deep-Brain Optogenetic Stimulator. *IEEE Transactions on Neural Systems and Rehabilitation Engineering* **23**, 655–664 (2015).
- [147] Montgomery, K. L. *et al.* Wirelessly powered, fully internal optogenetics for brain, spinal and peripheral circuits in mice. *Nat Meth* **advance online publication** (2015).
- [148] Park, S. I. *et al.* Soft, stretchable, fully implantable miniaturized optoelectronic systems for wireless optogenetics. *Nat Biotech* **advance online publication** (2015).
- [149] Jeong, J.-W. *et al.* Wireless Optofluidic Systems for Programmable In Vivo Pharmacology and Optogenetics. *Cell* (2015).
- [150] Rossi, M. A. *et al.* A wirelessly controlled implantable LED system for deep brain optogenetic stimulation. *Front. Integr. Neurosci* **9**, 8 (2015).
- [151] Al-Hasani, R. *et al.* Distinct Subpopulations of Nucleus Accumbens Dynorphin Neurons Drive Aversion and Reward. *Neuron* **87**, 1063–1077 (2015).
- [152] Stark, E., Koos, T. & Buzsaki, G. Diode-probes for spatiotemporal optical control of multiple neurons in freely-moving animals. *Journal of Neurophysiology* jn.00153.2012 (2012).
- [153] Abaya, T., Blair, S., Tathireddy, P., Rieth, L. & Solzbacher, F. A 3d glass optrode array for optical neural stimulation. *Biomed Opt Express* **3**, 3087–3104 (2012).
- [154] Zorzos, A. N., Scholvin, J., Boyden, E. S. & Fonstad, C. G. Three-dimensional multiwaveguide probe array for light delivery to distributed brain circuits. *Opt. Lett.* **37**, 4841–4843 (2012).
- [155] Zorzos, A. N., Boyden, E. S. & Fonstad, C. G. Multiwaveguide implantable probe for light delivery to sets of distributed brain targets. *Opt. Lett.* **35**, 4133–4135 (2010).
- [156] Pisanello, F. *et al.* Multipoint-Emitting Optical Fibers for Spatially Addressable In Vivo Optogenetics. *Neuron* (2014).
- [157] Pisanello, M. *et al.* Modal demultiplexing properties of tapered and nanostructured optical fibers for in vivo optogenetic control of neural activity. *Biomedical Optics Express* **6**, 4014 (2015).
- [158] Goßler, C. *et al.* GaN-based micro-LED arrays on flexible substrates for optical cochlear implants. *J. Phys. D: Appl. Phys.* **47**, 205401 (2014).
- [159] Moser, T. Optogenetic stimulation of the auditory pathway for research and future prosthetics. *Current Opinion in Neurobiology* **34**, 29–36 (2015).
- [160] McAlinden, N., Gu, E., Dawson, M. D., Sakata, S. & Mathieson, K. Optogenetic activation of neocortical neurons in vivo with a sapphire-based micro-scale LED probe. *Front Neural Circuits* **9** (2015).
- [161] Schwaerzle, M., Elmlinger, P., Paul, O. & Ruther, P. Miniaturized 3×3 optical fiber array for optogenetics with integrated 460 nm light sources and flexible electrical interconnection. In *2015 28th IEEE International Conference on Micro Electro Mechanical Systems (MEMS)*, 162–165 (2015).
- [162] Segev, E. *et al.* Patterned photostimulation via visible-wavelength photonic probes for deep brain optogenetics. *Neurophoton* **4**, 011002–011002 (2016).
- [163] Buskila, Y. *et al.* Extending the viability of acute brain slices. *Scientific Reports* **4** (2014).
- [164] Berdondini, L. *et al.* Active pixel sensor array for high spatio-temporal resolution electrophysiological recordings from single cell to large scale neuronal networks. *Lab Chip* **9**, 2644–2651 (2009).
- [165] Fiscella, M. *et al.* Recording from defined populations of retinal ganglion cells using a high-density CMOS-integrated microelectrode array with real-time switchable electrode selection. *Journal of Neuroscience Methods* **211**, 103–113 (2012).

- [166] CMOS-MEA5000-System | [www.multichannelsystems.com](http://www.multichannelsystems.com) (2016). URL <http://www.multichannelsystems.com/products/cmos-mea5000-system>.
- [167] Gunning, D. E. *et al.* Dense arrays of micro-needles for recording and electrical stimulation of neural activity in acute brain slices. *J Neural Eng* **10**, 016007 (2013).
- [168] Spira, M. E. & Hai, A. Multi-electrode array technologies for neuroscience and cardiology. *Nat Nano* **8**, 83–94 (2013).
- [169] Mathieson, K. *et al.* Large-area microelectrode arrays for recording of neural signals. *IEEE Transactions on Nuclear Science* **51**, 2027–2031 (2004).
- [170] Multichannel microelectrode arrays for electrophysiology - NeuroNexus. URL <http://neuronexus.com/>.
- [171] Byun, D., Cho, S. J. & Kim, S. Fabrication of a flexible penetrating microelectrode array for use on curved surfaces of neural tissues. *J. Micromech. Microeng.* **23**, 125010 (2013).
- [172] Atlas Neuroengineering. URL <http://www.atlasneuro.com/>.
- [173] Fiáth, R. *et al.* Large-scale recording of thalamocortical circuits: in vivo electrophysiology with the two-dimensional electronic depth control silicon probe. *Journal of Neurophysiology* jn.00318.2016 (2016).
- [174] Liu, J. *et al.* Syringe-injectable electronics. *Nat Nano* **10**, 629–636 (2015).
- [175] Jorfi, M., Skousen, J. L., Weder, C. & Capadona, J. R. Progress towards biocompatible intracortical microelectrodes for neural interfacing applications. *J. Neural Eng.* **12**, 011001 (2015).
- [176] Nicolelis, M. A. (ed.) *Methods for Neural Ensemble Recordings*. Frontiers in Neuroscience (CRC Press, Boca Raton (FL), 2008), 2nd edn. URL <http://www.ncbi.nlm.nih.gov/books/NBK1985/>.
- [177] Nicolelis, M. A. L. *et al.* Chronic, multisite, multielectrode recordings in macaque monkeys. *PNAS* **100**, 11041–11046 (2003).
- [178] Yoon, I. *et al.* Intracellular Neural Recording with Pure Carbon Nanotube Probes. *PLoS ONE* **8**, e65715 (2013).
- [179] BeMent, S., Wise, K., Anderson, D., Najafi, K. & Drake, K. L. Solid-State Electrodes for Multichannel Multiplexed Intracortical Neuronal Recording. *IEEE Transactions on Biomedical Engineering* **BME-33**, 230–241 (1986).
- [180] Kipke, D., Vetter, R., Williams, J. & Hetke, J. Silicon-substrate intracortical microelectrode arrays for long-term recording of neuronal spike activity in cerebral cortex. *IEEE Transactions on Neural Systems and Rehabilitation Engineering* **11**, 151–155 (2003).
- [181] Viventi, J. *et al.* Flexible, foldable, actively multiplexed, high-density electrode array for mapping brain activity in vivo. *Nat Neurosci* **14**, 1599–1605 (2011).
- [182] Nordhausen, C. T., Maynard, E. M. & Normann, R. A. Single unit recording capabilities of a 100 microelectrode array. *Brain Research* **726**, 129–140 (1996).
- [183] Robinson, J. T. *et al.* Vertical nanowire electrode arrays as a scalable platform for intracellular interfacing to neuronal circuits. *Nat Nano* **7**, 180–184 (2012).
- [184] Harrison, R. *et al.* A wireless neural interface for chronic recording. In *IEEE Biomedical Circuits and Systems Conference, 2008. BioCAS 2008*, 125–128 (2008).
- [185] Bai, Q., Wise, K. & Anderson, D. A high-yield microassembly structure for three-dimensional microelectrode arrays. *IEEE Transactions on Biomedical Engineering* **47**, 281–289 (2000).
- [186] Du, J. *et al.* High-Resolution Three-Dimensional Extracellular Recording of Neuronal Activity With Microfabricated Electrode Arrays. *Journal of Neurophysiology* **101**, 1671–1678 (2009).

- [187] Csicsvari, J. *et al.* Massively Parallel Recording of Unit and Local Field Potentials With Silicon-Based Electrodes. *Journal of Neurophysiology* **90**, 1314–1323 (2003).
- [188] Berényi, A. *et al.* Large-scale, high-density (up to 512 channels) recording of local circuits in behaving animals. *Journal of Neurophysiology* **111**, 1132–1149 (2014).
- [189] Du, J., Blanche, T. J., Harrison, R. R., Lester, H. A. & Masmanidis, S. C. Multiplexed, High Density Electrophysiology with Nanofabricated Neural Probes. *PLoS ONE* **6**, e26204 (2011).
- [190] Scholvin, J. *et al.* Close-Packed Silicon Microelectrodes for Scalable Spatially Oversampled Neural Recording. *IEEE Transactions on Biomedical Engineering* **63**, 120–130 (2016).
- [191] Mercanzini, A. *et al.* Demonstration of cortical recording using novel flexible polymer neural probes. *Sensors and Actuators A: Physical* **143**, 90–96 (2008).
- [192] Seidl, K. *et al.* CMOS-Based High-Density Silicon Microprobe Arrays for Electronic Depth Control in Intracortical Neural Recording. *Journal of Microelectromechanical Systems* **20**, 1439–1448 (2011).
- [193] Ozden, I. *et al.* A coaxial optrode as multifunction write-read probe for optogenetic studies in non-human primates. *Journal of Neuroscience Methods* **219**, 142–154 (2013).
- [194] Canales, A. *et al.* Multifunctional fibers for simultaneous optical, electrical and chemical interrogation of neural circuits in vivo. *Nature Biotechnology* (2015).
- [195] Rubehn, B., Wolff, S. B. E., Tovote, P., Lüthi, A. & Stieglitz, T. A polymer-based neural microimplant for optogenetic applications: design and first in vivo study. *Lab Chip* **13**, 579–588 (2013).
- [196] Wu, F. *et al.* An implantable neural probe with monolithically integrated dielectric waveguide and recording electrodes for optogenetics applications. *J. Neural Eng.* **10**, 056012 (2013).
- [197] Kim, E. G. R. *et al.* 3d silicon neural probe with integrated optical fibers for optogenetic modulation. *Lab Chip* **15**, 2939–2949 (2015).
- [198] Chamanzar, M., Borysov, M., Maharbiz, M. & Blanche, T. High-density optrodes for multi-scale electrophysiology and optogenetic stimulation. In *2014 36th Annual International Conference of the IEEE Engineering in Medicine and Biology Society (EMBC)*, 6838–6841 (2014).
- [199] Hoffman, L. *et al.* High-Density optrode-electrode neural probe using SixNy photonics for in vivo optogenetics (2015).
- [200] Im, M., Cho, I.-J., Wu, F., Wise, K. & Yoon, E. A dual-shank neural probe integrated with double waveguides on each shank for optogenetic applications. In *2011 Annual International Conference of the IEEE Engineering in Medicine and Biology Society, EMBC*, 5480–5483 (2011).
- [201] Fan, B. *et al.* A polycrystalline diamond-based, hybrid neural interfacing probe for optogenetics. In *2015 28th IEEE International Conference on Micro Electro Mechanical Systems (MEMS)*, 616–619 (2015).
- [202] Wu, F. *et al.* Monolithically Integrated  $\mu$ LEDs on Silicon Neural Probes for High-Resolution Optogenetic Studies in Behaving Animals. *Neuron* **88**, 1136–1148 (2015).
- [203] Zhang, J. *et al.* Integrated device for optical stimulation and spatiotemporal electrical recording of neural activity in light-sensitized brain tissue. *J. Neural Eng.* **6**, 055007 (2009).
- [204] Wang, J. *et al.* Integrated device for combined optical neuromodulation and electrical recording for chronic in vivo applications. *J. Neural Eng.* **9**, 016001 (2012).

- [205] Kwon, K. Y., Lee, H.-M., Ghovanloo, M., Weber, A. & Li, W. A wireless slanted optrode array with integrated micro leds for optogenetics. In *2014 IEEE 27th International Conference on Micro Electro Mechanical Systems (MEMS)*, 813–816 (2014).
- [206] Kwon, K. Y., Lee, H.-M., Ghovanloo, M., Weber, A. & Li, W. Design, fabrication, and packaging of an integrated, wirelessly-powered optrode array for optogenetics application. *Frontiers in Systems Neuroscience* **69** (2015).
- [207] Lee, J., Ozden, I., Song, Y.-K. & Nurmikko, A. V. Transparent intracortical microprobe array for simultaneous spatiotemporal optical stimulation and multichannel electrical recording. *Nat Meth* **12**, 1157–1162 (2015).
- [208] Hayashi, Y., Tagawa, Y., Yawata, S., Nakanishi, S. & Funabiki, K. Spatio-temporal control of neural activity in vivo using fluorescence microendoscopy. *European Journal of Neuroscience* **36**, 2722–2732 (2012).
- [209] Kwon, K. Y., Sirowatka, B., Li, W. & Weber, A. Opto- $\mu$ ECoG Array: Transparent  $\mu$ ECoG Electrode Array and Integrated LEDs for Optogenetics. In *2012 IEEE Biomedical Circuits and Systems Conference (BioCAS)*, 164–167 (2012).
- [210] Buzsáki, G. *et al.* Tools for Probing Local Circuits: High-Density Silicon Probes Combined with Optogenetics. *Neuron* **86**, 92–105 (2015).
- [211] Fan, B. & Li, W. Miniaturized optogenetic neural implants: a review. *Lab Chip* **15**, 3838–3855 (2015).
- [212] Dufour, S. & De Koninck, Y. Optrodes for combined optogenetics and electrophysiology in live animals. *Neurophoton* **2**, 031205–031205 (2015).
- [213] Grosenick, L., Marshel, J. H. & Deisseroth, K. Closed-loop and activity-guided optogenetic control. *Neuron* **86**, 106–139 (2015).
- [214] Franssila, S. *Introduction to Microfabrication* (Wiley-Blackwell, Chichester, West Sussex England, 2010), 2nd edition edition edn.
- [215] Bhushan, B. (ed.) *Springer Handbook of Nanotechnology* (Springer Berlin Heidelberg, Berlin, Heidelberg, 2010). URL <http://link.springer.com/10.1007/978-3-642-02525-9>.
- [216] Zahn, J. D. *Methods in bioengineering biomicrofabrication and biomicrofluidics* (Artech House, Boston, 2010).
- [217] Mack, C. *Fundamental Principles of Optical Lithography: The Science of Microfabrication* (John Wiley & Sons, Chichester, West Sussex, England ; Hoboken, NJ, USA, 2007), 1 edn.
- [218] Chen, Y. Nanofabrication by electron beam lithography and its applications: A review. *Microelectronic Engineering* **135**, 57–72 (2015).
- [219] Ocola, L. E., Rue, C. & Maas, D. High-resolution direct-write patterning using focused ion beams. *MRS Bulletin* **39**, 336–341 (2014).
- [220] Williams, K. & Muller, R. Etch rates for micromachining processing. *Journal of Microelectromechanical Systems* **5**, 256–269 (1996).
- [221] Williams, K., Gupta, K. & Wasilik, M. Etch rates for micromachining processing-Part II. *Journal of Microelectromechanical Systems* **12**, 761–778 (2003).
- [222] Shikida, M., Sato, K., Tokoro, K. & Uchikawa, D. Comparison of anisotropic etching properties between KOH and TMAH solutions. In *Twelfth IEEE International Conference on Micro Electro Mechanical Systems, 1999. MEMS '99*, 315–320 (1999).
- [223] Nojiri, K. *Dry Etching Technology for Semiconductors* (Springer, 2014).
- [224] Chi, T., Ballinger, T., Olds, R. & Zecchino, M. Surface texture analysis using dektak stylus profilers. *Veeco Instruments Inc* (2004).
- [225] Rothen, A. The Ellipsometer, an Apparatus to Measure Thicknesses of Thin Surface Films. *Review of Scientific Instruments* **16**, 26–30 (1945).

- [226] Balde, J. W. (ed.) *Foldable Flex and Thinned Silicon Multichip Packaging Technology*, vol. 1 of *Emerging Technology in Advanced Packaging Series* (Springer US, Boston, MA, 2003). URL <http://link.springer.com/10.1007/978-1-4615-0231-9>.
- [227] Colinge, J.-P. *Silicon-on-Insulator Technology: Materials to VLSI* (Springer US, Boston, MA, 1997). URL <http://link.springer.com/10.1007/978-1-4757-2611-4>.
- [228] Li, Y. *Microelectronic Applications of Chemical Mechanical Planarization* (John Wiley & Sons, 2008).
- [229] Lizotte, T. Laser dicing of chip scale and silicon wafer scale packages. In *Electronics Manufacturing Technology Symposium, 2003. IEMT 2003. IEEE/CPMT/SEMI 28th International*, 1–5 (2003).
- [230] Lu, D. & Wong, C. (eds.) *Materials for Advanced Packaging* (Springer US, Boston, MA, 2009). URL <http://link.springer.com/10.1007/978-0-387-78219-5>.
- [231] Harman, G. *Wire Bonding in Microelectronics* (McGraw Hill Professional, 2009).
- [232] Black, J. *Biological Performance of Materials: Fundamentals of Biocompatibility* (CRC Press, Boca Raton, 2005), 4 edn.
- [233] Cohen, M. R. & Newsome, W. T. What electrical microstimulation has revealed about the neural basis of cognition. *Current Opinion in Neurobiology* **14**, 169–177 (2004).
- [234] Penfield, W. & Perot, P. The Brain's Record of Auditory and Visual Experience. *Brain* **86**, 595–696 (1963).
- [235] Salzman, C. D., Britten, K. H. & Newsome, W. T. Cortical microstimulation influences perceptual judgements of motion direction. *Nature* **346**, 174–177 (1990).
- [236] Deisseroth, K. Optogenetics. *Nat Meth* **8**, 26–29 (2011).
- [237] CadSoft EAGLE PCB Design Software. URL <http://www.cadsoftusa.com/>.
- [238] Eurocircuits - Online PCB Prototype and small series specialist. URL <http://www.eurocircuits.com/>.
- [239] mcxyz.c. URL <http://omlc.org/software/mc/mcxyz/index.html>.
- [240] Schüz, A. & Palm, G. Density of neurons and synapses in the cerebral cortex of the mouse. *J. Comp. Neurol.* **286**, 442–455 (1989).
- [241] Elwassif, M., Kong, Q., Vazquez, M. & Bikson, M. Bio-Heat Transfer Model of Deep Brain Stimulation Induced Temperature changes. In *28th Annual International Conference of the IEEE Engineering in Medicine and Biology Society, 2006. EMBS '06*, 3580–3583 (2006).
- [242] Andersen, P. & Moser, E. I. Brain temperature and hippocampal function. *Hippocampus* **5**, 491–498 (1995).
- [243] Stujenske, J. M., Spellman, T. & Gordon, J. A. Modeling the Spatiotemporal Dynamics of Light and Heat Propagation for In Vivo Optogenetics. *Cell Reports* **12**, 525–534 (2015).
- [244] SCS Parylene Properties (2007). URL <http://scscoatings.com/corporate/technical-library/>.
- [245] Pennes, H. H. Analysis of Tissue and Arterial Blood Temperatures in the Resting Human Forearm. *Journal of Applied Physiology* **1**, 93–122 (1948).
- [246] Smith, A. N., Christian, M. P., Firebaugh, S. L., Cooper, G. W. & Jamieson, B. G. Predicting and managing heat dissipation from a neural probe. *Biomed Microdevices* **17**, 1–9 (2015).
- [247] Li, Y. *et al.* Thermal analysis of injectable, cellular-scale optoelectronics with pulsed power. *Proc. R. Soc. A* **469**, 20130142 (2013).

- [248] Becker, S. & Kuznetsov, A. *Heat Transfer and Fluid Flow in Biological Processes* (Academic Press, 2014).
- [249] Welch, A. J. & Gemert, M. J. v. *Optical-Thermal Response of Laser-Irradiated Tissue* (Springer Science & Business Media, 2011).
- [250] Niemz, M. H. *Laser-Tissue Interactions: Fundamentals and Applications* (Springer, Berlin u.a., 2007), 3rd ed. 2004 edition edn.
- [251] Long, G. *et al.* Histological and Finite Element Analysis of Cell Death due to Irreversible Electroporation. *Technol Cancer Res Treat* **13**, 561–569 (2014).
- [252] Sherar, M. D. *et al.* Comparison of thermal damage calculated using magnetic resonance thermometry, with magnetic resonance imaging post-treatment and histology, after interstitial microwave thermal therapy of rabbit brain. *Phys. Med. Biol.* **45**, 3563 (2000).
- [253] Shrestha, R., Choi, T.-Y., Chang, W. & Kim, D. A High-Precision Micropipette Sensor for Cellular-Level Real-Time Thermal Characterization. *Sensors (Basel)* **11**, 8826–8835 (2011).
- [254] Szentágothai, J. The modular architectonic principle of neural centers. In *Reviews of Physiology, Biochemistry and Pharmacology, Volume 98*, no. 98 in *Reviews of Physiology, Biochemistry and Pharmacology*, 11–61 (Springer Berlin Heidelberg, 1983). URL <http://link.springer.com/chapter/10.1007/BFb0033866>. DOI: 10.1007/BFb0033866.
- [255] Markram, H. *et al.* Interneurons of the neocortical inhibitory system. *Nat Rev Neurosci* **5**, 793–807 (2004).
- [256] Rudy, B., Fishell, G., Lee, S. & Hjerling-Leffler, J. Three groups of interneurons account for nearly 100% of neocortical GABAergic neurons. *Devel Neurobio* **71**, 45–61 (2011).
- [257] Houser, C. R., Vaughn, J. E., Hendry, S. H. C., Jones, E. G. & Peters, A. GABA neurons in the cerebral cortex. *Cerebral cortex* **2**, 63–89 (1984).
- [258] Ascoli, G. A. *et al.* Petilla terminology: nomenclature of features of GABAergic interneurons of the cerebral cortex. *Nat Rev Neurosci* **9**, 557–568 (2008).
- [259] Xu, H., Jeong, H.-Y., Tremblay, R. & Rudy, B. Neocortical Somatostatin-Expressing GABAergic Interneurons Disinhibit the Thalamorecipient Layer 4. *Neuron* **77**, 155–167 (2013).
- [260] Bortone, D. S., Olsen, S. R. & Scanziani, M. Translaminar Inhibitory Cells Recruited by Layer 6 Corticothalamic Neurons Suppress Visual Cortex. *Neuron* **82**, 474–485 (2014).
- [261] Harris, K. D. & Shepherd, G. M. G. The neocortical circuit: themes and variations. *Nat Neurosci* **18**, 170–181 (2015).
- [262] Pala, A. & Petersen, C. C. H. In Vivo Measurement of Cell-Type-Specific Synaptic Connectivity and Synaptic Transmission in Layer 2/3 Mouse Barrel Cortex. *Neuron* **85**, 68–75 (2015).
- [263] Klusta-Team. URL <https://github.com/klusta-team>.
- [264] Schmitzer-Torbert, N., Jackson, J., Henze, D., Harris, K. & Redish, A. D. Quantitative measures of cluster quality for use in extracellular recordings. *Neuroscience* **131**, 1–11 (2005).
- [265] Sakata, S. & Harris, K. D. Laminar Structure of Spontaneous and Sensory-Evoked Population Activity in Auditory Cortex. *Neuron* **64**, 404–418 (2009).
- [266] Sakata, S. & Harris, K. D. Laminar-dependent effects of cortical state on auditory cortical spontaneous activity. *Front. Neural Circuits* **6**, 109 (2012).
- [267] Buzsaki, G. *Rhythms of the Brain* (Oxford University Press, 2006).

- [268] Montemurro, M. A., Rasch, M. J., Murayama, Y., Logothetis, N. K. & Panzeri, S. Phase-of-Firing Coding of Natural Visual Stimuli in Primary Visual Cortex. *Current Biology* **18**, 375–380 (2008).
- [269] Pitts, W. Investigations on synaptic transmission. In *Cybernetics, Trans. 9th Conf. Josiah Macy, New York*, 159–162 (1952).
- [270] Nicholson, C. & Freeman, J. A. Theory of current source-density analysis and determination of conductivity tensor for anuran cerebellum. *Journal of Neurophysiology* **38**, 356–368 (1975).
- [271] Chen, Y., Dhamala, M., Bollimunta, A., Schroeder, C. & Ding, M. Current Source Density Analysis of Ongoing Neural Activity: Theory and Application. In Vertes, R. P., Stackman Jr., R. W. & Jr, R. W. S. (eds.) *Electrophysiological Recording Techniques*, no. 54 in *Neuromethods*, 27–40 (Humana Press, 2011). URL [http://dx.doi.org/10.1007/978-1-60327-202-5\\_2](http://dx.doi.org/10.1007/978-1-60327-202-5_2). DOI: 10.1007/978-1-60327-202-5\_2.
- [272] Freeman, J. A. & Nicholson, C. Experimental optimization of current source-density technique for anuran cerebellum. *Journal of Neurophysiology* **38**, 369–382 (1975).
- [273] Clark, K. L., Armstrong, K. M. & Moore, T. Probing neural circuitry and function with electrical microstimulation. *Proceedings of the Royal Society of London B: Biological Sciences* rspb20102211 (2011).
- [274] Blanche, T. J., Spacek, M. A., Hetke, J. F. & Swindale, N. V. Polytrodes: High-Density Silicon Electrode Arrays for Large-Scale Multiunit Recording. *Journal of Neurophysiology* **93**, 2987–3000 (2005).
- [275] Yuste, R. From the neuron doctrine to neural networks. *Nat Rev Neurosci* **16**, 487–497 (2015).
- [276] Buzsáki, G. Neural Syntax: Cell Assemblies, Synapsembles, and Readers. *Neuron* **68**, 362–385 (2010).
- [277] Hebb, D. O. *The Organization of Behavior* (John Wiley & Sons Inc, New York, 1949). URL <http://www.biblio.com/book/organization-behavior-donald-hebb/d/458613292>. Quantity Available: 1.
- [278] Hottowy, P. *et al.* Properties and application of a multichannel integrated circuit for low-artifact, patterned electrical stimulation of neural tissue. *J Neural Eng* **9**, 066005 (2012).
- [279] RHD2000 Amplifier Chips | Intan Technologies. URL [http://www.intantech.com/products\\_RHD2000.html](http://www.intantech.com/products_RHD2000.html).
- [280] Gunning, D. E. *High Density Microelectrode Arrays for In Vitro Retinal Studies*. Ph.D. thesis, University of Glasgow, Glasgow (2007).
- [281] Lei, X. *et al.* SiC protective coating for photovoltaic retinal prosthesis. *J. Neural Eng.* **13**, 046016 (2016).
- [282] Iliescu, C. & P., D. PECVD Amorphous Silicon Carbide ( $\alpha$ -SiC) Layers for MEMS Applications. In Hijikata, Y. (ed.) *Physics and Technology of Silicon Carbide Devices* (InTech, 2012). URL <http://www.intechopen.com/books/physics-and-technology-of-silicon-carbide-devices/pecvd-amorphous-silicon-carbide-sic-layers-for-mems-applications>.
- [283] Piccirillo, A. & Gobbi, A. L. Physical-Electrical Properties of Silicon Nitride Deposited by PECVD on III–V Semiconductors. *J. Electrochem. Soc.* **137**, 3910–3917 (1990).
- [284] Gunning, D. E. *et al.* Performance of ultra-high-density microelectrode arrays. *Nuclear Instruments and Methods in Physics Research Section A: Accelerators, Spectrometers, Detectors and Associated Equipment* **576**, 215–219 (2007).

- [285] Iwai, Y., Honda, S., Ozeki, H., Hashimoto, M. & Hirase, H. A simple head-mountable LED device for chronic stimulation of optogenetic molecules in freely moving mice. *Neuroscience Research* **70**, 124–127 (2011).
- [286] Park, S. I. *et al.* Ultraminiaturized photovoltaic and radio frequency powered optoelectronic systems for wireless optogenetics. *J. Neural Eng.* **12**, 056002 (2015).
- [287] Kendall Research Systems. URL <http://www.kendallresearchsys.com/>.
- [288] Zhang, S. *et al.* CMOS-Controlled Color-Tunable Smart Display. *IEEE Photonics Journal* **4**, 1639–1646 (2012).
- [289] Meitl, M. A. *et al.* Transfer printing by kinetic control of adhesion to an elastomeric stamp. *Nat Mater* **5**, 33–38 (2006).
- [290] X-Celeprint | Advanced Micro-Transfer-Printing Technology Solutions. URL <http://www.x-celeprint.com/#>.
- [291] Trindade, A. J. *et al.* Nanoscale-accuracy transfer printing of ultra-thin AlInGaN light-emitting diodes onto mechanically flexible substrates. *Applied Physics Letters* **103**, 253302 (2013).
- [292] Trindade, A. J. *et al.* Heterogeneous integration of gallium nitride light-emitting diodes on diamond and silica by transfer printing. *Opt. Express, OE* **23**, 9329–9338 (2015).
- [293] Boudet, A., Scharf, R., Dawson, M. & Mathieson, K. A diamond-based, hybrid optrode for multisite optogenetics. In *Frontiers in Optics 2016 (2016), paper FTh4D.5*, FTh4D.5 (Optical Society of America, 2016).
- [294] Ayub, S. *et al.* High-density probe with integrated thin-film micro light emitting diodes (LEDs) for optogenetic applications. In *2016 IEEE 29th International Conference on Micro Electro Mechanical Systems (MEMS)*, 379–382 (2016).
- [295] Element Six Synthetic Industrial Diamonds (2016). URL <http://www.e6.com>.
- [296] Diamond Materials GmbH (2016). URL <http://www.diamond-materials.com>.
- [297] Pop, E., Varshney, V. & Roy, A. K. Thermal properties of graphene: Fundamentals and applications. *MRS Bulletin* **37**, 1273–1281 (2012).
- [298] Zhang, Y. *et al.* Improved Heat Spreading Performance of Functionalized Graphene in Microelectronic Device Application. *Adv. Funct. Mater.* n/a–n/a (2015).
- [299] Charlieplexing - Reduced Pin-Count LED Display Multiplexing (APPLICATION NOTE 1880) (2003). URL <https://www.maximintegrated.com/en/app-notes/index.mvp/id/1880>.
- [300] Amkor Technology: 3d Packaging technology | Stacked Die Packaging | Package on Package PoP | Die Stacking. URL <http://www.amkor.com/go/3D-Stacked-Die-Packaging>.
- [301] Micron Technology, Inc. - Home | Memory and Storage Solutions (2016). URL <https://www.micron.com/>.
- [302] Banks, D. *Microengineering, MEMS, and Interfacing: A Practical Guide* (CRC Press, Boca Raton, FL, 2006).
- [303] Choi, H. W. *et al.* GaN micro-light-emitting diode arrays with monolithically integrated sapphire microlenses. *Applied Physics Letters* **84**, 2253–2255 (2004).
- [304] Tsonev, D. *et al.* A 3-Gb/s Single-LED OFDM-Based Wireless VLC Link Using a Gallium Nitride. *IEEE Photonics Technology Letters* **26**, 637–640 (2014).
- [305] Lasance, C. J. M. & Poppe, A. *Thermal Management for LED Applications* (Springer Science & Business Media, 2013).
- [306] Chamanzar, M. *et al.* Tether-less implantable upconverting microscale light bulbs for deep brain neural stimulation and imaging. In *2015 Conference on Lasers and Electro-Optics (CLEO)*, 1–2 (2015).

- [307] Seo, D., Carmena, J. M., Rabaey, J. M., Alon, E. & Maharbiz, M. M. Neural Dust: An Ultrasonic, Low Power Solution for Chronic Brain-Machine Interfaces. arXiv e-print 1307.2196 (2013). URL <http://arxiv.org/abs/1307.2196>.
- [308] Seo, D. *et al.* Wireless Recording in the Peripheral Nervous System with Ultrasonic Neural Dust. *Neuron* **91**, 529–539 (2016).
- [309] Winder, S. *Power Supplies for LED Driving* (Newnes, 2011).
- [310] Bryant, J. Current-Output Circuit Techniques Add Versatility to Your Analog Toolbox (2014). URL [http://www.analog.com/library/analogdialogue/archives/48-04/current\\_output.html](http://www.analog.com/library/analogdialogue/archives/48-04/current_output.html).
- [311] Carter, B. & Brown, T. R. Handbook of Operational Amplifier Applications (Rev. A) (2001).

# List of Publications

## Journals

- [1] Scientific Reports, June 2016  
*Depth-specific optogenetic control in vivo with a scalable, high-density  $\mu$ LED neural probe*  
R. Scharf, T. Tsunematsu, N. McAlinden, M. Dawson, S. Sakata, K. Mathieson  
doi: 10.1038/srep28381

## Conferences

(presenter highlighted in bold)

- [1] UK Nitrides Consortium Winter Conference 2015, Nottingham, UK  
*GaN-on-Si micro-LED probes for site-specific optogenetic activation of cortical neurons*  
**R. Scharf**, S. Sakata, D. Zhu, E. Gu, I. Watson, D. Wallis, C. Humphreys, M. Dawson,  
K. Mathieson
- [2] SPIE Photonics West 2015, San Francisco, USA  
*MicroLED probes for optogenetic control of cortical circuits* (Invited Paper)  
**K. Mathieson**, R. Scharf, N. McAlinden, E. Gu, S. Sakata, M. Dawson
- [3] SU2P Symposium 2015, St Andrews, UK  
 *$\mu$ LED probes for minimally invasive depth-specific optogenetic control in vivo*  
**R. Scharf**, K. Mathieson
- [4] BNA2015: FESTIVAL OF NEUROSCIENCE, Edinburgh, UK  
*Micro-LED probes for site-specific optogenetic activation of neural circuits at depth*  
**R. Scharf**, T. Tsunematsu, M. Dawson, S. Sakata, K. Mathieson
- [5] 7<sup>th</sup> International IEEE EMBS Neural Engineering Conference, Montpellier, France  
 *$\mu$ LED probes for site-specific optogenetic neural activation*  
**R. Scharf**, T. Tsunematsu, I. Watson, E. Gu, M. Dawson, S. Sakata, K. Mathieson
- [6] Society for Neuroscience annual meeting 2015, Chicago, USA  
*Microscale LED probe for massively parallel optogenetic control at depth*  
S. Sakata, **R. Scharf**, N. McAlinden, T. Tsunematsu, E. Gu, M. Dawson, K. Mathieson